AUTHOR:

TITLE:

YEAR:

OpenAIR citation:

This work was submitted to- and approved by Robert Gordon University in partial fulfilment of the following degree:
_____

OPTIMIZATION OF IDENTIFICATION OF PARTICLE IMPACTS USING ACOUSTIC EMISSION

AMIN MOHAMMAD HEDAYETULLAH

A thesis submitted in partial fulfilment of the requirements of the Robert Gordon University for the degree of Doctor of Philosophy

April 2018

To my daughter

Maryam Binte Amin

You have changed the meaning of life for me

Acknowledgement

In the name of GOD, the most merciful

It is a great privilege to take this opportunity to show my gratitude to the people without whom I would not have been able to complete this research and thesis.

First of all, my principal supervisor Prof. Iain Steel who was there for me at all the highs and lows of my research and in my personal life; who supported me to the very last moment with all the expertise and inspiration. No word is sufficient to express my gratitude towards him.

Thanks to my co supervisor Dr. Ghazi Droubi and all the support staff, at RGU, for their time to time compassionate care to make this a reality.

It is an honour to remember at this very moment my parents who despite all the odds of life paved the way for me to receive the best possible education at an early age.

Last but not the least, my wife Rifath Faruque who sacrificed countless things, day in day out, just to make sure that I can live up to my dream. Thank you very much dear. Life would not have been same without you.

Abstract

Air borne or liquid-laden solid particle transport is a common phenomenon in various industrial applications. Solid particles, transported at severe operating conditions such as high flow velocity, can cause concerns for structural integrity through wear originated from particle impacts with structure. To apply Acoustic Emission (AE) in particle impact monitoring, previous researchers focused primarily on dry particle impacts on dry target plate and/or wet particle impacts on wet or dry target plate. For dry particle impacts on dry target plate, AE events energy, calculated from the recorded free falling or air borne particle impact AE signals, were correlated with particle size, concentration, height, target material and thickness. For a given system, once calibrated for a specific particle type and operating condition, this technique might be sufficient to serve the purpose. However, if more than one particle type present in the system, particularly with similar size, density and impact velocity, calculated AE event energy is not unique for a specific particle type. For wet particle impacts on dry or wet target plate (either submerged or in a flow loop), AE event energy was related to the particle size, concentration, target material, impact velocity and angle between the nozzle and the target plate. In these studies, the experimental arrangements and the operating conditions considered either did not allow any bubble formation in the system or even if there is any at least an order of magnitude lower in amplitude than the sand particle impact and so easily identifiable. In reality, bubble formation can be comparable with particle impacts in terms of AE amplitude in process industries, for example, sand production during oil and gas transportation from reservoir. Current practice is to calibrate an installed AE monitoring system against a range of sand free flow conditions. In real time monitoring, for a specific calibrated flow, the flow generated AE amplitude/energy is deducted from the recorded AE amplitude/energy and the difference is attributed to the sand particle impacts. However, if the flow condition changes, which often does in the process industry, the calibration is not valid anymore and AE events from bubble can be misinterpreted as sand particle impacts and vice versa.

In this research, sand particles and glass beads with similar size, density and impact velocity have been studied dropping from 200 mm on a small cylindrical stepped mild steel coupon as a target plate. For signal recording purposes, two identical broadband AE sensors are installed, one at the centre and one 30 mm off centred, on the opposite of the impacting surface. Signal analysis have been carried out by evaluating 7 standard AE parameters (amplitude, energy, rise time, duration, power spectral density(PSD), peak frequency at PSD and spectral centroid) in the time and frequency domain and time-frequency domain analysis have been performed applying

Gabor Wavelet Transform. The signal interpretation becomes difficult due to reflections, dispersions and mode conversions caused by close proximity of the boundaries. So, a new signal analysis parameter - frequency band energy ratio - has been proposed. This technique is able to distinguish between population of two very similar groups (in terms of size and mass and energy) of sand particles and glass beads, impacting on mild steel based on the coefficient of variation (C_v) of the frequency band AE energy ratios. To facilitate individual particle impact identification, further analysis has been performed using Support Vector Machine (SVM) based classification algorithm using 7 standard AE parameters, evaluated in both the time and frequency domain. Available data set has been segmented into two parts of training set (80%) and test set (20%). The developed model has been applied on the test data for model performance evaluation purpose. The overall success rate of individually identifying each category (PLB, Glass bead and Sand particle impacts) at S1 has been found as 86% and at S2 as 92%.

To study wet particle impacts on wet target surface, in presence of bubbles, the target plate has been sealed to a cylindrical perspex tube. Single and multiple sand particles have been introduced in the system using a constant speed blower to impact the target surface under water loading. Two sensor locations, used in the previous sets of experiments, have been monitored. From frequency domain analysis it has been observed that characteristic frequency for particle impacts are centred at 300-350 kHz and for bubble formations are centred at 135 – 150 kHz. Based upon this, two frequency bands 100 – 200 kHz (E_1) and 300 – 400 kHz (E_3) and the frequency band energy ratio ($\frac{E_3}{E_1,}$) have been identified as optimal for identification particle impacts for the given system. $\frac{E_3}{E_1,} > 1$ has been associated with particle impacts and $\frac{E_3}{E_1,} < 1$ has been associated with bubble formations. Applying these frequency band energy ratios and setting an amplitude threshold, an automatic event identification technique has been developed for identification of sand particle impacts in presence of bubbles. The method developed can be used to optimize the identification of sand particle impacts. The optimal setting of an amplitude threshold is sensitive to number of particles and noise levels. A high threshold of say 10% will clearly identify sand particle impacts but for multiparticle tests is likely to not detect about 20% of lower (impact) energy particles. A threshold lower than 3% is likely to result in detection of AE events with poor frequency content and wrong classification of the weakest events. Optimal setting of the parameters used in the framework such as thresholds, frequency bands and ratios of AE energy is likely to make identification of sand particle impacts in the laboratory environment within 10% possible. For this technique, once the optimal frequency bands and ratios have been identified, then an added advantage is that calibration of the signal levels is not required.

Table of Contents

List of Figures

List of Tables

Abbreviations

ADC	Analog to digital converter
AE	Acoustic Emission
AET	Acoustic Emission Testing
CFRP	Carbon fibre reinforced polymer
CV	Coefficient of variation
DAQ	Data acquisition
FE	Finite Element
Fixed	Target plate attached to the Perspex cylinder
Fixed-Water	Target plate attached to Perspex cylinder and loaded under water
FN	False Negative
FP	False Positive
Free	Target plate resting freely on the wooden blocks
FT	Fourier Transform
ICDM	International Conference on data mining
IEEE	Institute of Electrical and Electronics Engineers
KE	Kinetic Energy
k-NN	K – Nearest Neighbours
Masked	Target plate attached to Perspex cylinder and target surface masked
Masked-Water	Target plate attached to Perspex cylinder, target surface masked and loaded under water
MSPI- Masked	Multiple (ten) sand particle impact tests after masking the whole target plate except 10 mm² at the centre to allow the particle impacts.
MSPI – Water	Multiple (three) sand particle impact tests without masking the water loaded target plate
NDT	Non destructive testing
NPV	Negative prediction value
PCA	Principal component analysis
PF	Pulverised Fuel
PIND	Particle impact noise detector
PLB	Pencil Lead Break
PPV	Positive prediction value
PSD	Power Spectral Density
PZT	Lead Zirconate Titanate

P-wave	Primary wave
ROC	Receptor Operating Characteristic
RMS	Root mean square
SBG	Single bubble generation in Perspex tube water column
SNR	Signal to noise ratio
SOM	Self-organizing map
SSPI - Air	Single sand particle impact on the target plate in air
SSPI - Masked	Single sand particle impact tests after masking the whole target plate except 10 mm² at the centre to allow the particle impacts.
SSPI – Water	Single sand particle impact tests without masking the water loaded target plate
STFT	Short time Fourier Transform
SV	Support Vector
SVM	Support vector machine
S-wave	Secondary wave
TP	True Positive
TN	True Negative
WT	Wavelet Transform

Nomenclature

c_l	Longitudinal wave speed
c_s	Shear wave speed
c_R	Rayleigh wave speed
S_n	Symmetric (extensional) modes
A_n	Anti symmetric (flexural) modes
S_0	Fundamental symmetric (extensional) mode
A_0	Fundamental anti symmetric (flexural) modes
f_0	Natural frequency of oscillation for zeroth mode volume pulsation
f_n	Frequency for the nth mode
P_0	Static pressure
γ	Ratio of the specific heat of the gas in the bubble
R_0	Mean radius of the bubble
ρ_l	Density of the liquid
T	Surface tension
E	Young's modulus of elasticity
ρ	density of the material
ν	Poisson's ratio
$\mathbf{w}$	SVM Decision boundary vector
$\mathbf{x}$	Feature vector (input vector)
b	Scalar bias (Threshold)
i	Iteration number
n	Training set number
$f(x)$	SVM decision function
α_i	Weighting vector
$\beta\ (x)$	Transformation function
$K(\mathbf{x}.\mathbf{y})$	Kernel function
C	Upper limit for α_i
γ	Parameter controlling width of the radial basis function for SVM
$V(t)$	Sensor output voltage at time t
t	time
Δt	Time window for calculating AE energy
E	Acoustic emission energy
E_1	AE energy between 100 – 200 kHz
E_2	AE energy between 200 – 300 kHz
E_3	AE energy between 300 – 400 kHz
E_{12}	AE energy between 100 – 200 kHz & 200 – 300 kHz
E_{13}	AE energy between 100 – 200 kHz & 300 – 400 kHz
E_{23}	AE energy between 200 – 300 kHz & 300 – 400 kHz
E_a	AE energy between 100 – 500 kHz
σ	Standard deviation
μ	Mean
C_v	Coefficient of variation

Chapter 1   Introduction

1.1 Background and Motivation

Transport of solid particles in gas or liquid flow is widespread in different industrial applications. For example, pharmaceutical, chemical, food processing, cement industries, transportation of Pulverised Fuel (PF) in coal-fired power plants and petrochemical (1,2) applications. A simple and reliable method for monitoring solid particle flow in fluid is required for system diagnosis as well as for performance monitoring of operations and processes. Under severe corrosive, high pressure/ temperature conditions non-intrusive monitoring systems, such as, acoustic emission, are more suitable (1,3) . In processes involving the movement of solid particles, acoustic emissions from the stress wave of the confining material can be generated from impingement or sliding of the moving particles among themselves or with the wall and from dynamics of the carrier fluid (3,4) . Acoustic emission sound generated in this way is a manifestation of the process operating system and hence can be used for monitoring purposes (4) .

Various Acoustic Emission (AE) parameters have been used to interpret the acquired AE signals obtained from the sensors monitoring the processes under consideration. In case of particle fluidization in a small fluidized bed granulator, mean AE amplitude value has been used for detecting fluidization activity by correlating with dimensionless excess gas velocity and dimensionless expanded bed height (4) . In a study (5) , a particle size distribution model is developed from the quantitative relationship between energy percentage of AE signals for different Wavelet scales and the particle sizes. In another study (6) , it has been shown that the frequency of the peak pressure is inversely proportional to the particle size and particle density and directly proportional to the particle impact velocity. A quantitative model, based on statistical parameters in the time domain (maximum, minimum, mean, standard deviation, Root mean square (RMS), skew and kurtosis) & the first 52 spectral characteristics of power density spectrum (0-200 Hz in the frequency domain), deduced a relationship for feed pressure, solid concentration, volume flow rate and mass flow rate from AE signals in a hydro cyclone (7) . RMS of the AE signals have been used for identifying the end point of solid-solid binary mixing processes and for the drying condition of wet particles or coating of solid particles with a liquid (8) . In petrochemical industry, where erosion due to sand particles, produced from the reservoir along with different petroleum fluid, is a major concern for equipment integrity, an unacceptable amount of sand production can in some cases be marked by an acoustic emission signal threshold once the system is calibrated for different sand concentration with corresponding AE amplitude/energy (2) .

For liquid/gas flow, AE signal variation from hydrodynamic pressure fluctuations can be used for flow regime identifications (8–10) .

A change in the operating condition results in calibrated AE signals being inaccurately interpreted. For example, in the case of sand monitoring in the petroleum industry, it is necessary to chart the background noise level over a representative flow range for a sand free condition and tabulation of sand injection at a reference rate in the fluid flow for sand noise. A fitted function curve or some form of look up table is prepared based on the obtained data. The level of noise exceeding a set look up value of background noise level is thus ascribed to sand production. The main drawback of this procedure is if the calibration drifts off by changing flow regime or flow composition, which it often does in practical cases in the form of bubble formation or other contaminant production, the calibrated background noise level is no longer a true representation of the scenario and hence the calculated sand rate from the output will be over or under estimated (11,12).

Particle impacts using AE techniques have drawn the attention of many researchers (13–19). From literature, the focus of the studies can be broadly divided into dry particle impacts on dry target plate and wet particle impacts on wet or dry target plate.

In case of dry particle impacts on dry target plate, free falling or air borne particle impacts were studied varying particle size, concentration, height, target material and thickness (13,15,20). Recorded AE signals were analysed evaluating detected AE events energy and correlated with the considered variables. For a given system, once calibrated for a specific particle type and condition, this technique might be sufficient to serve the purpose. However, if more than one particle type present in the system, particularly with similar size, density and impact velocity, calculated AE event energy is not unique for a specific particle type and any AE energy based technique fails to distinguish between different particle types in the system, as identified in (16). From literature, in the earlier research works, attempt on distinguishing different particle types, with similar size, density and impact velocity, has not been observed.

In case of wet particle impacts on dry or wet target plate (either submerged or in a flow loop), studies were performed varying particle size, concentration, target material, impact velocity and angle between the nozzle and the target plate (16,17,19,21,22). In these researches also, AE event energy was related to varying physical properties of the system. Due to the experimental arrangements considered in these studies, AE events from bubble formations were either absent or easily identifiable for lower than particle impacts' amplitude characteristics. No methodical effort to study the particle impacts in presence of bubbles has been noticed.

For dry particle impacts on dry target plate, an AE technique to differentiate particles with similar size, density and velocity and for wet particle impacts on wet target plate, identifying particle impacts in presence of bubble formations will facilitate the monitoring of processes involving solid particle movements in presence of more than one flow constituents. These will enhance the current state of the art knowledge in the related field and have been considered in this research.

1.2 Research Aim

As mentioned in the previous section, typical AE systems calibration is based on amplitude or energy of the event and can be misleading if the calibration condition changes. The simplest possible change is the presence of more than one flow constituent.

The aim of the current research is to develop AE monitoring techniques to differentiate particles with similar size, density and velocity, for dry particle impacts on dry target plate and to identify particle impacts in presence of bubble formations, for wet particle impacts on wet target plate. In these cases, for a given system and operating condition, methods for establishing optimum performance are also considered in this research.

1.3 Research Methodology

To accomplish the aim of the research, a small mild steel target plate has been chosen. To study dry particle impacts, with similar size, density and impact velocity on dry target plate, similar sized sand and glass beads are dropped from the same height on the target plate under gravitational force in air. To study wet particle impacts in presence of bubbles, a separate set of experiments have been carried out introducing air laden sand particle impingement in water in the presence of bubbles. Opposite to the impacting surface on the target plate, two sensor positions, one at the centre and one 30 mm off centred, have been considered. The acquired signals have been analysed following a general framework established in this research, as presented in the Figure 1.1, which is divided into three major steps:

Step A: Source specific AE tests have been carried out at this stage. Signals are recorded at the two sensor positions using two identical sensors.

Step B: Acquired particle impacts AE signals have been analysed evaluating 7 standard Time and Frequency domain parameters (amplitude, energy, rise time, duration, power spectral density(PSD), peak frequency at PSD and spectral centroid). Gabor Wavelet Transform have been applied for Time-Frequency domain analysis.
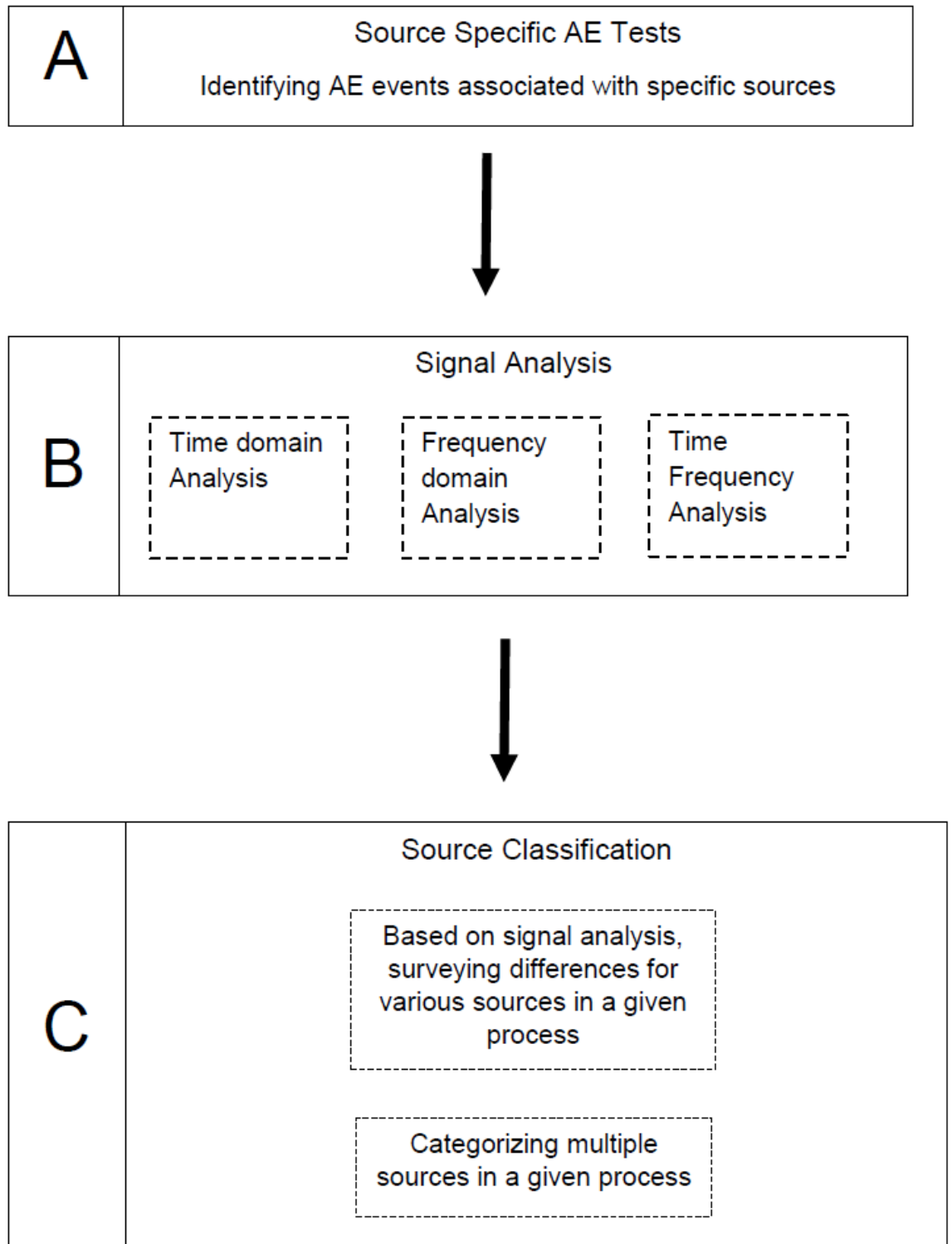
Figure 1.1: General analysis framework followed in this research.

Step C: Classification of sources have been performed. A frequency band energy ratio analysis technique has been proposed for source differentiation. For particle impacts in presence of bubbles experiments this technique has shown promising results

(Chapter 5). However, in case of particle impacts (glass beads and sand particles) with very similar properties (size, mass and energy) this can be useful to distinguish a population of particle impacts (Chapter 4). For individual similar type particle impact source identification, a further analysis, based on a Support Vector Machine (SVM) classification algorithm, has shown more potential.

1.4 Outline of the thesis

The thesis is outlined in the following manner

Chapter 1: Introduction

An overview of the brief background and motivation of the research is mentioned along with the research scope, aim & objectives. Research methodology and outcome of the research has been summarized.

Chapter 2: Literature Review

This chapter reviews published work related to the thesis topics. It includes standard AE system description, AE parameters, Frequency band signal analysis, and AE from particle impacts, AE from Bubble formations, Implication of wavelet transform in identifying different source types and Classification algorithm (Support Vector Machine) application in differentiating source types.

Chapter 3: Preliminary tests

A set of preliminary Pencil lead break (PLB) tests have been carried out for characterizing the sensor response on the target impact material used in this work. Sensor responses have been recorded & analysed for different fixtures and environments.

Chapter 4: Distinction of population of similar sized particle impacts on mild steel.

Similar sized sand particles and glass beads impacts with the mild steel surface, originated from free fall of the particles under gravitation from the same height in air is studied along with PLB. A frequency band energy ratio based signal analysis technique has been proposed to differentiate the population of the similar sized particles. The feasibility of SVM classification algorithm in identifying individual particles has been studied.

Chapter 5: An AE technique to distinguish sand particle impacts on mild steel target plate with fluid loading and air bubbles

Sand particle impacts on the mild steel target plate in the presence of bubbles is studied for both single and multiple particles. Sensitivity of the frequency band energy ratio, with respect to amplitude threshold, has been fully discussed in this experimental context.

Chapter 6: Discussion, Conclusion & Further recommendations

General discussions of the obtained results of the experiments are highlighted and conclusions are drawn. Further recommendations for future research has been made.

1.5 Highlights of the research

- Study of complex wave propagation on small thick, circular mild steel target plate with different fixtures and environments.
- Development and optimisation of a new frequency band energy ratio AE parameter.
- Discrimination between populations of particle impacts for sand and glass beads applying frequency band energy ratio.
- Identification of individual particle impacts for glass beads and sand particles using SVM classification algorithm.
- Discrimination of single and multiple sand particles from bubbles implementing frequency band energy ratio technique.
- Sensitivity study for quantification of sand particles using frequency band energy ratio and identification of optimum amplitude thresholds for the considered experimental setup.
- Evaluating an optimum sensor position on a short cylindrical mild steel surface under particle impacts.

Chapter 2   Literature Review

2.1 Introduction

This chapter introduces fundamentals of acoustic emission (AE), its advantages, limitations and the basic components of a data acquisition system (DAQ) used in acoustic emission testing (AET). A brief discussion on the acoustic wave propagation methods through the structure and various sources responsible for these wave generations is presented. Previous research works, related to particle impacts and bubble activities, are reviewed. A general discussion on various AE signal analysis techniques is followed by literature review on frequency and time frequency based AE signal analysis of particle impacts and bubble activities.

2.2 Acoustic Emission

Acoustic Emission (AE) refers to the transient elastic waves generated by the sudden internal stress redistribution of the materials due to changes in the internal structure. A structure subjected to an external stimulus like a change in pressure, load or temperature triggers a localized energy release in the form of stress waves. These stress waves propagate to the surface and with sensors and data acquisition equipment, can be recorded (23) . Figure 2.1 shows the basic of Acoustic emission detection principle.
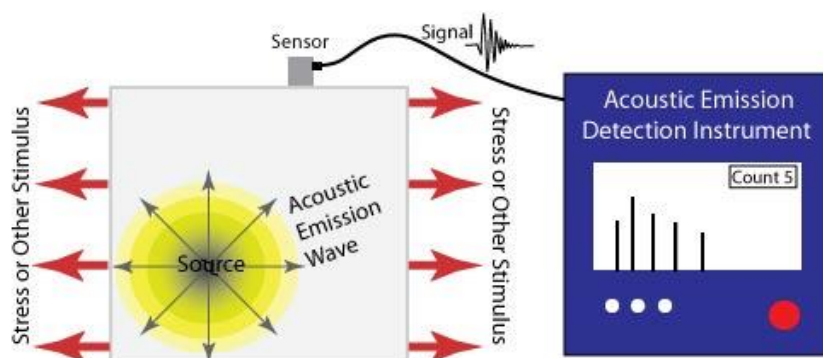
Figure 2.1: Acoustic Emission detection principle (23)

Acoustic emission is different from many other non-destructive testing (NDT) techniques in two aspects. First, with respect to origin of sources, AET is passive, sensing the wave energy released by the source, while other technics might involve external excitation of an object under examination. Second, AET deals with dynamic processes, or change, in a material, highlighting active features (e.g. crack growth) only (24) . AET monitors the sources of AE associated with processes or faults as opposed to the symptoms such as vibration response.

2.2.1 Advantages and Limitations

Like any other Non - destructive testing techniques, AET has its own advantages and limitations. The following are the major advantages of AET:

- Most of the machinery generated noise frequencies are less than 50 KHz. Using AE sensors of higher resonant frequencies than the mechanical noise frequencies ensure isolation from machinery related vibration signals which results in high signal to noise ratio (SNR) (25–27).

- AET can be used to monitor dynamic processes in real time without interrupting the normal operating condition (22,26–31).

- AET can be applied using a small number of sensors mounted on the surface of the structure or the specimen under consideration (29). Since the AE waves travel from the source to the sensor, event mapping is possible using AE testing procedures (29,32). In addition, inaccessible remote sources can be monitored using this technique (22,26).

The following are the main drawbacks of AET:

- In practice, high frequency resonant AE sensors are used predominantly as these are more sensitive than the broadband sensors. However, these narrow band sensors detect a small portion of the broad band signals emitted by an AE event (25). Also, High frequency signal sources, e.g., turbulence, electromagnetism, can interfere with signal acquisition (26).

- AE waves attenuate while propagating through the medium under test. In the near field, close to the source, due to geometric spreading a stress wave will attenuate. In the far field, absorption or conversion of elastic or kinetic energy of the acoustic wave into heat is prominent. Dissipation to adjacent media or scattering within the same medium due to inhomogeneity or geometric discontinuities can cause attenuation as well (25,33,34).

- AE events, in a bounded medium, can generate several wave modes in the medium which can propagate at the same time. Due to dispersion, wave modes of different frequencies travel through the medium at different speeds which can affect the acquired signal characteristics with respect to change in signal recording location (33,34).

In the following section, AE wave propagation through structures is discussed.

2.3 AE data acquisition system

Figure 2.2, shows a typical AE Data acquisition system; not all of these are mandatory for a given AE Data Acquisition System. Based upon specific requirement,

one or more component functionality can be merged together; even some components might be eliminated totally.

AE transducers: This transforms a local dynamic material displacement produced by a stress wave to an electrical signal. AE sensors are typically piezoelectric sensors made from special ceramic elements like lead zirconate titanate (PZT). Piezoelectric elements generate electric signals when mechanically strained. Other types of sensors include capacitive transducers, laser interferometers (35) .

Preamplifiers: Typically AE signals are very weak. So, to prevent signal loss a preamplifier is connected immediately after the transducer. Sometimes pre-amplifiers are embedded into the transducers (23) .

Filters: Signals are passed through filters to remove the environmental noise.

Amplifiers: Signals are amplified by an amplifier before sending it to the signal conditioning unit.
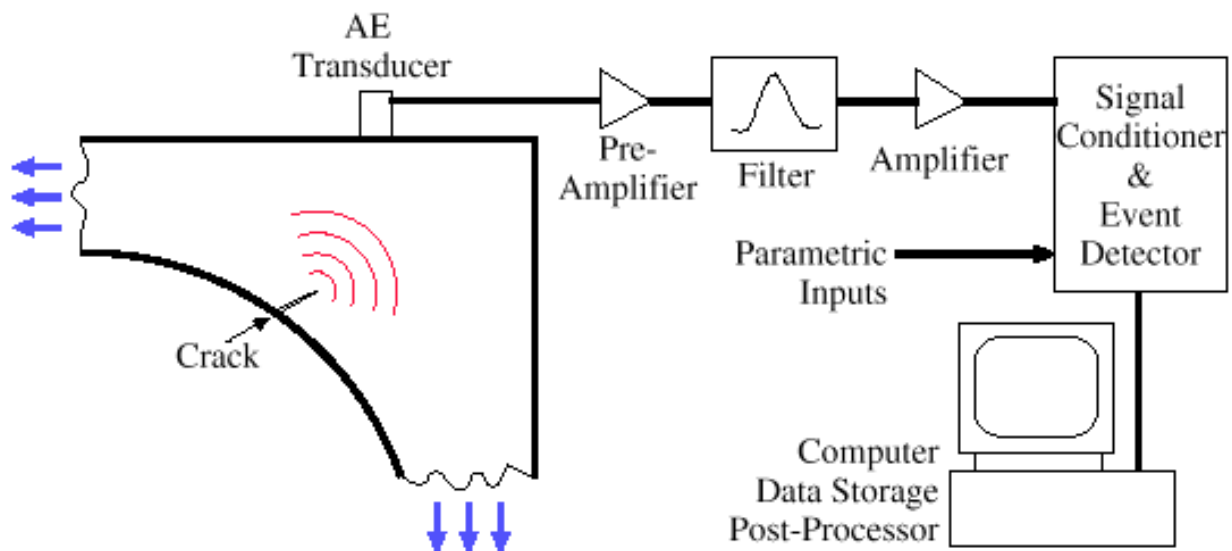
Figure 2.2: Typical AE Data Acquisition System (23)

Signal Conditioning Unit: Signal conditioning unit enhances the performance and the accuracy of the data acquisition system. Signal conditioning technologies include: amplification, attenuation, isolation, filtering, excitation, linearization, cold junction compensation, bridge completion (36) .

2.4 Wave propagation through structure

Impacts between two contacting bodies can cause local elastic deformation which in turn can propagate from the contact region as elastic waves. For an infinite media, only two types of waves are present: Longitudinal and Shear Waves. If the particles motion of the medium conveying the wave are back and forth along the direction of

propagation, it is called Longitudinal Wave (Primary or P-Wave) (37) , as shown in **Figure 2.3** (a).

(a)   (b)
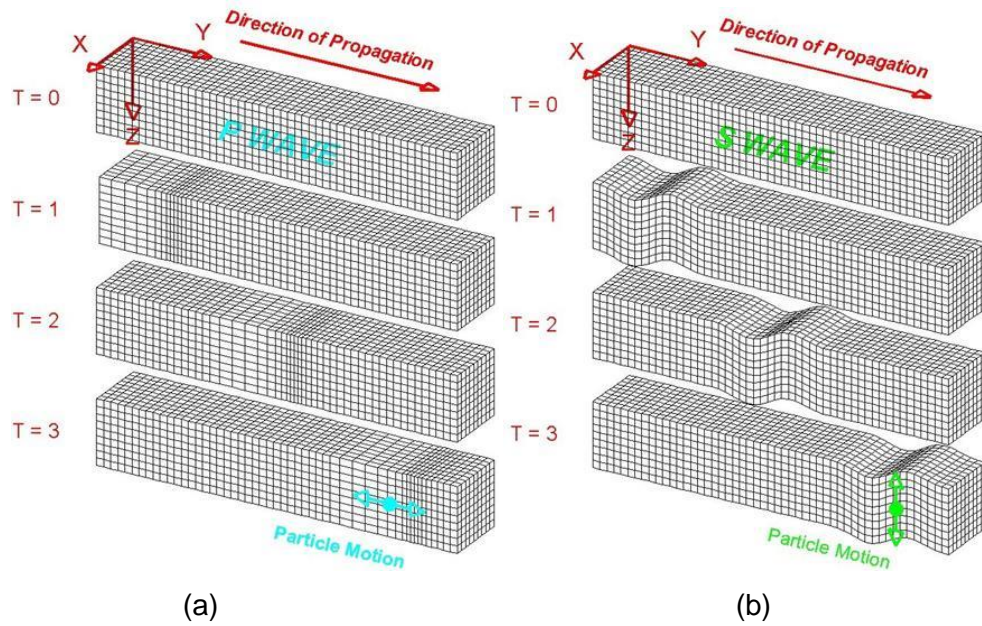
Figure 2.3 : (a) Longitudinal Wave, (b) Shear Wave (38) of an infinite solid medium

The speed (c_l) of the Longitudinal Wave is given by (39) :

$$c_l = \sqrt{\frac{E(1-\nu)}{\rho(1+\nu)(1-2\nu)}}$$ (2.1)

Where E is Young's modulus of elasticity, ρ is the and ν is Poisson's ratio of the material.

If the particles' motions of the medium conveying the wave are perpendicular to the direction of propagation of the wave itself, as shown in **Figure 2.3 (b)** then it is called Shear Wave (Transverse Wave, Secondary Wave or S-Wave) (37) .

The speed of the Shear Wave (c_s) is given by (39) :

$$c_s = \sqrt{\frac{E}{2\rho(1+\nu)}}$$ (2.2)

In the case of semi-infinite media, surface acoustic waves, named Rayleigh Waves (**Figure 2.4**), propagate along the surface of the medium. For Rayleigh Waves, particles in the surface layer move both up-down and back-forth tracing out elliptical paths (38) .
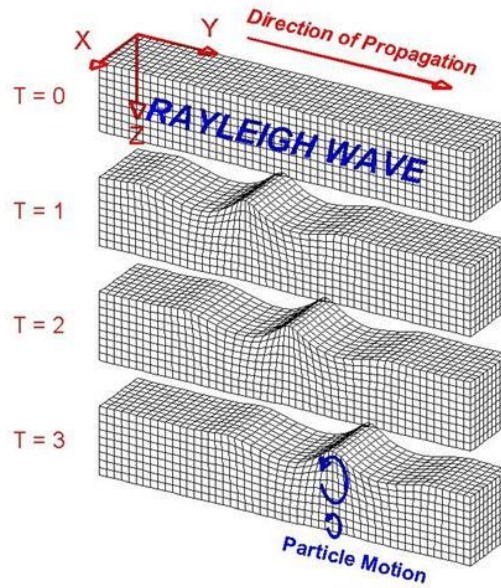
Figure 2.4: Rayleigh Wave in a semi infinite medium (38) .

A good approximation of the Rayleigh wave speed (c_R) is given by (40) :

$$c_R \cong \frac{0.862 + 1.14\nu}{1 + \nu} c_S \qquad \textbf{(2.3)}$$

The Rayleigh wave travels about at 90% of the shear wave speed (40) .

For double bounded media, e.g., plates, etc., transverse waves are trapped between the finite thickness of the media and called Lamb Waves. The relationship between the thickness and the wavelength induces different modes. Two main families of modes observed are : the symmetric (extensional) modes S_n and anti symmetric (flexural) modes A_n, where n is mode number (41) . In the first family, the motion is symmetrical (**Figure 2.5** (a)) about the median plane of the plate while for the second wave type it is asymmetrical (**Figure 2.5** (b)). For practical purposes, the lowest order (fundamental or parent) members of these families, denoted as S_0 and A_0 respectively, are the most important (42) .

(a)   (b)
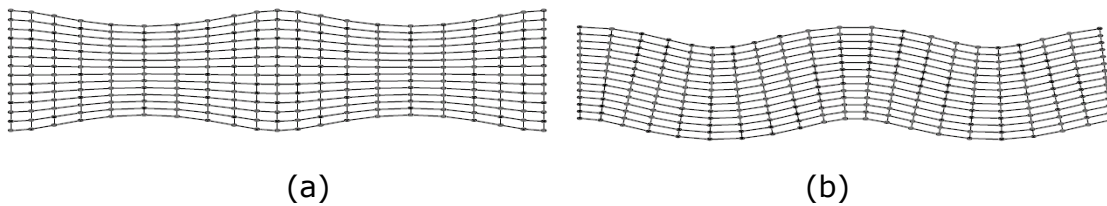
Figure 2.5: (a) Symmetric Lamb Wave, (b) Anti Symmetric Lamb Wave in a double bounded media (40)

To produce S_0 type of wave motion, the exciting force needs to be directed parallel to the plate. A sudden release of in plane tension can produce the same as well. On the other hand, exciting forces perpendicular to the plate or the forces parallel to the plate but offset from the centre line are responsible for producing A_0 type wave motions (23)

For elastic waves, having wavelengths shorter than the thickness of the plate, higher order symmetric and antisymmetric modes become available dependent on the plate thickness (43). **Figure 2.6** is an example of a typical dispersion curve for steel plate (44). At high frequencies, the velocities of both zero order modes approach the Rayleigh velocity. All other modes appear at a certain cut off frequency and approach the shear velocity at very high frequencies (40). For a fixed plate thickness, due to dispersion, the elastic wave with different frequency modes will travel at different velocities. While travelling through the medium, these modes may gradually change due to attenuation or convert to different modes if it encounters a boundary (44). Various sources can generate different modes combinations in plates (44).
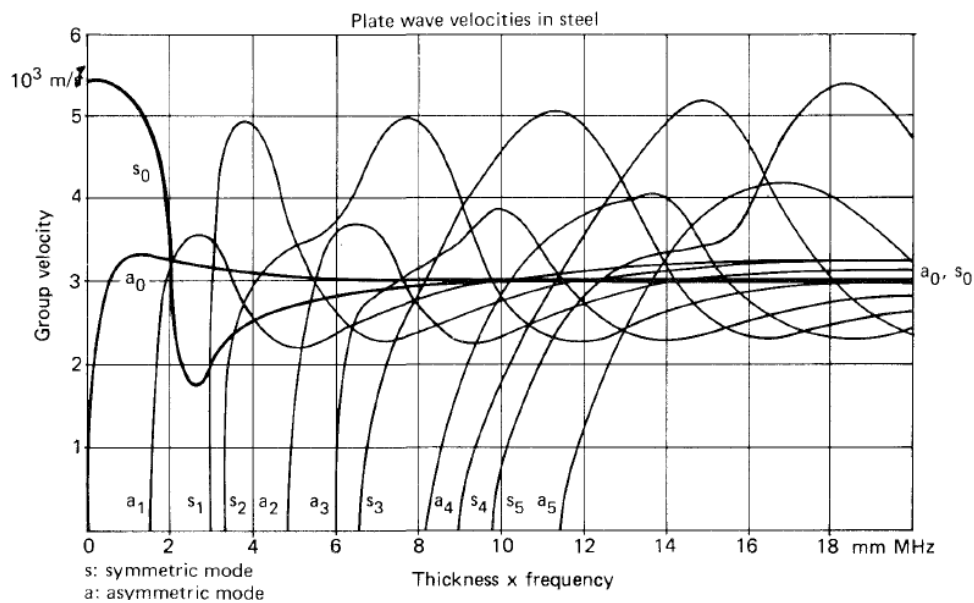
Figure 2.6: Dispersion curve of a steel plate (45). Depending upon the thickness of the plate & wavelength of the elastic wave, various plate modes with characteristic group velocities are possible (44).

Lamb waves provide the best estimation for propagation from the source at distances many times greater than the plate thickness. Close to the source, i.e., within one or two plate thicknesses longitudinal and shear waves are more likely to be dominant (23).

2.4.1 Thick circular plate response due to point impact

Sansalone et. Al (46) have carried out an extensive Finite Element (FE) analysis of a point impact at the centre of a thick circular plate. The diameter was varied between

31

1-2 m and thickness between 0.2-0.5m. The analysis was performed for aspect ratios (diameter to thickness) of 4.5 and 6.5. Contact times of 25 and 62 µs have been used for the study. These values simulate a small diameter (5 - 10 mm) steel sphere dropping onto concrete. Results obtained from the FE analysis was compared with Green's function solution for point impact on an infinite plate. Initial portion (0 – 400 µs) of the circular plate response was similar to the infinite plate response. Afterwards, displacements due to the waves reflected back and forward between the top and bottom surface were superimposed by reflected and mode converted waves from the plate side boundaries. Changing the aspect ratio was reflected in the spectrum shift of the obtained displacement signal at a point 0.05m from the impact point on the top surface. For a specific aspect ratio, detailed analysis on monitoring locations at different locations of the top and bottom surface showed that in general the major mode frequencies were the same but the contribution of these modes from point to point varied significantly along with absence of few modes at certain locations. Also, shorter impact duration excited higher plate modes resulting in more complicated response.

2.5 AE Sources

When a loaded material undergoes plastic deformation atomic planes slip past each other through the movement of dislocations. These release energy in the form of elastic waves i.e. AE signals. In the case of an existing crack in a metal, stress level in front of the crack tip is several times higher than the surroundings. Therefore, when this crack tip undergoes plastic deformation, AE activity is observed (23,47).

For fatigue, emissive particles (e.g. non-metallic inclusions) at the origin of the crack tip are less ductile than the surrounding material. These tend to break more easily when the metal is strained, resulting in an AE signal. Small-scale cleavage produced by triaxial stresses can act as an AE source in this regard (47) .In composite materials, matrix cracking, disbanding and fibre fracture can act as AE sources (24) .

Other than the sources mentioned above, other mechanisms produce AE signals which can be detected by AE equipment. Examples includes friction (as in rotating bearings), solid-solid phase transformation, liquefaction and solidification, leaks, flow noise, cavitations and realignment or growth of magnetic domains (Barkhausen effect). These are also referred as Secondary or Pseudo sources to distinguish from the classical AE caused by mechanical deformation of materials under stress (24,47–49) .

The following two sections are concentrated on a review on the AE generated from particle impacts & bubble activities.

2.5.1 AE from particle impacts

When a hard, solid particle strikes a target, the incident kinetic energy (KE) of the particle is converted into plastic strain energy (causing permanent deformation of the target and/or the impacting particle), elastic strain energy (rebound kinetic energy) and elastic waves which propagate through the target material (15). For the plastic impact a rigid spherical erodent on a massive target, Hutchings (50,51) has approximated 1-5% of the incident KE is radiated as elastic waves, 90% is used in plastic deformation and the remaining portion recovered through rebounding KE as shown in **Figure 2.7**.
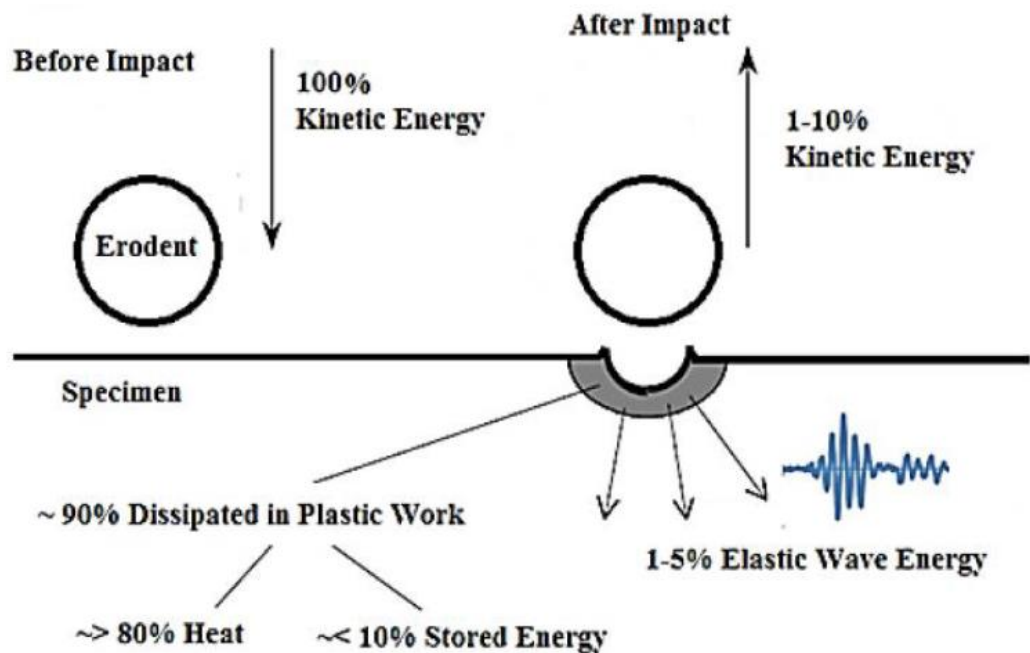
Figure 2.7: Schematic of AE energy release from a solid particle impact with a solid surface. (50,51).

Hunter (52) determined less than 1% of the incident KE is converted into elastic waves during normal impact of a hard steel sphere on a steel target whereas Reed (53) suggested about 4.5% of the KE is converted into elastic waves. Applying finite element analysis, Wu (54) showed that less than 1% of the incident KE is converted to elastic waves if there is more than one reflection occurs during the impact whereas approximately 6% of the incident KE is dissipated as elastic waves if there are no reflections at all. Ferrer et al. (19) used individual glass beads of 720 μm diameter, in a solution of Na_2SO_4 at velocity between $1 - 16$ m/s, to impinge on a 304L stainless steel target with AE sensor attached on the rear surface. They have found that KE radiated as elastic waves is below 1%.

Despite the theoretical deduction of a little amount of incident KE conversion into elastic waves, due to high temporal resolution, AE originated from impacts can be used

as a measurement tool for characterizing impacts (13–15,21,33,55) . In a study, Scruby et al. (13) dropped small spherical bronze and glass particles of nominal diameters of 53 – 63 µm and 75 – 90 µm respectively in vacuum onto steel or aluminium target plate at velocities between 2.5 – 7.1 m/s. Mounting broadband sensors on the opposite surface of the plate AE signals were acquired at the impact epicentre. Applying Green's theorem, they calculated impact forces by deconvolution from acquired AE signals and measured particle size distributions. Petersen (14) dropped four different sized steel spheres of radius within 2.5 – 11 mm from three different heights of 0.1 – 0.3 m on aluminium alloy plate and acquiring signal at a distance of 20 mm from the source on the same surface, correlated the first two peaks of the signals to the loading and unloading of the impacting bodies. Droubi et al (15) investigated the amount of recorded AE energy due to particle impacts by correlating AE energy with different particle diameters and velocities in dry and wet particle conditions. They proposed that AE energy increases with the third power of particle diameter, i.e. the mass, and with the second power of the velocity. They observed that the diameter exponent was only valid up to particle sizes of around 1.5 mm, while for velocity exponent the general level of the energy were lower for multiple impacts than for single impacts due to particle interactions in the guide tube and/or near the surface. Similar type of conclusion was reached by Duclos et al. (17) monitoring streams of various sized particle impacts at different concentrations and flow rate in a water loop. They showed the AE energy per particle was approximately proportional to the cube of the particle diameter except for the large particles attributable to the particle drop out following Stokes law. In an environment of nonsaline solution saturated with nitrogen, Ukpai et al. (18) used a submerged impingement jet on X65 carbon steel material to measure particle impacts. Subtracting baseline AE event count rate from count rate of various flow velocity and sand loading. At 7 and 10 m/s, measured particle impact counts agreed well with theory. Deviations for 15 m/s flow velocities were attributed to rebounding particles which have been detected with sand impacts and the overlapping of the AE events difficult to separate in time. Hou et al. (7) used a stepwise regression analysis technique to derive relationships between concentration, mass flow rate, volume flow rate and the statistical and spectral characteristics of the recorded AE. In another study, Droubi et al (21) developed a log normal distribution function for the AE energy from particle impacts which related the nominal mass and nominal speed of the impinging particles. Pecorari (55) proposed a statistical model to measure particle flow numbers which used average signal power, flow velocity and a function dependent on system parameters, such as, plate or pipe wall thickness, sensitivity and bandwidth of the transducer. For successful application of this procedure a proper calibration process for the function is required.

2.5.2 AE and sounds from bubble activities

The sound generated by the presence of bubbles was reported in the literature as early as 1921 (56,57) . Since then many researchers have done lots of researches which enriches the knowledge of bubble acoustics (26,27). The acoustics caused by the bubble is mainly associated with different phases of a bubble as described below.

a) Bubble formation

In laboratory, generally, bubbles are created by injecting air into a fluid using nozzle or nozzle like equipments (e.g. syringes). There is a minimum flow rate (termed as 'incipient fluidization rate') when the bubble starts to develop as a void surrounded by the fluid. Once the void reaches its size limit the void wall is pressurized by the surrounding fluid. The 'neck' of the void becomes the weakest region of the interface and eventually bubble pinch-off takes place (58) as shown in **Figure 2.8** .

Figure 2.8 : Photography of an air bubble just before pinch-off from a nozzle (59)

Minnaret first theoretically showed that at pinch off every bubble releases sound (57). Strasberg (60) observed bubble inception at an underwater nozzle using high speed camera and synchronised simultaneously recorded oscillograph of the sound accompanying with the event. The recorded work presented in Figure 2.9 shows that at pinch off from the nozzle tip, the bubble generated the highest sound pressure pulse.
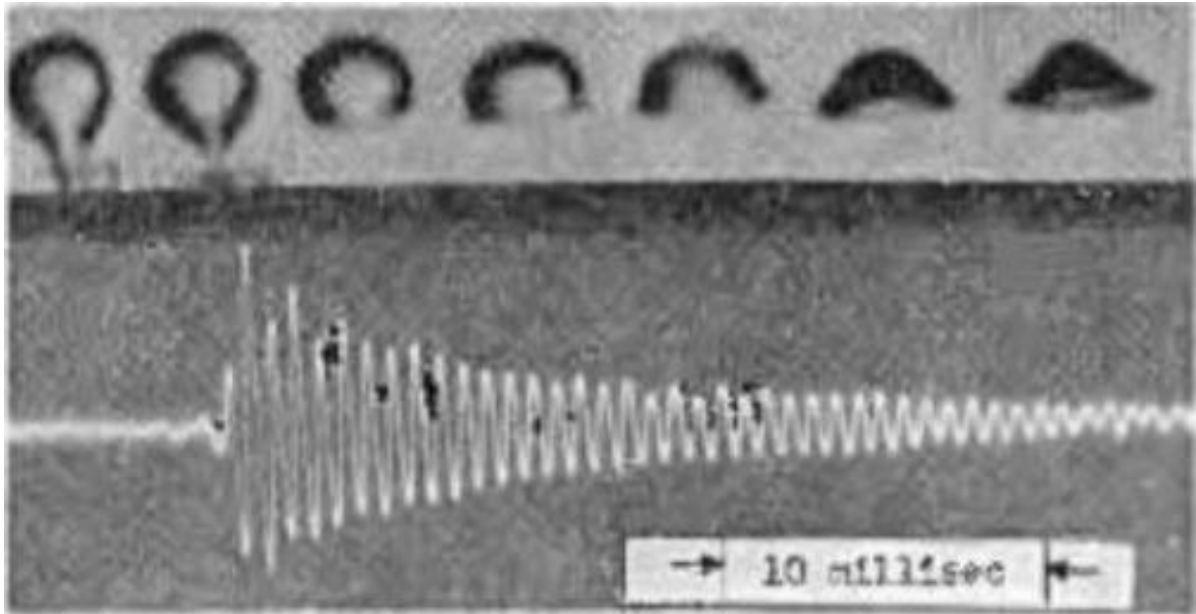
Figure 2.9 : Sound pulse Oscillogram of an individual bubble leaving a nozzle. The highest pressure pulse noted at the bubble pinch off (60).

Similar type of results have been obtained by Manasseh et al. (61). Using high speed camera and underwater microphone, Deane et al. (62) also recorded different stages of bubble pinch off and associated pressure signal as shown in **Figure 2.10**. However, the highest pressure pulse was recorded not at the pinch off but 320μs after detachment from the nozzle tip, as in b(iii) of **Figure 2.10**, showing a small re-entrant water jet forming within the collapsing neck.
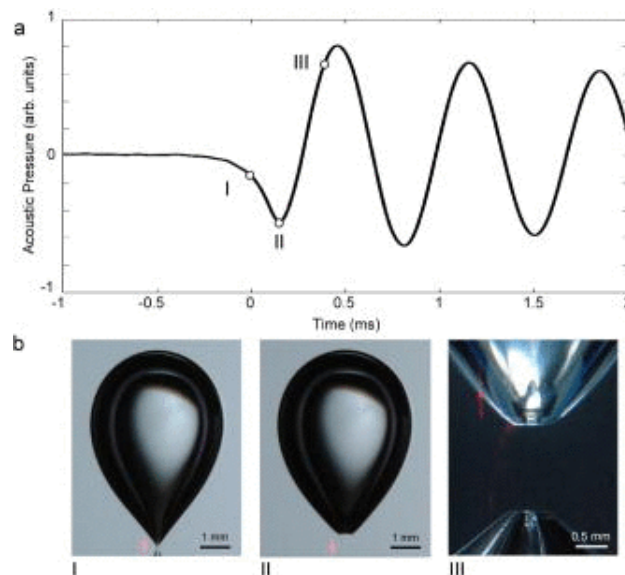
Figure 2.10 : (a) Recorded acoustic pressure amplitude associated with (b) bubble detachment from an underwater nozzle. Marked points I, II & III on Figure (a) represents observed pressure amplitudes for different stages of a bubble release corresponding to Figure (b) (62).

After formation of the bubble, before reaching equilibrium state, it undergoes volumetric oscillation which generates pressure waves (26) . Also the oscillation might be of different types (60) . Four major oscillation orders are presented in **Figure 2.11**.
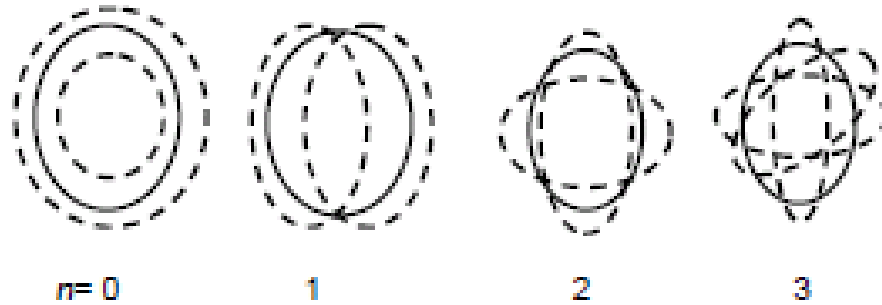
Figure 2.11: Four modes of spherical bubble oscillations (60).

In Figure 2.11, the zeroth mode (n=0), corresponds to the volume pulsation, i.e. change in volume, with fixed shape. The first mode (n=1), represents translational oscillation with fixed shape and volume about a fixed point. The second and third modes (n= 2 & 3, respectively), resemble complex shape changes with fixed volume.

The natural frequency of the zeroth mode volume pulsation is calculated by Minnaert's model (57) :

$$f_0 = \frac{(3\gamma P_0/\rho)^{1/2}}{2\pi R_0} \tag{2.4}$$

And natural frequencies of other three oscillation modes are calculated according to Lamb's model (63) :

$$f_n = \frac{\left((n^2 - 1)(n + 2)T/\rho R_0\right)^{1/2}}{2\pi R_0} \tag{2.5}$$

Where

f_0 is the natural frequency of oscillation for zeroth mode volume pulsation

f_n is the frequency for the nth mode

P_0 is the static pressure

γ is the ratio of the specific heat of the gas in the bubble

R_0 is the mean radius of the bubble

ρ_l is the density of the liquid

T is the surface tension

Many researchers have investigated the sound generated during the oscillations of the bubble after the pinch off when it goes through different shape changes as shown in **Figure 2.11**. Meyer and Tamm (60) first experimentally associated the emitted sound to volumetric bubble pulsations. Pandit et al. (64) suggested that bubbles, entrained in water or liquid, when subjected to external pressure fluctuation can generate large sound due to the volume pulsations originated from the oscillatory motion of the bubble walls. Leighton et al. (65) observed that the recorded emitted sound was dominated by the zero order mode pulsations of the bubble while the other higher order modes contributed little to the recorded pressure signal. Applying micro – PIV velocity field measurement on the recorded photographs, Tho et al. also detected a similar type of effect.

b) Bubble Coalesce and Splits

Following bubble formation or pinch off, the bubble rises with a velocity known as 'Bubble terminal velocity' (58) . Sometimes during this ascent of the bubble, splitting as well as coalesce could occur (58) . The existing hydrodynamic stresses and surface tensions at the bubble region influence the bubble split by stretching of the bubble due to viscous shear at the bubble surface. When the split occurs it results in an emission of a decaying pressure pulse (27) . Similarly, if two bubbles are formed in quick succession, as shown in **Figure 2.12**, their coalescence can become a source of bubble acoustic as well (61) . The recorded sound amplitude during coalescence was an order of magnitude higher than the primary bubble pinch – off. Also, the sound intensity increased with the increasing size of secondary bubble, for a given primary bubble diameter.
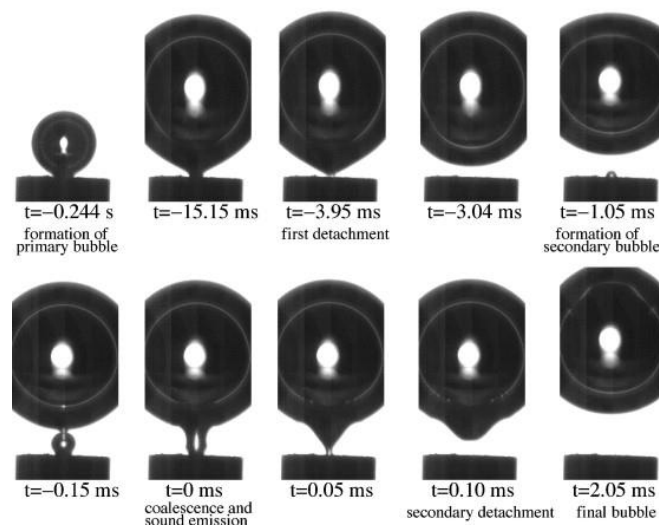
Figure 2.12: Bubble formation and coalescence sequence from a nozzle under static height of water column using a high speed camera (61) .

Kracht et al. (66) studied coalescence of air bubbles, injected through a submerged capillary glass tube. From the recorded hydrophone signals, a decaying sinusoid was observed for a single non coalescing bubble production. For the bubble coalescence event, the primary decaying sinusoid, associated with the initial bubble formation, was followed by a secondary decaying sinusoid of higher amplitude. The hydrophone used in the study was having an operating frequency range of 0 – 85 kHz. No comparable results have been noticed in the literature using AE systems.

c) Bubble burst at free surfaces

The final evaluation in bubble life cycle is bubble burst which takes place at the free surfaces. This phenomenon is widely known in any industrial set up in various terminologies. During collapse, bubbles do not vanish but rather form micro bubbles with 2-10% of the original bubble radius (67,68). At the moment of bubble burst, surrounding liquid gets compressed and a high pressure wave front radiates from the collapse centre (69). If the liquid compression due to bubble burst is high enough, it can cause shock waves in the surrounding liquid as well (67,70,71). About 10 to 15% of the bubble energy contributes to the generation of pressure pulse during bubble collapse (72). Energy released by the bubble bursting is related to the bubble size and liquid properties (27) .

Using wall mounted AE sensors, Shuib et al. (27,58) studied single bubble activities by introducing bubbles through a submerged nozzle at the bottom of a rectangular tank. They observed that AE amplitude of the bubble burst at the free surface increases with an increase in the bubble size. Also, it was noticed that, for a given bubble size, higher viscosity increases the bubble burst AE amplitude. In a different study, involving bubble burst at the free surface of a non-Newtonian fluid, Divoux et al. (73) detected that, different bubble burst amplitude recorded from the same experimental conditions. They concluded that due to high sensitivity to the film bursting dynamics, to characterise bubble burst events, frequency is more reliable indicator than the amplitude and energy of the recorded signal (73).

2.6 AE signal analysis

To identify correlations between recorded AE signals and the physical events associated with it, AE signals are analysed using different signal analysis procedures. AE signal analysis can be broadly divided into time domain and frequency domain analysis. The following sections provide a brief overview of these techniques.

2.6.1 Time domain based analysis

For time domain signal analysis, real time captured AE signal records are used. Analysing different parameters of the recorded signal, corresponding to physical events

are characterised. Referring to **Figure 2.13**, definitions of the most widely used AE signal analysis parameters in the time domain are listed below. (28,47,74) .
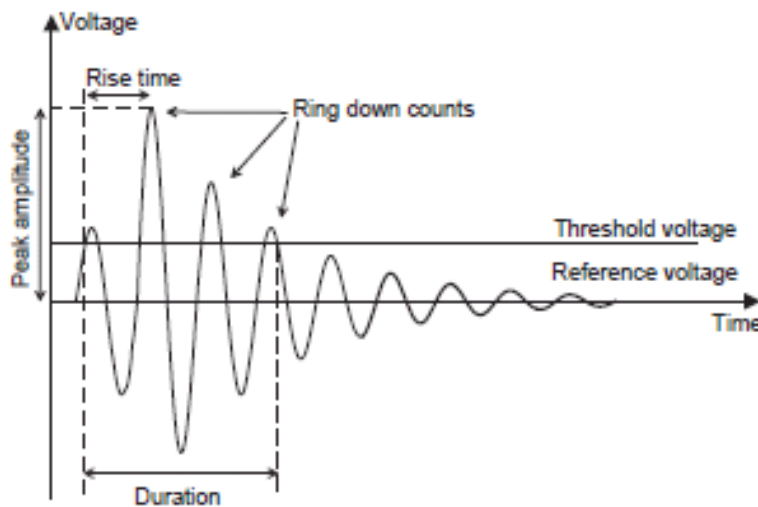
Figure 2.13: Standard AE parameters used for time domain signal analysis (75)

Hit: A signal that exceeds the threshold and causes a system channel to accumulate data. It is frequently used to show the AE activity with counted number for a period (rate) or accumulated numbers. In **Figure 2.13**, one waveform correspond one "hit".

Counts: It refers to the number of times a signal crosses the threshold within a duration. It is dependent on the set threshold and operating frequency. In the **Figure 2.13**, four counts are observed.

Amplitude: This is the greatest measured voltage in a waveform. Amplitudes are usually expressed on a decibel scale. It is closely related to the magnitude of the source event and often analyzed with frequency distribution. It also determines the detectability of the signal. Signals with amplitude below the threshold will not be detected.

Duration: It is the time interval between the first and the last interval crossing. It can be used to identify different types of sources and noise.

Rise Time: It is the time interval between the first threshold crossing and the peak signal. It relates the wave propagation of AE source and sensor.

Energy: The true energy of an AE event in a material is proportional to the area under the AE waveform. The advantage of energy over ring down count is that it can be directly related to important physical parameters (such as mechanical energy in the emission hit, strain rate or deformation mechanisms). It also improves AE measurement when the signal amplitudes are low.

2.6.2 Frequency and Time-Frequency based analysis

Advanced mathematical transformation based Frequency domain analysis, e.g., Fourier Transform (FT), Short Time Fourier Transform(STFT) and Wavelet Transform (WT), enables additional feature extractions, other than the information obtained from time domain analysis, of the recorded signal which aids in characterising associated AE events (24,27).

Fourier Transform decomposes the recorded signal into various frequency components and estimates energy distribution of the components from the time series data (76). Frequency spectrum of the decomposed signal can be used as a diagnostic tool or can be used for improving signal to noise ratio by removing noise from the signal, provided the noise has a distinct frequency signature than the event (16).

STFT involves truncation of the signal into sections (windowing) and analysing each section at a time by using Fourier transform. It maps the time series data to a frequency – time domain and provides information about the time and frequency of the event. STFT is based on fixed window width and the precision of the obtained information is dependent on the window size (76).

Wavelet Transform (WT) is similar to STFT except incorporating variable window lengths. Longer time interval provides more precise low-frequency information and shorter time interval provides high frequency information (76).

2.6.2.1 Frequency and Time Frequency based analysis of particle impact signals

AE waves propagate through a structure in a variety of modes. Separation of these modes at the sensors can retrieve information about the source which produced the wave (77) . Prosser et al (33) conducted experiments on small aluminium and composite plates on which steel and cylindrical nylon balls were fired. For all the cases, plate extensional and/or flexural modes were detected and the amplitude of the modes increased with a change in velocity. For steel bars, Dunegan (78) identified two frequency bands of 100kHz-1MHz and 20KHz-70 kHz that would allow the separation of the extensional and flexural waves respectively Similarly, Holford et al (79) separated signals into extensional (above 100 kHz) and flexural (below 100 kHz) modes for source location on a 12m long steel beam.

For simple geometrical structures, a large lateral dimension along the wave propagation direction facilitates identification of propagating wave modes clearly. However, for complex structures, with small dimension and/or structural joints or discontinuities, reflection, dispersion, mode conversion significantly complicate the propagated waves and hence the identification of modes become difficult (33,80) .

For wave propagation in dispersive media, identification of the same frequency mode at more than one sensor (81) or different frequency modes at single sensor (77,82)

can improve the source location accuracy. Due to inherent time frequency representation characteristics, WT is a natural candidate for such an application and executed promisingly in the studies observed in (81,83) .

Modal analysis and WT in dispersive media have been used to characterize different source types (82) . Hamstad (84) used a Finite Element Modelled(FEM) database of monopole and dipole AE signal sources to compare with experimental pencil lead break (PLB) tests. The entire FEM signals were numerically processed with 40 kHz (four pole Butterworth) high pass filter and a similar typed band pass filter of 100-300 kHz. Two modes were clearly identified on the WT and peak amplitude ratios of flexural modes to extensional modes were used for different source types. In another study (82) , FEM was used to distinguish different source types. However, the ratio did not uniquely classify the AE source types.

For a plate-like test specimen, the propagating waves in the far field are governed by Lamb waves. For thin plates, typically only fundamental symmetric and anti symmetric wave modes are present (81,85) and their dispersion characteristics can be predicted (77) and for a wide plate geometry the reflection effects are minimised. However, in thick plates, additional higher order Lamb modes contribute to the signals (85) and this is verified by Dunegan (78) . Also Hamstad (82) showed that for a small coupon specimen, edge and surface reflections distort the signals and hence individual modes cannot be easily identified on the time-frequency plane of WT. Ding et al (80) showed a generic way of determining important wave modes arrival by applying wavelet packets for source location on CFRP laminates. Contaminations of signals by reflections are observed. For current research, where specimen thickness supports higher order lamb wave modes and reflections distort the acquired signals, applying WT does not help to identify different wave modes. Also, for each particle impact wavelet packet based analysis cannot identify any distinct particle properties. For example, AE energy or amplitude would not be unique to a specific particle impact because energy could vary due to other physical properties such as impact angle and velocity. So, for two similar sized different types of particles, energy or amplitude cannot distinguish between particles. This work is focused on developing a novel technique using frequency band energy ratios to distinguish different particle types for impacts on a small mild steel stepped cylindrical plate.

2.6.2.2 Frequency and Time Frequency based analysis of bubble activities signals

Attaching a steel plate to a steel tube of an existing hydraulic loop, Hutton experimentally studied the applicability of AET in differentiating plastic deformation of the plate from the flow and cavitation originated noise (86). It was observed that plastic

deformation had a frequency content of above 1.5 MHz and the flow or cavitation had a spectral content predominantly below 1 MHz.

Mounting a 500 kHz resonant AE transducer on a high pressure piston pump, Darlington and Johnston conducted a cavitation test (87). It was noted that introduction of cavitation increased the mean AE signal output and the collapse of the bubbles caused wide band noise upto 1 MHz.

To study bubble acoustics, Leighton et al. (88) introduced a single bubble at a time using a vertical syringe at the bottom of a tank. To record bubble activities, an underwater microphone and a high speed camera, along with an illuminating lamp, were used. They have observed that higher gas flow rates produced higher frequency sound from smaller bubbles.

With a similar arrangement of hydrophone, high speed camera and water tank, Boyd and Varley (8) have used water jet aimed vertically downward to generate bubbles. A shift to the lower frequency in the spectrum was noticed from larger bubbles associated with increasing height. In another study (89) of bubble cloud generation under a water fall and a water jet entrainment, lower frequency in the spectrum was observed for larger bubble sizes. In this study, a time frequency based GWT was applied for signal analysis.

Shuib et al. (58) have carried out a detailed analysis on single bubble activities. They have used four different size of metal nozzle between 1.4 mm – 8.4 mm at the bottom of a rectangular tank, full of either water, salt water or glycerine, to introduce bubbles in the tank and recorded the bubble activities using both intrusive and non-intrusive AE sensors at different height along the wall of the tank. AE signals were recorded at the time of bubble formation and bubble burst at the free surface and time-frequency based Gabor wavelet transformation (GWT) was applied for bubble activity analysis.

Figure 2.14 & **Figure 2.15** shows recorded AE signal (top) and wavelet analysis (bottom) of bubble activities obtained from 8.4mm nozzle in a water filled tank. From **Figure 2.14**, during bubble formation the highest intensity of frequency observed around 250 kHz whereas from **Figure 2.15** during bubble burst at free surface, the peak activity occurred around 150 kHz.

File: C:\Users\user name\Documents\Mba-AE\Bubble Form at Nozzle Underwater (Water), Size 8.4 mm Diameter.tra
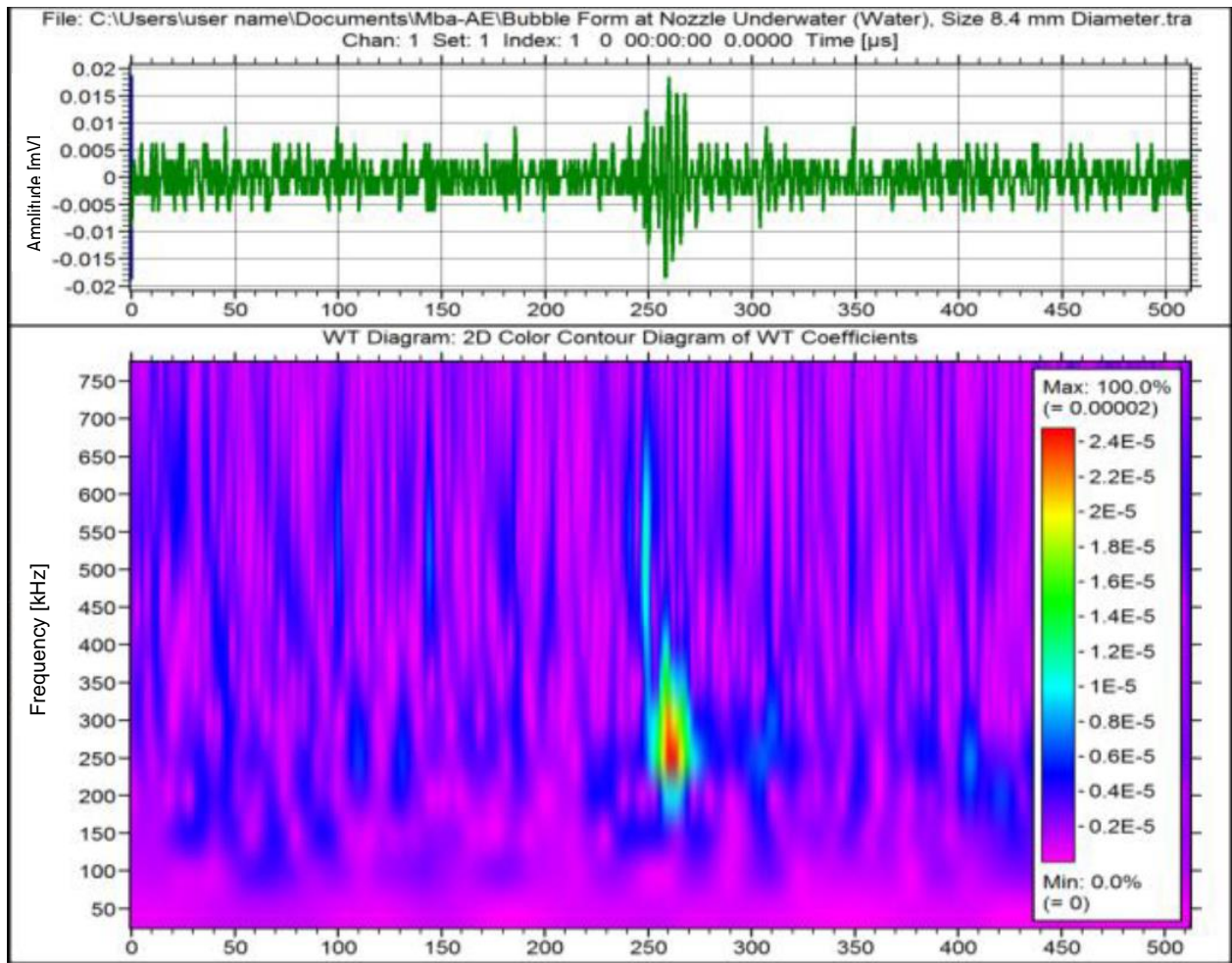
Wavelet transform calculated by AGU-Vallen

Figure 2.14: Typical waveform (top) and Gabor wavelet transform (bottom) of bubble inception from nozzle size of 8.4mm in water (58).

Comparing **Figure 2.14** & **Figure 2.15**, higher amplitude and longer event duration were observed for AE waves associated with bubble burst both on the time domain signal and wavelet transform. Also, the beginning of the AE wave, for both bubble formation and burst, is associated with wide frequency content between 100 – 750 kHz.
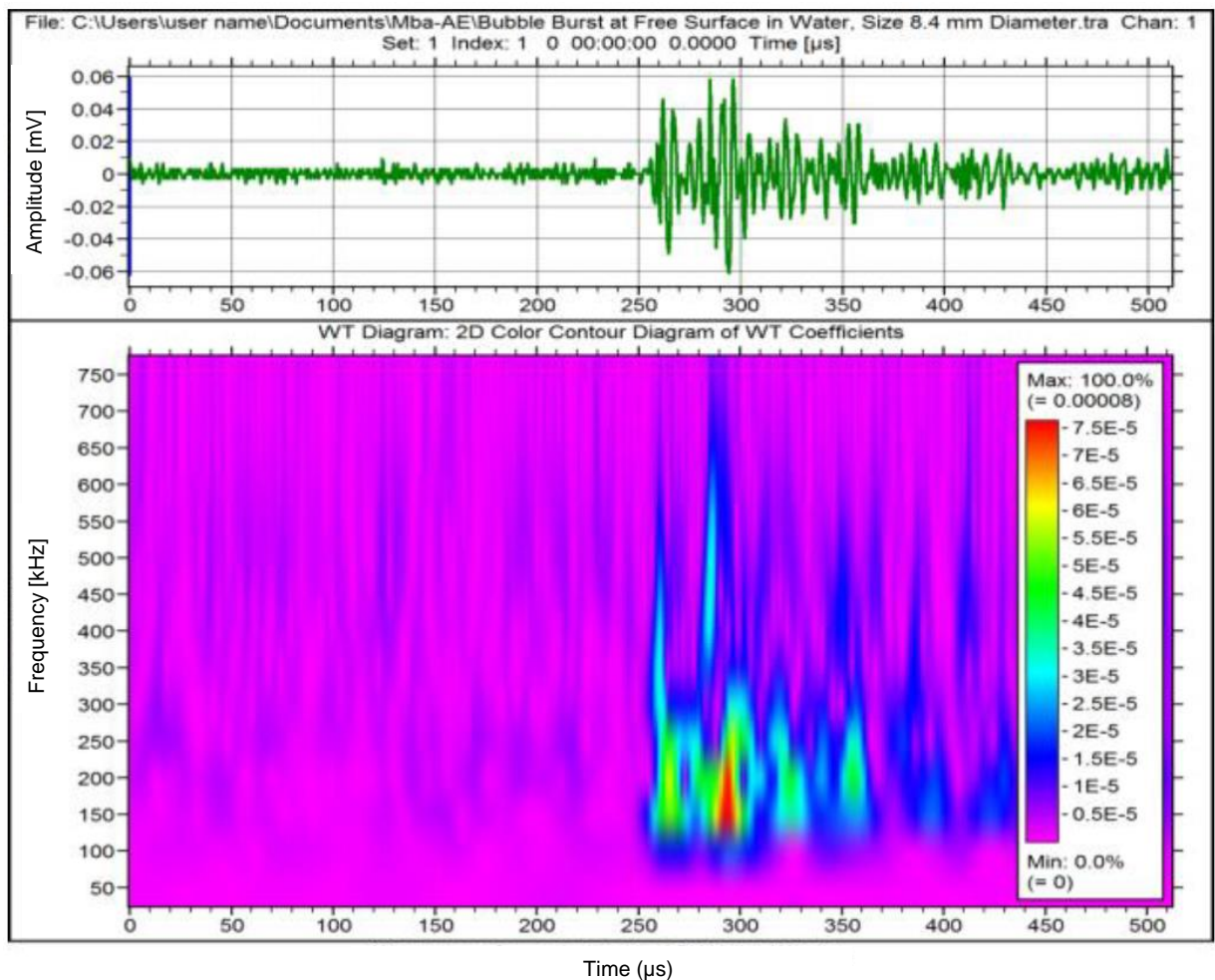
Figure 2.15: Typical waveform (top) and Gabor wavelet transform (bottom) of bubble burst example. The bubble was originated from nozzle size of 8.4mm in water (58).

2.6.3 Pattern recognition in AE analysis

If the recorded signals are influenced by source position, dispersion or attenuation within the specimen, interpretation of recorded AE signal based on conventional standard AE parameters evaluation in time and frequency domain or correlation plot of time-frequency domain becomes difficult (90). Multivariate analysis technique, e.g., Pattern recognition, is required for such cases (91).

AE signal based pattern recognition techniques have been successfully applied in many disciplines. For example, monitoring various failure mechanisms in composite materials using k – means, k-Nearest Neighbours (k-NN), Self-organizing map (SOM), fuzzy C-means and Principal Component Analysis (PCA) based pattern recognition algorithms (90,92–98); for rotating machine condition (99), machine coolant system diagnostics (100), bearing (101) and gearbox faults detections (102) using artificial neural network based algorithms; various engine fault detections using generic algorithm (103).

In particle impact related AE applications, implementation of pattern recognition based analysis has been noticed primarily for loose particle detection tests in sealed electronic devices (104–108). In Particle Impact Noise Detection (PIND) tests, the sealed electronic device under observation is vibrated with a shaker and AE signals recorded by the mounted sensors (within typical range of 10 – 200 kHz) on the shaker base for identification of loose particles with considerable mass (106). Standard practice is human expertise dependent and accuracy of particle detection is around 44% (104). Neural network based detection methods proposed in (104,105) improves the performance but subjected to successful misjudgement reduction of the neural network due to environmental noise and electromagnetic noise (105). A recent work has implemented Principal Component Analysis (PCA) and Support Vector Machine (SVM), using nine features in time and frequency domain, to classify 250 samples each for Wire, Aluminium and Tin, from 0.5 - 2 mg particle impact signals, with better environmental noise handling capabilities resulting in a detection success rate reported between 90-95% (106). However, no literature has been noticed related to smaller particle, in the diameter range of ~μm commonly found in different process industries, related impacts identification detection based on acquired AE signal analysis.

2.6.3.1 Basic steps of pattern recognition and classification

Figure 2.16 shows the basic steps of a pattern recognition and classification technique (109).First step of pattern recognition and classification is measurement of physical variables. For superior quality data, bandwidth, sensitivity, signal to noise ratio, resolution of the data acquiring devices are important. In the second step, acquired data are represented in terms of features to characterize the measured physical event.
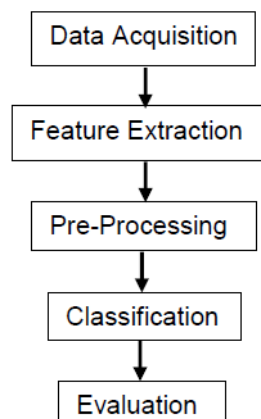
Figure 2.16: Basic steps of pattern recognition and classification.

The next step is processing the data into usable format for different classification techniques. Pre-processing step can include feature selections, additional feature

calculation from the extracted features, normalizing the data to scale within the same range and transforming the data with zero mean or unit variance (110). Sometimes, for reducing very large feature space, dimensionality reduction method, e.g., principal component projection, is applied in addition. In classification step, two main methods are followed: Unsupervised and Supervised. For Unsupervised classification, without the prior knowledge about the data origin, measured data sets are grouped into similar categories. For example, K-means and hidden Markov model based classification. Supervised classification directly implements previous knowledge or a derived rule from the previous knowledge of measured data sets to categorize newly available data. For example, k-NN, Neural Network and SVM classification. The last step of pattern recognition and classification is the evaluation of the developed classifier. For Unsupervised classification, performance is assessed based on the rank assigned to resulting classes for being distinct and compact after several runs of the clustering algorithm (110). For Supervised classification, the accuracy of the developed classifier is evaluated by applying it to categorize the known portion of acquired data which has not been used for classifier development (110).

There are various algorithms available to perform a classification job. There is not a unique universal best classification technique which fits all purposes (111,112). However, in the International Conference on Data Mining (ICDM) in December 2006 by IEEE, top 10 data mining algorithms have been identified (112). Among these 10 algorithms, Support Vector Machine (SVM) has been termed as a 'must try' considering its accuracy and robustness among all the algorithms available (112). It's further supported by seminal research work by Fernandez et al. (111) who evaluated 179 classifiers from 17 different families on 121 data sets and concluded that Random forest is the best performing with SVM as the second best without any statistically significant difference. research,

In this research, populations of particle impacts on a mild steel target plate from glass beads and sand particles with similar size, density and velocity were studied and presented in Chapter 4. Analysis was performed using standard AE parameters in the time and frequency domain and included in the Appendix C. Further statistical analysis was done introducing frequency band energy ratio for different particle impact types and shown in the section 4.4. It has been observed that, for the off centred sensor position (S2), the coefficient of variation analysis can distinguish the type of the particle impacts for a given experimental population. However, due to similar size, density and velocity, the signal features obtained from these analyses are highly overlapped for the glass beads and sand particle impacts and are insufficient to identify each impact event individually in the population. SVM is a robust and reliable supervised statistical learning

technique which can distinguish highly overlapping features data set by nonlinear mapping of the features in the higher dimension followed by separation of each category constructing a hyperplane in the higher dimension. So, SVM has been implemented in this research for classification of each individual particle impact type in a given population.

2.6.3.2 SVM as a classification technique

Let us consider a data set separable into two classes in a two dimensional feature space, as shown in **Figure 2.17** by circles (class A) and squares (class B). SVM tries to separate the two classes by placing a boundary (a hyperplane - for 2D, a line) between the two class, shown as solid line in **Figure 2.17**. To ensure maximum separability between the two classes, two parallel hyperplanes (in 2D, a line) are created going through the nearest data points, as shown in **Figure 2.17** by the dotted lines going through the gray circle and square. These two hyperplanes are called 'Margin' and the points going through the hyperplanes are called 'Support vectors' (SV). SVM attempts to orient the boundary to maximize the Margin between SVs (101,113,114).
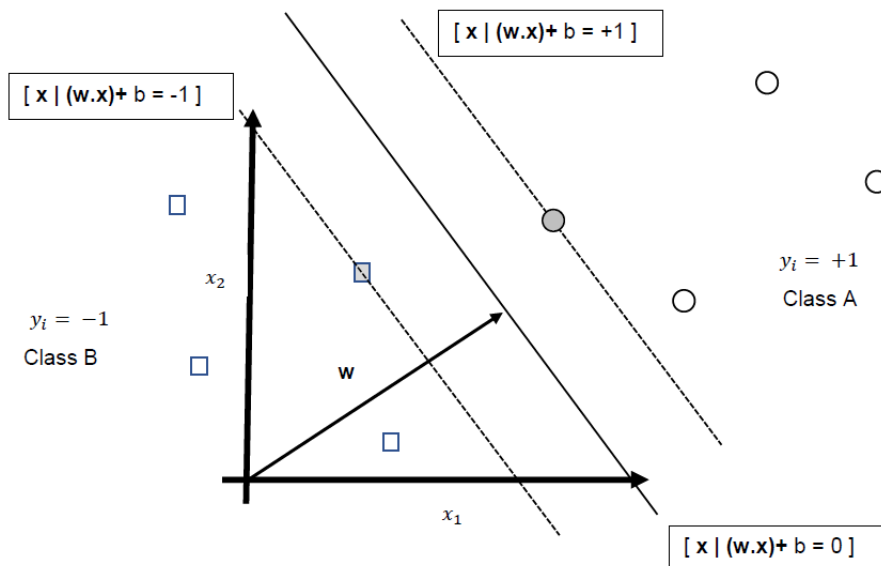
Figure 2.17: Demonstration of SVM algorithm applied on a completely separable two class data set with two features x_1 and x_2 (114).

The boundary differentiating two classes can be defined as (101,113,114):

$$(\mathbf{w}.\mathbf{x}) + b = 0, \mathbf{w} \in R^N, b \in R \qquad\qquad \textbf{(2.6)}$$

48

Where, the vector **w** describes the boundary, **x** is the feature vector (input vector) of dimension N and b is the scalar bias (threshold).

For the two classes A & B, at the margins, the equations are defined respectively by (101,113,114):

$$(\mathbf{w}.\mathbf{x}) + b = 1 \tag{2.7}$$

$$(\mathbf{w}.\mathbf{x}) + b = -1 \tag{2.8}$$

SVs are the extreme points of the two classes. So, for all the data points, belonging to either A or B, the decision function can be expressed as (101,113,114):

$$f(x) = sign((\mathbf{w}.\mathbf{x}) + b) \tag{2.9}$$

The optimum hyperplane can be constructed by minimizing the function (101,113,114)

$$\delta(x) = \frac{1}{2}\|w\|^2 \text{ Subjected to}$$
$$y_i((\mathbf{w}.\ x_i) + b \geq 1),\ i = 1, \dots \dots, n \tag{2.10}$$

Where n is training sets number.

Unique solution for this constrained quadratic problem can be formulated by (101,113,114):

$$w = \sum \alpha_i x_i \tag{2.11}$$

Where α_i is a weighting factors to determine the data points from the training set to be used as SVs.

From Equation (2.9) and (2.11), the decision function can be expressed as:

$$f(x) = sign\left(\sum_{i=1}^{n} \alpha_i(x.x_i) + b\right) \tag{2.12}$$

If linear hyperplane is not sufficient to differentiate the two classes, higher dimensional feature space conversion of the input data can be possible through transformation function $\beta\ (x)$.

From Equation (2.12), replacing transformation function, the decision function can be presented as:

$$f(x) = sign\left(\sum_{i=1}^{n} \alpha_i(\beta(x).\beta(x_i)) + b\right) \tag{2.13}$$

The transformation into higher dimensional space can be performed by evaluating a simpler kernel function (101,113,114). For example, for a higher dimensional

transformation involving any two vectors **x** and **y** , the kernel function can be defined by (101,113,114):

$$K(\mathbf{x}.\mathbf{y}) = \boldsymbol{\beta}(\mathbf{x}).\boldsymbol{\beta}(\mathbf{y}) \tag{2.14}$$

The decision function is represented by:

$$f(x) = sign\left(\sum_{i=1}^{n} \alpha_i K(x.x_i) + \mathrm{b}\right) \tag{2.15}$$

Different kernel functions can be used to formulate SVM. However, the most common four are: linear, polynomial, radial basis function (RBF) and sigmoid (115). In this work, radial basis function has been used. A general definition of radial basis kernel involving two variables x & y can be presented as (101,113,114):

$$K(x,y) = \exp(-\gamma(x-y)^2) \tag{2.16}$$

Where γ is a constant related to the width of the radial basis function.

Selection of the parameter α_i affects the data points to be used as SVs and the error allowed in training the classification model. For a completely separable data set, $0 < \alpha_i < \infty$. However, for non-separable data set, $0 < \alpha_i < C$, where C is a constant. For radial basis function based SVM, C & γ are the two parameters available for tuning a model.

SVM has the following advantages and limitations (112,116–120):

- Performance of SVM is not directly dependant upon the dimension of the training data set.

- Comparing to other methods, (e.g., Artificial Neural Network), SVM is less prone to data overfitting.

- SVM uses a technique called 'kernel trick' which can operate, using appropriate kernel functions, in lower dimensional space on the training data points to evaluate the relationship among the data points in the higher dimensional space without calculating complex transformation functions.

- Applying quadratic programming method involves large matrix calculation which is computationally expensive.

- Larger training time required due to slow learning method.

- With the number of training data points, training time increases quadratically requiring larger memory.

2.6.3.2.1 Model Performance Evaluation

To evaluate the reliability of a classification model various performance assessment methods are available, e.g., ROC (Receptor Operating Characteristic) curve, misclassification error, mean misclassification cost and confusion matrix (121). In

this research, Confusion Matrix based evaluation procedure has been implemented as this provides a comprehensive performance measurement of the classification model's ability to predict a particular class when some of classes are more difficult to predict than others (121).

For example, in a two-class prediction task, after building the classification model based on training data set, the model is applied on a test data set to evaluate the performance of the model. In this case, to evaluate the performance of the model on one of the classes can be represented by the confusion matrix, shown in **Table 2.1** (121–123). The convention used here is: 'Positive' or 'Negative' denotes to the class labels predicted by the model and 'True' or 'False' associated with the actual labels of the predictions based on prior observations.

Table 2.1: Confusion Matrix of a two class classification task.

Observed Class	Predicted Class	
	True	False
True	TP	FN
False	FP	TN

TP: True Positive
TN: True Negative
FP: False Positive
FN: False Negative

From this confusion matrix, the following performance measurement parameters can be evaluated (121–123).

Sensitivity: The ratio of successfully classifying True instances as Positive out of all True observed instances:

$$\text{Sensitivity} = \frac{\text{TP}}{\text{TP} + \text{FN}} \qquad \textbf{(2.17)}$$

Specificity: The ratio of labelling all False events successfully as Negative out of all observed False instances.

$$\text{Specificity} = \frac{\text{TN}}{\text{TN} + \text{FP}} \qquad \textbf{(2.18)}$$

Accuracy: The ratio of correctly classifying all 'True' instances as 'Positive' and all 'False' instances as 'Negative' out of all observed instances by the model.

$$\text{Accuracy} = \frac{\text{TP} + \text{TN}}{\text{TP} + \text{TN} + \text{FP} + \text{FN}} \qquad \textbf{(2.19)}$$

Positive Prediction Value (PPV): This is the reliability of all the 'Positive' labelled instances and defined by the ratio of 'True' observed instances classed as 'Positive' to all the instances classed as 'Positive'.

$$\text{PPV} = \frac{\text{TP}}{\text{TP} + \text{FP}} \qquad \textbf{(2.20)}$$

Negative Prediction Value (NPV): This is the reliability of all the 'Negative' labelled instances and defined by the ratio of 'False' observed instances classed as 'Negative' to all the instances classed as 'Negative'.

$$NPV = \frac{TN}{TN + FN} \qquad \textbf{(2.21)}$$

2.7 Conclusion

Many researchers have studied acoustic emission generated from particle impacts on a target plate. Test environments considered are: (i) dry particle impacts on dry target plate (15), (ii) wet particle impacts on dry target plate (16) and (iii) wet particle impacts on wet target plate (16,18). Effect of varying particle types, particle sizes, flow rates, impact angles and concentrations were studied for each case.

For case (i), it was observed that for a specific particle type, over a particle size range (125 – 1500 µm) and particle impact velocities (0.9 – 16 m/s), AE energy is proportional to the incident kinetic energy (15). Though AE event energy has been successfully correlated with particle diameter upto 1.5 mm (15), no attempts have been noticed to correlate with the particle types from the literature. In this thesis, analysis has been carried out to discriminate similar sized different particle types using conventional time series based AE parameters, introducing a new frequency based parameter – frequency band energy ratio and using SVM based classification algorithm.

For case (ii) & (iii), in general, the measured AE energy was found to be proportional to concentration, velocity squared, particle size cubed and $\sin^2$ of the nominal impact angle (16). Weaker relationships for smaller and slower particles were observed.

For case (ii) and (iii), AE energy can be originated from bubble activities in addition to particle impacts. For the controlled test conditions, AE energy from bubbles were found to be lower than AE energy from particle impacts (17,19). However, in practical case, e.g., in petroleum production, AE energy based monitoring technique misinterpreted sand particle impacts as bubbles and vice versa (11, 12). This thesis shows the viability of frequency band energy ratio to distinguish particle impacts from bubble events on a steel plate in a laboratory environment.

Chapter 3 Preliminary pencil lead break experiments

3.1 Introduction

This chapter focuses on preliminary pencil lead break tests (Hsu Nielsen sources) on the target plate (test specimen) which were carried out at the beginning of each set of experiments (distinction of similar sized particle impacts on mild steel target plate, described in chapter 4 and distinction of sand particle impacts on mild steel target plate in presence of bubbles, described in chapter 5). This chapter begins with the description of the data acquisition (DAQ) system used in this research followed by a brief overview of Hsu Nielsen test procedure. Standard range of time and frequency domain acoustic emission signal features are analysed. The chapter ends with a discussion of the suitability of those AE parameters in relation to the test specimen and informs a new analysis framework developed in the following chapters.

3.2 Acoustic emission data acquisition system

Figure 3.1 shows the AE DAQ system used for all the experiments conducted in this research. The major components of the system include: A pair of sensors, couplant, a pair of Preamplifiers, Power supply unit, DAQ Card and Operating Software.

The sensors are of type Micro-80D from Physical Acoustics. The built in differential preamplifier results in lower noise output eliminating common mode noise. The wide band sensors have relatively flat frequency response output over the range 175 kHz to 900 kHz and an operating range between -65 to 177°C. An in house designed magnetic clamp was used to hold down the sensors on the test surface. Silicon grease was used as a couplant to ensure good AE transmission by filling any gaps between the sensor and the test surface, caused by surface roughness.

To amplify acquired signals at the sensors, additional preamplifiers (type PAC 1220A) were installed between the sensors and the data acquisition card. These preamplifiers have internal high pass filters of 20kHz. A switchable gain of 20dB, 40dB and 60dB facilitates magnifications of 10x,100x and 1000x of the acquired signal at the sensors. An in house built 28 V power supply unit was used to power the sensors as well as the preamplifiers. A connector block (from National Instruments) was used to feed in multiple sensor signal output to the DAQ card. For all the connections between the preamplifiers and the power supply unit and between the preamplifiers and the connector block, BNC cables were used.

To record the acquired signals from the sensors a National Instruments' PCI-6115 card was installed on the PC. This DAQ card is an analog to digital converter (ADC) with

a capability of recording 4 channels of signals simultaneously with a maximum speed of 10M samples/s for 4 channels cumulatively or 1 channel individually.

LABVIEW, from National instruments, was used for controlling DAQ card to record signals on the PC hard drive and for on screen interface to view real time signal acquisition and to define signal acquisition features e.g., sampling frequency, threshold, pre trigger samples, number of samples.
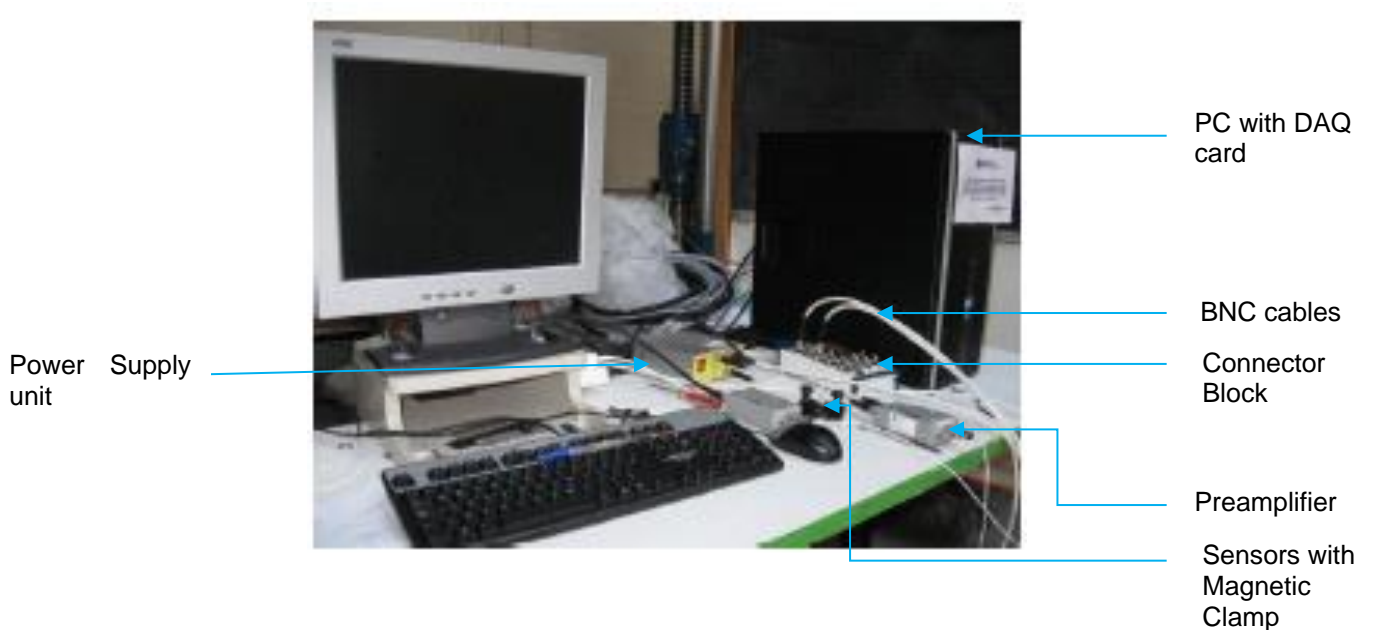
Figure 3.1: Acoustic emission data acquisition system and its various components used for the research

3.3 Test Specimen and setup

The test specimen (target plate) used for this research was a circular stepped mild steel disc with dimensions shown in **Figure 3.2**. The disc was placed on wooden blocks to isolate it from the surroundings. Sensor S1 was held down by the magnetic clamp at the epicentre and Sensor S2, at a radius of 30 mm on the target plate as shown in **Figure 3.2**.

Top View

Front View
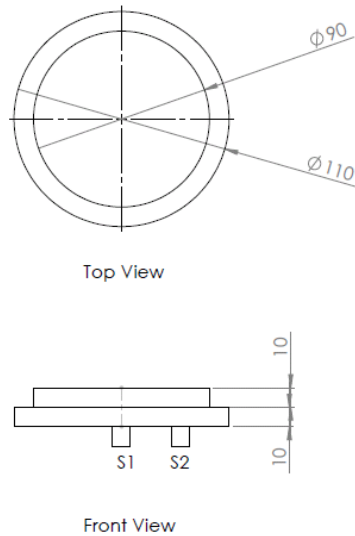
Figure 3.2: Schematic diagram of the mild steel target plate used in the experimental set up (dimensions in mm).

At the centre of the test specimen, 15 pencil lead were broken one at a time following standardised Hsu Nielsen test procedure (124) as shown in **Figure 3.3.** The propelling pencil consists a graphite lead of hardness 2H, diameter 0.5 mm and length 3 mm. The guide ring was used to ensure the same pencil lead breaking angle at each test. Manual pencil lead break (PLB) by pressing it against the test surface generates a pulsed AE source.
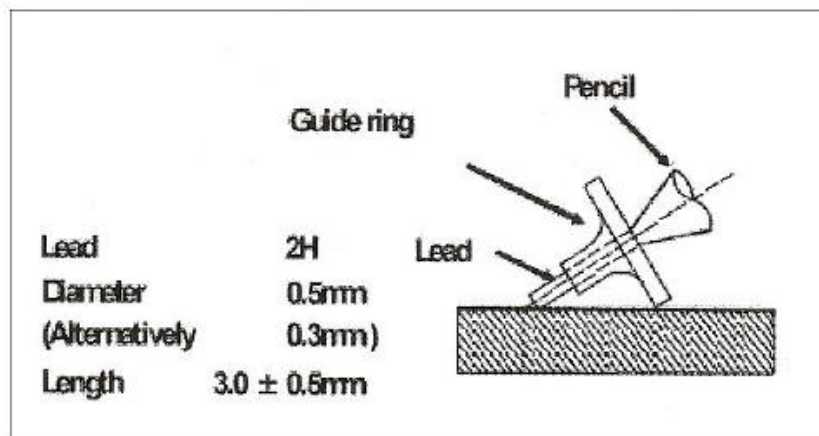
Figure 3.3: Hsu Nielsen source (124)

Signals were recorded at the sensors attached on the opposite surface. The sensors were detached and mounted again to repeat the same procedure 3 times.

Further experiments were carried out attaching the target plate, fixing it into the end of a Perspex cylinder bottom cover as shown in **Figure 3.4**.
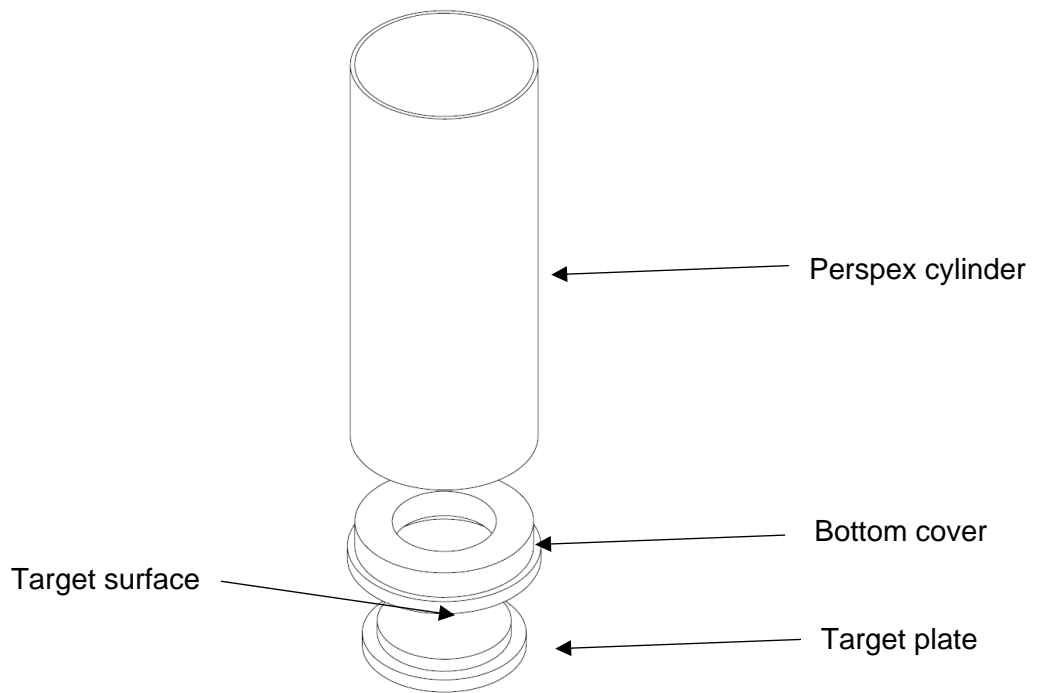
Figure 3.4: Target plate attached to the bottom cover of a Perspex cylindrical tube.

Sensors were attached at the opposite, outside, surface of the target plate, one at the centre and another 30 mm from the centre, similar to free target plate experiments. PLB were applied at the centre of the target plate on the inner surface. Two experiments, each repeated 10 times, were performed - one in air and another one loading the target plate with a 30 mm water column inside the cylinder. To analyze the effect of masking, the target surface was masked with plastic tape leaving a 30 mm² rectangular area at the centre uncovered and two experiments, each repeated 10 times, were carried out – one in air and another one loading the masked fixed target plate with a 30 mm water column. Between the experiments, the sensors were removed and re-attached. **Table 3.1** summarizes description of all the performed PLB experiments.

Table 3.1: Summary of all the performed PLB experiments.

Experiment Description	Abbreviation	No of Experiments performed	No of tests per Experiment	Total Signal records (including S1 & S2)
Target plate resting freely on the wooden blocks	Free	4	15	120
Target plate attached to the Perspex cylinder	Fixed	1	10	20
Target plate attached to Perspex cylinder and loaded under water	Fixed - Water	1	10	20
Target plate attached to Perspex cylinder and target surface masked	Masked	1	10	20
Target plate attached to Perspex cylinder, target surface masked and loaded under water	Masked - Water	1	10	20

3.4 Signal Analysis

The acquired AE signals were analysed in the time domain, frequency domain and time frequency domain. The following sections summarise the findings for different signal analysis performed.

3.4.1 Time domain signal analysis

Figure 3.5 shows typical AE signals acquired at Sensor 1 (S1) and Sensor 2 (S2) from PLB on the mild steel target plate while resting on the wooden blocks. **Figure 3.6** (a) & (b) shows the AE signals for the first 0.1 ms. For comparison, **Figure 3.7** presents typical AE signals (0.1 ms) at S1 and S2, acquired from PLB on the fixed target plate. For sensor S1 a low amplitude fast wave is observed, quickly followed by a high amplitude slow wave which arrives about 0.015 ms after the fast wave. Signals are slightly more highly damped as would be expected when the target is attached to the cylinder structure. At sensor S2 the presence of two wave types is more difficult to observe due to the different path lengths, reflections and mode conversions causing more complex wave fields.

(a)

(b)
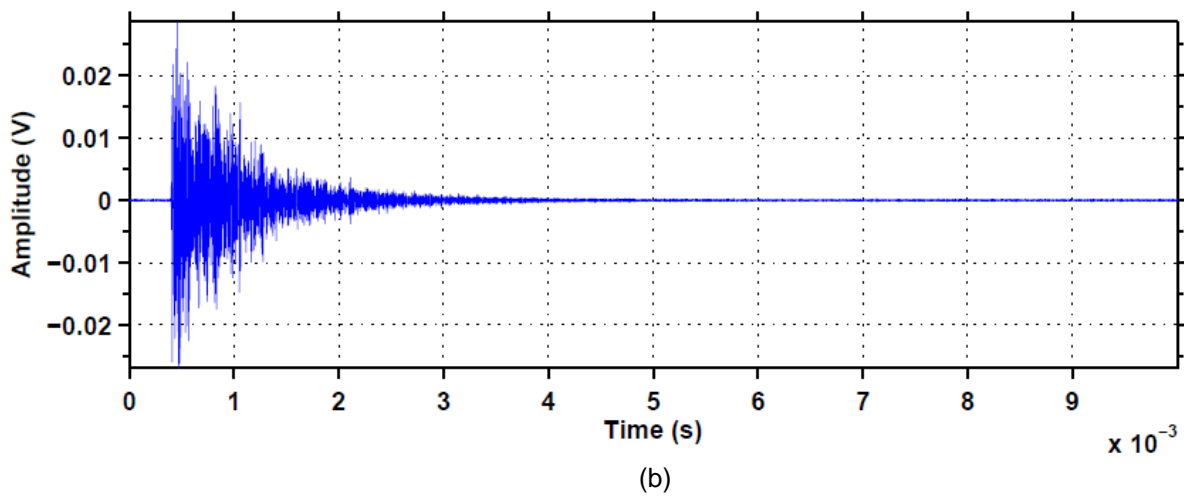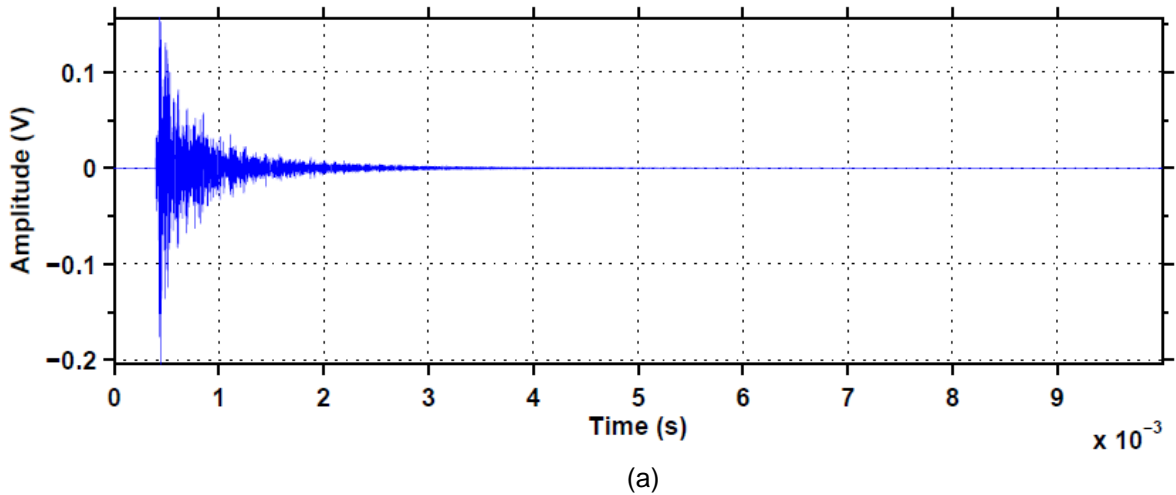
Figure 3.5: Typical AE signal from PLB at (a) S1 and at (b) S2 on free target plate.

(a)

(b)
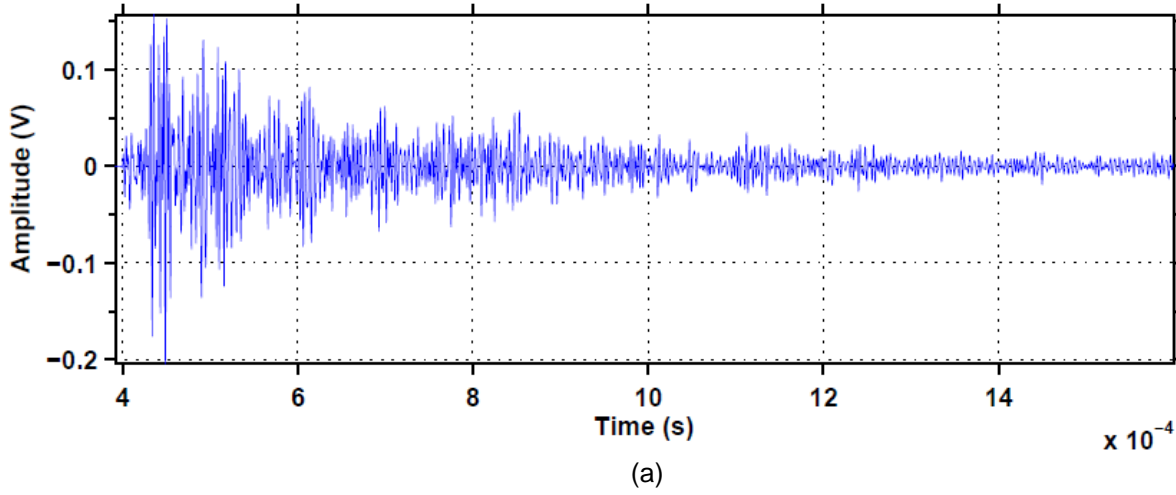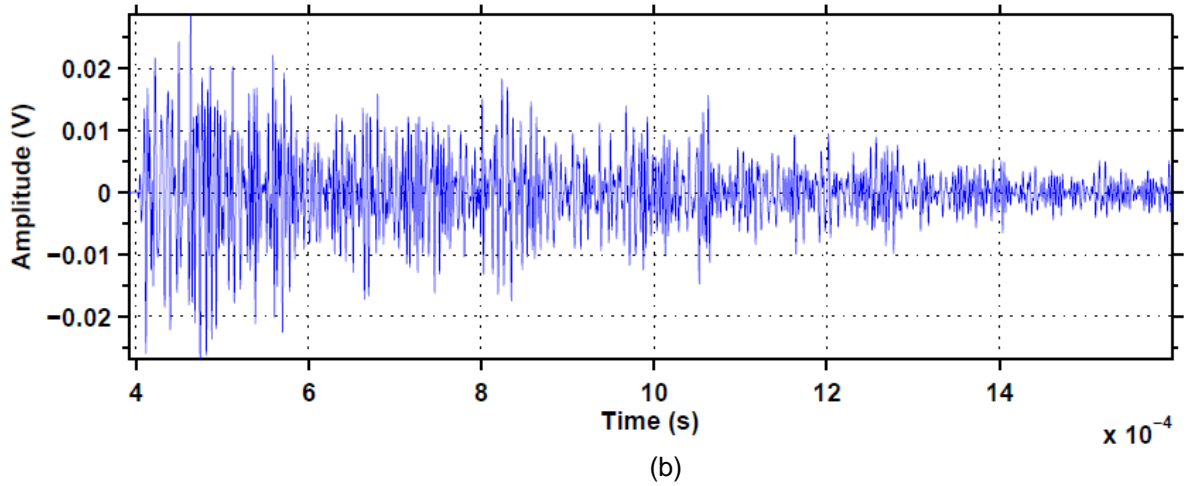
Figure 3.6: First 0.1 ms of the Figure 3.5 AE signal at sensor (a) S1 and (b) S2.

(a)

(b)
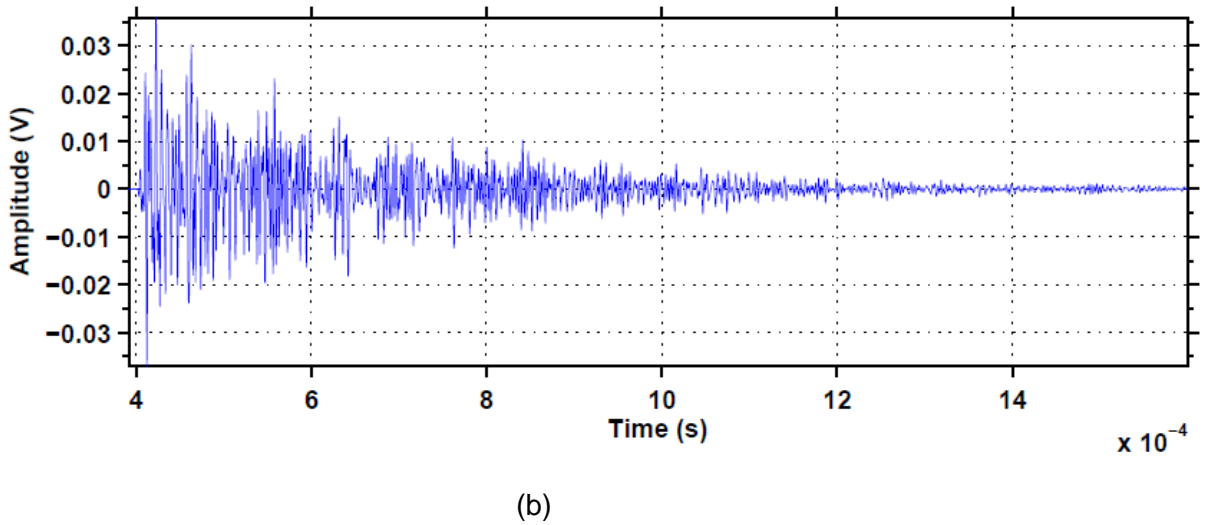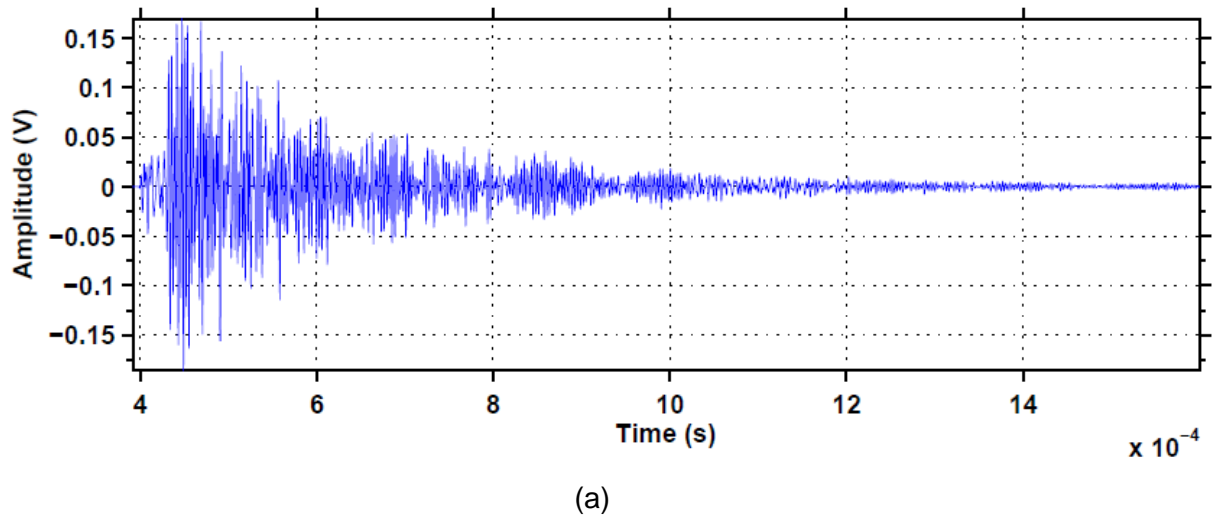
Figure 3.7: Typical AE signal from PLB at (a) S1 and at (b) S2 on fixed target plate.

Similar signal characteristics are observed in all PLB tests carried out in this work and previously published work by other researchers (16,29,125). Appendix A shows the results obtained for other fixed target plate PLB experiments performed in different environments: Fixed – water, Masked & Masked – Water, as described in **Table 3.1**.

For all the PLB AE signal records, 4 time based parameters have been evaluated: Maximum Amplitude, Duration, Rise time and AE Energy. Detailed results are presented in Appendix B. For all the experiments, signals at S1 are stronger than S2 as observed from Maximum Amplitude and AE energy. For duration and rise time it was found to be fairly consistent for both sensors and for free or fixed support conditions. The variations in the experiment results when the target plate was fixed in the end of the cylinder were found to be higher than that where the target plate was freely supported. The reasons behind these findings are discussed in the following section.

3.4.2 Frequency domain analysis

Figure 3.8 presents the power spectral density (PSD) of 4 PLB experiments, each repeated 15 times on the free target plate for 800 µs records and from 100 kHz to 500 kHz at S1 & S2. Signals are 10 - 20 times stronger at S1 than signals at S2.
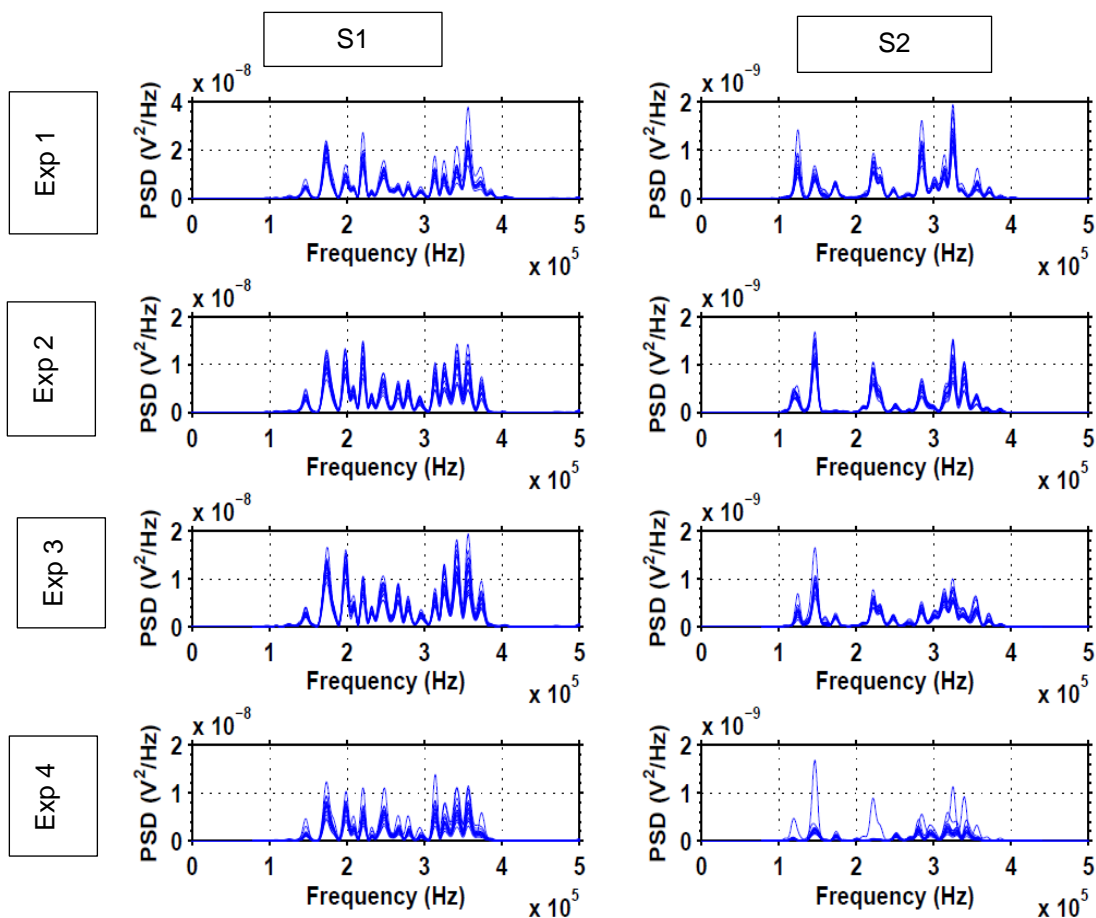
Figure 3.8: PSD of filtered signals on free target plate at S1 and S2 for 4 experiments.

From **Figure 3.8,** for a given experiment, at S1, there are 15 dominating peaks in the PSD between 0.1 MHz and 0.4 MHz. At S2, the relative amplitude of the peaks in the PSD have changed. From **Figure 3.8**, within an experiment, signal PSD is found to be more repeatable for all the records than comparing records across different experiments. The variations between experiments can be attributed to the change in coupling conditions due to detaching and remounting of sensors between experiments which is consistent with findings from other researches.

Figure 3.9 & **Figure 3.10** show PSD of AE signals recorded at S1 and at S2, respectively, for four experiments performed in different environments with the target plate fitted into the end of the cylinder, fixed. Fewer peaks are observed for signals recorded at both the sensor positions when compared to the plate test when the plate is freely supported, **Figure 3.8**. At S1, from **Figure 3.9**, unlike free target plate PLB, as shown in **Figure 3.8**, the dominating frequency contents are found primarily above 300 kHz. Maximum amplitudes above 300 kHz are 2- 5 times stronger than for freely supported target plate signal components.
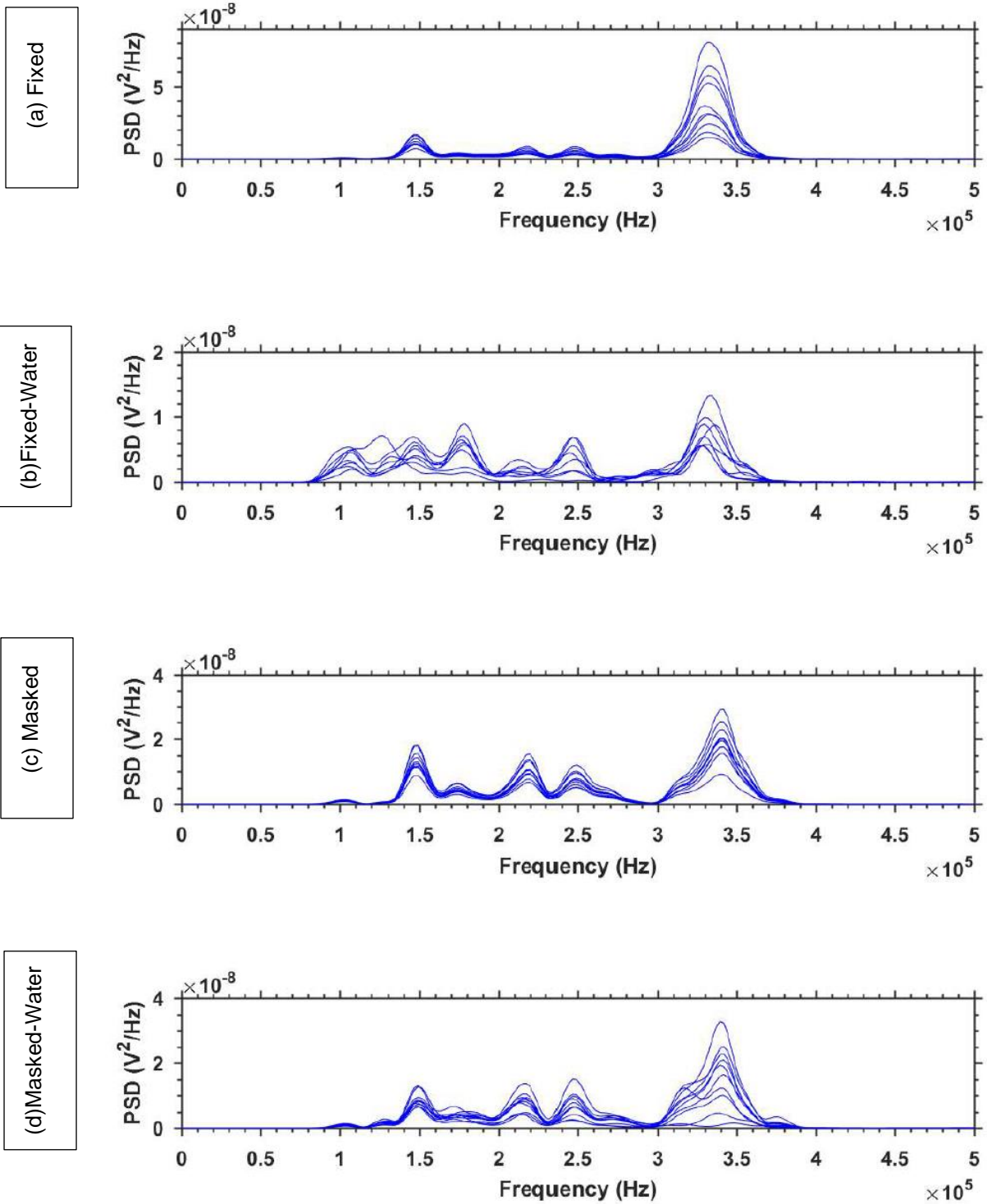
Figure 3.9: PSD of the filtered AE signals reorded at S1 on fixed target plate for four different experimental environments.
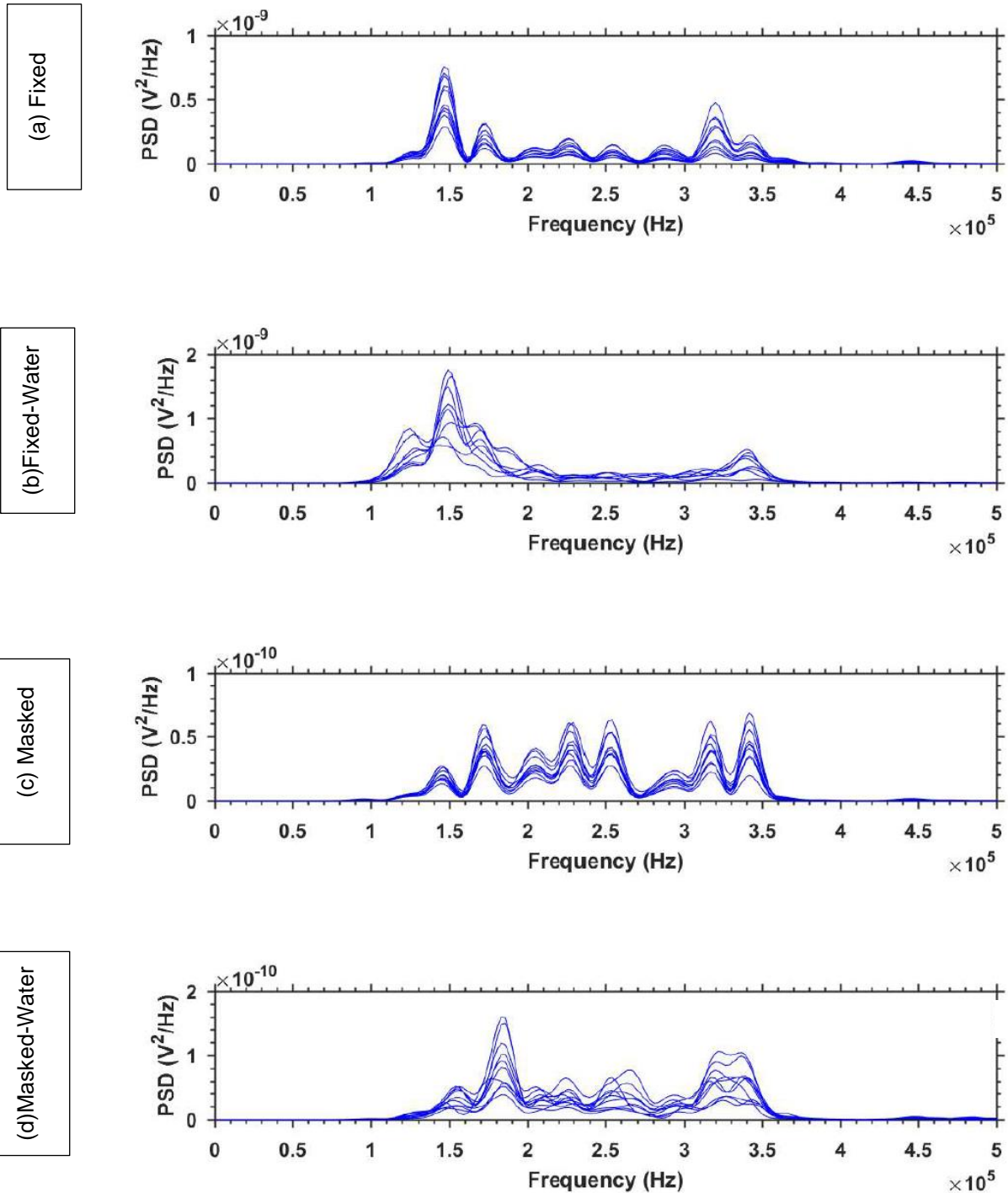
Figure 3.10: PSD of the filtered AE signals reorded at S2 on fixed target plate for four different experimental environments.

At S2, as shown in **Figure 3.10**, for unmasked experiments, above 300 kHz, maximum amplitudes of the signal components are either similar (Masked in air) or halved (Masked Water loaded experiment conditions) and between 100 – 200 kHz, similar maximum amplitudes are observed. For masked experiments, the maximum PSD, at S2, as shown in **Figure 3.10**, is an order of magnitude smaller in comparison

with free target plate signal components shown in **Figure 3.8**. Three peaks have been noticed between 100 – 200 kHz for four experiments, at S2, with the target plate fixed at the end of the cylinder which is similar to when it is freely supported for PLB experiments, as in **Figure 3.8**, but varying in amplitudes. In general, at S2, below 300 kHz, more variations in frequency content and in amplitudes, have been observed for signal components among four experimental conditions for the fixed target plate experiments (**Figure 3.10**) in comparison with free supported plate experiments (**Figure 3.8**).

The change in relative amplitudes of the signal peaks for fixed target plate experiments, can be attributed to the change in experimental set up and change in PLB procedure. Earlier research showed that changing the circular disk fixture from free to fixed can change both the relative amplitude and frequency response of the signal (126). Also, for PLB on the free target plate, the guide ring was rested on the target surface as shown in

Figure 3.11, as per Tsu-Nielsen test procedure described in **section 3.3**. However, for PLB on the fixed target plate, the Cylindrical Perspex tube wall shown in **Figure 3.4** restricts the pencil/guide ring assembly to be placed at the same angle (θ) on the target surface along with possible slight change in orientation between the experiments. Previous research work (127) showed that a change in PLB angle and orientation can affect the frequency content and amplitude of the observed signals.
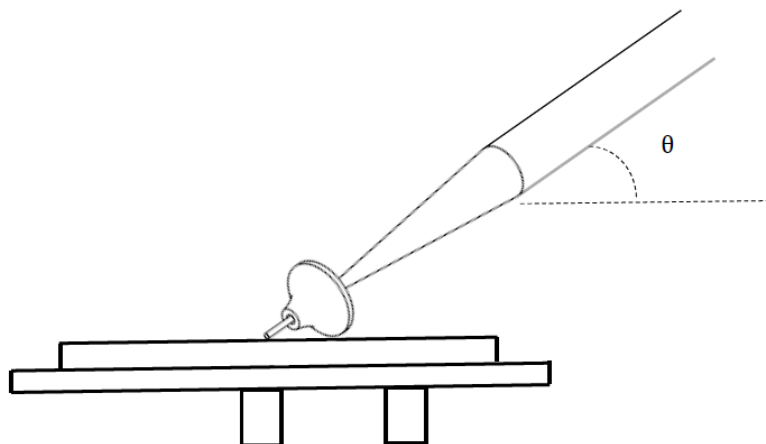
Figure 3.11: For PLB on free target plate, the guide ring was rested on the target surface at an angle **θ**.

Less repeatability of PLB due to above mentioned restrictions of cylindrical Perspex glass wall and changes in coupling due to attaching and dismounting of sensors between the experiments on fixed target plate, causes larger variation in PSD, both in

amplitude and frequency contents. These variations were found to be greater for water loaded fixed target plates due to additional complexity in placing the pencil tip on slippery target surface.

3.4.3 Time Frequency domain analysis

In this section, time frequency analysis results have been presented. For this analysis, GWT method has been implemented using AGU Vallen Wavelet software (82,128).

Figure 3.12 shows GWT of acquired AE signal from PLB on free target plate. From **Figure 3.12** (a), for S1, at the beginning of the signal, frequency contents are concenrated between 300 - 350 kHz and around 170 kHz which shifts mainly towards 170 kHz after 150 μs.

(a)

(b)
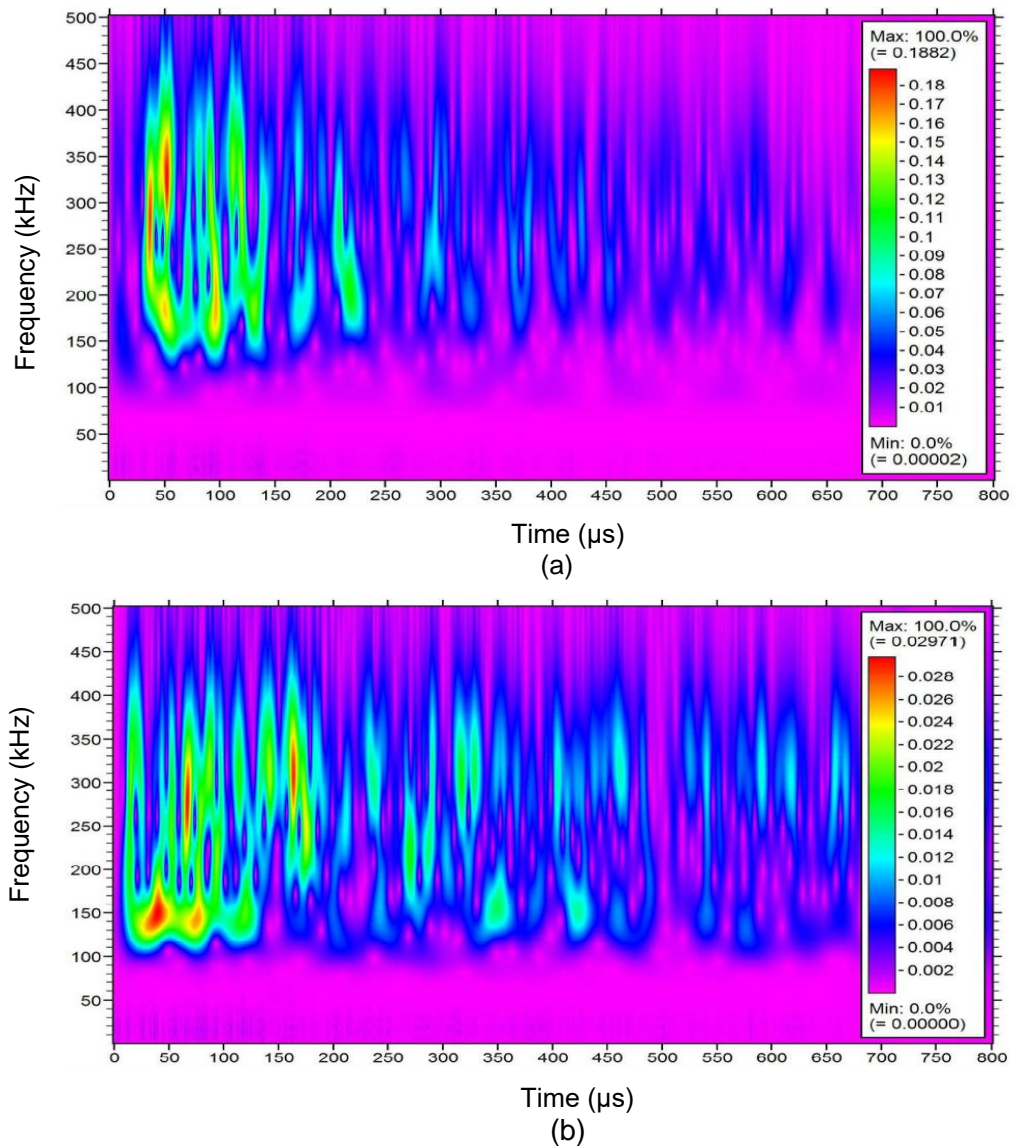
Figure 3.12: GWT of typical PLB AE signal at (a) S1 and at (b) S2 on free target plate.

From **Figure 3.12** (b), for S2, at the beginning of the signal, the main frequency contents begin at frequencies around 300 kHz and 150 kHz and then predominantly shifts towards 300 kHz after 150 µs.

Figure 3.13 and **Figure 3.14** shows GWT of typical AE signal, at S1 and S2 respectively, from PLB in four different experimental conditions: (a) Fixed, (b) Fixed – Water, (c) Masked and (d) Masked – Water, as described in **Table 3.1**.
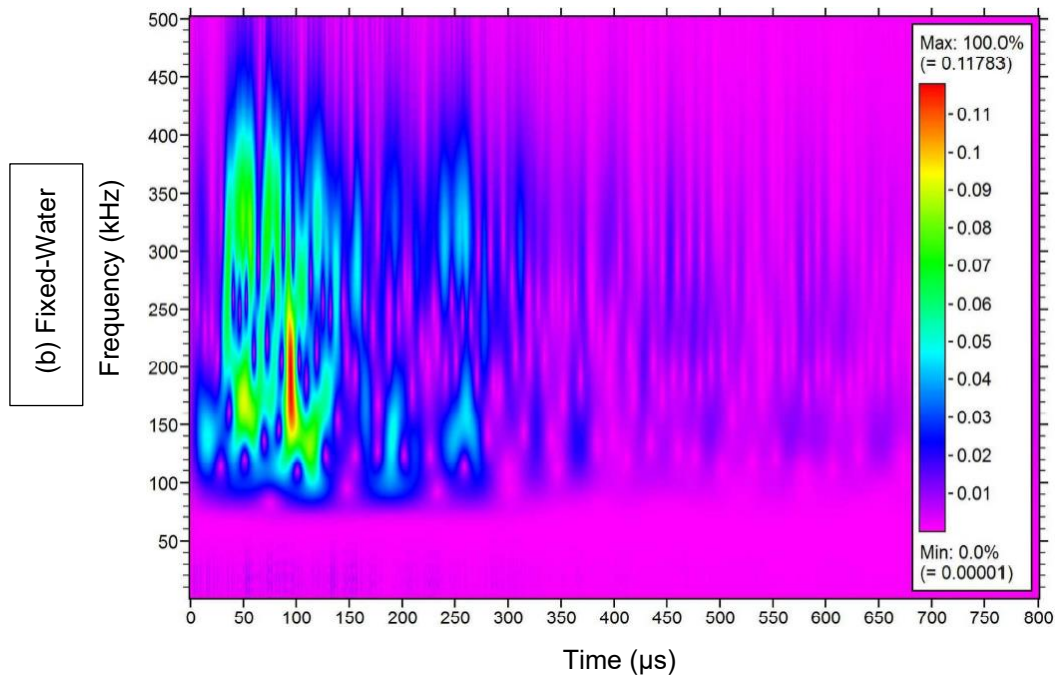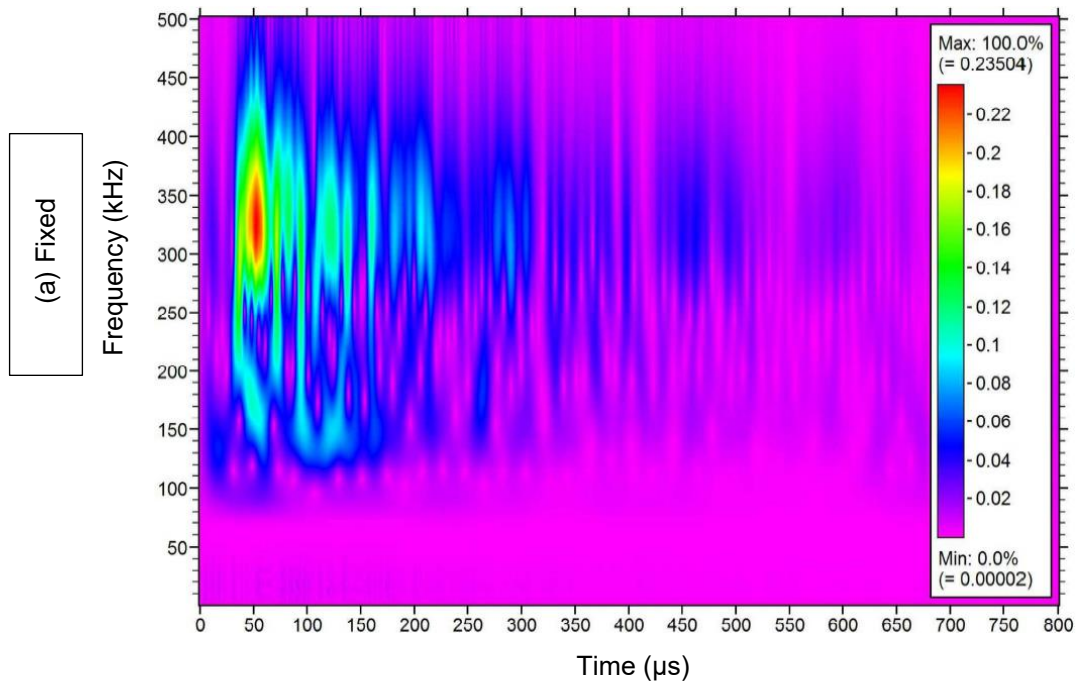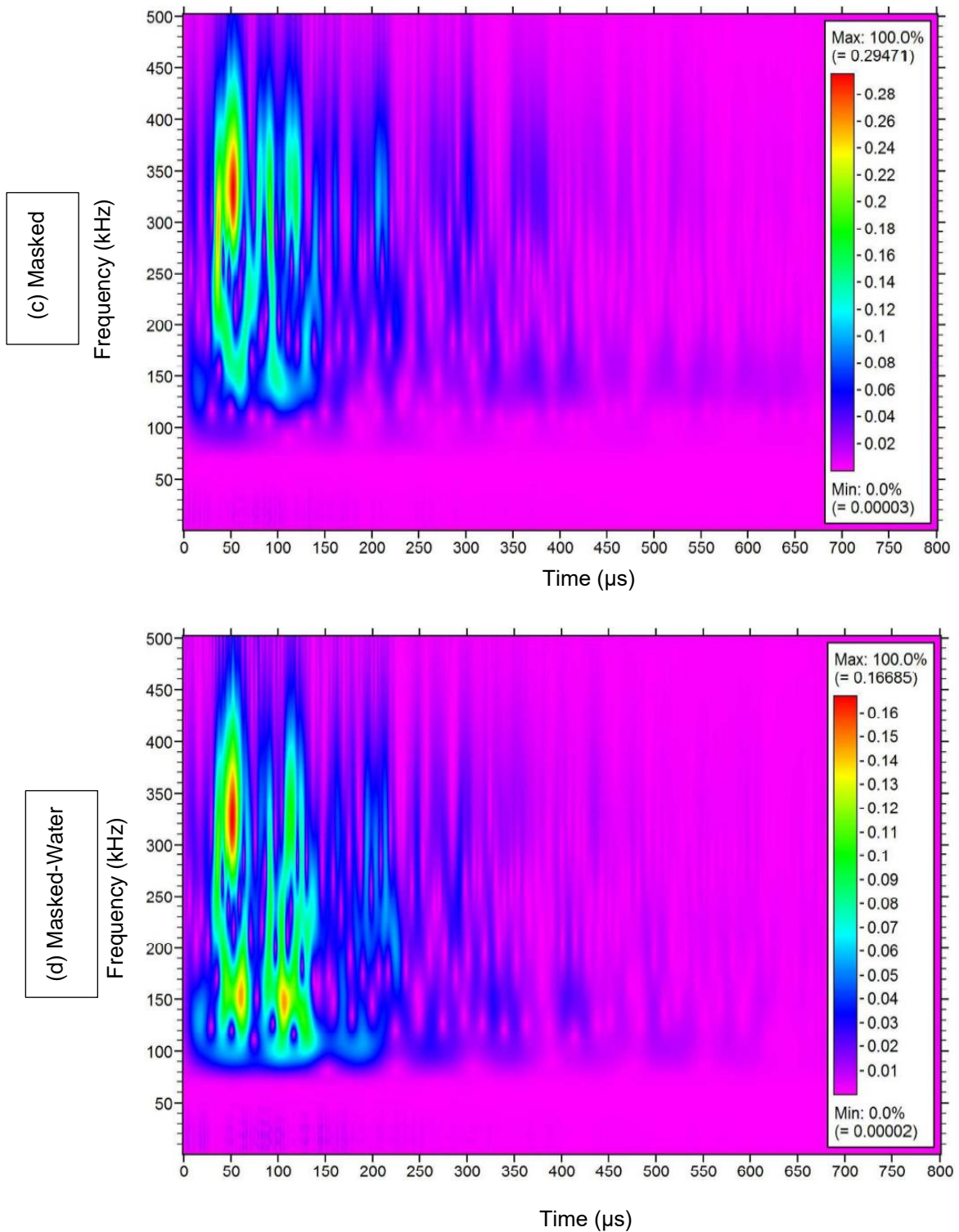
Figure 3.13: Wavelet transform of typical AE signal of PLB at S1 for four different experimental environments: (a) Fixed, (b) Fixed – Water, (c) Masked and (d) Masked – Water.

(a) Fixed
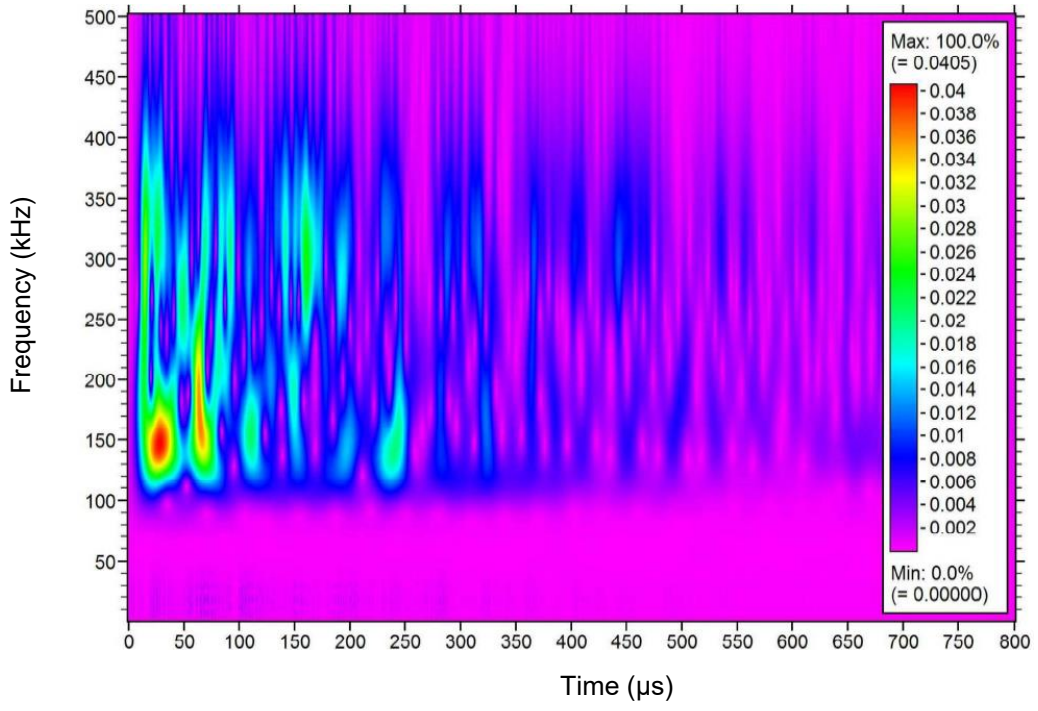
(b) Fixed-Water
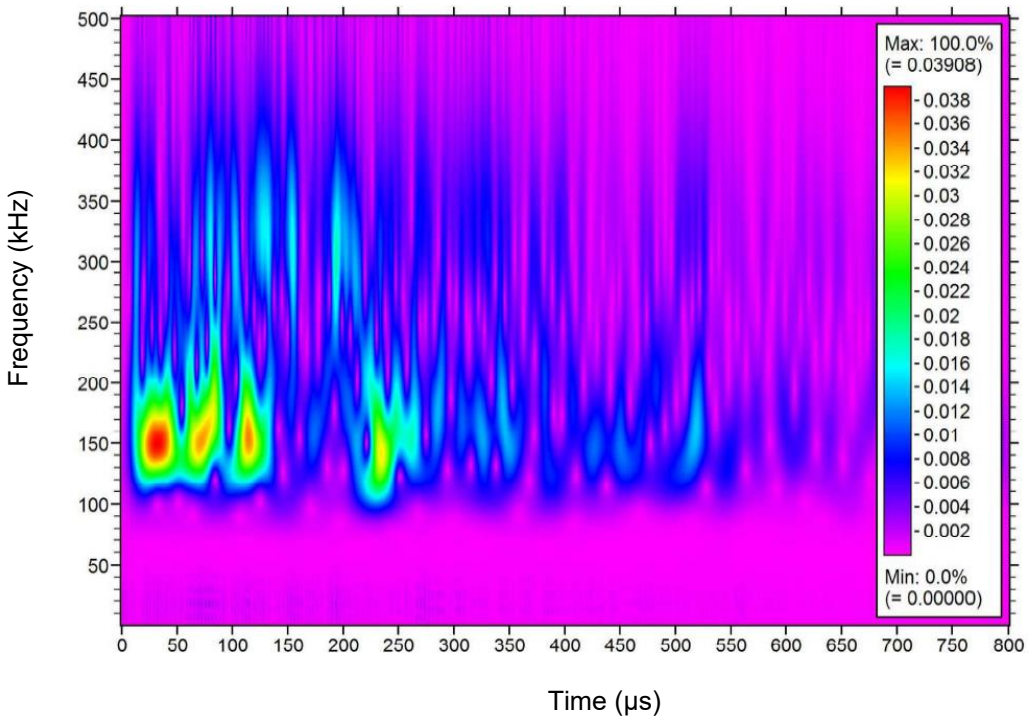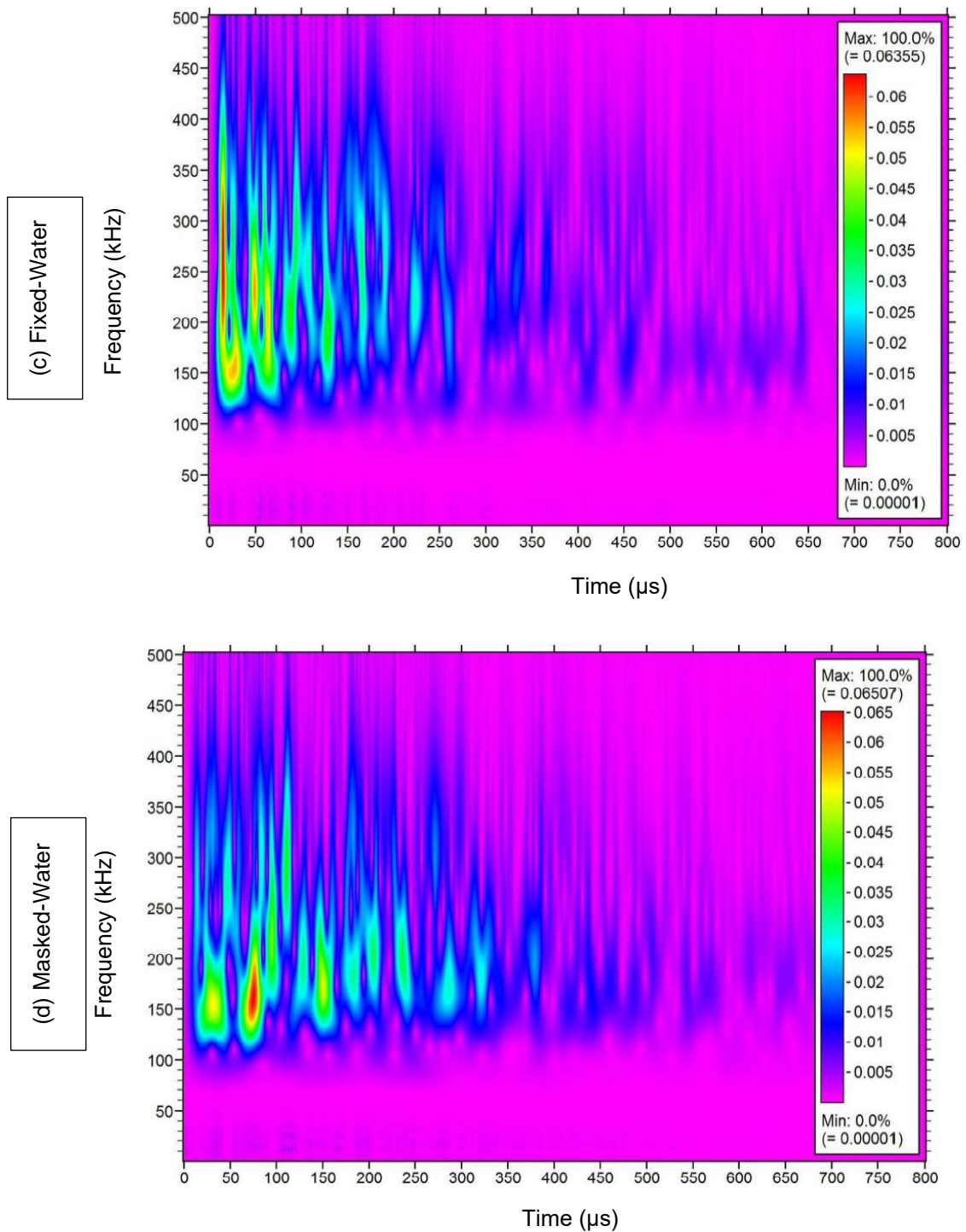
Figure 3.14: GWT of typical AE signal of PLB at S2 for four different experimental environments: (a) Fixed, (b) Fixed – Water, (c) Masked and (d) Masked- Water

From **Figure 3.13** (a) & (c), for Fixed & Maksed experiments respectively, the main frequency contents are around 325 kHz. For these experiments weaker frequency contents around 150 kHz was observed in initial 150 μs of the signals . From **Figure 3.13** (b) & (d), for Fixed – Water and Masked – Water experiments respectively, the main frequency contents around 325 kHz and 150 kHz are observed. For masked

69

experiments, at S1, as shown in **Figure 3.14** (c) & (d), strongest signal activites are noticed within first 150 µs.

From **Figure 3.14**, for four experiment conditions, at S2, primary frequency contents are found at 150 kHz with weaker components around 325 kHz. The weaker components at 325 kHz decay quickly after first 0.25 ms.

For analysis purposes these results indicate that for PLB the important signal parameters to consider are the first 0.4 ms and three frequency bands around 0.1 - 0.2 MHz, 0.2 - 0.3 MHz and 0.3 - 0.4 MHz. These signal parameters are used in this research.

3.5 Summary

This chapter presents the analysis of PLB experiments on the target plate. The target plate was freely supported for four experiments and fixed on the bottom cap of a Perspex cylindrical tube for another 4 experiments. When the target plate was fixed, two PLB experiments were carried out: one in air and the other one loading the target plate with water. Then the target plate was masked and the same PLB experiments on the fixed target plate, in air and water, were performed. Each experiment was carried out at least 10 times. All the AE signals were acquired at two different locations: one at the centre and one off-centre position. Acquired AE signals for both the locations have been analysed using different signal analysis procedures and compared for different experimental conditions.

For any PLB test, a stronger signal was obtained at the centre which is directly underneath the PLB location but on the opposite surface. This is evident from amplitude, event energy or power spectral density analysis.

Within an experiment, among different tests, the frequency contents were repeatable. However, variations in frequency contents have been noticed between the experiments for both sensor locations of about 1.5 in signal strength. This has been apparent through the frequency domain PSD analysis and from GWT of the acquired signals.

Though the frequency contents have been changed for different set ups, the peak frequencies were detected at few specific frequencies. It is identified from the peak PSD analysis and from GWT. This can be ascribed to the sensor response characteristics. The sensors are wide band in nature although at certain frequencies these are more responsive.

The effect of fixing the target plate was apparent from the event duration and rise time analysis. Shorter event duration for fixed target plate can been identified from the time frequency representations (GWT) of the analysed AE signals.

For fixed target plate experiments, from all the performed signal analysis results, it is evident that in water PLB experiments showed more variations than that of in air experiments. It can be attributed to the fact of usual in water experimental challenges, such as difficulties in placing the pencil lead at the same location each time PLB carried out in water. This variation is not unusual but does reinforce the need to analyse sets of repeated tests before making any comparisons.

In general, variation among different test results within an experiment, is due to deviation in PLB from one test to another while keeping all the other test conditions the same. Between the experiments, the sensors were dismounted and attached again which changed the coupling condition of the setup.

Chapter 4 Distinction of populations of similar sized particle impacts on mild steel

4.1 Introduction

In this chapter, a technique to distinguish between two very similar populations of particles, sand particles and glass beads of similar size, mass and velocity, impacting on mild steel is presented. This laboratory work involves characterisation of acoustic emission on a target disc made of mild steel. In the laboratory, sets of individual particles are dropped onto the target disc. The acquired AE is then analysed in the time and frequency domain. A study of the AE energy in three broad frequency bands is carried out and frequency band energy ratios are identified to distinguish the populations of particles. Investigation of the coefficient of variation of these frequency band ratios enables development of a new framework for the distinction between populations of these very similar particles for these tests. SVM classification algorithm based analysis has been performed to evaluate individual glass beads and sand particle impact event identification with greater success.

4.2 Experimental setup and methodology

The circular stepped mild steel disc, as shown in **Figure 3.2**, was used as the target plate and was freely supported, placed on wooden blocks to isolate it. The sensors and data acquisition system, described in Section 3.3, was used. A small perspex tube of 10 mm diameter was fixed vertically above the centre of the top surface of the target plate to facilitate particle dropping at the centre of the target plate.

The experiments carried out involved dropping individual particles on the small mild steel target plate. For each test 15 sand particles and 15 glass beads were selected and dropped, one at a time, from a height of 205 mm onto the target plate reaching a velocity of around 2 m/s. The whole test procedure, including replacement of sensors and new populations of particles, was repeated four times so that effects of experimental variations relating to changing sensor coupling and different populations of sand and glass particles could be observed.

Glass beads and sand particles used in the experiments were sieved and the particle size fraction of 300-425 μm was used in these tests. During each of the four tests, 45 AE events (15 pencil lead breaks (PLB), 15 sand particles, 15 glass beads) were acquired at two sensor positions. During a specific test the experimental set up was not changed and sensors were not moved during a test. Between each test the experimental setup was dismantled.

4.3 Time domain signal analysis

Typical acquired AE signals for individual AE records of 0.01 seconds duration are shown in **Figure 4.1)** and **(4.2)** for PLB, single glass bead and single sand particle impacts at Sensor 1 and Sensor 2 respectively.

(a)

(b)

(c)
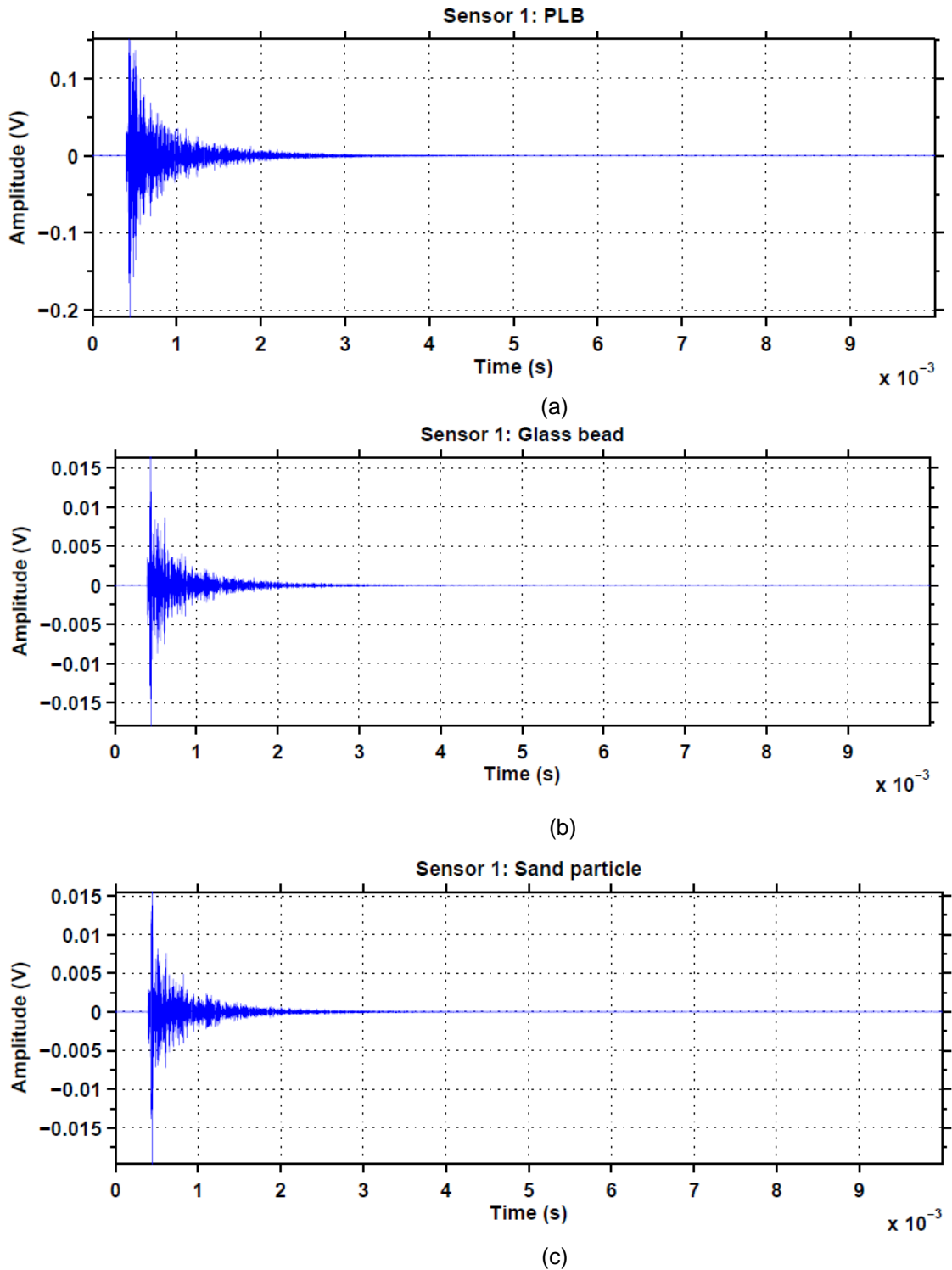
Figure 4.1: Typical time domain signal recorded at Sensor 1 for (a) PLB, (b) Single Glass bead impact & (c) Single sand particle impact

Sensor 2: PLB

(a)

Sensor 2: Glass bead

(b)

Sensor 2: Sand particle
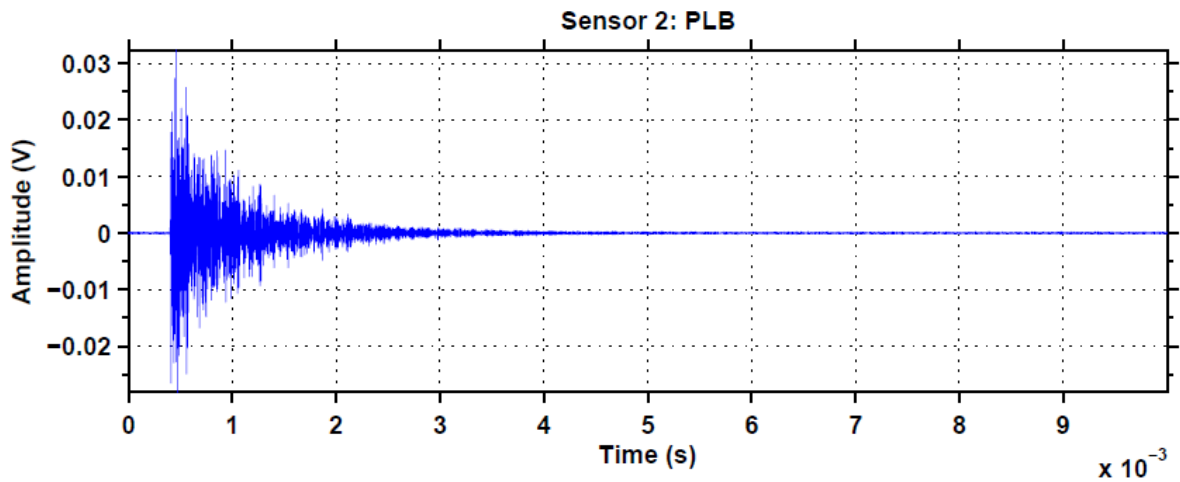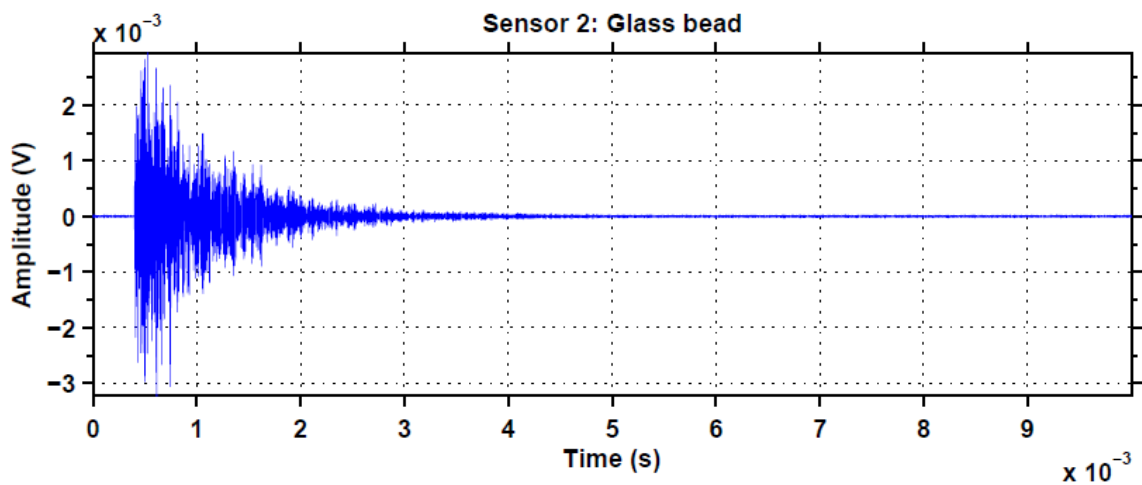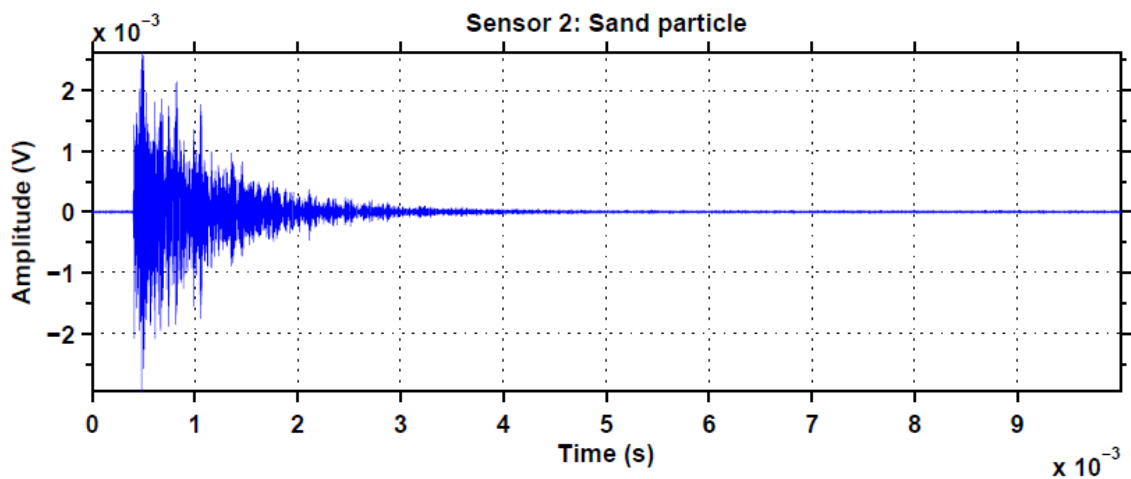
(c)

Figure 4.2: Typical time domain signal recorded at Sensor 2 for (a) PLB, (b) Single Glass bead impact & (c) Single sand particle impact

Each acquired record includes 25000 data points. The first 1000 data points were pre-trigger.   Sensor 1 was located directly on the opposite surface of the AE event

occurrence and hence the recorded amplitudes are higher than the ones recorded at Sensor 2 for all the three cases. Also, the pencil lead breaks generated stronger AE signals than the glass bead and sand particle impacts. The signals acquired at sensor 2 are more diffuse. To analyse all the recorded signals, a series of detailed analysis procedures were applied which are described in the following sections.

For each record, standard AE parameters that have been evaluated are: for time domain analysis, maximum amplitude, event duration, rise time & event energy and for frequency domain analysis, maximum power spectral density, peak frequency & frequency centroid. Calculations were carried out according to the definition presented in the literature review (Section 2.6.1). For each parameter, to compare the variation in obtained results within each experiment set (consists of 15 repeats each for PLB, Glass bead and sand particle impacts) and across 4 experiments, statistical analysis were performed by calculating mean, standard deviation and coefficient of variance. The results of most interest are described here and all the results are presented in Appendix C.

In this chapter, it is shown that among the seven AE parameters mentioned above, for both Sensor 1 and Sensor 2, maximum amplitude, event energy and maximum power spectral density distinguishes PLB events from glass bead and sand particle impacts very easily. However, for glass bead and sand particle impacts the parameters overlapped for all the experimental sets and hence they cannot be used to distinguish between populations of these very similar particles. Similar trends of difficulties in differentiability between glass beads and sand particles, based on standard AE parameters calculations, have been found in other researchers works as well (16).

4.4 Time Frequency domain analysis

AGU Vallen Wavelet software has been used to carry out a GWT to produce frequency/time/amplitude data for each record. An example of the wavelet transform, for S1 and S2, obtained from PLB, a glass bead and a sand particle impact at the centre of the specimen is shown in **Figure 4.3.**
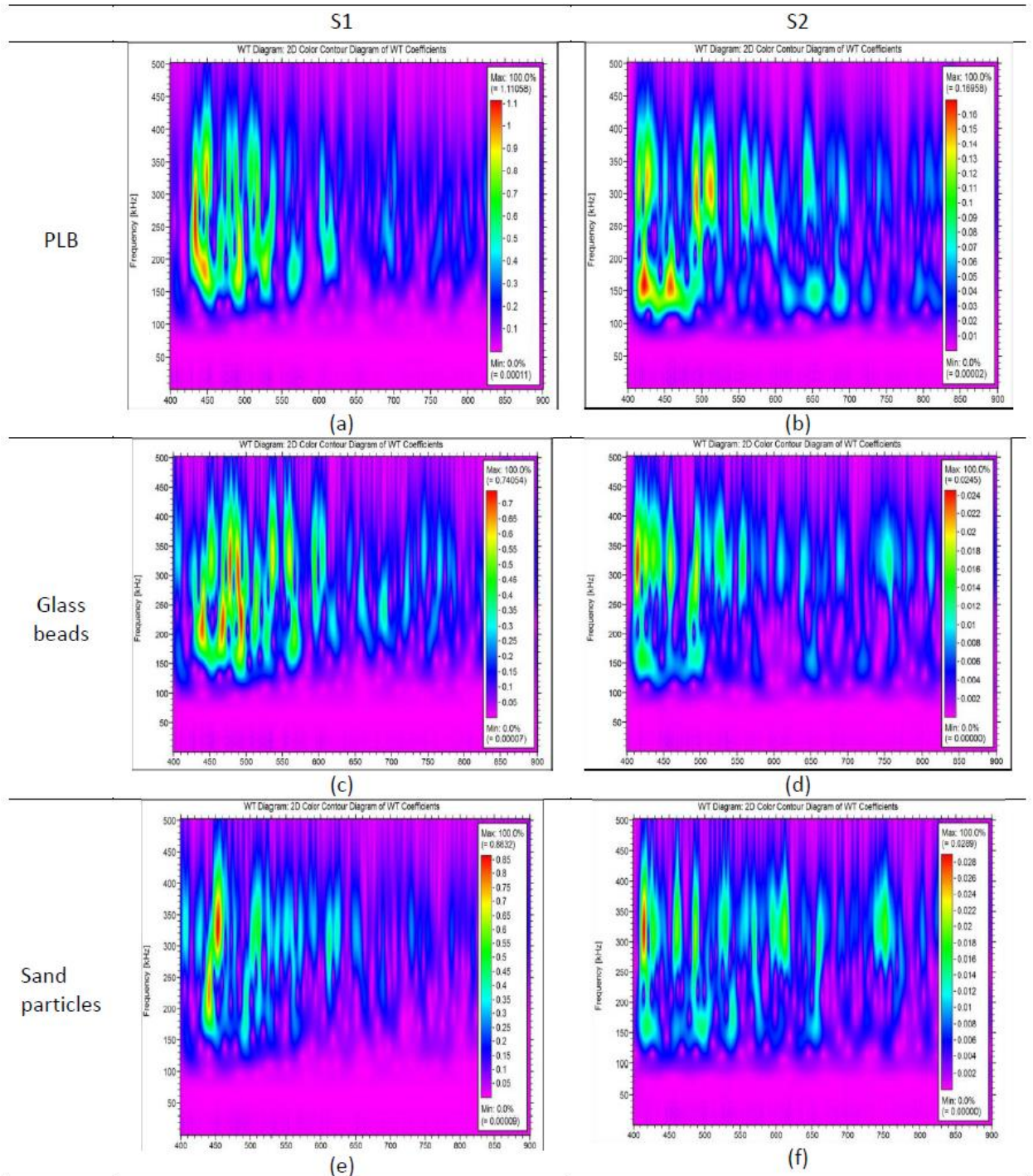
Figure 4.3: Time frequency analysis using GWT of PLB, glass bead and sand particle for 500 µs, after trigger, at sensor S1 and sensor S2.

This shows the diffusion of the waves in the time/frequency domain and enables identification of the important time window and frequency bands. For clarity, wavelets of only the first 500 µs, after trigger, are shown for frequencies between 100- 500 kHz. There are no significant frequency contents in the signals above 500 kHz, and a 100 kHz

high pass Chebychev filter has been applied to remove low frequency structural vibration components. So for all successive signal processing, records are passed through 100-500 kHz Chebychev band pass filter.

For both sensors there are significant broad frequency components around 150 kHz and 350 kHz of high amplitude, just after triggering. The amplitude then fluctuates and disperses due to effects of wave modes, speed, reflections and conversions. For S1 the frequency dispersion moves towards a broad band of energy around 300 kHz after about 200 μs. For S2 the frequency dispersion moves towards two broad bands of energy at around 350 kHz and 150 kHz.

Figure 4.4 shows 15 examples of frequency spectra obtained for each of the sources being PLB, glass or sand particles and for both sensors S1 and S2. The results again suggest that there are three broad frequency bands which can be considered for this laboratory setup, being, 1. 100 - 200 kHz, 2. 200 - 300 kHz, 3. 300 - 400 kHz.

In **Figure 4.4**, for S2 and for sand particles, the three frequency bands selected are labelled E_1, E_2 and E_3.
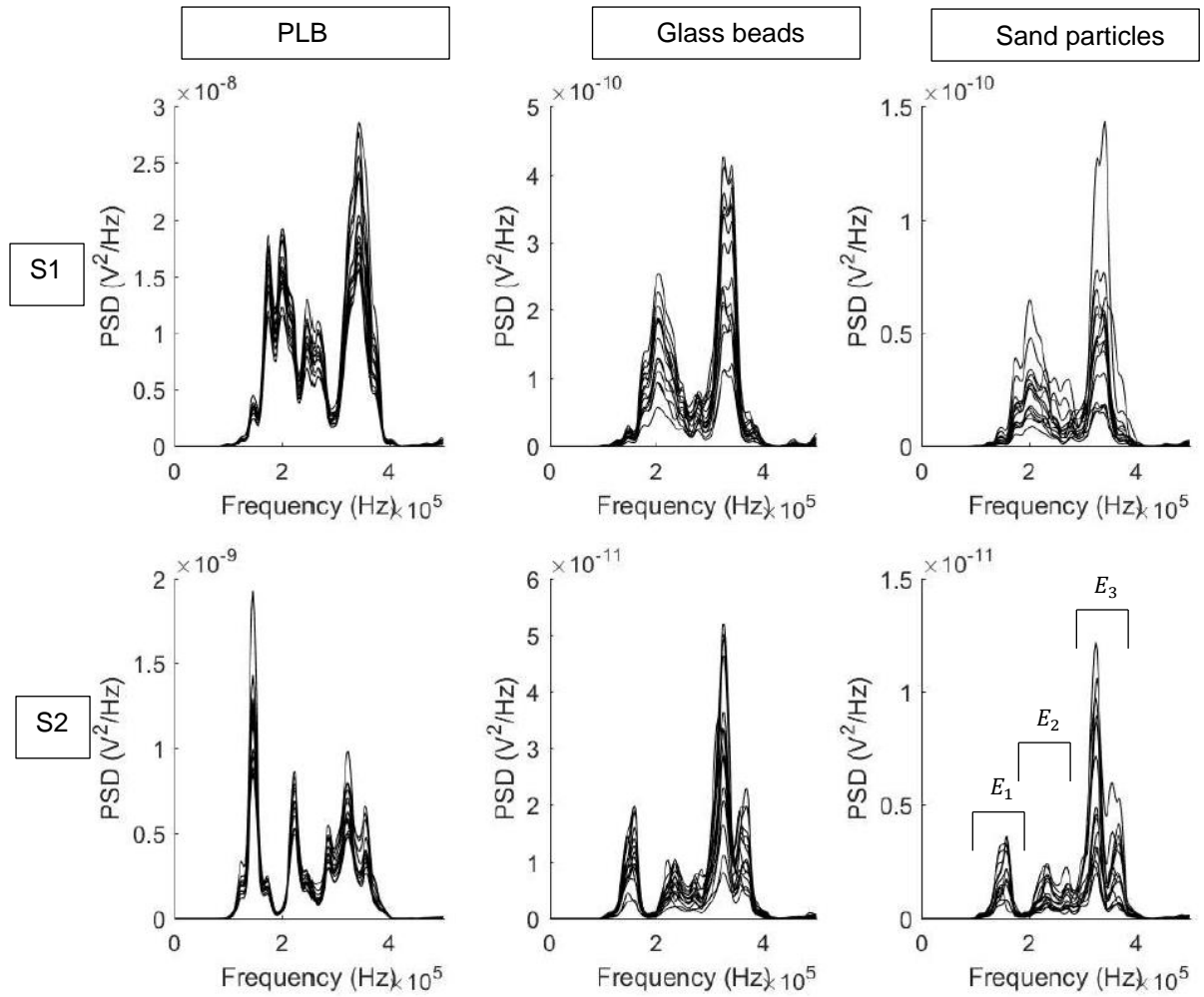
Figure 4.4: Power spectral density of the acquired signals for PLB, Glass and sand particles at sensors S1 and S2.

The energy in each frequency band was calculated for every record. For example for the energy in the frequency band from $100 - 200$ kHz, E_1, the record has been band passed through Chebychev $100 - 200$ kHz band pass filter. Similarly, for E_2 and E_3 corresponding filters have been used. The AE energy is then calculated using the equation [21],

$$E = \int_0^{\Delta t} [V(t)]^2 dt \qquad \textbf{(4.1)}$$

Where, E is the acoustic emission energy estimation $V(t)$ is the sensor output voltage at any time t, and Δt is the time window.

The AE energy has been calculated for each of the three frequency bands E_1, E_2 and E_3 and also for the frequency range of 100 kHz $-$ 500 kHz (E_a). It is observed, in **Figure 4.3** & **Figure 4.4**, that the amplitudes and the energy levels in each of the three frequency bands E_1, E_2 and E_3 vary and that the various possible ratios of the AE energies also vary for every individual record. However, between records, while the

amplitude might vary considerably, the energy ratios are more repeatable. **Table 4.1** shows seven frequency bands which have been considered in this work.

Table 4.1: Frequency bands used for signal energy calculations.

	E_1	E_2	E_3	E_{12}	E_{13}	E_{23}	E_a
Frequency range(kHz)	100-200	200-300	300-400	100-200 +200-300	100-200 +300-400	200-300 +300-400	100-500

There are twelve combinations of energy ratios that can be considered. For each event the frequency band energy ratios were calculated varying the window length Δt from the first 10 μs up to 1000 μs. The standard deviation (σ), the mean (μ) and the coefficient of variation (C_v) were calculated [21] for all the frequency ratios and time windows. For each population of events it was found that for $\Delta t \geq 400$μs, the ratio of C_v for glass beads and sand particles stabilizes around a specific value for any specific frequency band energy ratio. For example, in Test 4, this ratio stabilizes at around 1.5 for $\frac{E_{23}}{E_1}$. So, for all further calculations, $\Delta t = 400$ μs was used. The values of these energy ratios are plotted individually for each of the three sources for each of the twelve frequency bands (giving 12x45=540 data points for each test). For Test 4, the obtained results are shown in Figure 4 for both the sensors. Also for the population of events, σ and μ of AE energy ratios are indicated on the **Figure 4.5** (a).

For sensor S1, from **Figure 4.5** (a), data overlap for all the three sources PLB, sand and glass particles, whereas for sensor S2, from **Figure 4.5** (b), particle impact and PLB events can be independently clustered, with very few or no overlapped events, for 8 out of the 12 frequency band energy ratios and for these ratios the mean value for PLB events are easily distinguishable from that of particle impact events. So, in this study, sensor position S2 is more suitable for distinguishing particle impacts from PLB events based on mean value of frequency band energy ratios. However, when comparing glass beads and sand particles, the data points are overlapped in such a way that the particles are not individually distinguishable even for sensor S2. Similar trends have been identified for all other tests.
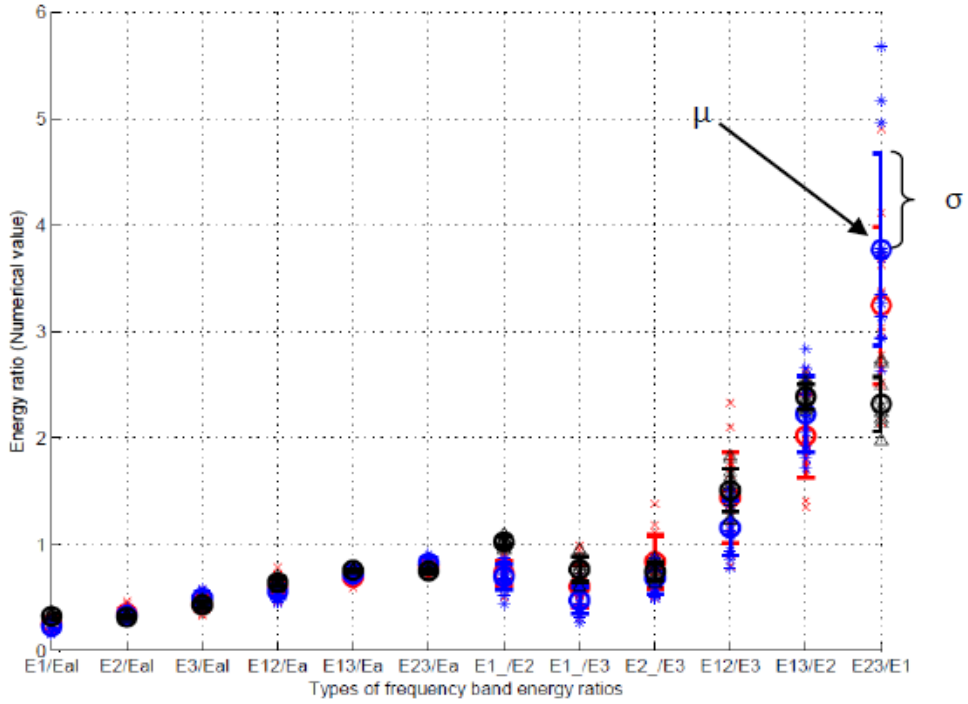
(a) Sensor S1
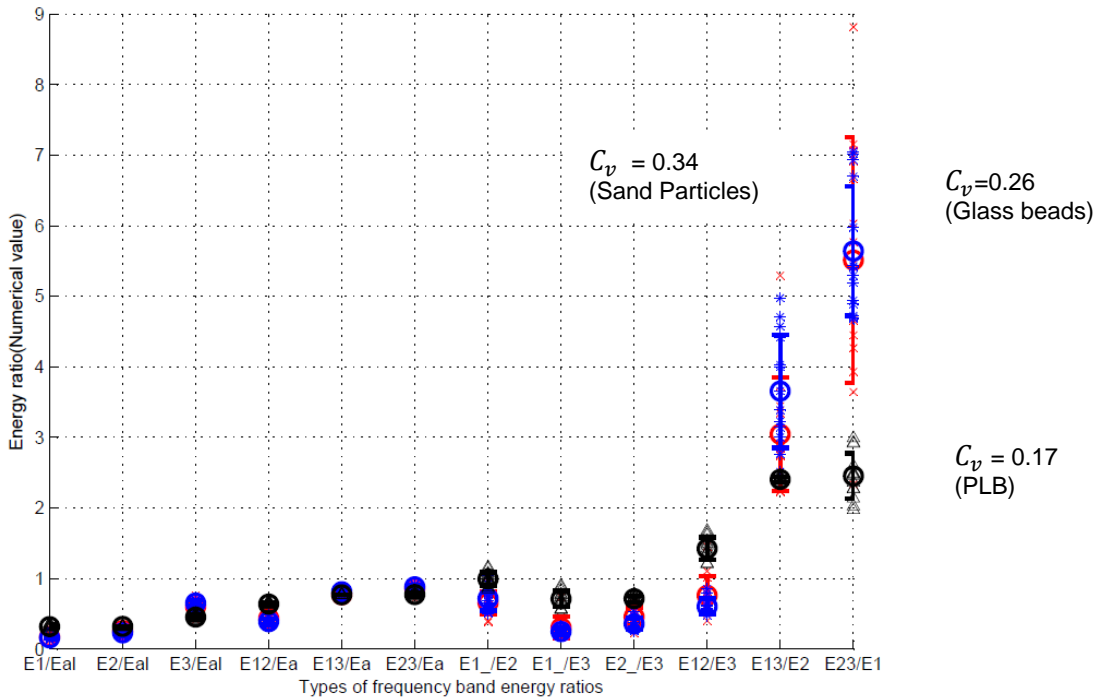
(b) Sensor S2

Figure 4.5: Frequency band energy ratios for test 4, (a) at S1 and (b) at S2. Blue, Black and Red data points indicate Glass beads, PLB and Sand particles respectively. Mean (μ) and standard deviation (σ) is shown graphically in (a) and C_v is denoted in (b) for corresponding population.

In this work, the amount of acquired data enables consideration of populations of events. In **Figure 4.5** (b), the C_v for the three populations of PLB, glass beads and sand particles are labelled for $\frac{E_{23}}{E_1}$. For all the experiments, the C_v for all the three categories are plotted in **Figure 4.6** (a) and (b) for S1 and S2, respectively. From **Figure 4.6** (b), for S2, the C_v for sand impact is found to be greater than glass bead impact and PLB, for all four experiments. The geometry and structure of the glass particles would be expected to be more regular than for sand particles. It might be expected that the variation in results for sand would be slightly greater than for glass particles, and this is the case. Analysis of all the data for the twelve frequency band ratios shows that other frequency ratios $(\frac{E_3}{E_1}, \frac{E_2}{E_3}, \frac{E_{12}}{E_3}, \frac{E_{13}}{E_2})$ shows similar trend.
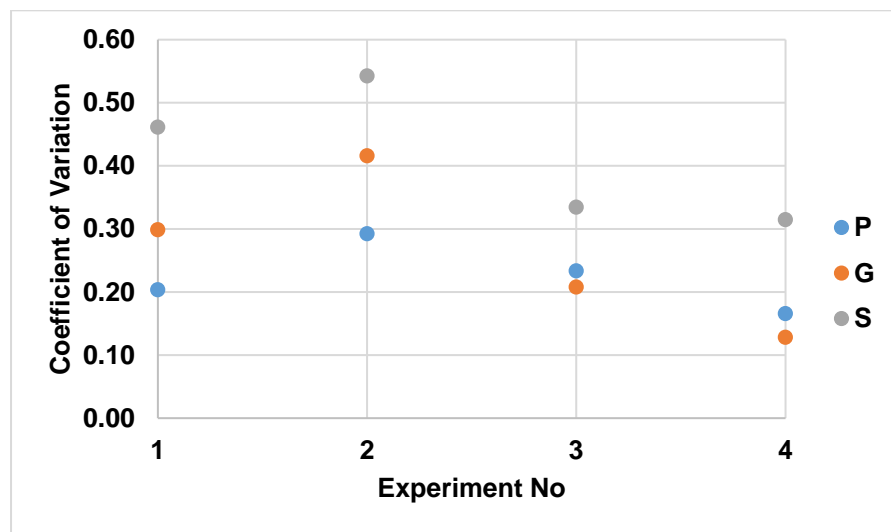
(a)
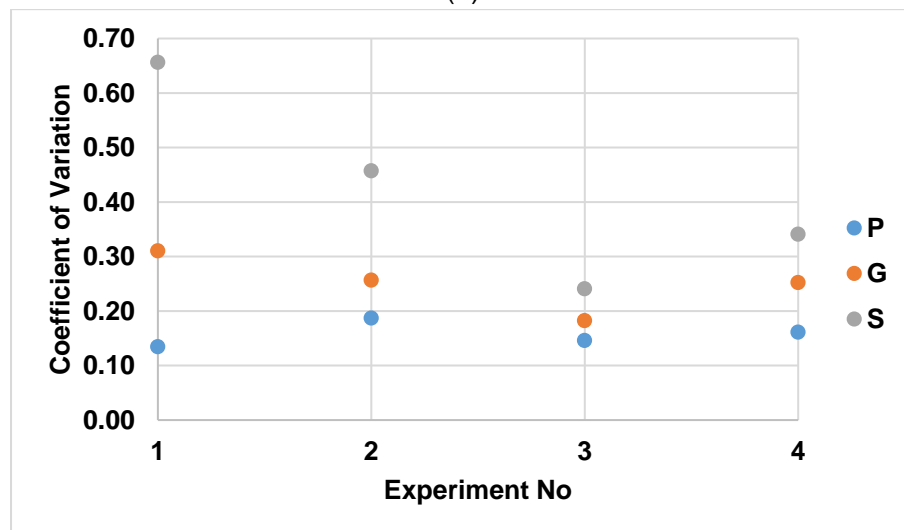
(b)

Figure 4.6: (a) C_v of $\frac{E_{23}}{E_1}$ for S1 for four tests, (b) C_v of $\frac{E_{23}}{E_1}$ for S2 for four tests. Here P,G and S stands for PLB, Glass bead and Sand particle respectively.

From **Figure 4.6** (b), for any test, the data of $\frac{E_{23}}{E_1}$ for PLB is independent of that for glass or sand particles and the C_v is very small. Within any individual test the C_v for sand is always highest. But between tests, the C_v for sand and glass beads show more variations. Normalising the ratios for sand or glass beads, with respect to the PLB results does not reduce the variation between tests. The main reason behind this is PLB tests are much more repeatable than the particle impact tests, as shown in all of the data. For any specific experimental setup this technique can distinguish between a population of glass beads and sand particles even when they are of similar size, mass and density and velocity.

4.5 Classification using SVM

In **section 4.3**, it has been shown that the standard time and frequency domain AE parameters , namely, amplitude, event energy, event duration, rise time, PSD, maximum frequency at PSD and spectral centroid, and time-frequency domain analysis (GWT), considered in this research, are unable to distinguish similar sized glass beads and sand particle impacts. In **section 4.4**, populations of similar sized glass beads and sand particle impacts were identified using coefficient of variations of proposed frequency band energy ratio technique. This method is appropriate for a system involving a population of more than one type of particle impacts, even with similar size, density and impact velocity. To facilitate each individual event identification in the population, further analysis has been performed applying a supervised machine learning algorithm, Support Vector Machine-Radial basis function (SVM-RBF), described in the **section 2.6.3.2**.

4.5.1 Model construction

For SVM analysis, the above mentioned 7 AE parameters, described in the **section 2.6.3.1** and calculated in the **section 4.3**, have been considered for the model training. AE event energy and event duration are directly related to the physical properties of the AE generating source (24,48,49). Amplitude reflects the detectability of the signal for a given coupling condition and background noise (24,48,49). Rise time, PSD and maximum frequency at PSD are affected by the geometry of the target plate and the sensor characteristics (24,48,49). Change in the spectral centroid associated with the change in the AE energy distribution in the considered frequency range (24,48,49). All of these AE parameters together provide a comprehensive monitoring of the given system under consideration and have been used as features for training the method.

For each sensor, per file, 7 data points associated with 7 AE parameters, are generated for the feature space of the supervised classification algorithm training. There

are 45 files from each experiment: 15 each from PLB, glass beads and sand particle impacts. Out of 180 available AE records, 80% records (144) were used for training the classification algorithm while the rest (36) were used for testing. For 7 AE parameters, each sensor generates 45*7 = 315 data points in the feature space resulting a total of 4*315 = 1260 data points from four experiments.

Open source R language based Classification and Regression Training package ('Caret') has been used for this analysis (129,130). For example, **Figure 4.7** shows the code snippet used for reading the data for S1, from an .csv file containing the 7 AE parameters data, originated from all the experiments, described in the **section 4.2**. In the .csv file, the 7 AE parameters are arranged in the columns with the associated parameter headings and an extra 8th column was added at the end with the corresponding class identity. So, each row of the .csv file corresponds to the value of the AE parameters in a single observation. The function `createDataPartition`, shown in the **Figure 4.7** and defined in the Caret package has been applied to divide the data obtained from the file into the training and test sets (126,127).

```
#Read Data file
stdAEdata = read.csv(file="S1_stdAEpara.csv",head=TRUE,sep=",");
#Create Partition in the data into training and test set
trainIndex <- createDataPartition(stdAEdata$Class,p=.8,list=T)
trainData <- stdAEdata[trainIndex,]
testData  <- stdAEdata[-trainIndex,]
```

Figure 4.7: Code snippet used in R programming language for data reading and partitioning.

Figure 4.8 presents the code snippet used for training the model and tuning the model parameter. From the **Figure 4.8**, the function `train`, described in the caret package, has been applied for training the classification model (112,113). In the function `train`, arguments are used for: adopting previously partitioned data for training purpose; scaling and centering the data; choosing SVM-Radial basis function for training the model and setting the model tuning parameter `sigma & C`, representing C & γ, respectively, of the Radial basis function for the SVM method, as described in the **section 2.6.3.2**. Performing linear grid search iteration and cross validation technique (115), the optimum values for the tuning parameters C & γ, were set as : For S1, $\gamma = 0.4$ and $C = 8$ and for S2, $\gamma = 0.67$ and $C = 7.7$.

```
# Use the expand.grid to specify the model parameters
grid <- expand.grid(sigma = c(0.4),
                         C = c(8))
# Train the model
svm.model <- train(Class~ ., data = trainData,
                 preProc = c("center","scale"), # Centering & Scaling
                 method = "svmRadial",   # Radial kernel
                 tuneGrid = grid, # The model parameter
                 )
```

Figure 4.8: Code snippet used in R programming language for training the model and setting the tuning parameter.

4.5.2 Model Evaluation

The trained model has been evaluated using the partitioned test data set of 36 (12 each for PLB, Glass beads and Sand particle impacts). The test data set has not been used in the model training and shows the probable performance of the trained model on any unseen future data acquired from the given system. The obtained results are summarized in the following Confusion Matrix in Table 4.2 (a) & (b) for S1 and S2 respectively :

Table 4.2: (a) Confusion matrix for S1

Predicted	Observed		
	Glass	PLB	Sand
Glass	10	0	3
PLB	0	12	0
Sand	2	0	9

(b) Confusion matrix for S2

Predicted	Observed		
	Glass	PLB	Sand
Glass	10	0	1
PLB	0	12	0
Sand	2	0	11

From **Table 4.2**, for both the sensors, all the expected 12 PLB events were successfully identified without any error. Out of 12 Glass particle impacts, 10 were detected correctly at both the sensors. Out of 12 sand particle impacts, 9 were noticed at S1 and 11 were noticed at S2 correctly. At S1, 3 Sand impacts were identified as Glass impacts and 2 Glass impacts were identified as Sand impacts wrongly. At S2, 1 Sand impact was identified as Glass impact and 2 Glass impacts were identified as Sand impacts erroneously.

Table 4.3 shows performance parameters of the applied SVM algorithm. The definition and formula for these parameters are described in section 2.6.3.2.1. For all the calculated performance parameters, shown in Table 4.3, PLB is completely separable. As shown in Appendix C for all the calculated 7 standard AE parameters, PLB found to be distinctive in nature even for single parameter analysis. For the applied SVM algorithm, a higher dimensional feature space created from 7 AE parameters has differentiated all the PLB events completely from the rest of the particle impact events. Considering the overlapping in calculated 7 AE parameters data, for glass bead and sand particle impacts, the obtained performance is encouraging. For this research, with the given target plate & sensor arrangement, S2 performs better for the applied SVM algorithm. It may be attributed to the larger variations in calculated AE parameters of the obtained signals at S2.

Table 4.3: (a) Performance parameters of applied SVM algorithm on data set for S1.

	Glass	PLB	Sand
Sensitivity	0.83	1	0.75
Specificity	0.87	1	0.92
PPV	0.77	1	0.82
NPV	0.91	1	0.88
Accuracy	0.83	1	0. 75

(b) Performance parameters of applied SVM algorithm on data set for S2

	Glass	PLB	Sand
Sensitivity	0.83	1	0.92
Specificity	0.96	1	0.92
PPV	0.91	1	0.85
NPV	0.92	1	0.96
Accuracy	0.83	1	0.92

4.6 Summary

For many applications simple AE parameters such as number of events, peak AE or AE Energy may be sufficient [21] to distinguish sources. To use such parameters usually requires some form of calibrations, standardisation or normalisation. However, for small coupon geometries, typical in engineering applications, the presence of close boundaries makes the interpretation difficult if not invalid due to reflections, dispersions and mode conversions. So, a unique frequency band energy analysis technique has been proposed. For this technique, once the optimal frequency bands and ratios have been identified, then an added advantage is that calibration of signal levels is not required. This technique is able to distinguish between population of two very similar groups (in terms of size and mass and energy) of sand particles and glass beads, impacting on mild steel based on the C_v of the frequency band AE energy ratios.

Further analysis has been performed using SVM based pattern recognition algorithm using 7 standard AE parameters. Available data set has been segmented into two parts of training set (80%) and test set (20%). The developed model has been applied on the test data for model performance evaluation purpose. The overall success rate of individually identifying each category (PLB, Glass bead and Sand particle impacts) at S1 was found as 86% and at S2 as 92%.

In these tests, the target plate material, geometry, particle impact velocity, impact angle, particle size, the experimental fluid medium (air) and the sensors were the same. A change in any of the above mentioned parameter along with more varied particle type investigation will establish the robustness of the technique. It has been shown that for nominally identical sensors, the frequency content can vary widely and based upon the driving frequency, the same sensor response signal amplitudes can differ. In this study, the sensors used are broad brand and analysis is based on broad frequency bands as well, rather than choosing a single frequency. In addition, the analysis is centred on frequency band energy ratios, not on amplitude. So, the proposed technique can overcome the issues of variation in peak frequency amplitude with respect to different driving frequency & variation in frequency contents among nominally identical sensors. However, for other sensor type, target material and geometry, other frequency bands or associated energy ratios might be optimal.

Chapter 5 An AE technique to distinguish sand particle impacts on mild steel target plate with fluid loading and air bubbles

5.1 Introduction

In this chapter, an AE technique to distinguish sand particle impact, on a mild steel plate, in presence of another AE source (bubble) has been developed. Individual air bubble insertion on a water loaded target plate and individual sand particle impact on the same target plate in air have been studied in time and frequency domain to identify bubbles' and sand particles' signature characteristics from associated AE signals respectively. In frequency domain, for PSD, a repeatable trend of higher frequency contents for sand particles between 300 – 400 kHz and for bubbles between 100 - 200 kHz has been observed. Based on this knowledge, frequency band energy ratio parameters were developed in Chapter 4 which can be used for automatic event identification technique for sand particle impacts in the presence of bubbles. The developed technique has been implemented in the analysis of single and multiple sand particle impacts experiments, in a bubbly environment. In analysis, varying threshold settings, the performance of the technique has been monitored comparing sand counts logged from the recorded AE signals using the developed technique with the known amount of sand particles inserted in the system.

5.2 Experimental setup and methodology

A schematic diagram of the experimental test rig used for these experiments is shown in **Figure 5.1.** A Perspex cylinder, 270 mm in length & 130 mm in diameter, is used with the target plate at the base. A centre hole in the top plate has a 420 mm vertical mild steel tube of 3 mm inner diameter which is connected to a plastic 90° connector tubing bend and a second horizontal, 440 mm steel guide tube of 3 mm inner diameter. The mild steel, circular stepped-specimen target plate, used for preliminary pencil lead break calibration experiments (Chapter 3) and for distinction of similar sized particles impacts experiments (Chapter 4), was sealed into the fixed lower plastic cap of the Perspex cylinder using silicon glue. Liquid can be poured inside the cylinder by removing the upper cap. The experimental rig rested upon two wooden blocks to isolate the equipment from the lab environment. **Table 5.1** shows all the experiments performed.
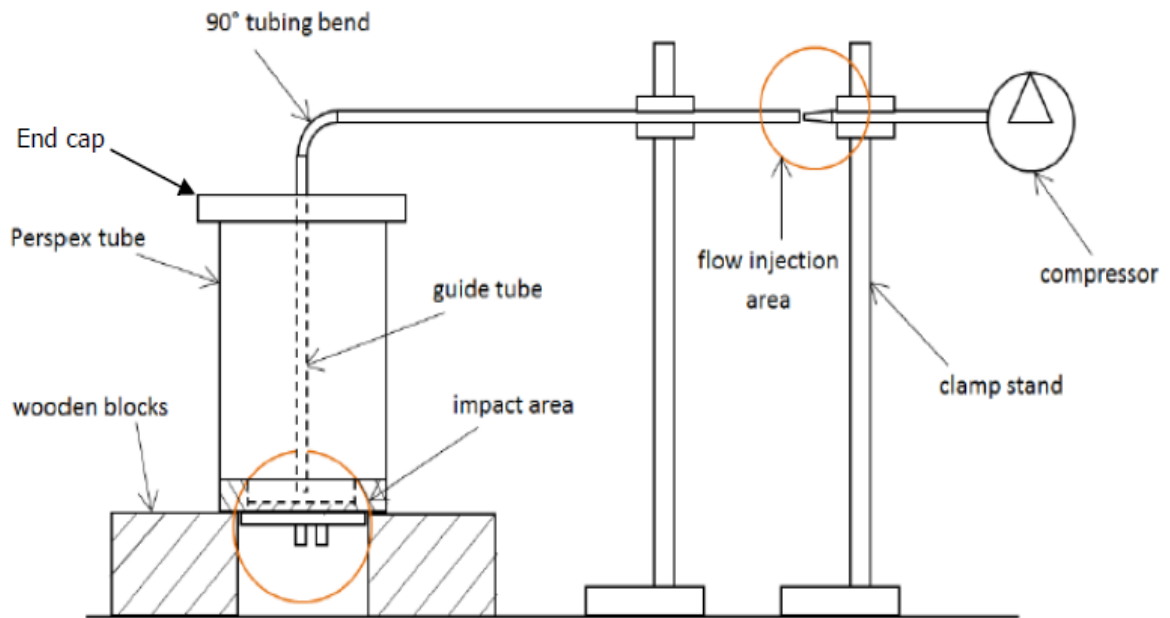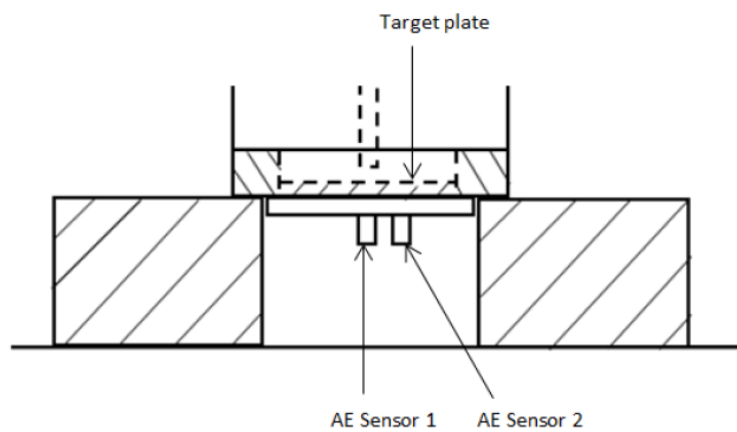
Figure 5.1: (a) Schematic diagram of the experimental set up and (b) close up of target plate and sensors arrangements.

Table 5.1: Summary list of all the particle fluid loaded experiments performed

Experiment Description	Abbreviation	No of Experiments performed	No of tests per Experiment	Total Signal records (including S1 & S2)
Single bubble generation in Perspex tube water column	SBG	1	5	10
Single sand particle impact on the target plate in air	SSPI - Air	1	5	10
Single sand particle impact tests without masking the water loaded target plate	SSPI - Water	1	10	20
Multiple (three) sand particle impact tests without masking the water loaded target plate	MSPI - Water	1	10	20
Single sand particle impact tests after masking the whole target plate except 10 mm² at the centre to allow the particle impacts.	SSPI - Masked	1	10	20
Multiple (ten) sand particle impact tests after masking the whole target plate except 10 mm² at the centre to allow the particle impacts.	MSPI- Masked	1	8	16

For all the experiments, except the single sand particle impact on target plate in air (SSPI - Air), the Perspex tube was filled with 30 mm depth of water. The free end of the vertical tube was dipped 10 mm under the standing water column inside the Perspex tube and cleared by 20 mm from the target plate top surface. For all the experiments, except the single bubble generation (SBG) experiment, the end of the horizontal guide tube a nozzle - held by a clamp - directs a flow of air driven by a compressor through the assembly towards the centre of the target plate surface. The compressor produces a constant air flow of 0.6 litre/min at 250 psi. To maintain a constant atmospheric pressure inside the Perspex tube, at the top end cap, a small vertically through thickness hole of 1 mm diameter was created.

For single bubble generation, the air flow injection end of the horizontal guide tube was coupled with a 10 cc plastic syringe via a 20 mm length of plastic tubing. Slowly depressing the syringe plunger introduces a single bubble at the free end of the vertical tube under water and generates AE signals.

For sand particle experiments, at the air flow injection end of the horizontal guide tube, sand particles are placed using tweezers. Introduction of air flow, from the compressor at this end drives the particles and air through the guide tubes and then through the fluid to hit the mild steel target. This results in particle impacts on the target plate. Except for SSPI-Air, other particle impacts experiments were associated with air bubble generations in presence of water column.

AE data was recorded at 2.5MHz sampling frequency rate with a preamplifier gain of 60dB. In every case the experiment was repeated several times as shown in the **Table 5.1**. Sensor positions & preamplifier gain were kept constant for all the experiments. The data acquisition system used for these experiments was same as described in section 3.2.

5.3 Signal analysis

5.3.1 Single bubble signal analysis

5.3.1.1 Time domain signal analysis

Figure 5.2 (a) & (b) show typical single bubble signals at S1 and S2 respectively, originated from inserting air at the flow injection area, shown in

Figure 5.1. For this experiment, over 5 performed tests, maximum amplitude of single bubble event for S1 varied between 0.5×10^{-4} - 1.4×10^{-4} V and for S2 between 2×10^{-5} - 6×10^{-5} V. Shuib et al. reported typical single bubble inception amplitudes in the order of $2.5\times10^{-3} - 10\times10^{-3}$ V , varying nozzle sizes between 1.4 – 8.4 mm in a standing water column where the AE signals were generated by depressing a syringe using compressed cylinder air and recorded at the sensors mounted on aluminum side wall of a large rectangular structure containing the water column (27). AE event energy, event duration and rise time are calculated following the method described in section 2.6.1. For S1, AE event energy varied between 0.2×10^{-13} - 1×10^{-13} V²s and for S2 between 0.5×10^{-14} - 3×10^{-14} V²s. Event duration for the recorded signals are 800 µs with a signal rise time of 100 µs for both S1 and S2. For all the recorded single bubble signals, these four calculated time domain parameter values are presented graphically in Appendix D.
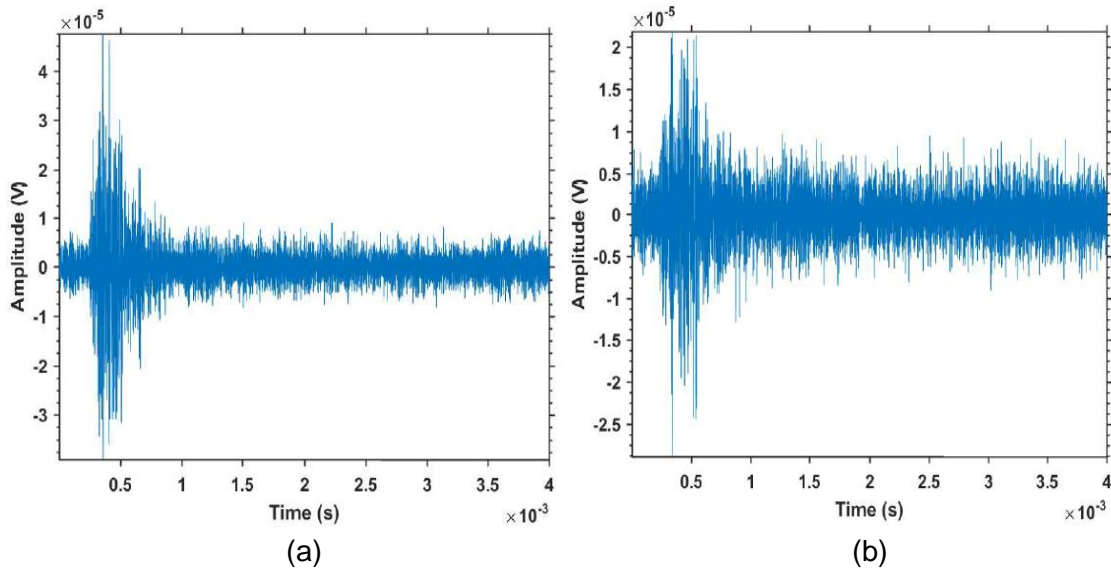
Figure 5.2: Typical single bubble insertion AE signal at (a) S1 and (b) S2

5.3.1.2 Frequency domain signal analysis

Figure 5.3 (a) & (b) shows PSD of the 5 single bubble tests at S1 & S2 respectively. From **Figure 5.3**, the major frequency contents are observed between 100 – 200 kHz for both S1 and S2, with S2 PSD being an order of magnitude smaller than S1 PSD. From other research work, similar major frequency characteristics were associated with single air bubble insertion through nozzles in a water column (27). For S1, above 200 kHz, a few other smaller peaks are noticed between 200 – 400 kHz while for S2 above 200 kHz, the predominant peaks are concentrated between 300 – 400 kHz. For this experiment, calculated Spectral centroid for S1, is between 175 – 210 kHz and for S2 is between 190 – 210 kHz. For S1, Maximum PSD obtained between $0.2 \times 10^{-14} - 2 \times 10^{-14} \, V^2/Hz$ and for S2 between $0.5 \times 10^{-15} - 3 \times 10^{-15} \, V^2/Hz$. Maximum PSD obtained between 110 – 170 kHz for S1 and between 110 – 160 kHz for S2. All these frequency domain parameter values for this experiment are graphically presented in Appendix D.
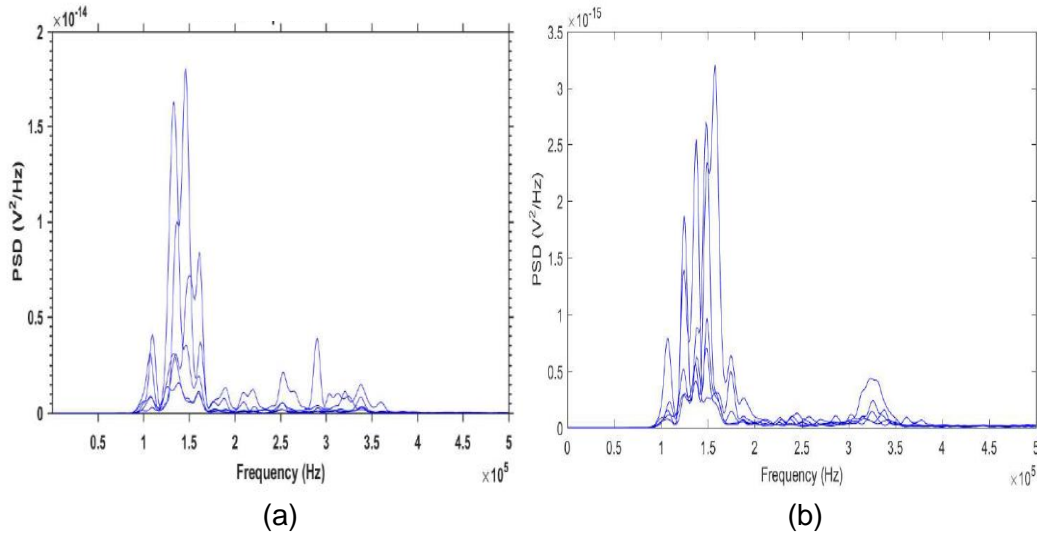
Figure 5.3: Frequency domain representations of single bubble insertion signals at (a) S1 and (b) S2

5.3.1.3 Time Frequency domain signal analysis

Figure 5.4 (a) & (b) shows the GWT of the typical time domain single bubble signal of **Figure 5.2** (a) & (b) respectively. For this specific AE signal, the maximum frequency content for S1 is found at 130 kHz and dominant between 100 – 525 μs. For S2, the maximum frequency content at 140 kHz is found mainly between 150 – 500 μs. These results are in agreement with other research work where major frequency contents in spectrogram analysis of single bubble inception in a standing water column was observed between 100 – 200 kHz (27).

Time (μs)

(a)

Time (μs)

(b)
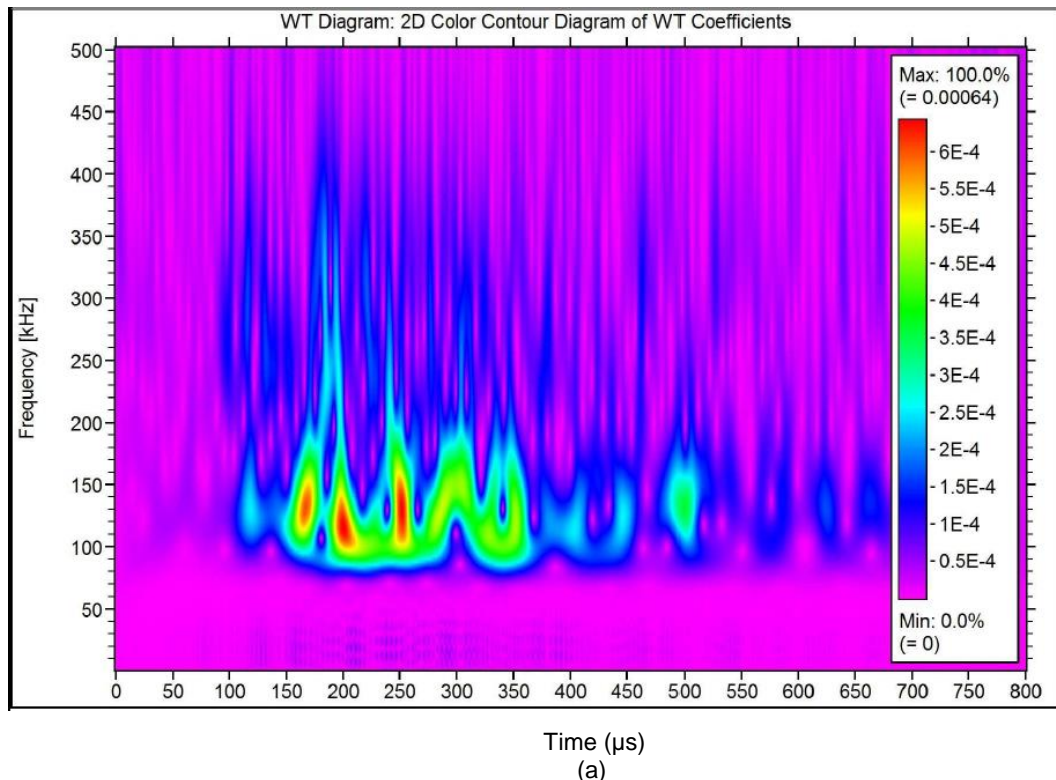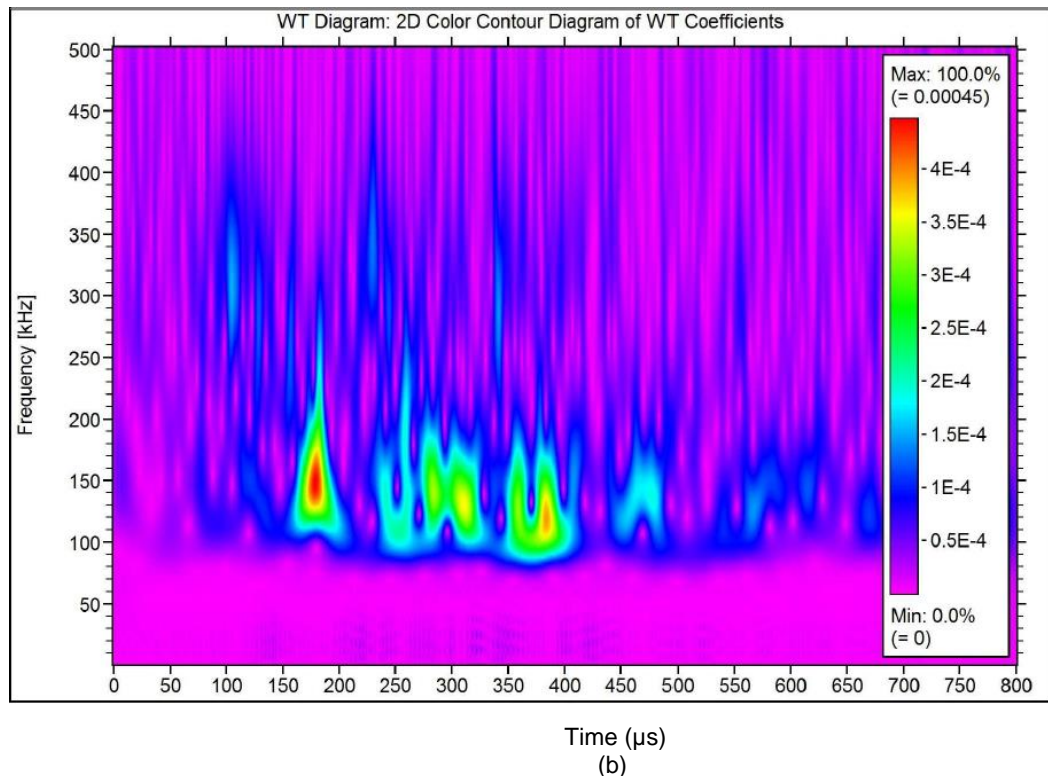
Figure 5.4: GWT of a typical single bubble insertion signal at (a) S1 and (b) S2. The major frequency content was observed between 100 – 200 kHz for both the cases.

5.3.2 Single sand particle impact (in air) signal analysis

5.3.2.1 Time domain signal analysis

Single sand particle (SSPI-air) introduced at the end of the horizontal tube was transported by the constant air flow from the compressor and upon impacting the target surface generated typical AE signals as shown in **Figure 5.5** (a) & (b) for S1 and S2 respectively. For the SSPI-air experiment, maximum amplitude of single sand particle impact for S1 varied between 5.2×10^{-3} – 6.1×10^{-3} V and for S2 between 3×10^{-3} – 5.5×10^{-3} V. AE event energy, for S1, varied between 1×10^{-6} - 9×10^{-6} V²s and for S2 between 1×10^{-6} – 5.5×10^{-6} V²s. Event duration for the recorded signals are between 500 - 800 μs for S1 and between 740 – 780 μs for S2. Signal rise time for both S1 and S2 varied between 40 – 140 μs. These four calculated time domain parameters for all the single sand particle impact records are included in Appendix E.

(a)   (b)
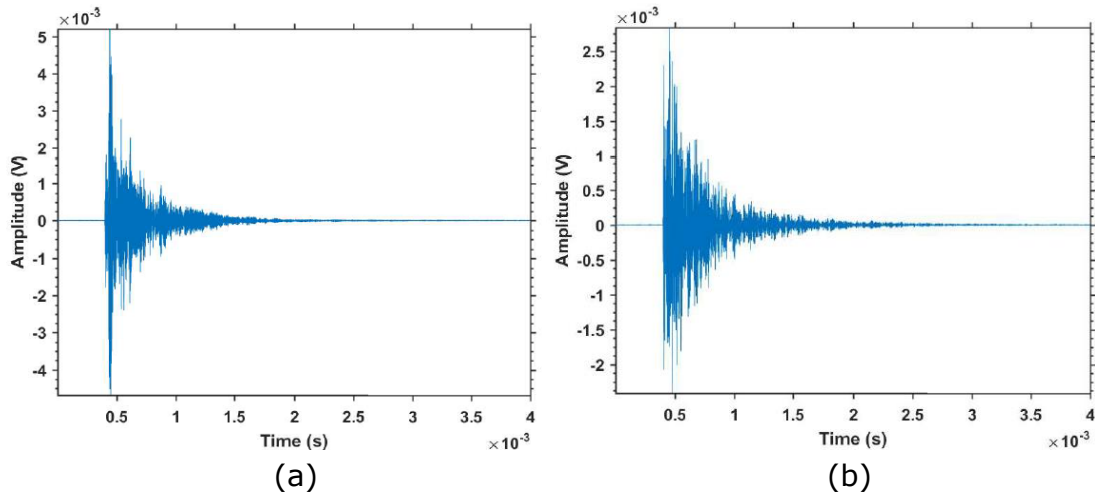
Figure 5.5: Typical single sand particle impact on fixed target plate signal at (a) S1 and (b) S2

Frequency domain signal analysisFigure 5.6 (a) & (b) shows PSD of the 5 SSPI-air tests at S1 & S2 respectively. From Figure 5.6, for S1, the major frequency contents concentrated around 325 kHz with several minor frequency contents below 300 kHz. For S2, the dominant frequency contents are spread over 300 – 400 kHz and at 225 kHz and 150 kHz other major frequency contents are observed. Spectral centroid for both the sensor signals are between 230 – 250 kHz. For S1, Maximum PSD obtained between $0.4{\times}10^{-10} - 1.2{\times}10^{-10}$ V^2/Hz and for S2 between $0.5{\times}10^{-11} - 2.5{\times}10^{-11}$ V^2/Hz. For this experiment, the evaluated frequency domain parameter values are presented in Appendix E.

(a)   (b)
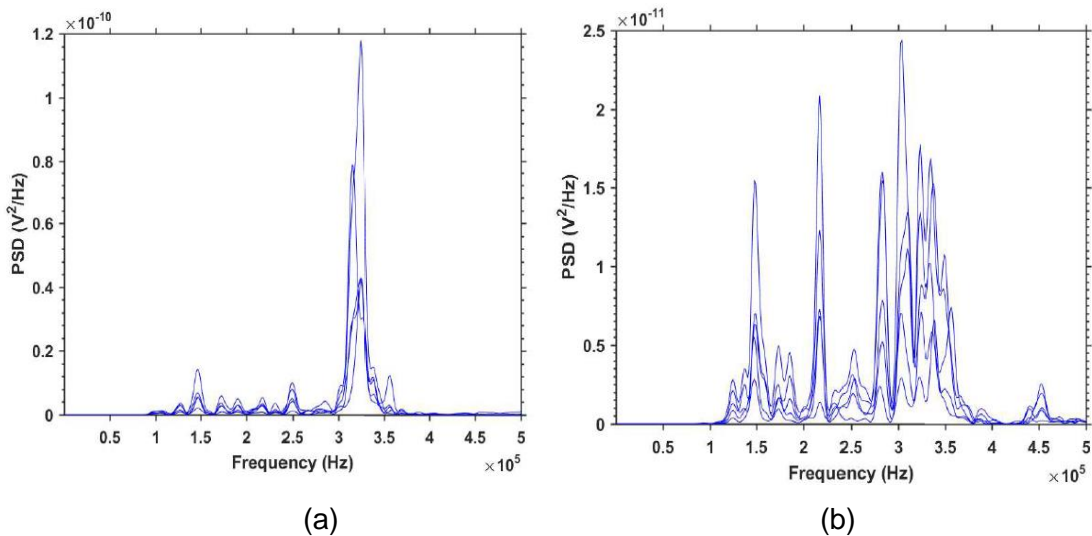
Figure 5.6: Frequency domain representations of single sand particle impacts on fixed target plate signals at (a) S1 and (b) S2

5.3.2.2 Time Frequency domain signal analysis

Figure 5.7 (a) & (b) shows the GWT of the typical time domain SSPI-air signal of **Figure 5.5** (a) & (b) respectively.

Time (µs)

(a)

Time (µs)

(b)
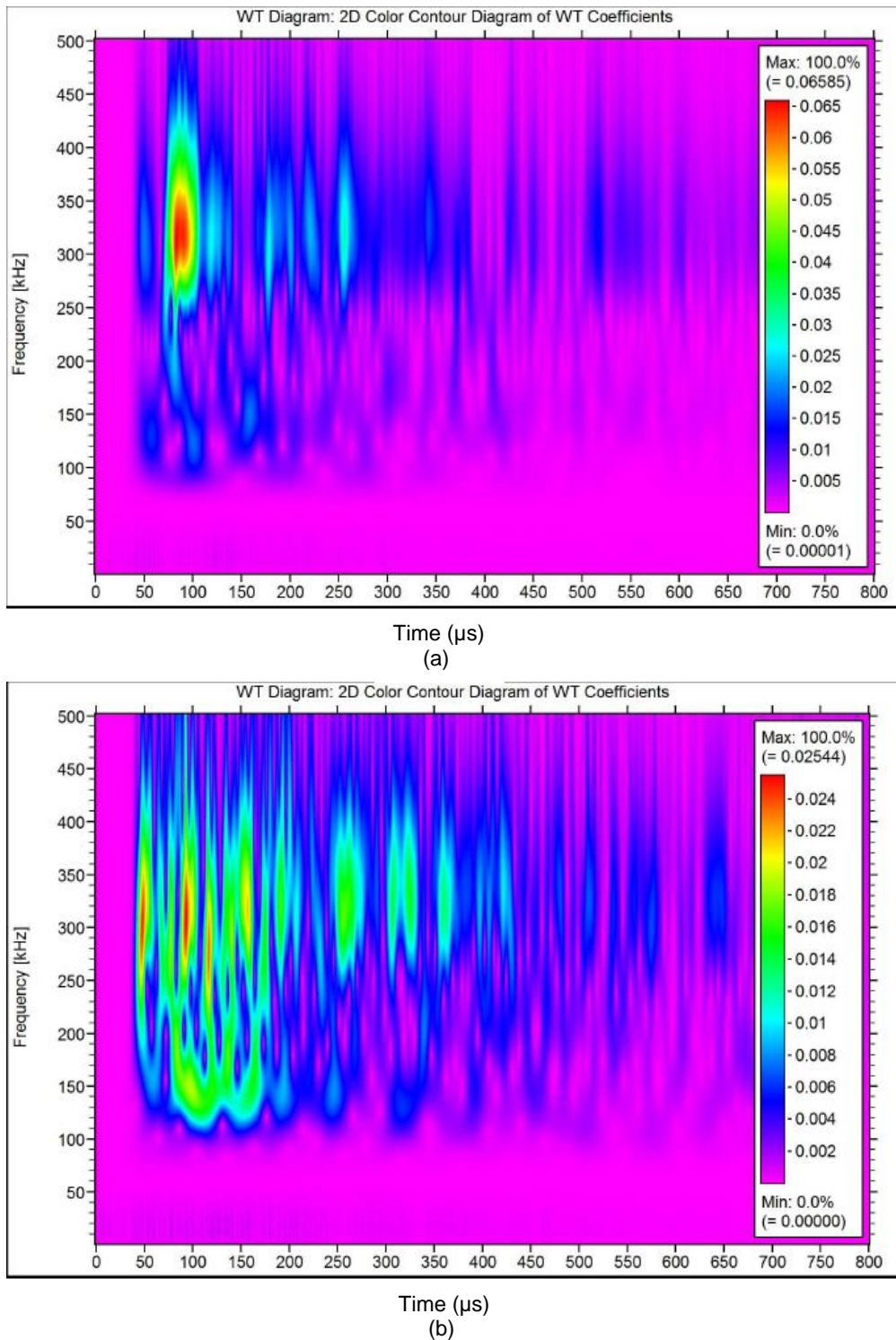
Figure 5.7: GWT of a typical single sand particle impact on fixed target plate in air signal at (a) S1 and (b) S2. The major frequency content was observed between 300 – 400 kHz for both the cases.

From **Figure 5.7** (a), the maximum frequency content for S1 is at 325 kHz and dominant between 50 – 100 µs and slowly fades away by 300 µs. A weaker frequency content around 130 kHz is observed between 50 - 200 µs.

For S2, **Figure 5.7** (b), two major frequency bands are noticed: one between 250 – 400 kHz and the other between 100 – 200 kHz. The first frequency band signal components are dominant between 50 – 450 µs, slowly fading away afterwards and the later frequency band signal components observed mainly between 50 - 200 µs.

5.3.3 Single sand particle impact (in water) signal analysis

For the SSPI-Water experiment, constant air flow from the compressor carried the single sand particle and hit the target plate under 30 mm water column. **Figure 5.8** (a) & **Figure 5.9** (a) shows a typical single sand particle impact on the target plate under water loading. From **Figure 5.8** (a) & **Figure 5.9** (a), a high amplitude event, denoted as Event 2 in both the figures, was recorded in the middle of lots of smaller amplitude events. In sections 5.3.1.1 and 5.3.2.1 it has been shown that the amplitude of particle impacts in air (SSPI-air) were 10 - 100 times higher, depending on sensor position S1 or S2, than bubble generated AE amplitude in SGB experiments. For this experiment, only one sand particle was introduced to the system which was expected to be of higher amplitude than bubble events, and there would be many bubble events. So, the recorded highest amplitude event, which is Event 2 in **Figure 5.8** (a) & **Figure 5.9** (a), is expected to be associated with the sand particle impact and the rest are potentially the bubble events. To verify this, from all the recorded signals, the expected sand event or similar to Event 2 in **Figure 5.8** (a) & **Figure 5.9** (a) and a possible bubble event from the rest of the lower amplitude events, in this case the first recorded event or similar to Event 1 in **Figure 5.8** (a) & **Figure 5.9** (a) , are considered for further analysis in the following sections. Obtained results are compared with the analysis performed in previous sections for single bubble and SSPI-Air experiments.
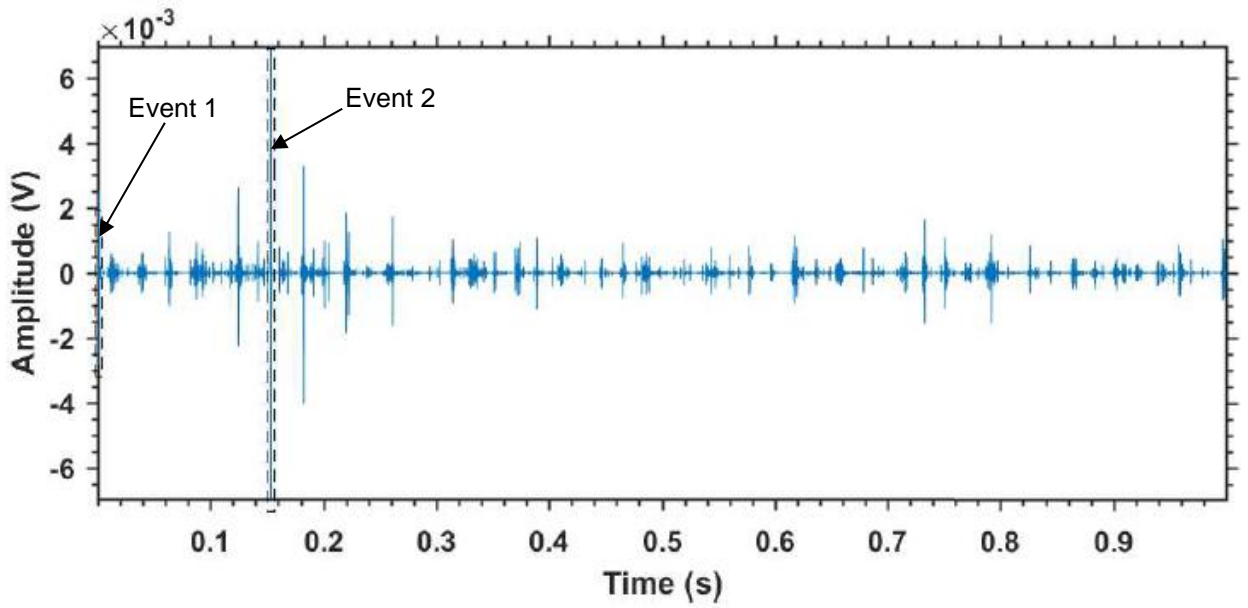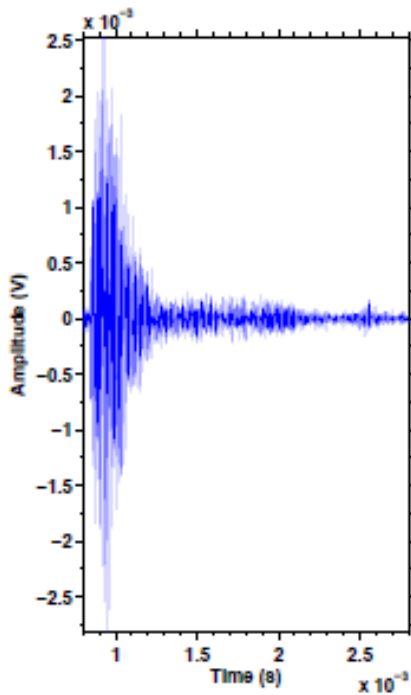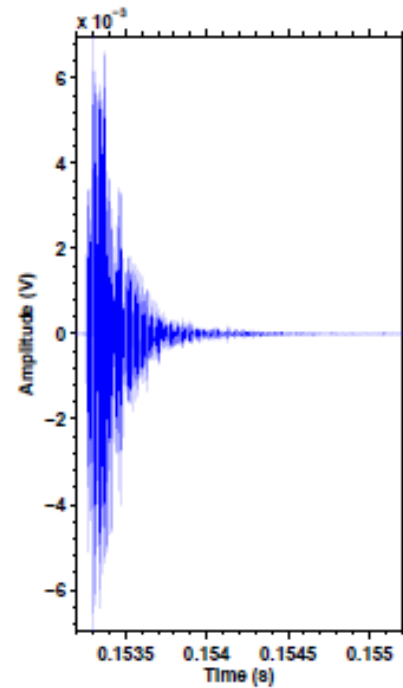
Figure 5.8: (a) At S1, typical single sand particle impact on fixed target plate in presence of bubbles. Event 1 is a potential bubble event and Event 2 is a potential sand particle impact event. Event 1 & Event 2 are shown in figure (b) & (c) respectively.
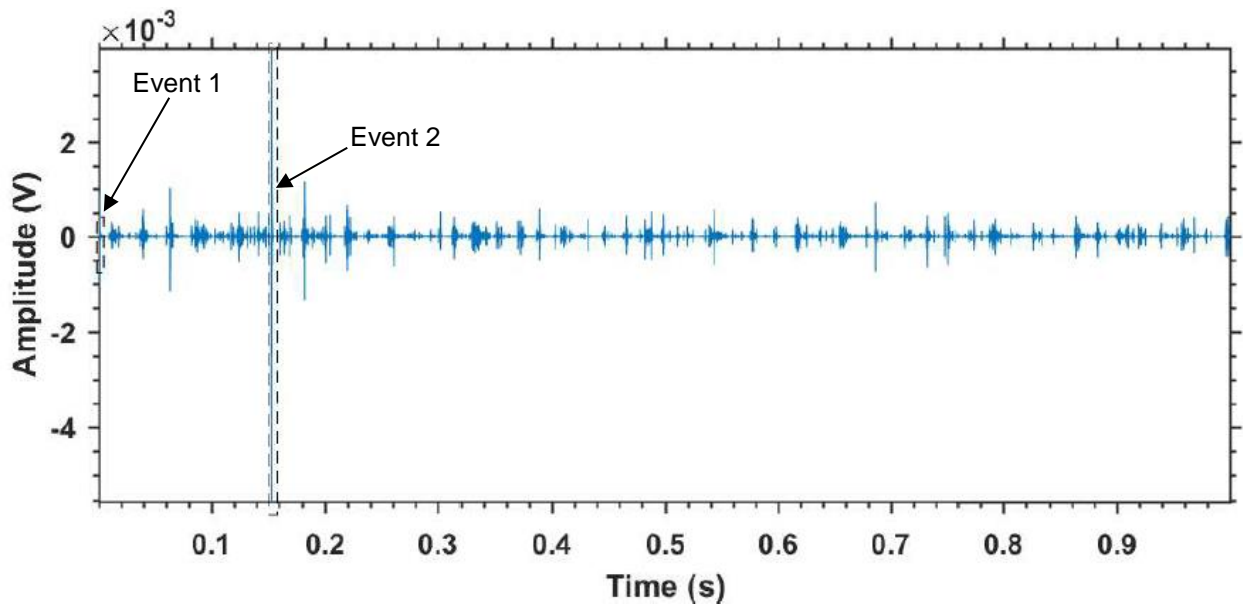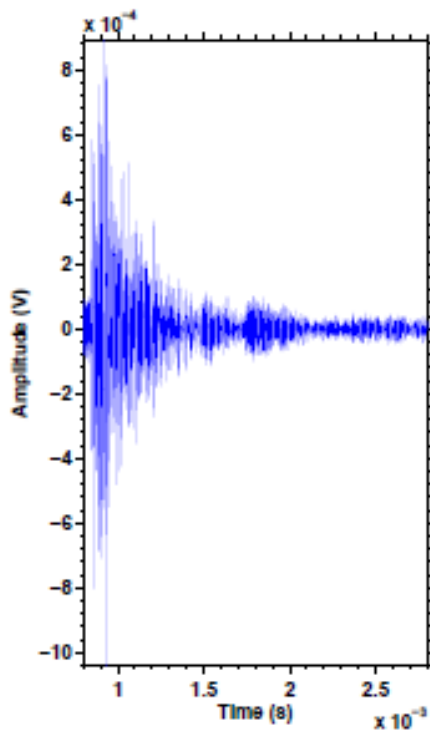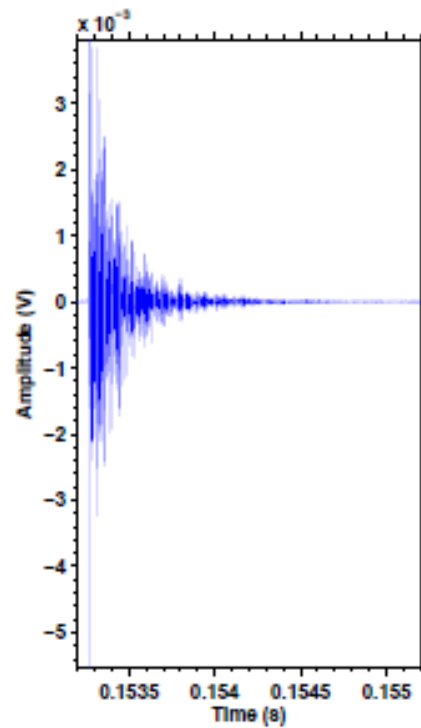
Figure 5.9: (a) At S2, typical single sand particle impact on fixed target plate in presence of bubbles. Event 1 is a potential bubble event and Event 2 is a potential sand particle impact event. Event 1 & Event 2 are shown in figure (b) & (c) respectively.

5.3.3.1 Time domain signal analysis

In this section, the expected bubble and sand events from all the records, similar to Event 1 & Event 2 respectively in **Figure 5.8** (a) & **Figure 5.9** (a), are analysed for four standard time domain AE signal parameters: Maximum amplitude, AE event energy, AE event duration and Event rise time as described in the **section 2.6.1**.

Figure 5.10 (a) & (b), shows the maximum amplitude variations, between 10 tests for S1 & S2 respectively, in the SSPI-Water experiment for expected bubble and sand events.
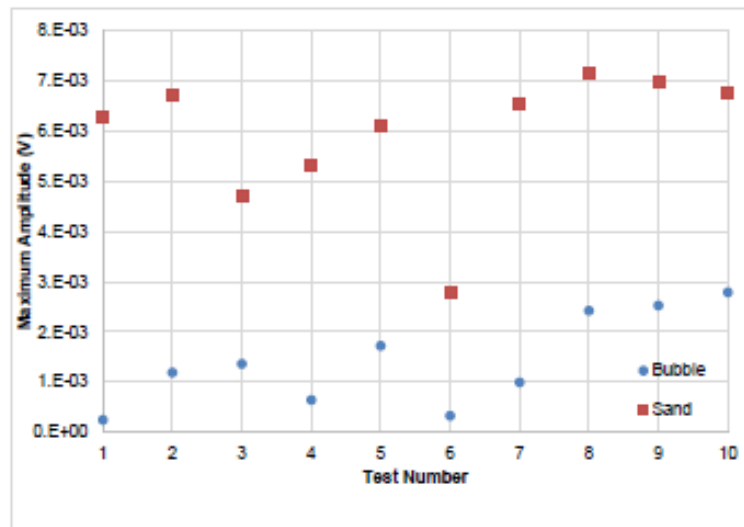
(a)
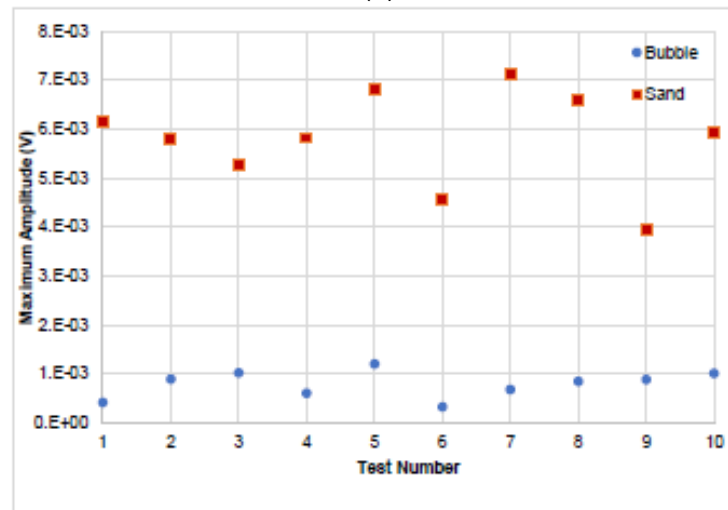
(b)

Figure 5.10: Variation in maximum amplitude over 10 test records in SSPI-Water experiment for potential single bubble and single sand particle impact events at (a) S1 and (b) S2.

For S1, as shown in **Figure 5.10** (a), the maximum amplitude for considered bubble like events varies between $0.3 \times 10^{-3} - 2.8 \times 10^{-3}$ V for expected sand like events varies between $2.8 \times 10^{-3} - 7.1 \times 10^{-3}$ V. For S2, for considered bubble like events the

maximum amplitude varies between $0.36{\times}10^{-3} - 1.2{\times}10^{-3}$ V and for expected sand events, varies between $4{\times}10^{-3} - 7.12{\times}10^{-3}$ V as shown in **Figure 5.10** (b). The change in amplitude of considered bubble like events than the single bubble amplitude observed SBG experiment, discussed in section 5.3.1.1, can be attributed to the higher air velocity used for bubble generation in the later experiment. Other research work confirmed that increase in air velocity can increase in AE energy due to increase in bubble contents and for bubble dynamics associated with it (131).

Figure 5.11 (a) & (b) shows AE event energy for considered bubble and expected sand events at S1 & S2 respectively for all the records.
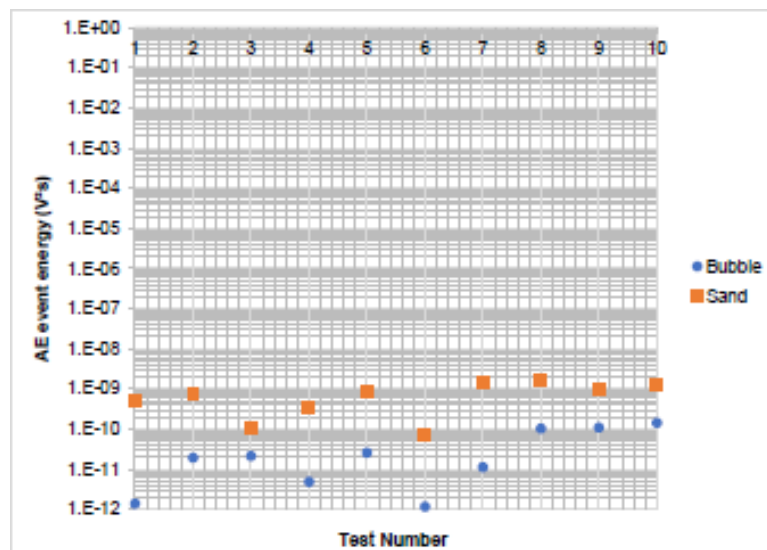
(a)
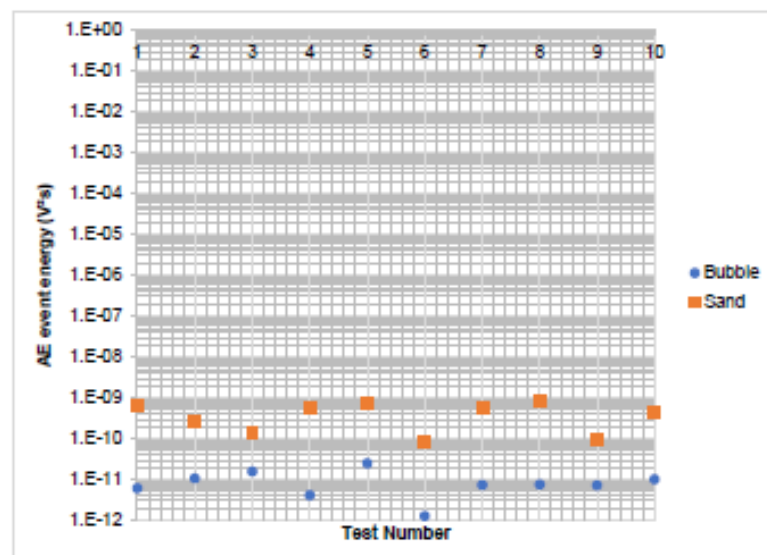
(b)

Figure 5.11: Variation in AE energy over 10 test records in SSPI-Water experiment for potential single bubble and single sand particle impact events at (a) S1 and (b) S2. These plots are in Logarithmic scale.

For S1, as shown in **Figure 5.11** (a), bubble events' energy varies between $1.38 \times 10^{-12} - 1.42 \times 10^{-10}$ V²s and expected sand events energy varies between $7 \times 10^{-11} - 1.5 \times 10^{-9}$ V²s. For S2, bubble events' energy varies between $2 \times 10^{-12} - 2.5 \times 10^{-11}$ V²s and expected sand events' energy $0.9 \times 10^{-11} - 7 \times 10^{-10}$ V²s, as shown in **Figure 5.11** (b).

Figure 5.12 (a) & (b), shows considered bubble and expected sand event durations for all the records at S1 & S2 respectively. From **Figure 5.12** (a), at S1, considered bubble events' duration is between 350 – 800 µs and for expected sand impact events 320 – 600 µs. At S2, as shown in **Figure 5.12** (b), for bubbles, event duration is recorded predominantly between 600 – 800 µs and for sand events, 300 – 600 µs.
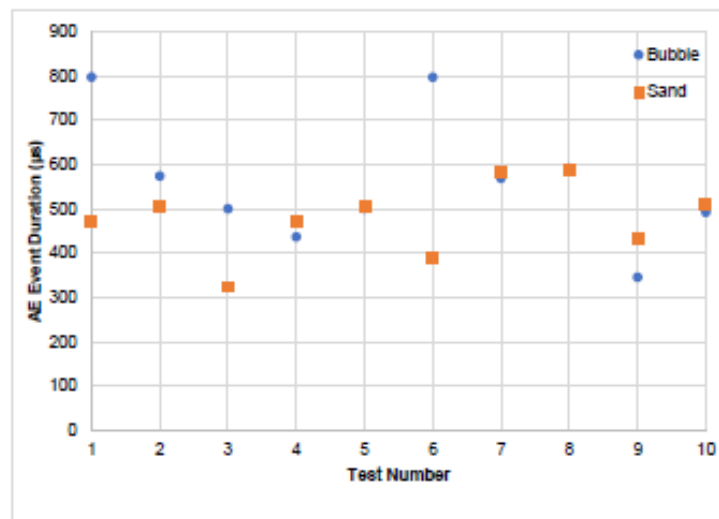
(a)
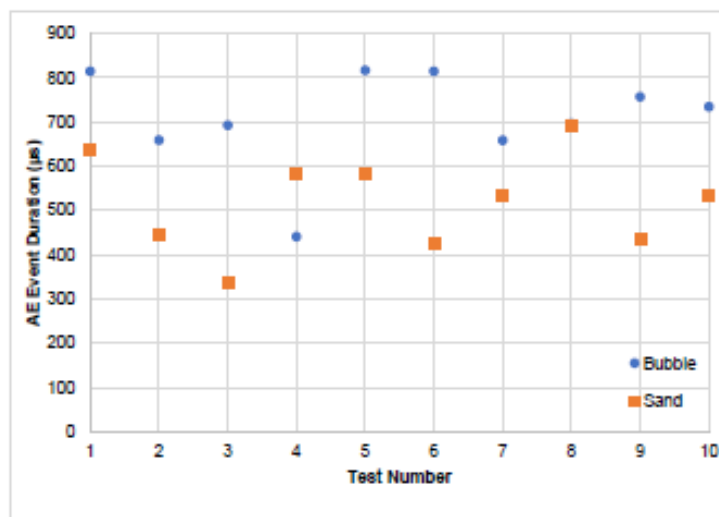
(b)

Figure 5.12: Variation in AE event rise time over 10 test records in SSPI-Water experiment for potential single bubble and single sand particle impact events at (a) S1 and (b) S2.

Figure 5.13 (a) & (b), shows considered bubble and sand like events' rise time for all the records at S1 & S2 respectively. At S1, as shown in **Figure 5.13** (a), considered bubble like events' rise time is between 38 – 122 µs and for expected sand impact like events 28.4 – 120 µs. From **Figure 5.13** (b), at S2, for bubble like events, rise time is recorded predominantly between 39.6 – 263.6 µs and for sand like events between 4 – 67.2 µs.
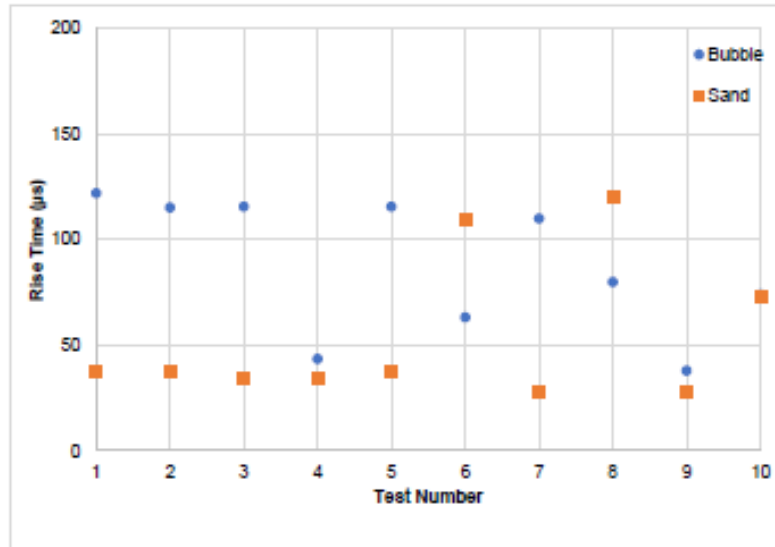
(a)
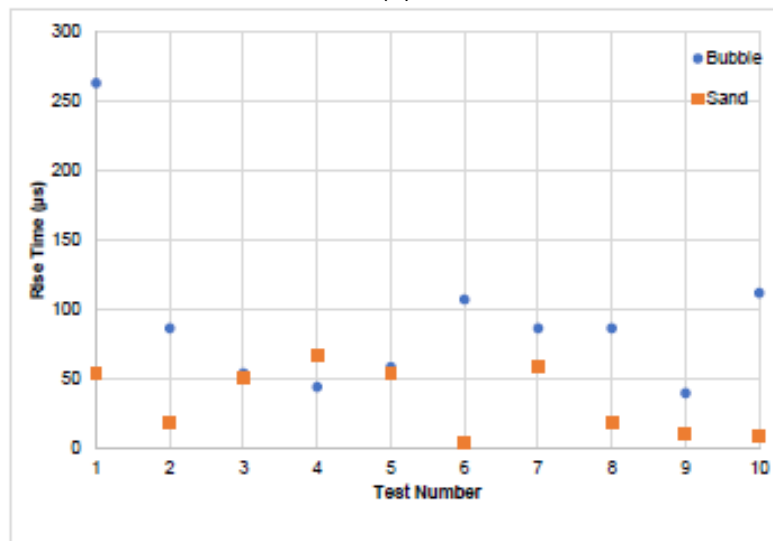
(b)

**Figure 5.13:** Variation in rise time over 10 test records in SSPI- Water experiment for potential single bubble and single sand particle impact events at (a) S1 and (b) S2.

5.3.3.2 Frequency domain signal analysis

This section presents considered bubble and sand like events' frequency domain analysis performed for all the records. **Figure 5.14** (a) & (b) shows PSD for all the considered bubble events at S1 and S2 respectively and **Figure 5.14** (c) & (d) shows the PSD for all the expected sand events at S1 and S2 respectively.

S1   S2

(a)   (b)

(c)   (d)
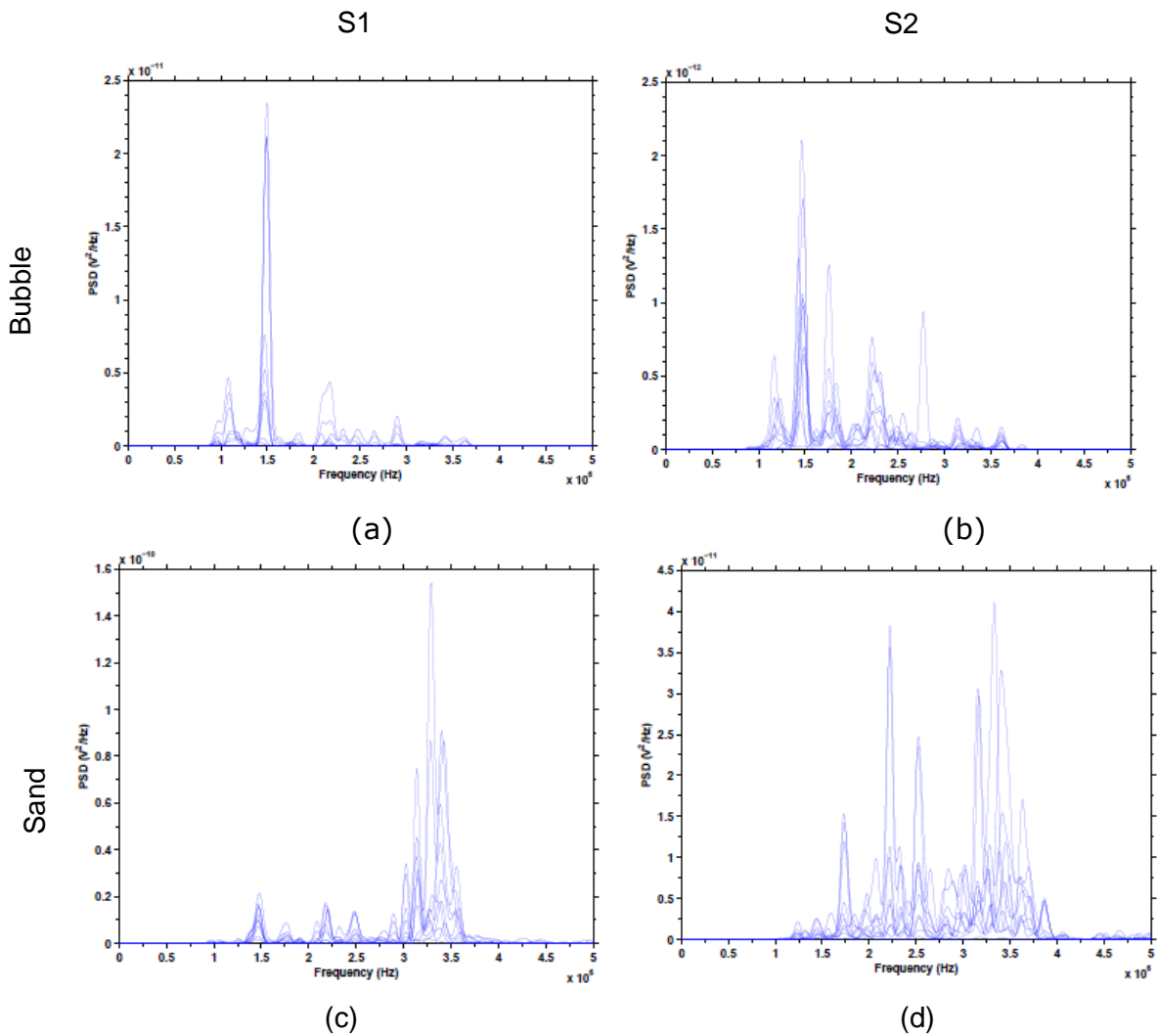
Figure 5.14: Frequency domain representations of considered bubble and sand events at S1 and S2 for all records in SSPI-Water experiment.

From **Figure 5.14** (a) & (b), for bubbles at S1 & S2 respectively, the major frequency content is centred at 150 kHz. For S1, 8 frequency peaks observed between 200 -400 kHz with amplitude an order of magnitude or even smaller. Same frequency peaks for S2 noticed with a change in relative amplitudes. For sand events, as shown in **Figure 5.14** (c) & (d) for S1 and S2 respectively, the main frequency contents are found between 300 – 400 kHz. For S1, between 100 – 300 kHz, an order of magnitude smaller frequency peaks are observed from **Figure 5.14** (c). For S2, shifts in the frequency contents between 100 – 300 kHz with change in relative amplitude noticed.

As a part of frequency domain analysis three standard AE parameters were calculated: Spectral Centroid, Maximum PSD and Frequency at maximum PSD. **Figure 5.15** (a) and (b) shows spectral centroid of considered bubble and sand like events for S1 and S2 respectively. For S1, from **Figure 5.15** (a), spectral centroid for bubble like events vary between 150 – 220 kHz and for sand like events vary between 220 – 250

kHz. At S2, as shown in **Figure 5.15** (b), spectral centroid for bubble like events vary between 170 – 210 kHz and for sand like events between 230 – 250 kHz.
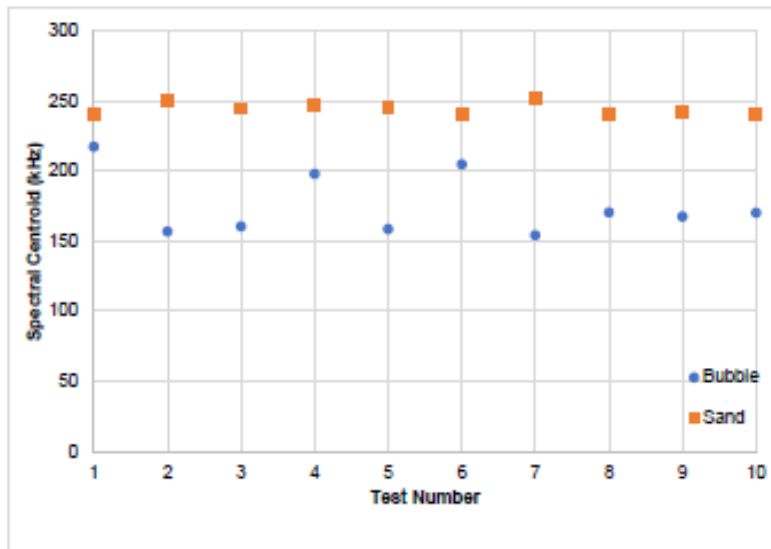

(a)
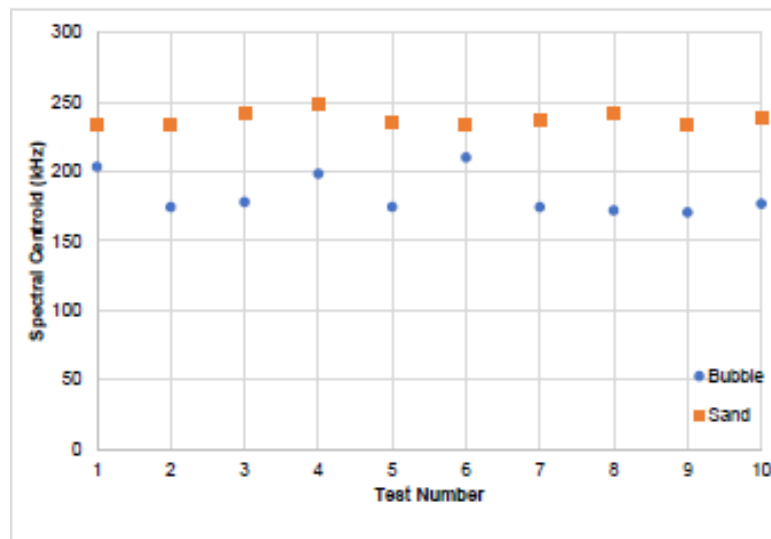
(b)

Figure 5.15: Variation in spectral centroid over 10 test records in SSPI-Water experiment for potential single bubble and single sand particle impact events at (a) S1 and (b) S2.

Figure 5.16 (a) & (b) shows variations in Maximum PSD for considered bubble and sand events for S1 and S2 respectively. For S1, maximum PSD for bubble events vary between $2.25 \times 10^{-13} - 2.04 \times 10^{-11}$ V²/Hz and for sand events between $6.39 \times 10^{-12} - 1.34 \times 10^{-10}$ V²/Hz. For S2, maximum PSD for bubble events are between $2.31 \times 10^{-13} - 2.1 \times 10^{-12}$ V²/Hz and for sand events between $3.78 \times 10^{-13} - 3.89 \times 10^{-11}$ V²/Hz.
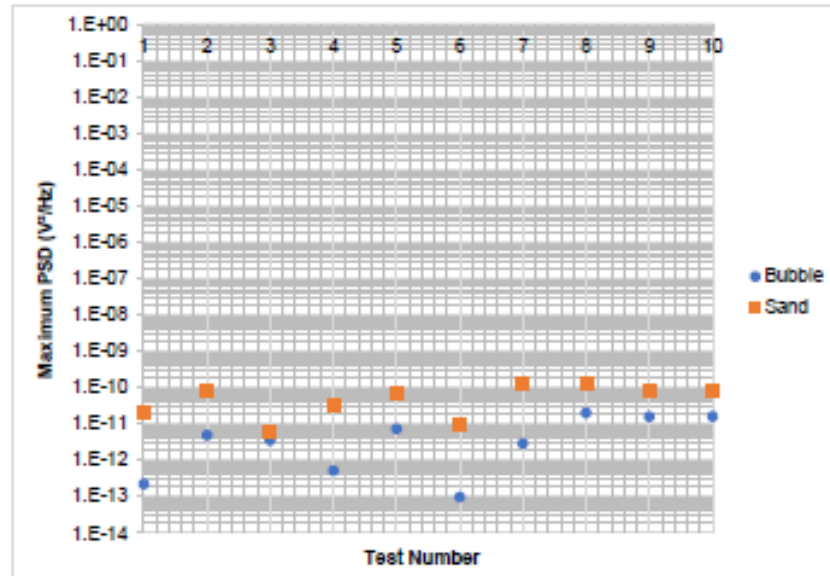
(a)
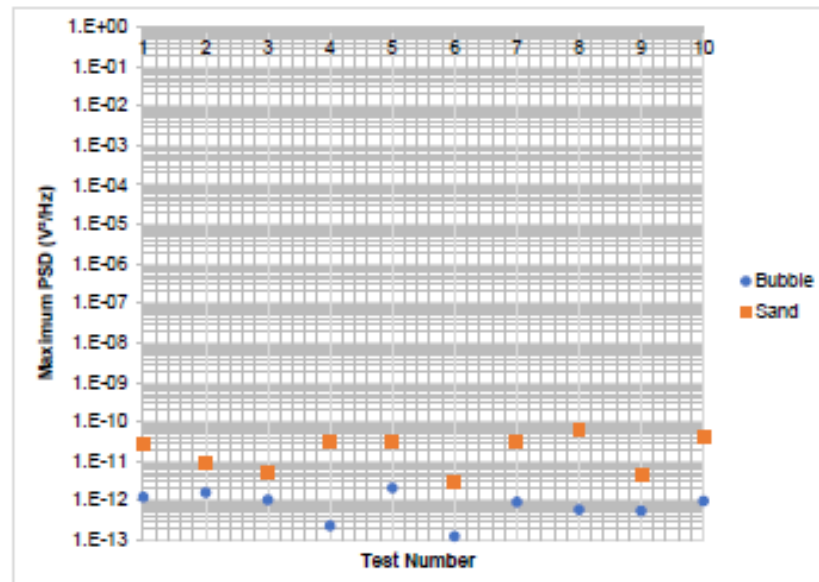
(b)

Figure 5.16: Variation in maximum PSD over 10 test records in SSPI-Water experiment for potential single bubble and single sand particle impact events at (a) S1 and (b) S2.

Large variations in AE energy for both potential bubble and sand events over 10 records can be attributed to the spreading effect of the flow. From previous research works, associated with slurry impingement on a target plate, it was observed that due to spreading of the flow, practical impingement angle can be different from normal impingement angle which can cause significant change in particle impact energy (18,19,132,133).

Figure 5.17 (a) & (b) shows, at S1 and S2 respectively, the frequency at which maximum PSD occurs.
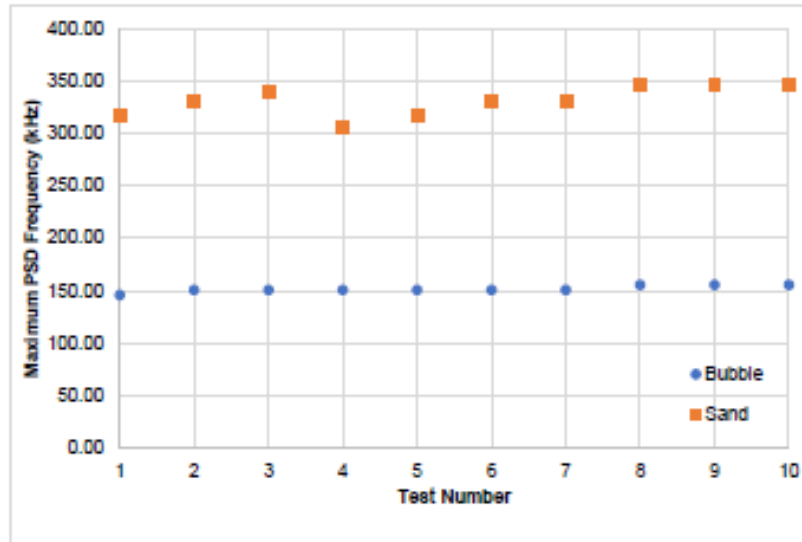
(a)
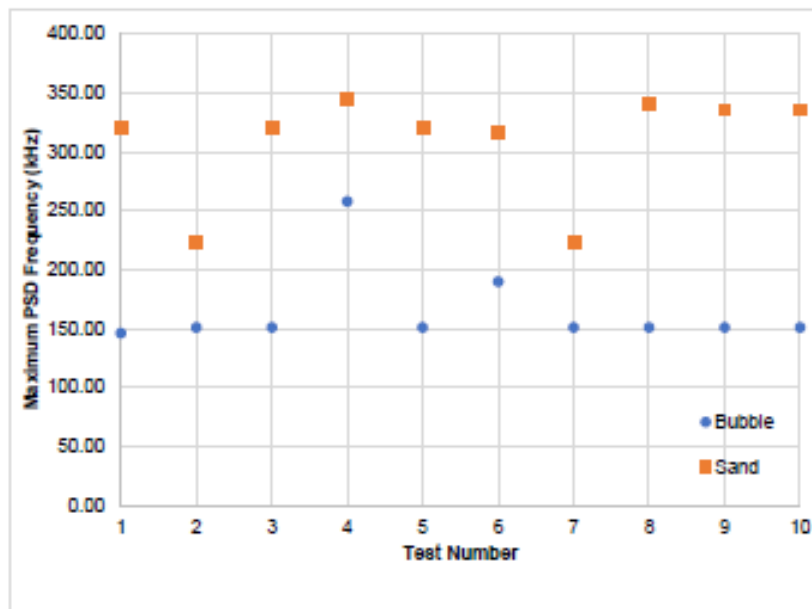
(b)

Figure 5.17: Variation in maximum PSD frequency over 10 test records in SSPI-Water experiment for potential single bubble and single sand particle impact events at (a) S1 and (b) S2.

At S1, from **Figure 5.17** (a), maximum PSD frequency for bubbles is at 150 kHz and for sand vary between 300 – 350 kHz. From **Figure 5.17** (b), at S2, maximum PSD frequency for bubbles is predominantly at 150 kHz and for sand events primarily between 300 – 350 kHz. Ferrer et al. also has noticed higher frequency contents associated with particle impacts and lower frequency contents associated with bubbles in an impingement flow of glass beads on a stainless steel target (19).

5.3.3.3 Time Frequency domain signal analysis

GWT has been used for analyzing recorded bubble and sand events of SSPI-Water experiment in time frequency domain.

Figure 5.18 (a) & (b) shows GWT of a typical bubble event, logged at S1 & S2 and shown in **Figure 5.8** (b) & **Figure 5.9** (b) respectively.

Time (µs)

(a)

Time (µs)

(b)
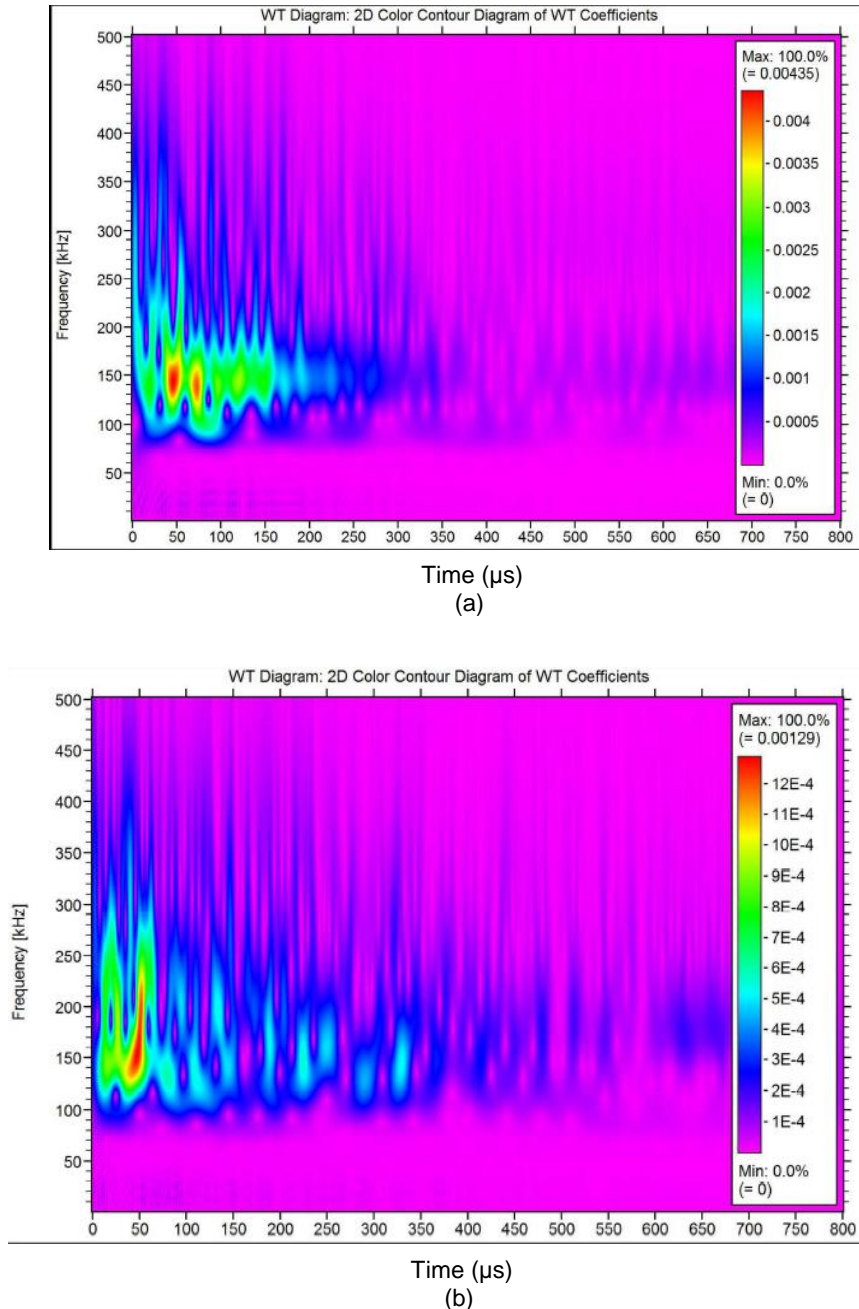
Figure 5.18: GWT of the typical bubble event at (a) S1 and (b) S2 of Figure 5.8 (b) & Figure 5.9 (b) respectively.

Figure 5.19 (a) & (b) shows GWT of the typical sand event considered in **Figure 5.8** (c) **& Figure 5.9** (c) for S1 and S2 respectively. Both for S1 and S2, the major

frequency contents are spread between 300 – 400 kHz with presence of shorter and weaker frequency contents between 100 – 200 kHz and between 200 – 300 kHz.

Time (µs)

(a)

Time (µs)

(b)
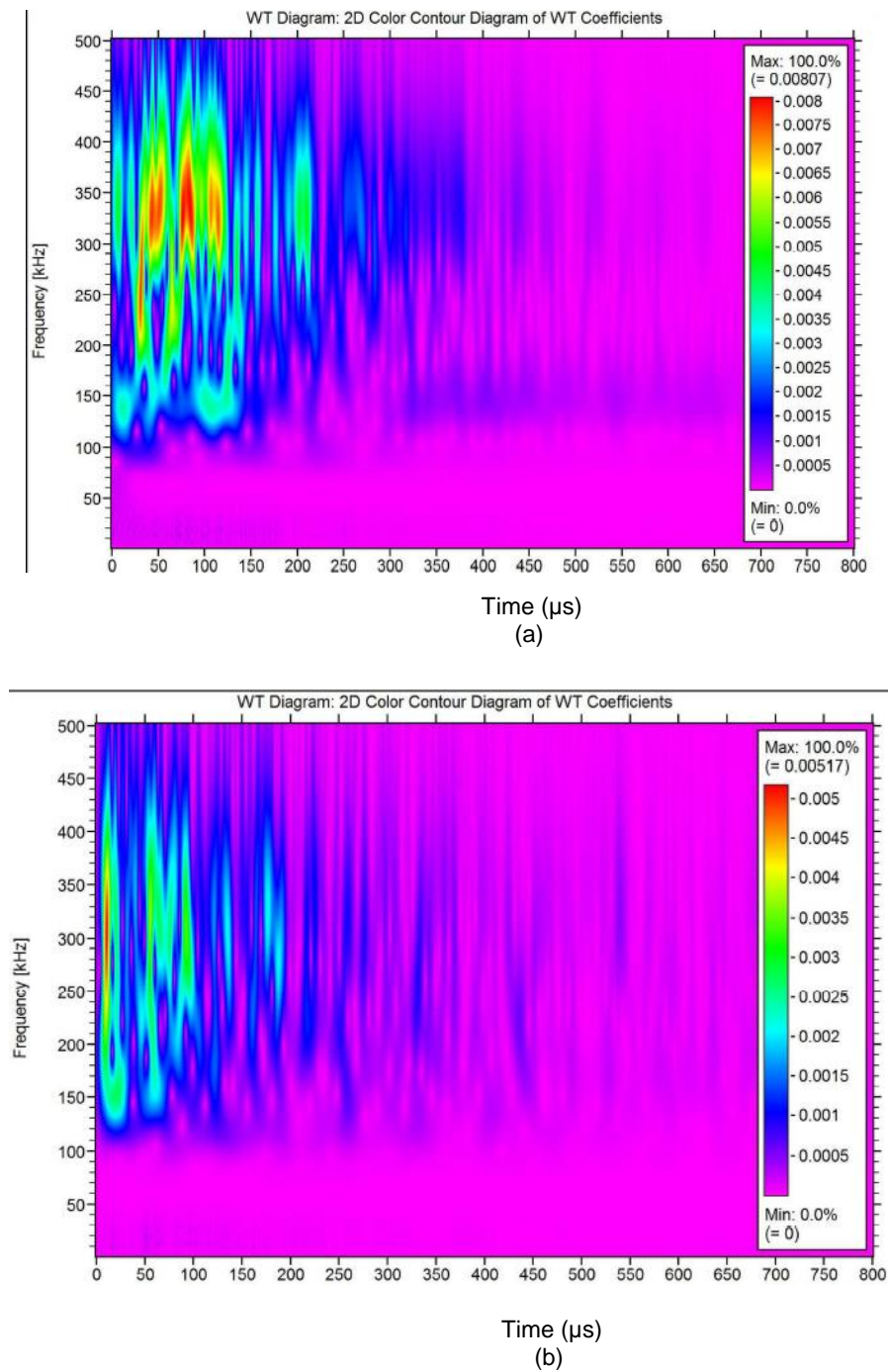
Figure 5.19: GWT of the typical sand event at (a) S1 and (b) S2 of Figure 5.8 (c) & Figure 5.9 (c) respectively.

5.4 Automatic event identification technique

Establishing a robust and repeatable AE signature of bubble and sand events is a prerequisite for developing a general event identification technique. In previous sections

5.3.1- 5.3.3 recorded AE signals, from single bubble, SSPI-Air, SSPI-Water experiments, have been analyzed in time domain, frequency domain and time frequency domain to characterize various AE features of bubble and sand events. From these analysis, a repeatable trend in frequency domain has been noticed for bubble and sand events. For bubbles, the major frequency contents are found to be between 100 – 200 kHz and for sand impact events broadly between 300 - 400 kHz for both the sensors. Based on this observation, calculating energy for frequency band 100 – 200 kHz (denoted as E1) and for frequency band 300 – 400 kHz (denoted as E3) creates options for formulating a simple ratio $\frac{E_3}{E_1}$ >1 for identifying sand events and $\frac{E_3}{E_1}$<1 for identification of bubble events. This framework is summarized in **Figure 5.20**.

AE signal

Setting event identification amplitude threshold

Identify Frequency bands energy (E1, E3) calculation for each detected event

Event identification

$\frac{E_3}{E_1}$>1 as sand

$\frac{E_3}{E_1}$<1 as bubble
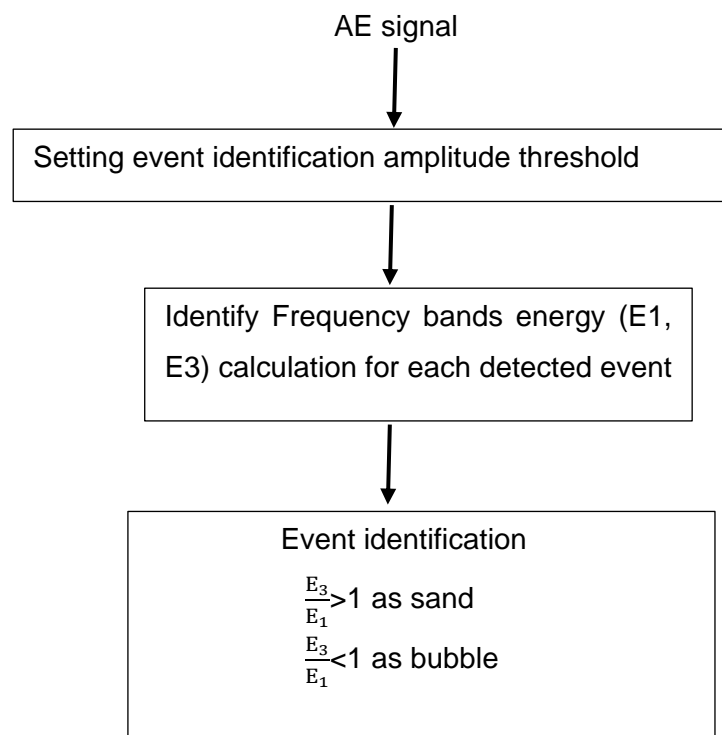
Figure 5.20 : Automatic event identification framework.

Based upon this technique, all the signals have been analysed. For example, a typical single sand particle impact test signal at S1 is shown in **Figure 5.21** (a). For event identification, signal was squared and threshold was set at 10% of the maximum amplitude, as shown in **Figure 5.21** (b). Identified events' energy are calculated for different frequency bands, as described in section 4.4. Implementing the frequency band energy ratio technique, i.e., the event with $\frac{E_3}{E_1}$> 1 as Sand and other detected events with $\frac{E_3}{E_1}$< 1 as bubbles, the events are identified. A lower threshold setting will detect more events to be identified.
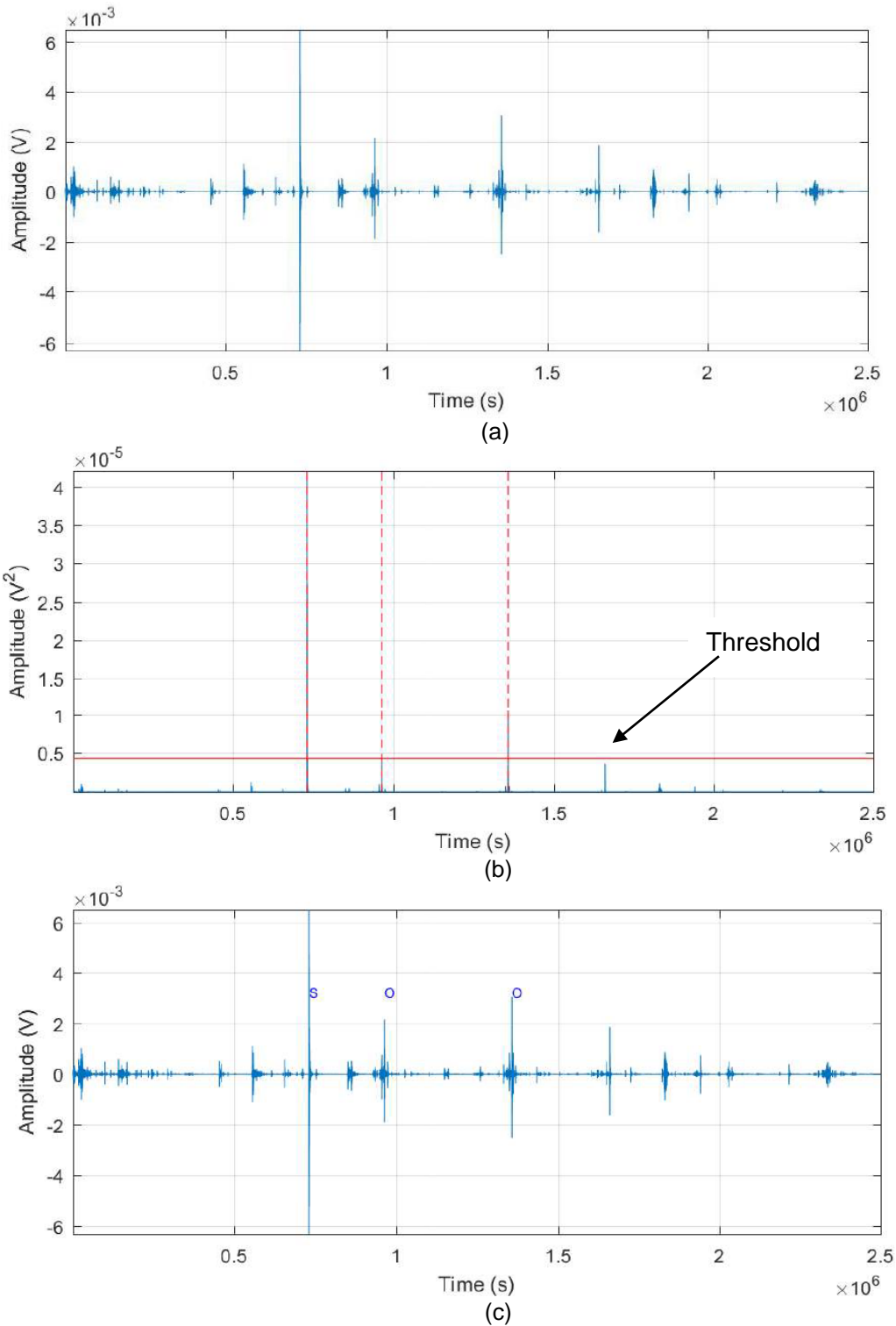
Figure 5.21: (a) Typical single sand particle impact test signal at S1, (b) Event threshold setting & (c) Event identification of the detected events (S for Sand, O for Bubble)

If the threshold had been set lower than 10% of peak then more events would be identified. The number of events identified is sensitive to the setting of the threshold which is therefore very important and is investigated in the following sections.

5.4.1 Sensitivity Analysis of automatic event identification technique

Referring to the framework defined in **Figure 5.20**, in the first step of the automatic event identification process, a percentage of maximum amplitude is set as threshold for event detections. To check the sensitivity of the process, with respect to setting the amplitude threshold, all the recorded signals from single and multiple sand particle impact experiments have been analyzed. The obtained results are tabulated and discussed in the following sections.

5.4.1.1 Single sand particle impacts in water

Table 5.2 (a) & (b) shows the effect of changing amplitude threshold between 10% ~ 1% on total event and sand event counts for all the considered bubble and sand event signals, recorded at S1 and S2 respectively, in the SSPI-Water experiment. From **Table 5.2** (a), for S1, at 10% threshold, 22 AE events are logged from 10 records. Out of these 22 events, 10 events are detected as sand, one per record, as expected. Lowering the threshold to 7% & 5% increases the number of logged events with the anticipated number of sand events still being 10. Decreasing threshold to 3% increases both the bubble event and sand event counts. A potential reason of detecting more than expected sand events might be the circulation of other foreign particles, rust formed on the water loaded steel target plate or even recirculation of the same sand particle, which due to lower impact energy were not identified as events when higher amplitude threshold was used.

Table 5.2: At different amplitude thresholds, event detections from all the records of SSPI in water experiments, for (a) S1 and (b) S2.

(a) S1

File No	Event detection amplitude threshold									
	10%		7%		5%		3%		1%	
	Event	Sand	Event	Sand	Event	Sand	Event	Sand	Event	Sand
1	2	1	2	1	6	1	7	2	19	6
2	1	1	1	1	2	1	4	1	10	7
3	2	1	2	1	3	1	3	2	8	4
4	1	1	1	1	2	1	2	1	9	2
5	1	1	1	1	1	1	3	1	12	8
6	1	1	2	1	2	1	5	1	9	5
7	1	1	1	1	1	1	2	1	6	1
8	2	1	2	1	2	1	4	1	11	4
9	10	1	12	1	14	1	18	2	30	9
10	1	1	2	1	2	1	2	1	11	4
Total	22	10	26	10	35	10	50	13	125	50

(b) S2

File No	Event detection amplitude threshold									
	10%		7%		5%		3%		1%	
	Event	Sand	Event	Sand	Event	Sand	Event	Sand	Event	Sand
1	1	1	1	1	1	1	1	1	3	1
2	1	1	1	1	1	1	3	1	13	5
3	1	1	1	1	2	1	3	2	4	2
4	1	1	1	1	1	1	2	1	2	1
5	1	1	1	1	1	1	1	1	15	5
6	2	1	2	1	2	1	4	1	15	5
7	1	1	1	1	2	1	2	1	6	2
8	1	1	1	1	1	1	1	1	6	3
9	5	1	8	1	11	1	26	1	50	4
10	1	1	2	1	2	1	5	1	12	5
Total	15	10	19	10	24	10	48	11	126	33

A further reduction in threshold to 1% sets the threshold very close to the background noise level and the fidelity of the frequency domain analysis is even more

dubious in this region.For S2, the event identification trend due to change in amplitude threshold is similar to that for S1 as shown in **Table 5.2** (b). Since the general trend of event signal strength is to get weaker at S2, as found in 5.3.3.1, fewer total events are registered but without affecting sand event counts performance at higher thresholds (10% ~ 5%).Table 5.3 (a) & (b) shows the effect of changing amplitude threshold between 10% ~ 1% on total event and sand counts for all signals, recorded at S1 and S2 respectively, in SSPI-Mask experiment. Setting threshold between 10% ~ 5% detects the expected one sand event per record with an increase in total event counts with decreasing threshold. At 3% threshold, more than expected sand counts are observed due to the possible sources of unintended presence of foreign particles, rust or secondary impact of the same particle within the recording time. Further reduction of threshold to 1% sets the threshold close to background noise level and performance of frequency domain analysis becomes very poor. This trend of event detection also observed in SSPI-Water experiments as shown in **Table 5.2** (a) & (b). However, introduction of the mask reduced the total events registered, in comparison with the threshold sensitivity analysis performed for the SSPI-Water experiment, without affecting performance in sand event counts.

Table 5.3: At different amplitude thresholds, event detections from all the records of SSPI-Mask experiments, for (a) S1 and (b) S2.

(a) S1

File No	Event detection amplitude threshold									
	10%		7%		5%		3%		1%	
	Event	Sand	Event	Sand	Event	Sand	Event	Sand	Event	Sand
1	1	1	1	1	1	1	2	1	5	2
2	2	1	2	1	2	1	3	1	6	3
3	2	1	2	1	2	1	2	1	3	1
4	1	1	2	1	2	1	2	1	11	4
5	2	1	2	1	2	1	2	1	7	1
6	1	1	1	1	1	1	1	1	5	3
7	2	1	2	1	6	1	9	2	23	7
8	1	1	1	1	1	1	1	1	8	3
9	1	1	1	1	1	1	1	1	4	1
10	1	1	2	1	3	1	5	1	9	3
Total	14	10	16	10	21	10	28	11	81	28

File No	Event detection amplitude threshold									
	10%		7%		5%		3%		1%	
	Event	Sand	Event	Sand	Event	Sand	Event	Sand	Event	Sand
1	2	1	2	1	2	1	3	2	10	2
2	2	1	3	1	3	1	3	1	12	3
3	2	1	3	1	3	1	3	1	16	3
4	1	1	2	1	2	1	5	1	12	5
5	1	1	2	1	2	1	3	1	11	3
6	1	1	1	1	2	1	3	1	6	2
7	1	1	1	1	1	1	1	1	4	1
8	1	1	1	1	1	1	1	1	5	2
9	1	1	1	1	1	1	1	1	4	1
10	1	1	1	1	1	1	4	1	11	1
Total	13	10	17	10	18	10	27	11	91	23

5.4.1.2 Three sand particles impact in water

Table 5.4 (a) & (b) shows summary of threshold sensitivity analysis performed on all the records obtained at S1 & S2 respectively in MSPI-Water experiment. For 8 records, 24 sand events were expected. From **Table 5.4** (a), at S1, for 10% threshold, 26 events were logged in. Out of these 26 events, 22 are detected as sand. From **Table 5.4** (b), at S2, for 10% threshold, out of 24 expected sand events 19 are detected. One possible reason of lower sand count might be due to interaction among the particles the amplitude of some sand impacts decreased below threshold. Lowering the threshold to 7% & 5% increases the total event count for both S1 and S2 and increase in sand events, from 19 to 20, are noticed for S2. Further lowering of threshold to 3% increases the sand counts beyond expectation. As described for single sand particle impact tests in the previous section, the chance of other non-sand foreign particle, formed rust or recirculation of the same particle event detection increases at this threshold reduces and is a possible cause of higher than expected sand counts. Lowering the threshold to 1% sets the possibility of poor fidelity of frequency domain analysis due to proximity of background noise level.

Table 5.4: At different amplitude thresholds, event detections from all the records of SSPI-Mask experiments, for (a) S1 and (b) S2.

(a)S1

File No	Event detection amplitude threshold									
	10%		7%		5%		3%		1%	
	Event	Sand	Event	Sand	Event	Sand	Event	Sand	Event	Sand
1	3	3	4	3	5	3	7	3	10	3
2	3	3	4	3	5	3	6	3	8	4
3	4	3	5	3	5	3	5	3	11	6
4	2	2	2	2	2	2	3	2	10	3
5	3	2	4	2	4	2	7	5	11	8
6	3	3	4	3	4	3	5	3	6	5
7	5	3	5	3	5	3	5	3	9	6
8	3	3	4	3	4	3	4	3	12	8
Total	26	22	32	22	34	22	42	25	77	43

(b)S2

File No	Event detection amplitude threshold									
	10%		7%		5%		3%		1%	
	Event	Sand	Event	Sand	Event	Sand	Event	Sand	Event	Sand
1	3	3	3	3	3	3	3	3	4	3
2	3	2	3	2	3	2	3	2	4	3
3	3	3	3	3	4	3	5	3	6	5
4	2	2	2	2	2	2	3	2	10	3
5	1	1	2	2	2	2	3	2	5	4
6	2	2	2	2	2	2	3	2	4	3
7	3	3	3	3	3	3	3	3	5	3
8	3	3	3	3	3	3	4	4	6	5
Total	20	19	21	20	22	20	27	21	44	29

5.4.1.3 Ten sand particles impact in water

Table 5.5 (a) & (b) shows summary of threshold sensitivity analysis performed on all the records obtained at S1 & S2 respectively in MSPI-Mask experiment. For 8 records, total 80 sand events were expected. From **Table 5.5** (a), at S1, for 10% threshold, 44

sand events and for S2, as shown in **Table 5.5** (b), 49 sand events were recorded. Lowering the threshold increases the sand counts for both the sensors. However, at 1% threshold, some unanticipated particle like events possibly from foreign particles, rust or recirculating particle are identified in a few individual signals, for example, file numbers 3 & 7 in **Table 5.5** (a).

Table 5.5: At different amplitude thresholds, event detections from all the records of MSPI-Mask experiments, for (a) S1 and (b) S2.

(a) S1

File No	Event detection amplitude threshold									
	10%		7%		5%		3%		1%	
	Event	Sand	Event	Sand	Event	Sand	Event	Sand	Event	Sand
1	6	6	7	7	7	7	8	8	10	8
2	4	4	4	4	8	8	9	9	9	9
3	6	6	8	8	9	9	9	9	14	12
4	4	4	6	6	6	6	7	7	8	8
5	5	5	6	6	6	6	7	7	8	8
6	7	7	8	8	8	8	8	8	9	9
7	8	7	9	8	9	8	11	9	17	14
8	5	5	5	5	5	5	5	5	8	7
Total	45	44	53	52	58	57	64	62	83	75

(b) S2

File No	Event detection amplitude threshold									
	10%		7%		5%		3%		1%	
	Event	Sand	Event	Sand	Event	Sand	Event	Sand	Event	Sand
1	5	5	5	5	7	7	8	8	8	8
2	7	7	7	7	8	8	8	8	10	9
3	6	6	7	7	7	7	9	9	16	12
4	6	6	6	6	6	6	7	7	8	8
5	7	7	8	7	8	7	8	7	7	6
6	5	5	6	6	8	8	9	9	9	9
7	9	8	9	7	9	7	9	7	20	9
8	6	5	7	5	8	6	9	6	25	14
Total	51	49	55	50	61	56	67	61	103	75

5.5 Summary

This chapter has presented all of the results for the experiments listed in **Table 5.1** The main findings have been that the values of the simplest AE parameters for sand particle impacts can vary widely making them difficult to identify in the presence of other sources of AE like bubbles and noise. Two main sources of AE have been considered in the laboratory experiments carried out, being sand particle impact and bubbles. They have been found to have distinct frequency signatures and this has been used to develop a new automatic identification framework which has been tested in the laboratory. The method developed can be used to optimize the identification of sand particle impacts. The optimal setting of an amplitude threshold is sensitive to number of particles and noise levels. A high threshold of say 10% will clearly identify sand particle impacts but for multiparticle tests is likely to not detect about 20% of lower (impact) energy particles. A threshold lower than 3% is likely to result in detection of AE events with poor frequency content and wrong classification of the weakest events. Optimal setting of the parameters used in the framework such as thresholds, frequency bands and ratios of AE energy is likely to make identification of sand particle impacts in the laboratory environment to within 10% possible.

Chapter 6   Discussion

The findings from all the experiments performed in this research, are discussed in this chapter within the context of previous research works and established theories. The chapter is divided according to the three major contributing areas of the research: Preliminary pencil lead break experiments, Similar sized particle impacts test and Particle impacts in presence of bubble experiments.

6.1 Preliminary pencil lead break experiments

For a given AE monitoring system, the recorded signals are influenced by the AE generating source, wave propagation methods present in the system and the characteristics of the monitoring sensors (134). PLB Tests (Hsu-Nielsen Tests), as described in the Section 3.3, has been used widely as a standard AE generating source in the experimental AE studies (24,84). In this research, PLB has been used for studying and comparing the signal characteristics across different test environments.

Elastic wave propagation methods in a solid is primarily affected by the geometry of the structure under consideration (126). Earlier research works in the AE used specimen geometries and sensor positions to record longitudinal bulk waves in several radiation directions (84). Later AE researches involved plate like test specimens where far field AE signal observations are dominated by Lamb waves for which analytical results are available for infinite plate (85,135,136). In a thin plate like specimen, generated AE signals are propagated in fundamental symmetric and anti symmetric Lamb wave modes of particular characteristic frequencies (33,136). Identifying these wave propagation modes facilitate characterizing the AE signals as shown by numerous researchers (33,84,136–138). A thick small stepped cylindrical mild steel coupon specimen has been considered in this research, as shown in the Figure 3.2. In addition to the fundamental symmetric and anti symmetric wave modes, as found in the thin plates, due to the thickness of the plate, the higher order Lamb modes become available to contribute to the recorded AE signals (85). Also, close boundaries initiate multiple reflections and mode conversions, as described in (80,85,135). So, presence of different modes, their reflections and mode conversions due to close boundaries make identifying individual wave propagation modes unachievable in this regard for further analysis. However, AE sensors, with wide frequency band response, used in this research made it possible to identify two specific frequency bands,100 - 200 kHz, 200 – 300 kHz & 300-400 kHz, as described in the Section 3.4.2, which facilitated further signal analysis. Based upon the structural geometry and the sensor response characteristics, for another physical arrangements, some other frequency bands might be optimal. However, this forms the basis for a more general approach of considering frequency bands based

analysis technique whenever complex geometry makes it difficult to identify single mode or frequency for analysis purpose.

Two AE sensor locations, one at the epicentre of the impact point (S1) and another off centred by 30 mm (S2), were considered, as shown in the Figure 3.2. In general, the signals obtained at S1 are stronger than the signals recorded at S2, as observed from the amplitude, event energy or PSD analysis included in the Appendix B. Earlier researcher showed that, on a circular thick specimen, at different recording locations, the major frequencies remain the same though the relative contributions may vary (46). Similar trends have been observed in this research, as shown in the Figure 3.8. In the same study (46), it was shown that, at a certain location on a thick circular plate, any particular mode might disappear if the location happens to be the point of zero displacement for that particular mode. In this research, frequency bands have been considered rather than a particular frequency or a specific mode. So, the change in the relative contributions of different modes or disappearance of any particular mode, if any, has not affected the analysis.

In this research, two boundary conditions of the target plate were considered: free, simply supported on the wooden block and sealed at the bottom of a cylindrical perspex tube, as shown in the Figure 3.4. At a specific location on a circular specimen, varying the boundary condition changes the contributing wave propagation modes' characteristics, as shown in (126). Even though particular modes or their individual contributions have not been studied in this research, changes in frequency contents have been observed for Free and Fixed boundary conditions, as shown in the Figure 3.9 and Figure 3.10, for S1 and S2 respectively. Also, shorter event durations and rise times, associated with fixed target plate experiments, have been observed, as shown in the Figure B-6.

Couple of target plate loading environments, i.e. air and water, have been considered in this research for fixed plate experiments. Due to usual challenges faced in water experiments, such as difficulties in placing the pencil lead at the same location, attributed to the wider variations observed in the frequency contents of the signals recorded at both sensor positions, as presented in the Figure 3.9 and Figure 3.10.

In general, within an experiment, among different tests, good repeatability in frequency contents have been noticed. Between the experiments, sensors were dismounted and attached again which contributed to the relative change in the signal strength due to change in coupling conditions. This supports earlier research findings that variability among different experiments due to coupling is higher than the variability among different tests within an experiment for a given sensor coupling arrangement (16).

6.2 Similar sized particle impact test

Several researchers have studied free falling or airborne particle impacts on the target plate using AE sensors. Dropping the free falling or air borne stream of particles from different height on plates with varying thickness, earlier researchers correlated the calculated average power of the recorded AE signals to the plate thickness, to the second power of the impact velocity and the third power of particle diameter (13,15,55). For a given system, calibrating AE energy with the particle impact across the operating range, as presented in the above mentioned researches (13,15,55), might be sufficient for monitoring a single particle type present in the system. However, if several particle types, with similar size, velocity and density is present in the system, the AE energy or amplitude would not be unique for the particle types and hence evaluating AE impact energy can not distinguish different particle types, as noticed in (16) .

A number of previous research works attempted to use frequency informations, derived from acquired signal analysis, to relate with impacting particle size and velocity (6,55). Other researchers used plate like specimens with large lateral dimensions which facilitated particular modes identification in the specimens according to Lamb wave theory and performed signal analysis related to specific modes for source characterization (33,84,137,138). Of these studies, a particular important one related to the current research is performed by Hamstad et al. (84) where they used an FEM data of an aluminium plate to study the surface response of dipole sources buried at different depths. Obtaining peak WT coefficients of the anti symmetric and symmetric modes, they have found that, the ratio of the modes differentiate different sources when they are buried at the same depth of the plate and the observations are made at the same propagation distance. However, the ratio overlaps for different source types buried at different depths with varied propagation distances and impossible to uniquely identify each source type when mixed depths and propagation distances are present.

In this research, a thick small stepped cylindrical mild steel coupon specimen has been used for studying the glass beads and sand particles dropping under gravitational force from the same height. Geometry of the coupon specimen makes individual mode identification for signal analysis impossible due to dispersion, reflection or multiple mode conversions. The complex geometry, along with the particle impacts with similar size, density and impact velocity, makes it difficult to differentiate the particle types either analysing the impact signals in the time domain, considering 4 standard time domain parameters (Amplitude, AE event Energy, Rise Time and Event Duration) or in the frequency domain, considering 3 standard frequency domain parameters (PSD, Peak frequency at PSD and Spectral Centroid), as shown in the Appendix C. In this research, the response characteristics of the sensors, helped to formulate frequency band energy

energy ratio, a new AE parameter introduced in this research, as described in the section 4.4. It has been found that the coefficient of variation of the frequency band energy ratio for the experimental population can distinguish the glass beads and sand particle impacts with similar size, density and velocity, as shown in the section 4.4.

The above mentioned technique can be used for discriminating a given population of particle impacts present in a system. However, it is inadequate in identifying each individual particle impacts. To facilitate each particle impact event identification, SVM classification technique, as described in the section 2.6.3.2, implemented in the section 4.5. The application of the classification techniques in AE based particle impact monitoring systems is relatively new and have been studied primarily for loose particle/object impact identification (104–108). For example, in a research, to study loose material types identification, a sealed device filled with Wire, Aluminium & Tin of 0.5 - 2 mg was vibrated by an automated shaker (106). A wall mounted AE sensor was used for recording the loose particle impacts. No prior research has been noticed related to the application of classification techniques in particle impacts identification with similar size, density and velocity. To perform SVM based classification algorithm, 7 standard AE parameters, in the time and frequency domain, as mentioned above, have been considered. Available data set has been segmented into two parts of the training set (80%) and test set (20%). The developed model has been applied on the test data for model performance evaluation purpose. The overall success rate of individually identifying each category (PLB, Glass bead and Sand particle impacts) at S1 was found as 86% and at S2 as 92%.

6.3 Particle impacts in presence of bubble experiments

To study the abrasive potential of particle laden fluid, earlier researchers have used AE for studying particle streams in a water-flow loop or slurry jet impinging at a target surface (16–19,22). The measured AE energy was related linearly with the impacting particle's concentration, velocity squared, diameter and the impact angle between the nozzle and the target plate.

The experimental conditions considered in the above mentioned researches facilitate with no or very low amplitude bubble formations. An AE event amplitude or energy based analysis technique is sufficient enough for these cases to differentiate between the particle impacts and the generated bubbles, if any, present in the system. However, in real industrial cases, AE amplitude or energy generated from the bubbles can be high enough to be comparable with the particle impacts present in the system (11). In this research, particle impacts in presence of bubbles were considered. To differentiate bubble events from sand particles impact events, frequency band energy

ratio of recorded AE events, introduced in section 4.4, has been applied instead of AE amplitude, energy or peak frequency.

Before preforming experiments on particle impacts in presence of bubbles, individual bubble formation and single particle impacts on a fixed target plate has been studied, as presented in the section 5.3.1 & 5.3.2 respectively. Time and Frequency domain analysis of the acquired signals were performed evaluating 7 standard AE parameters and time-frequency domain analysis has been carried through GWT. From frequency domain analysis of the single bubble events, as shown in the Figure 5.3 & Figure 5.4, it has been observed that, for the considered two sensor positions, the primary frequency contents were centred between 135 - 150 kHz. At the beginning of the signals, the higher frequency contents, upto 500 kHz, were observed though quickly dissipated (after first 150 µs) to the primary frequency contents. In a similar study of single bubble activities by Shuib et al. (27,58,131), for the acquired bubble events' signals, frequency contents of upto 700 kHz were observed at the beginning of the signals. In the same study, it was noticed that 120 kHz was the most sensitive frequency for all the bubble sizes and all the viscosities considered in the study.

Similar to the single bubble signal analysis, time, frequency and time-frequency domain analysis has been performed for all the single sand particle impact AE signals. While single bubble events were generating primary frequency contents between 135 - 150 kHz, the single particle impacts were generating primary frequency contents between 300 – 350 kHz, as shown in the Figure 5.6 & Figure 5.7, for both the sensor positions. Similar frequency characteristics observed in a study of slurry impingement jet particle impacts at a target surface where Ferrer et al. (19) attributed the higher frequency contents (>300 kHz) associated with the particle impacts (glass bead) and lower frequency contents (< 200 kHz) associated with the bubbles generated in the system.

To study particle impacts in presence of bubble events, the next experiment was performed introducing single particle at a time at a constant compressor air flow rate to hit the water loaded target plate. For all the AE signals, obtained from SSPI-Water experiment, it has been noticed that one event with higher amplitude in the middle of lots of smaller amplitude events. From previous experiments, it was observed that single gas bubble events are of lower amplitude and lower frequency contents than single particle impacts in air. So, in the recorded signals from SSPI_Water experiments,the higher amplitude are expected sand particle impacts and other lower amplitude events are potential bubble events. To verify this, for all the recorded signals from SSPI experiment, the corresponding higher amplitude events and one of the lower amplitude events have been selected for further time, frequency and time-frequency domain signal analysis.

From the frequency domain and time frequency domain analysis, the higher amplitude events showed the same frequency characteristics as observed from the SSPI-Air experiment and the lower amplitude events showed the same frequency characteristics of single gas bubble events as noticed in SGB experiment, as presented in the sections 5.3.3.2 & 5.3.3.3.

Further analysis has been carried out for each events in SSPI-Water experiment by calculating energy for the frequency bands 100 – 200 kHz (E1) and 300 – 400 kHz (E2). It has been found that, the energy ratio $\frac{E_3}{E_1}$ >1 can be associated with all the analyzed sand events while $\frac{E_3}{E_1}$ <1 can be attributed to the analyzed bubble events.

Based upon this observation, an automatic event identification technique has been proposed to differentiate sand particle impacts in presence of bubbles. For any given signal, 10% of the maximum amplitude has been set as a threshold for event identification purpose. Each identified event then passed through 100 – 200 kHz & 300 – 400 kHz band pass filters separately and the frequency band energy ratio ($\frac{E_3}{E_1}$) have been calculated for each filtered event signal. If $\frac{E_3}{E_1}$ >1, the event is detected as sand particle impacts and if $\frac{E_3}{E_1}$ <1, it is detected as bubble events.

To observe the efficiency of this technique in case of multi particle impacts, two other experiments, each consisted of eight repeated tests, have been carried on introducing three and ten sand particles respectively. The threshold set at 10% of the maximum amplitude can identify all the sand events incase of single particle impacts but unlikely to detect 20% of the lower impact energy particles for multiple particle impacts. To find an optimum threshold for multiple particle impacts, further analysis has been performed setting thresholds at 7%,5%,3% and 1%. It has been noticed that, threshold set at 3% or lower is likely to detect weak rebounded particle impacts or due to close proximity of the background noise level result in poor frequency content leading to wrong classification of detected AE events. For this research, threshold setting at 5% found to be optimal.

For any given system, the successful application of this developed technique depends upon the identification of optimum frequency bands for the sensors used, finding an optimum relationship among the frequency bands, for example the frequency band energy ratio in this research, related to the different source types present in the system and obtaining an optimum threshold for events detection.

Chapter 7 Conclusions and Future Recommendations

This chapter summarizes all the major findings from this work including discrimination of similar sized particle impacts on a freely supported target plate and identifying sand particles in the presence of bubbles on a fixed target plate. These laboratory experiments were preceded by pencil lead break tests performed on the target plate in varied environments.

In general, this work shows the potential of an alternative, frequency band energy ratio based AE technique which has advantages over more basic amplitude based AE techniques currently in practice for different industrial applications such as sand monitoring in oil and gas, for particle detection in nuclear reactor or in process industries(8,9,12).

The main findings from these experiments are presented below.

7.1 Preliminary pencil lead break experiments

- For any PLB test, higher amplitude signals were obtained at sensors positioned at the centre of the target plate (S1) than the off-centred sensor position (S2). This is also evident from event energy and power spectral density analysis.

- The effect of fixing the target plate into the end of a cylinder is to shorten PLB event duration and cause changes in the time frequency representations (PSD & GWT) of the analysed AE signals.

- For any particular set of tests the frequency content is repeatable. However, between tests the frequency content shifts for both sensor locations. This is observed through the frequency domain PSD analysis and from GWT of the acquired signals.

- Though the frequency content in signals between tests have been changed the peaks in the frequency spectra remain the same due to the broad band frequency response of the sensors used.

- For experiments where the target plate is fixed in the end of a cylinder, from all the performed signal analysis results, the results of PLB tests in water are slightly more varied than in air.

- For any specific sensor location, the changes in frequency content and amplitude can be attributed to the variations in coupling, test set up, test environment and PLB procedure among different tests.

- For a specific test, variations in signal characteristics between two sensor locations are associated with the signal travel path differences, reflections and mode conversions due to varying boundary conditions.
- For calibration, the variation in PLB AE signal strength means that an average response is needed for calibration for every test. Techniques using frequency response ratios offered a way around this problem. However some calibration of every individual application, be it in the laboratory or industry, will be required.

7.2 Similar sized particle impact test

- Applying standard AE parameters such as number of events, peak AE or AE Energy may be sufficient to distinguish sources for many simple applications. However, for small coupon geometries, typical in engineering applications, the presence of close boundaries makes the interpretation difficult if not invalid due to reflections, dispersions and mode conversions.
- A unique frequency band energy ratio analysis technique has been proposed to distinguish between two very similar groups (in terms of size, mass and energy) of sand particles and glass beads, impacting on mild steel. Optimum Frequency band AE energy ratio to distinguish the particles has been identified for this experimental set up.
- For applying standard AE parameters, in applications, usually requires some form of calibrations, standardisation or normalisation. For the developed technique in this research, once the optimal frequency bands and ratios have been identified, then an added advantage is that calibration of signal levels is not required. However the proposed framework for applying this new technique must be carried out with initial experimentation to characterize the optimum frequency band for any particular industrial application.
- The symmetrical structure of the cylindrical target plate facilitates two main sensor position consideration: centred and off-centred. Among these two sensor positions it has been found that the off-centred sensor position (S2) is more suitable for differentiating populations of two very similar particle impact types (glass beads and sand particle) originated at the centre of the cylindrical surface for this experiment.
- Part of the available data set (80%) has been used for developing a classification technique implementing SVM classification algorithm based on standard AE parameters. The developed model has been tested on the rest of the data set. The overall success rate of individual particle impact classification (glass beads and sand particles) for S1 is 86% and for S2 is 92%.

125

7.3 Particle impacts in presence of bubble experiments

- Two main sources of AE, sand particle impact and bubbles, have been considered in the laboratory experiments. For this specific experimental arrangement and used sensors characteristics, lower frequency contents have been found to be associated with bubble events and higher frequency contents have been related to sand particle impacts.

- The distinct frequency signatures of bubble and sand particle impact events have been used to develop a new automatic event identification technique and has been tested on the acquired laboratory signals.

- The developed technique is sensitive to the amplitude threshold settings for event identification. Higher threshold, e.g., 10% of the maximum amplitude, will clearly identify sand particle impacts but for multiparticle tests is likely to not detect about 20% of lower (impact) energy particles. Lower threshold, e.g., 3% of the maximum amplitude, is likely to result in detection of AE events with poor frequency content and wrong classification of the weakest events.

- Increasing the number of particles for multiparticle testing increases the chances of particle interactions which can result in lower particle impact energy or non-separable impact events.

- For this experimental set up and sensors used, the performance of the developed method has not been affected by the sensor locations considered.

- Optimising the particle impacts identification has been achieved dependent upon setting optimum threshold, finding optimum frequency bands and establishing optimum relation among the frequency bands.

7.4 Contributions and Future Recommendations

- Large lateral dimension along the direction of wave propagation, for thin simple structures, enables individual wave modes detection present in the structure (23,76). However, for thick small coupon specimen with close boundary, signal distortion due to dispersion, reflection and mode conversion becomes prominent making individual mode identification very difficult (74,78,81). For such structures, any signal analysis technique based on individual mode characterization in time, frequency or time-frequency domain, as described in (76,77), will not work. In this research, a small cylindrical stepped specimen with close boundary has been considered. It has been found that though mixing of different wave modes makes the signal interpretation difficult but also due to frequency response characteristics of the sensors used in the research, certain frequency bands become more reactive to the physical sources that generated

126

the received AE signal. This frequency band information can be used for appropriate signal processing to characterize the sources.

- Prior researches involving particle impacts on small coupon specimen established relationships between AE energy with particle diameters and velocities for different particle sizes and different environmental conditions (wet and dry) (40,47,48,49,51,52). However, this does not assure impacted particle type identification if there is more than one type of particles present since AE energy is not unique to a particle type and can be dependent upon various factors such as velocity and impact angle. A frequency band energy ratio based parameter evaluation, developed in this research, helps to identify populations of very similar type (size, mass and energy) particle impacts. Also, an SVM classification algorithm based technique, implementing standard AE parameters, has been discussed which has shown significant success.

- In a laboratory set up like the one considered in this research and previous research works (40,50,52), generally the amplitude of particle impacts is higher than the bubble related AE signals. However, in practical case (11), bubble energy is comparable to the particle impacts energy and can be misinterpreted if the condition of the system calibration, based on signal amplitude or energy, changes. In this research, an automatic particle impact event identification in presence of bubbles is presented. The success of this technique, based on frequency band energy ratio, depends upon detection of optimum frequency bands and establishing a classification relationship between these frequency bands as well as setting an optimum amplitude threshold to identify the actual amount of impacts correctly.

The following points can be considered for any future research work carried:

- For performed experiments, sensors characteristic frequency behaviours facilitates identification of different types of constituents. Sensors with different frequency characteristics should be the next step.

- In this research, one classification algorithm (SVM) has been implemented. Other classification algorithm, such as Random Forest, Neural Network can be considered for similar sized particle impacts identification.

- To validate the developed frequency band AE energy based technique, a real life application, for example, AE records from sensors mounted on petroleum flow line subjected to sand production will be possible.

- More different fluid types and constituents for more varied conditions can verify the robustness of the technique in a wider perspective.

- With a better controlled environment, identification of various bubble formation stages and interaction among different bubbles can be studied and could aid in better understanding of particle impact identifications in the presence of bubbles in practical cases.

Appendix A : Time domain AE signals for various fixed target plate experimental environments

A1. Fixed – Water PLB experiment
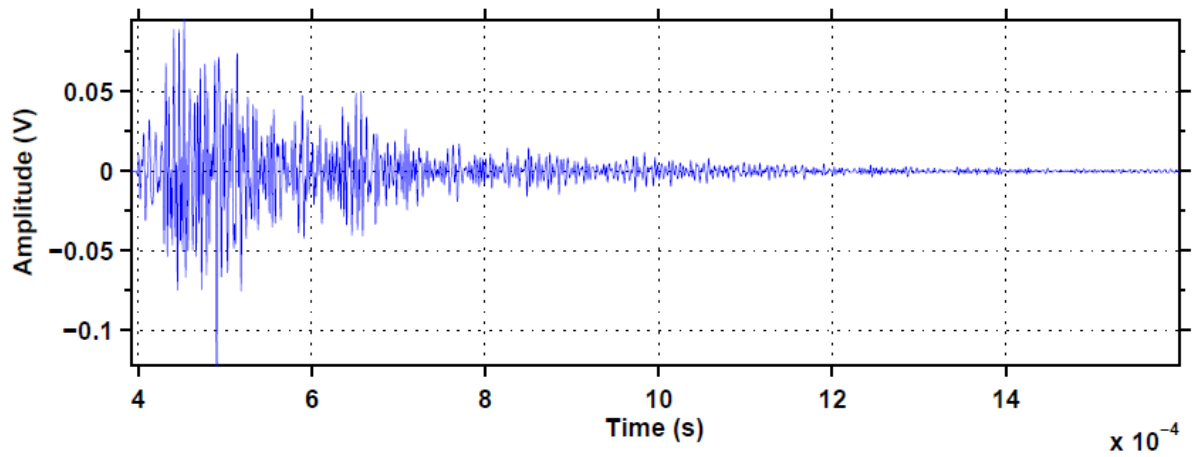
(a)
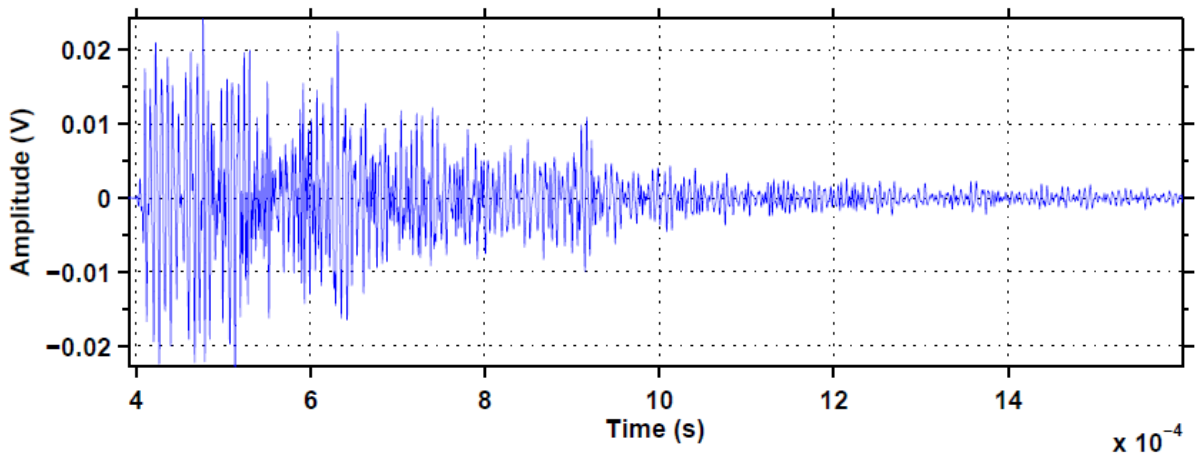
(b)

Figure A - 1: Typical AE signal from PLB at (a) S1 and at (b) S2 for Fixed – Water experiment.

A2. Masked PLB experiment

(a)

(b)
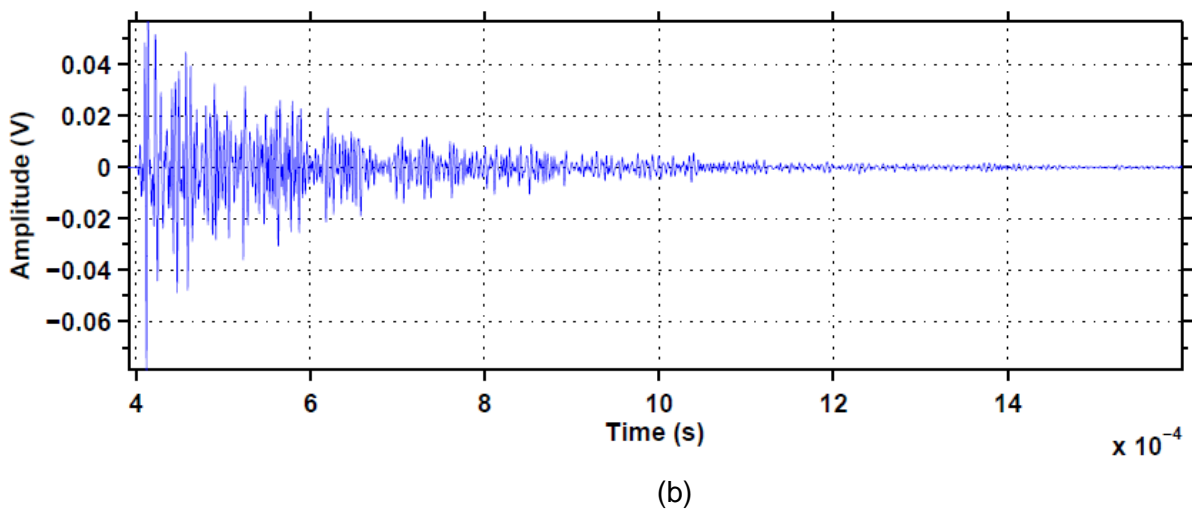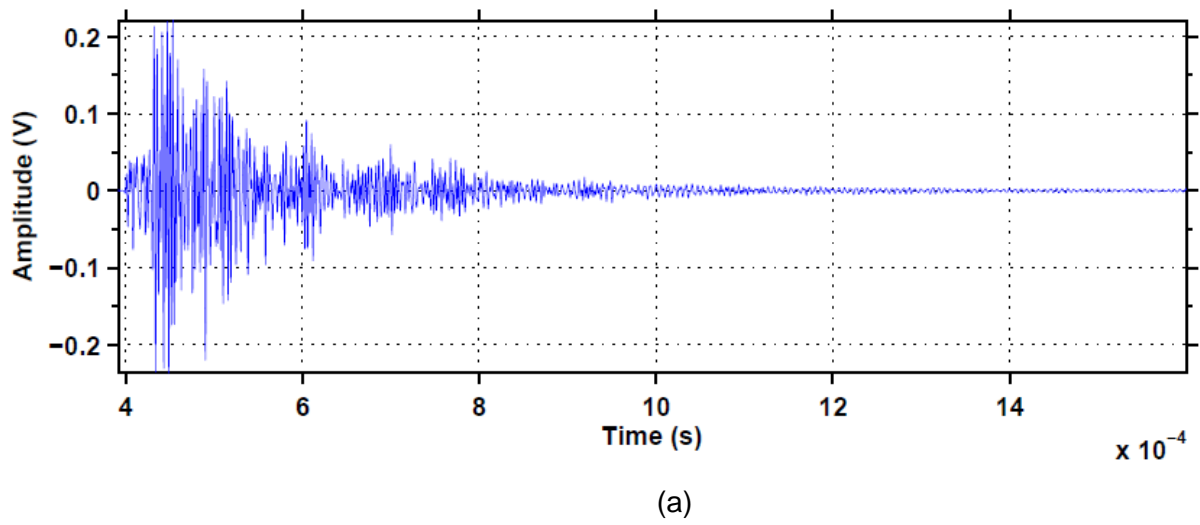
Figure A - 2: Typical AE signal from PLB at (a) S1 and at (b) S2 for Masked experiment.

A3. Masked – Water PLB experiment
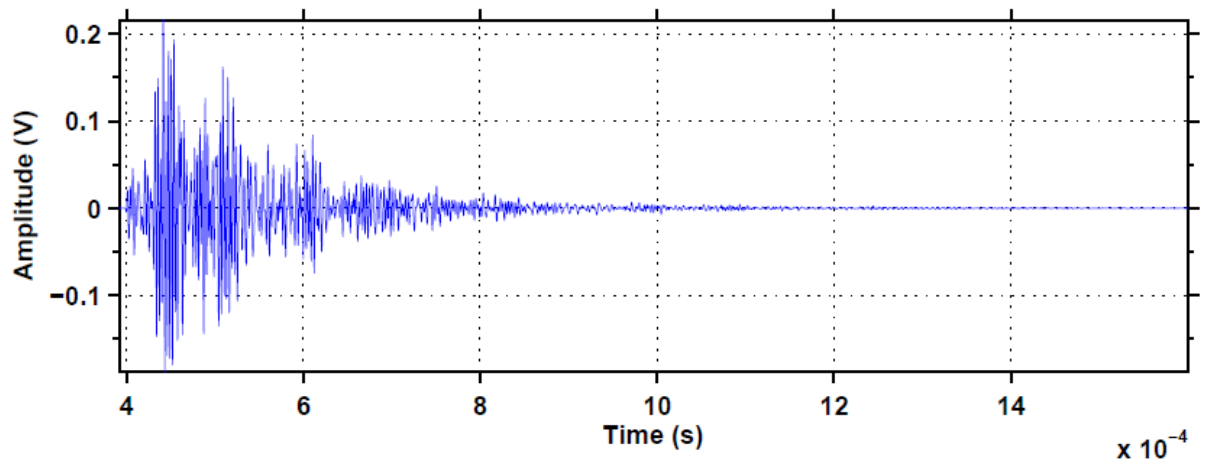
(a)
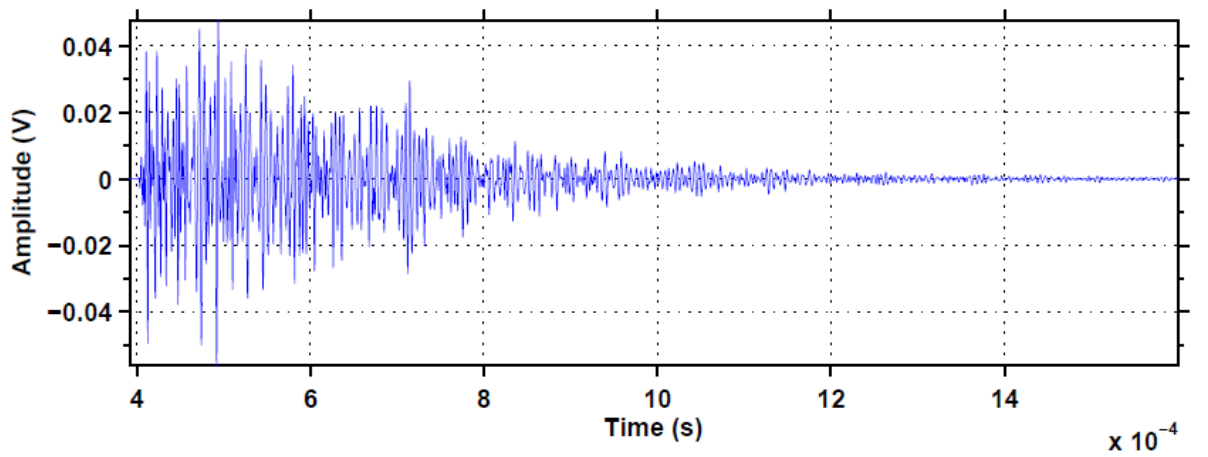
(b)

Figure A - 3: Typical AE signal from PLB at (a) S1 and at (b) S2 Masked – Water experiment.

Appendix B : Standard time domain AE parameter analysis for PLB

B1. Maximum Amplitude
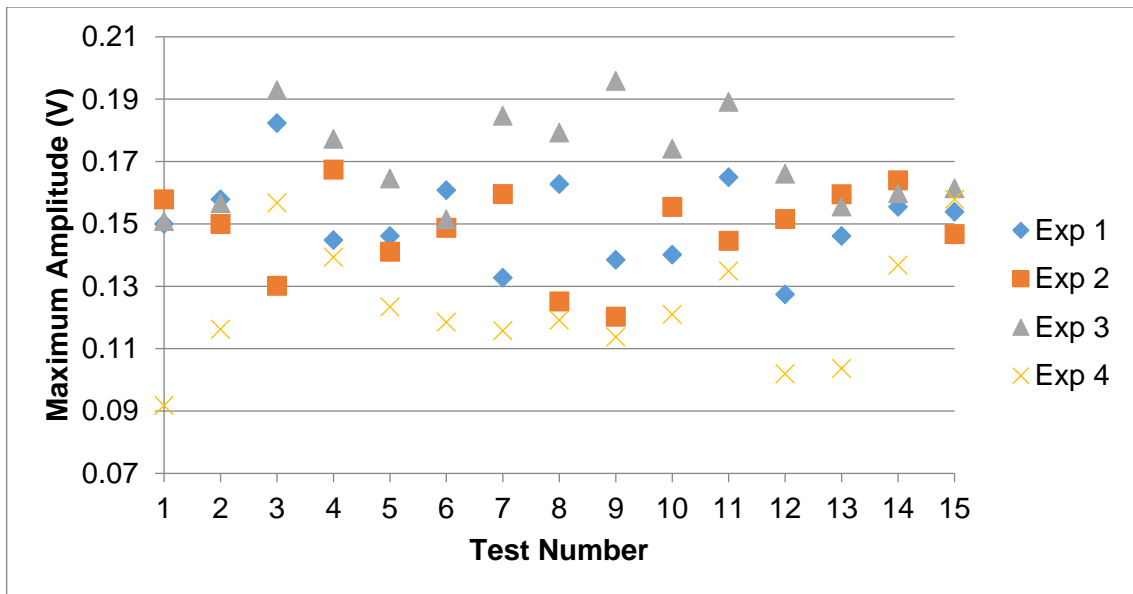
(a)
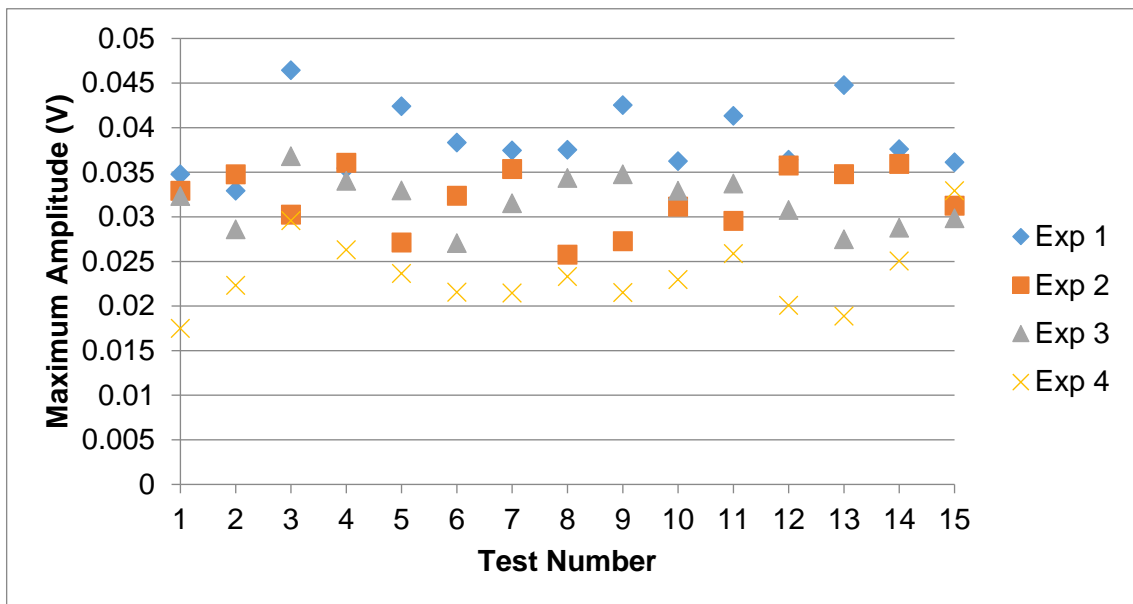
(b)

Figure B - 1: At (a) S1 and (b) S2, variation of maximum amplitude for recorded AE signals for all the experiments.
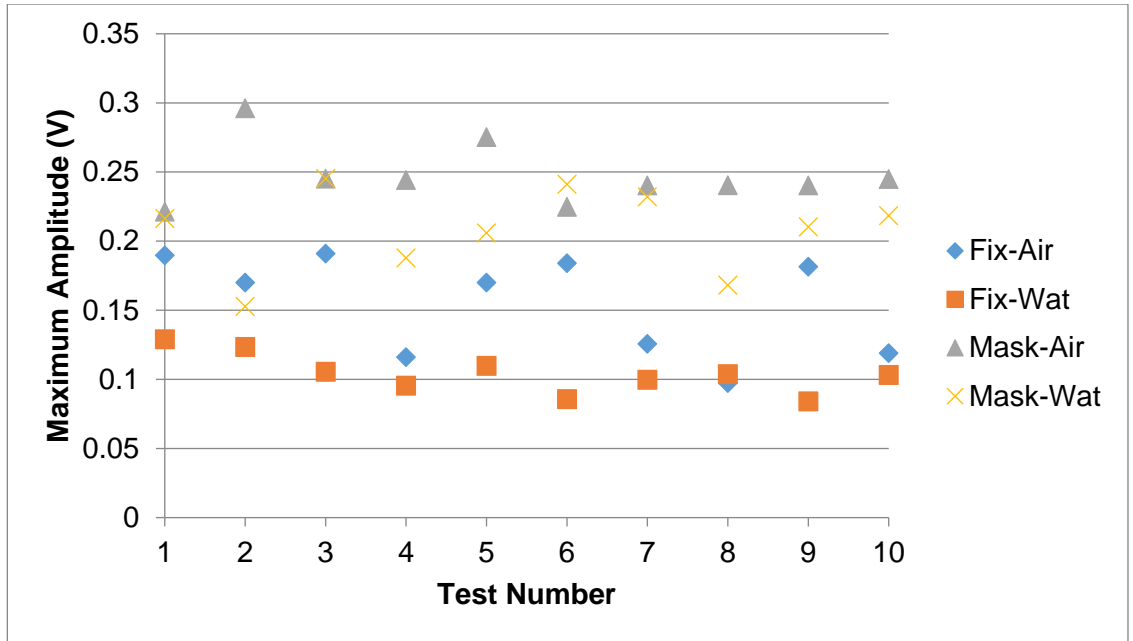
(a)
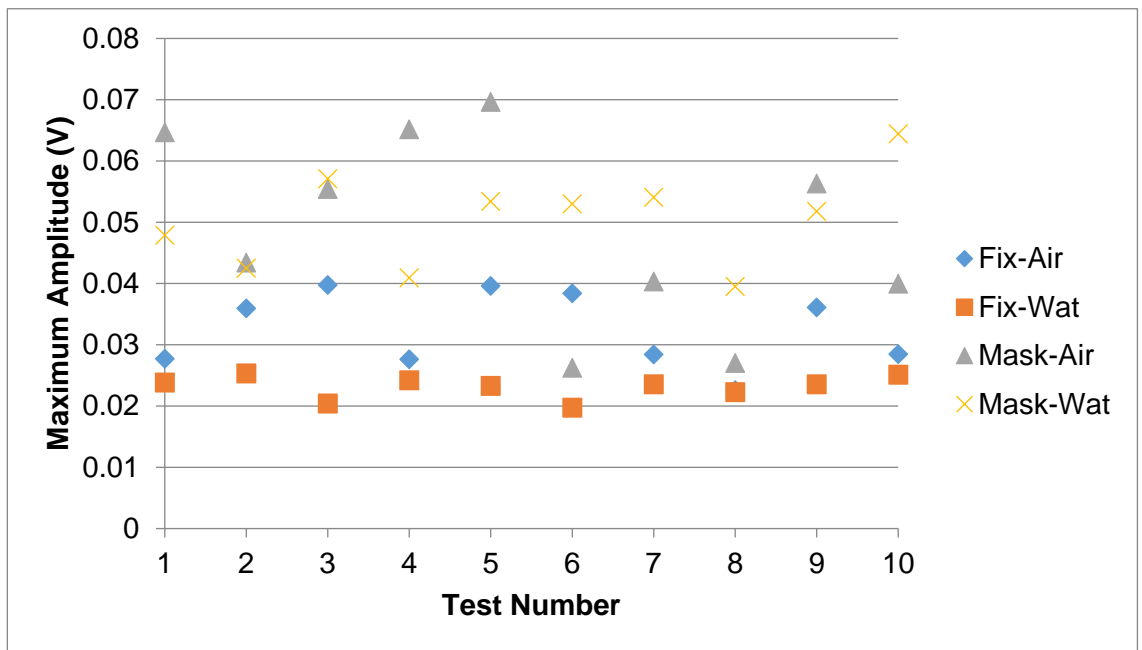
(b)

Figure B - 2: At sensor positions, (a) S1 and (b) S2, the variation of maximum amplitudes for all the recorded AE signals for four different test environments.

B2. Duration
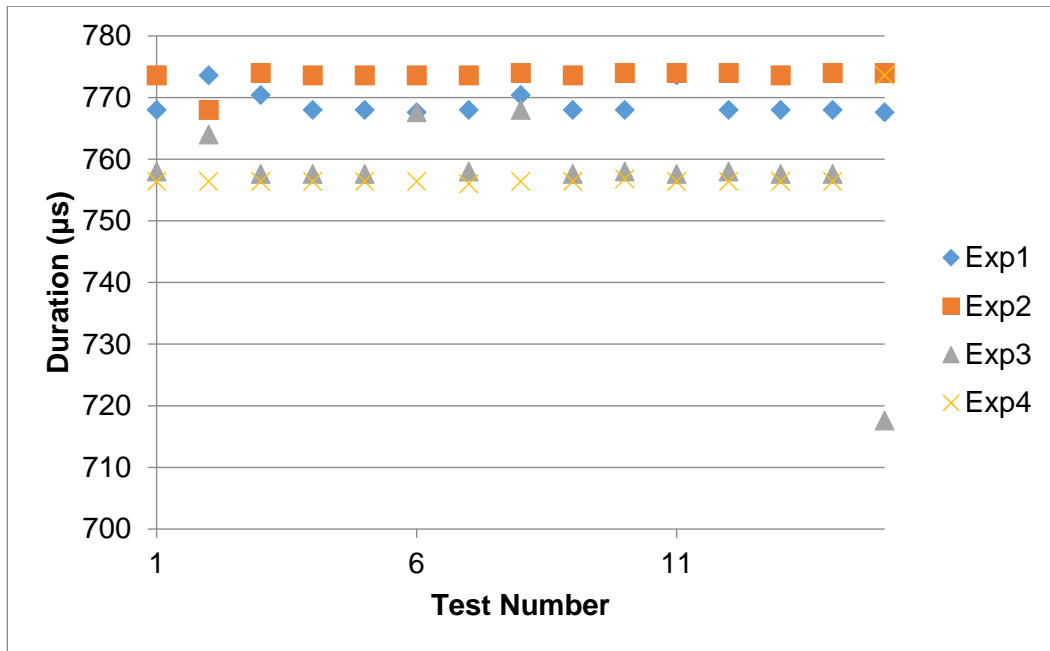
(a)
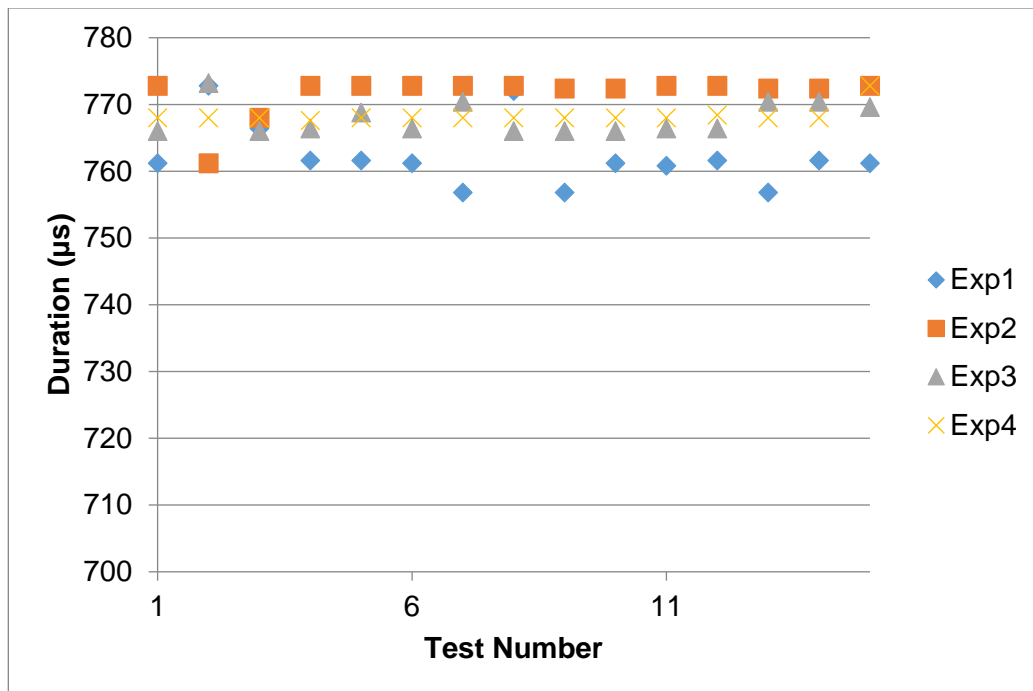
(b)

Figure B - 3: At (a) S1 and (b) S2, variation in event duration of the recorded AE signals for all experiments.
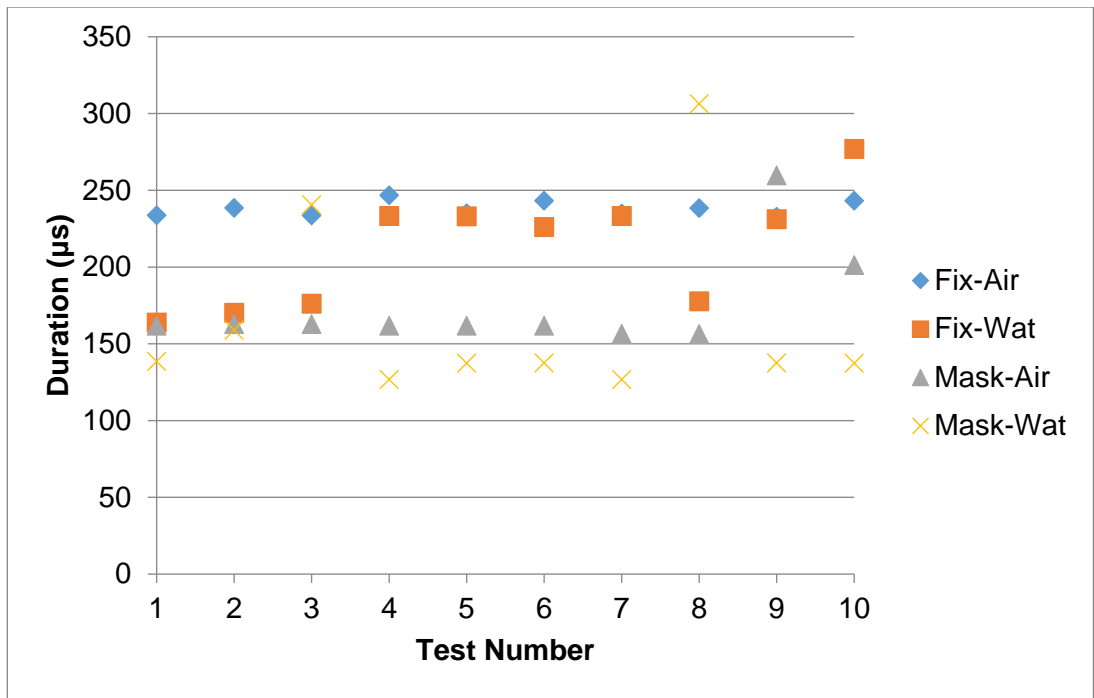
(a)
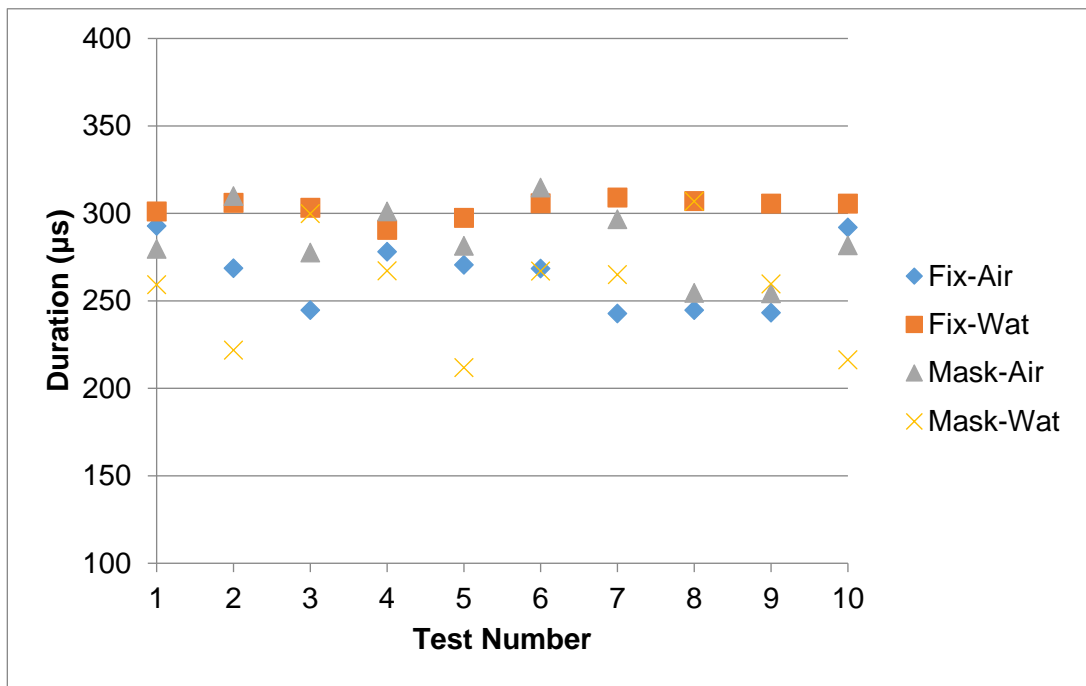
(b)

Figure B - 4: At sensor positions, (a) S1 and (b) S2, the variation of event duration for all the recorded AE signals at different test environments.

B3. Rise Time
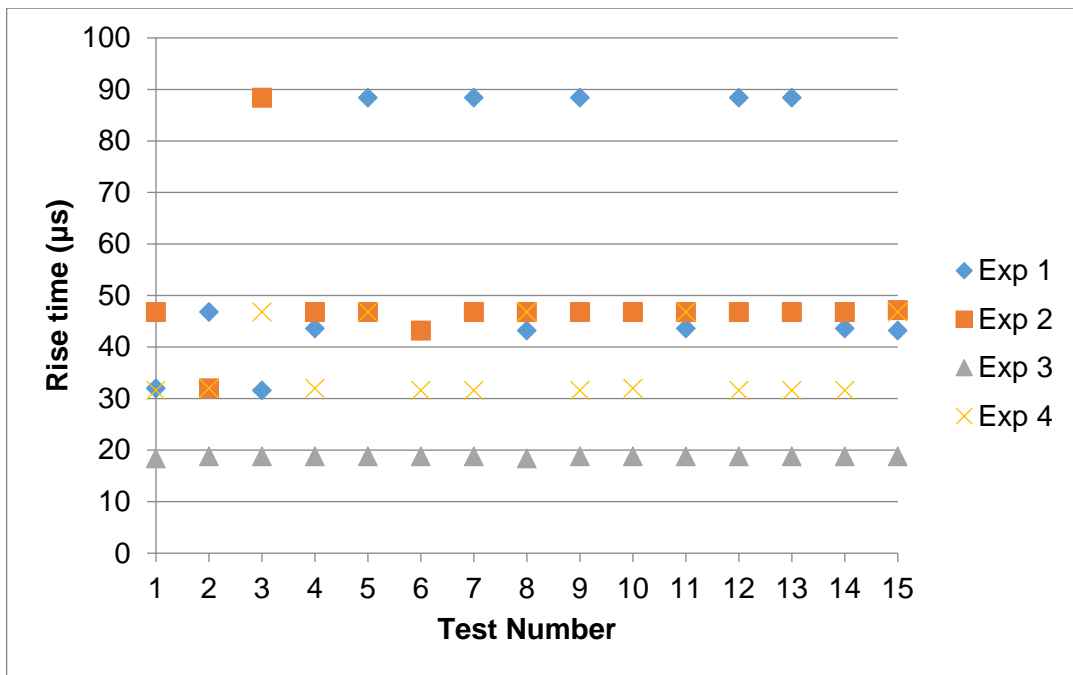
(a)
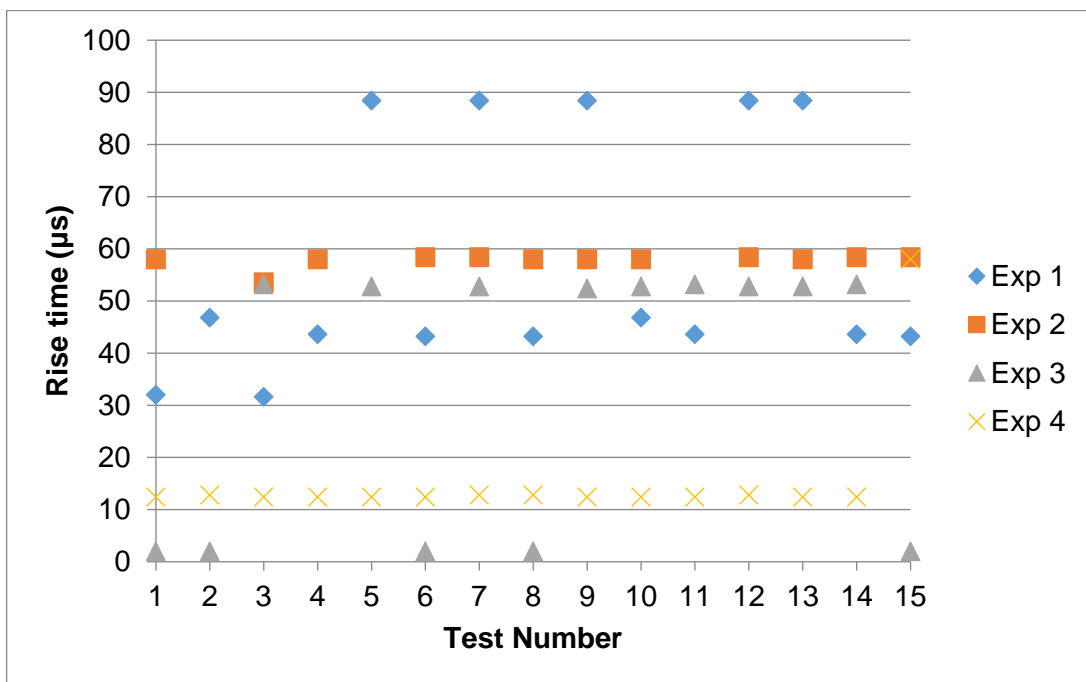
(b)

Figure B - 5: At (a) S1 and (b) S2, variation in rise time of the recorded AE signals for all the experiments on free target plate.
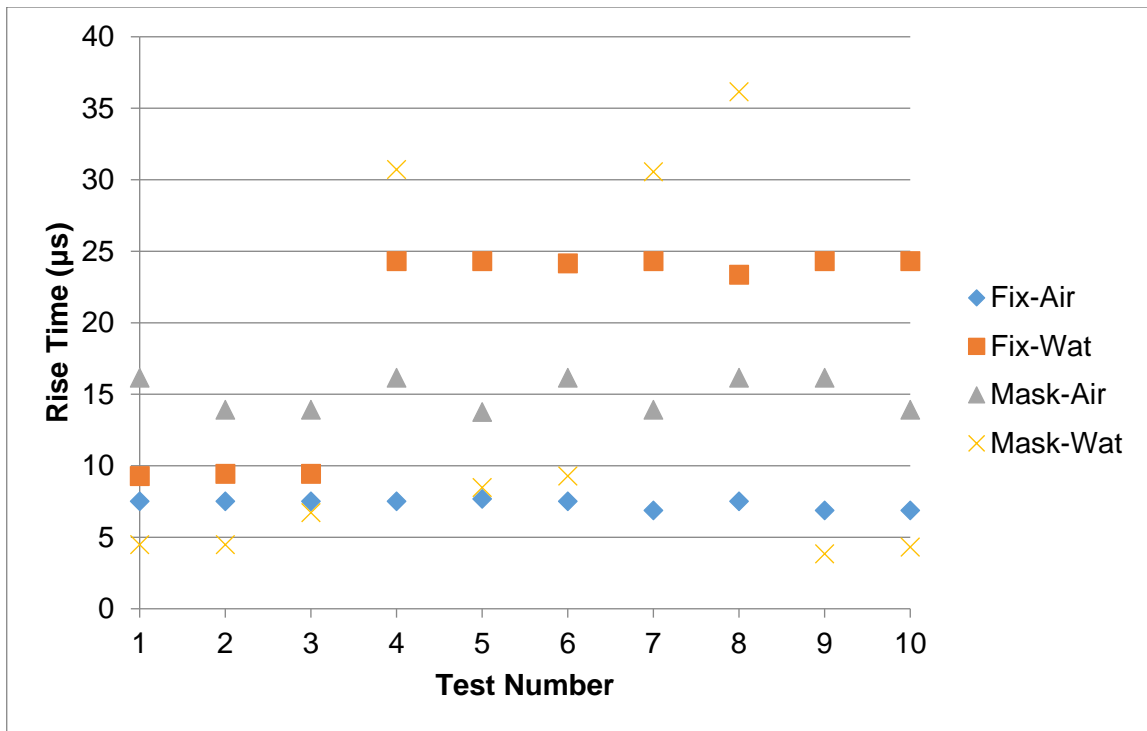
(a)
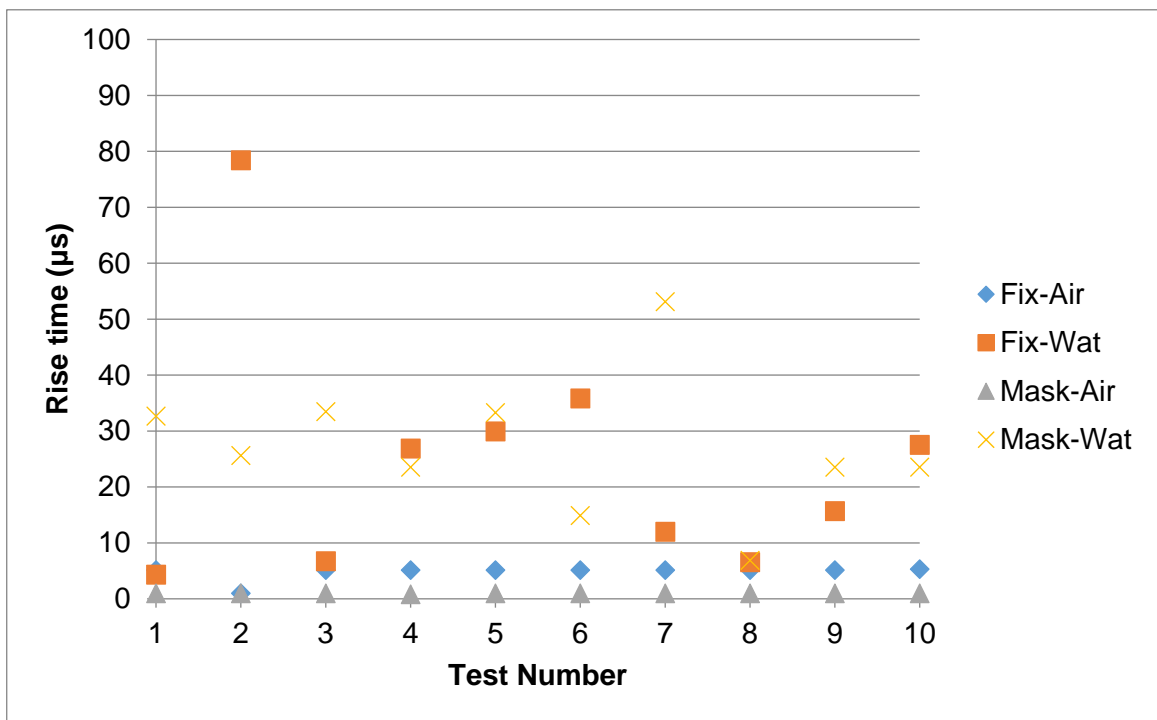
(b)

Figure B - 6: At sensor positions, (a) S1 and (b) S2, variation of rise time for all the recorded AE signals with masked and without masked target plate, in air and water.

B4. AE Energy
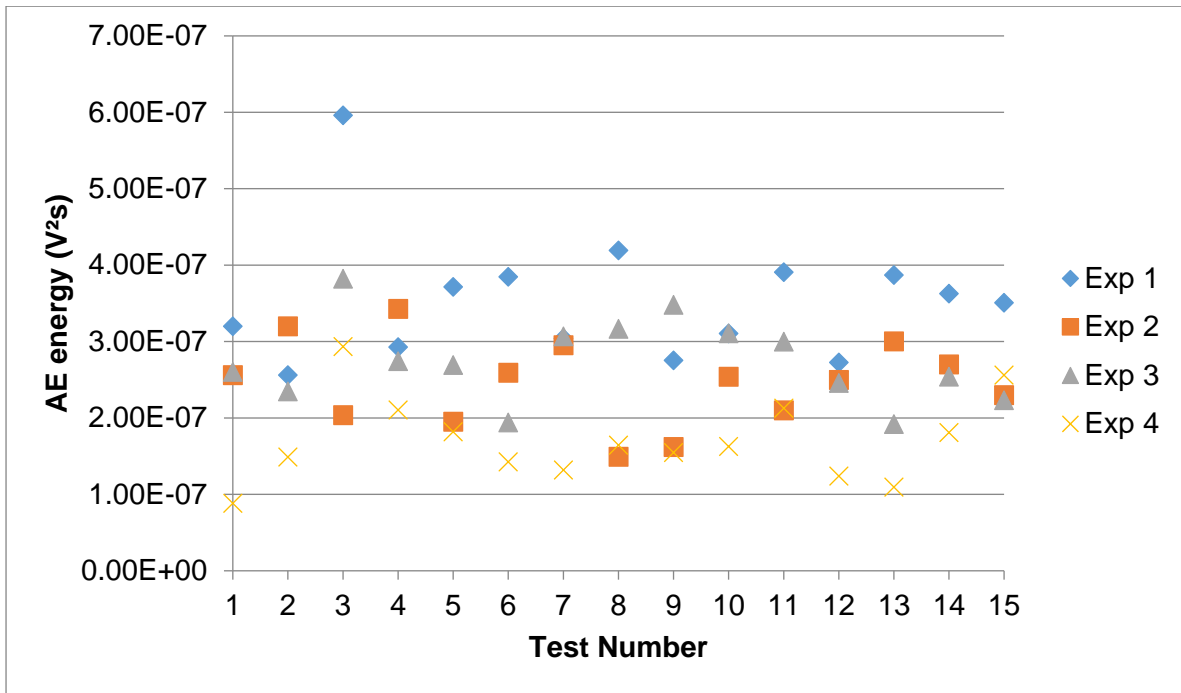
(a)
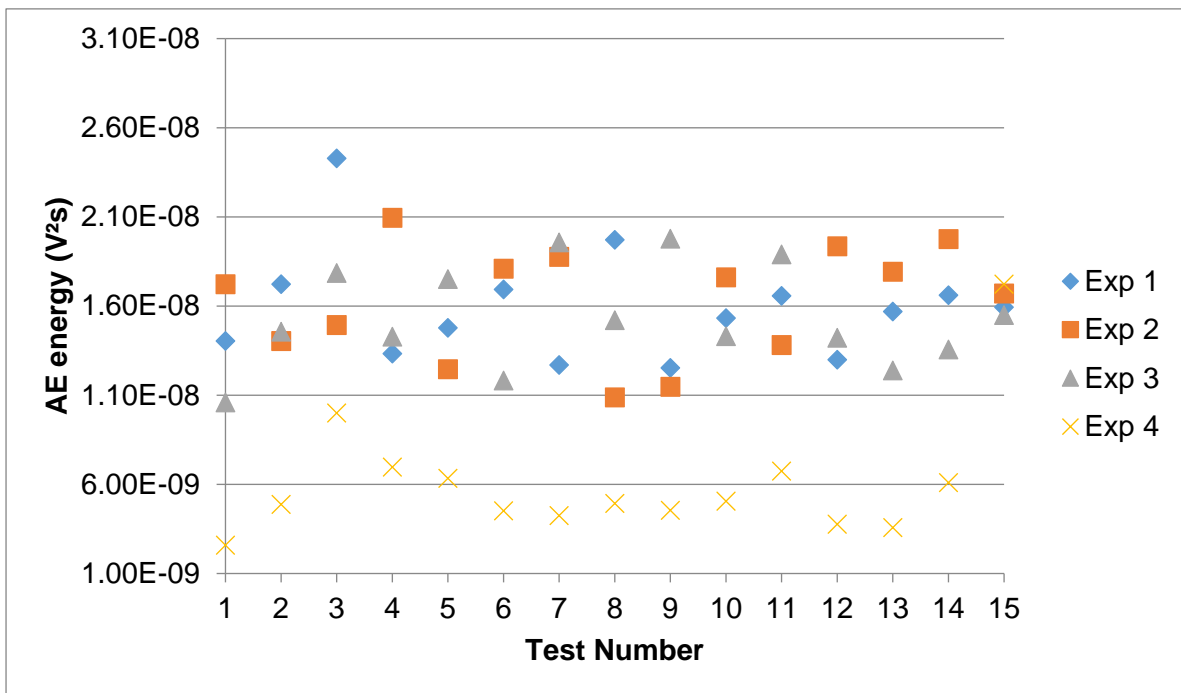
(b)
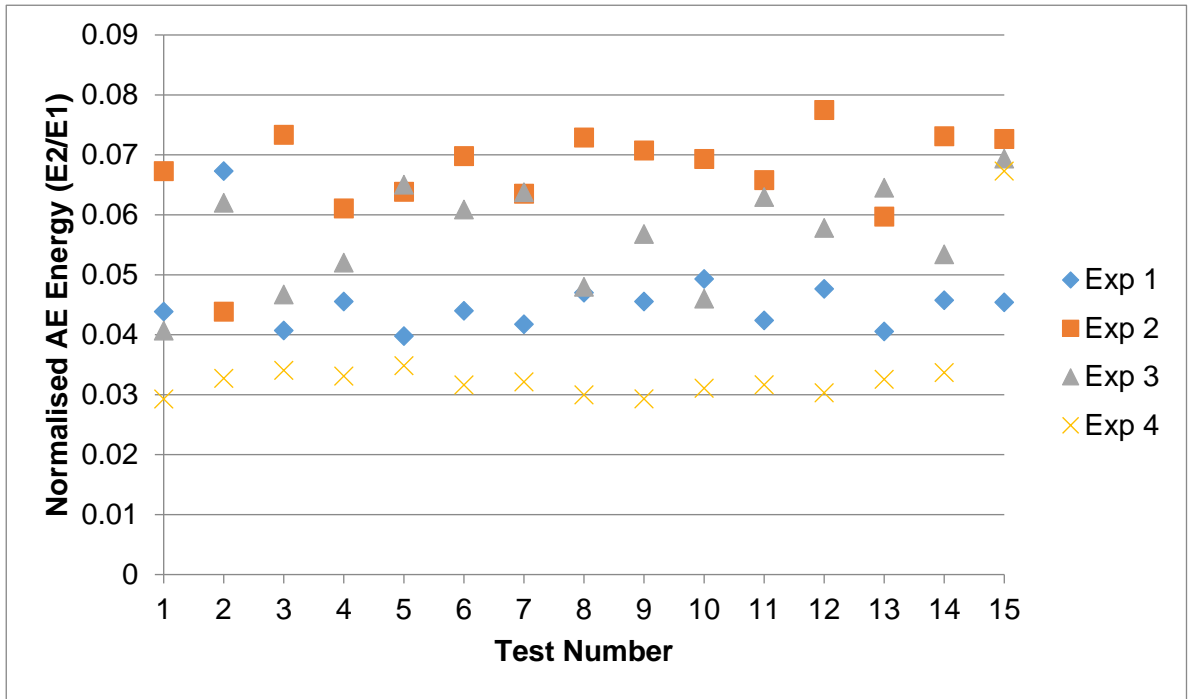
(c)

Figure B - 7: At (a) S1 and (b) S2, variation in AE energy of the recorded AE signals for all the experiments. (c) Normalised AE energy of the sensors. E1 and E2 refers to energy at S1 and S2 respectively.
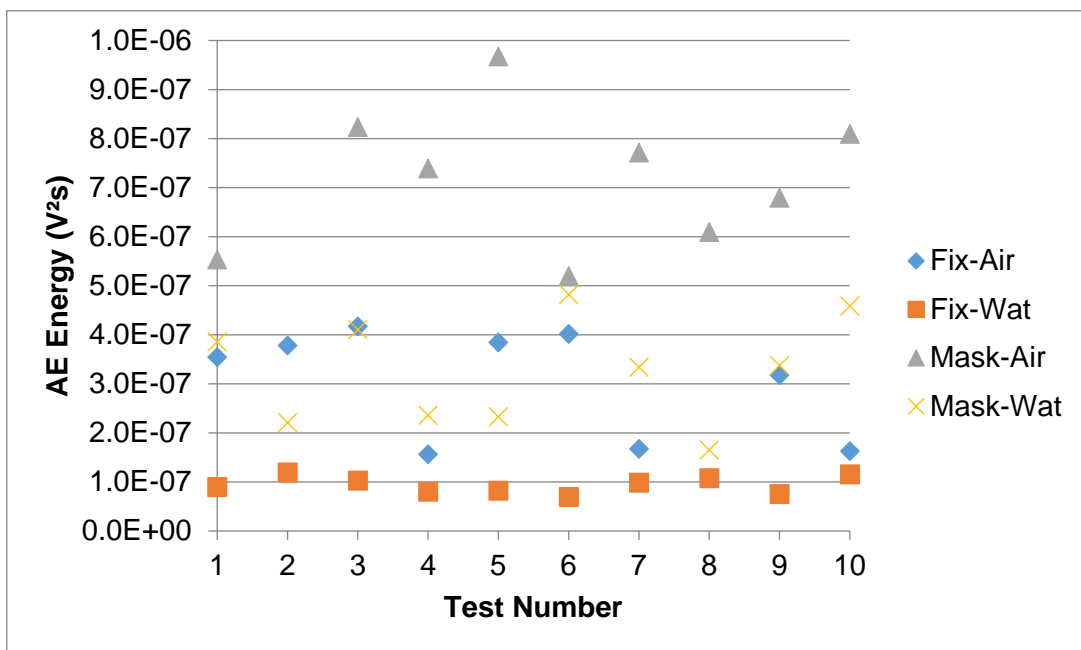
(a)
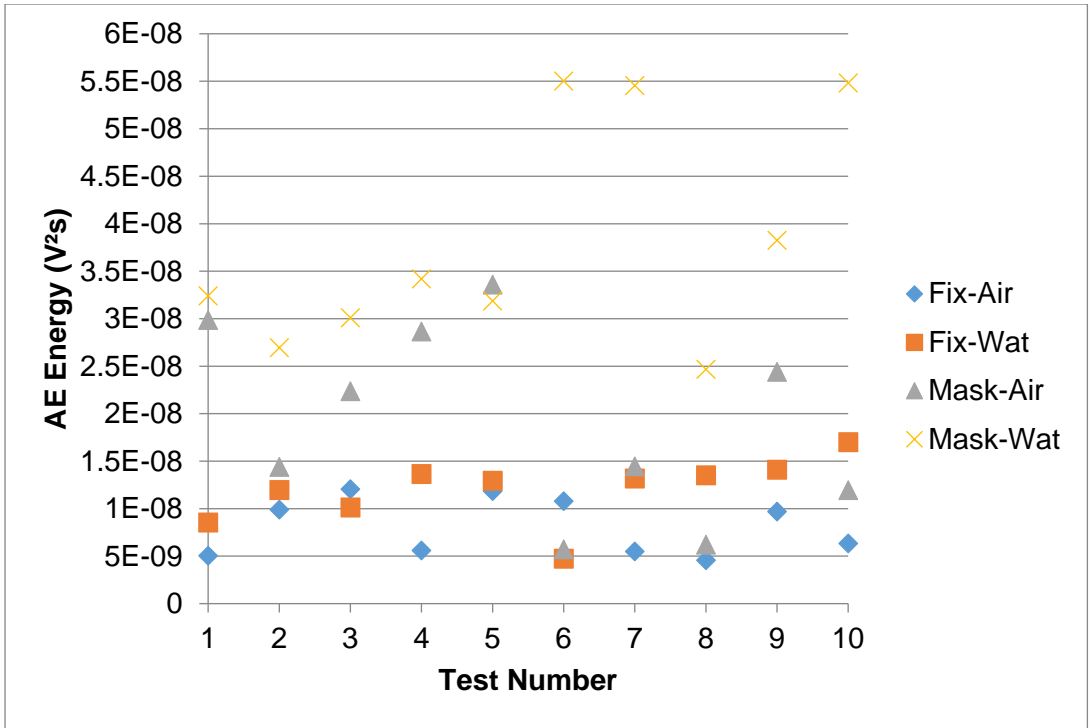
(b)

Figure B - 8: At sensor positions, (a) S1 and (b) S2, variation of AE energy for all the recorded AE signals with masked and without masked target plate, in air and water.

B5. Spectral Centroid
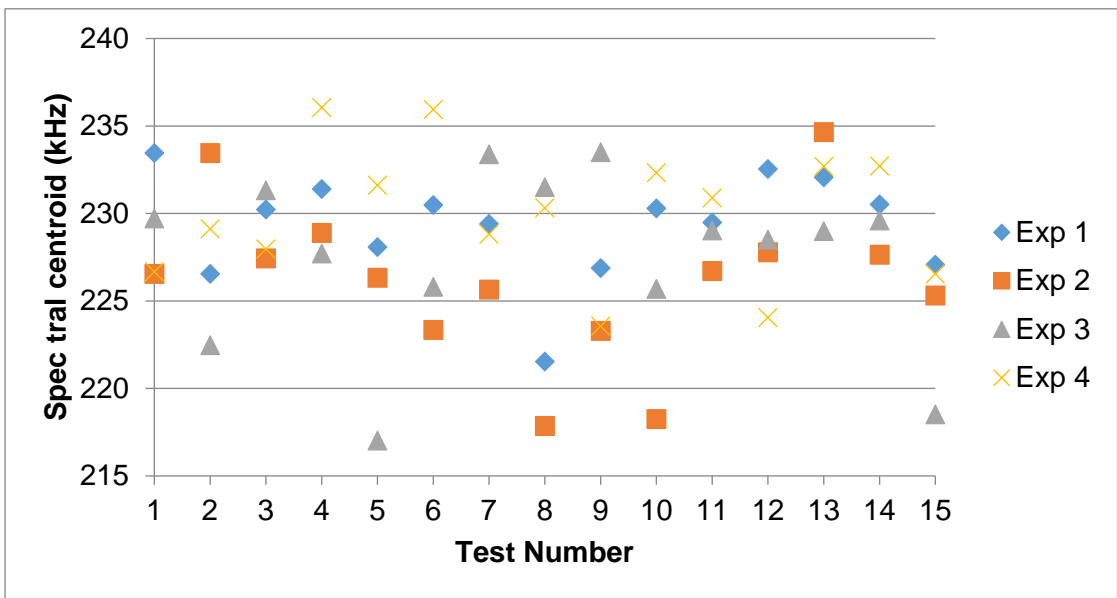
(a)
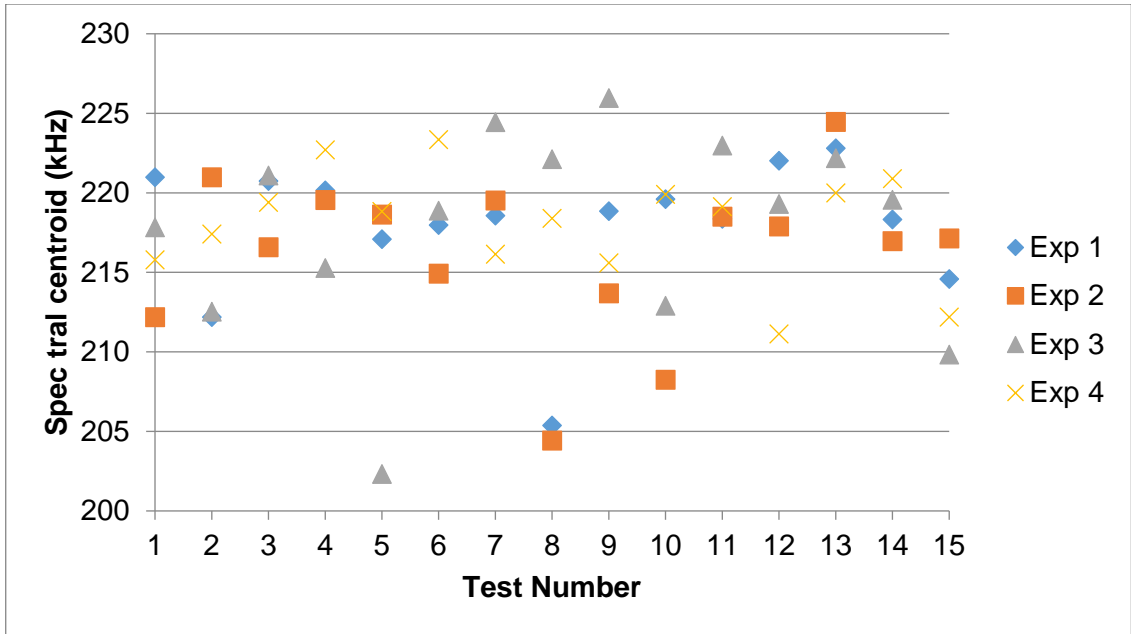
(b)

Figure B - 9: At (a) S1 and (b) S2, variation in event duration of the recorded AE signals for all the experiments.
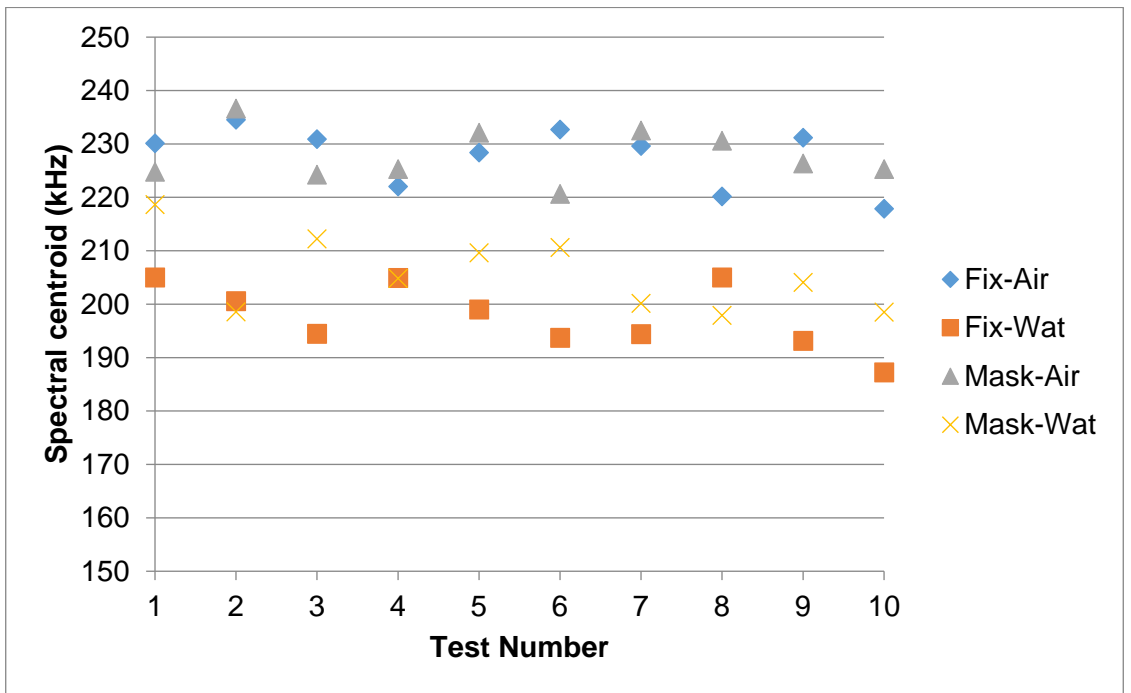

(a)
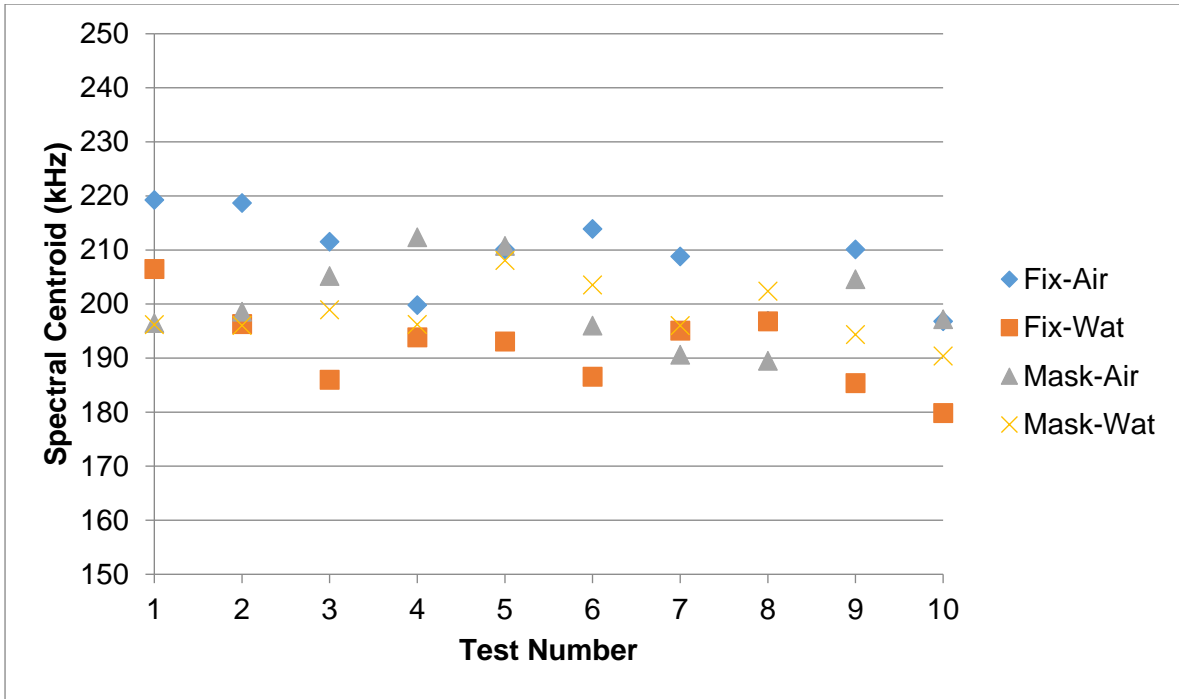
(b)

Figure B - 10: At sensor positions, (a) S1 and (b) S2, variation of spectral centroid for all the recorded AE signals with masked and without masked target plate, in air and water.

B6. Power Spectral Density
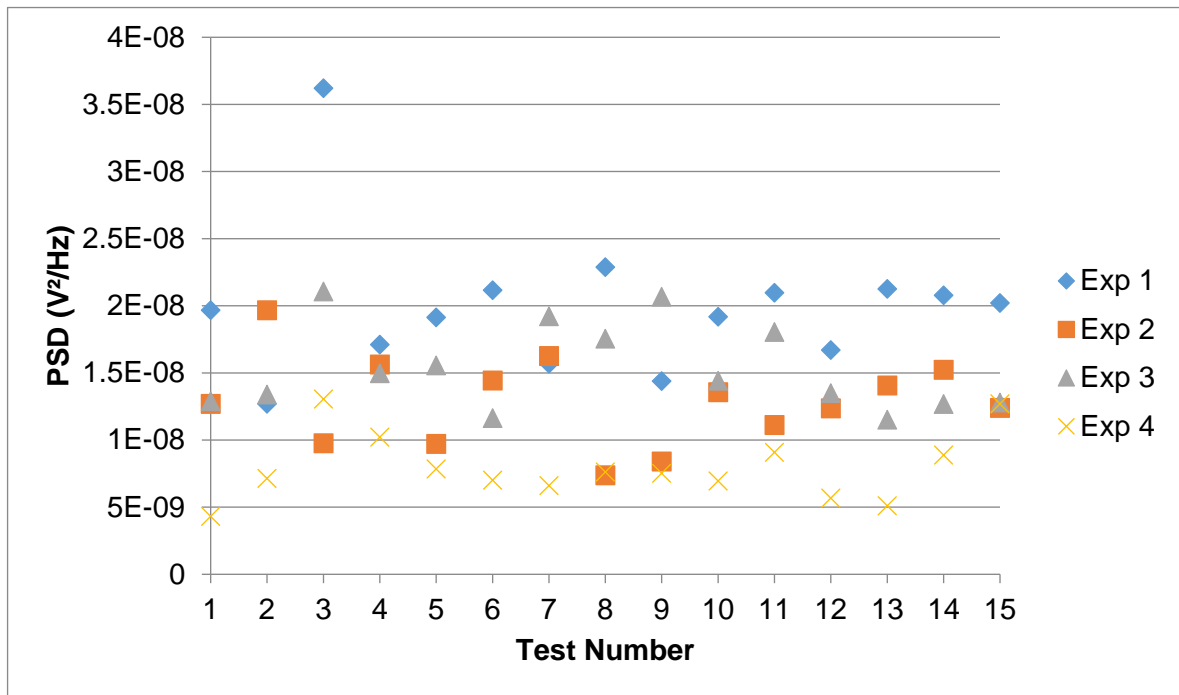
(a)
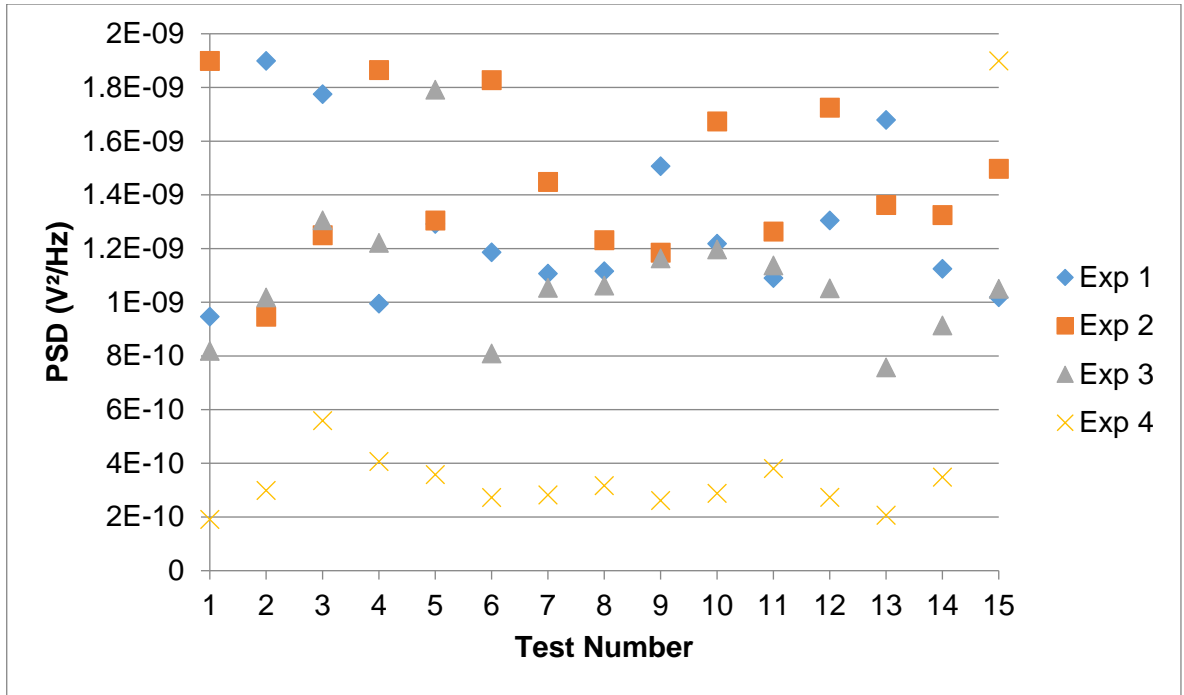
(b)
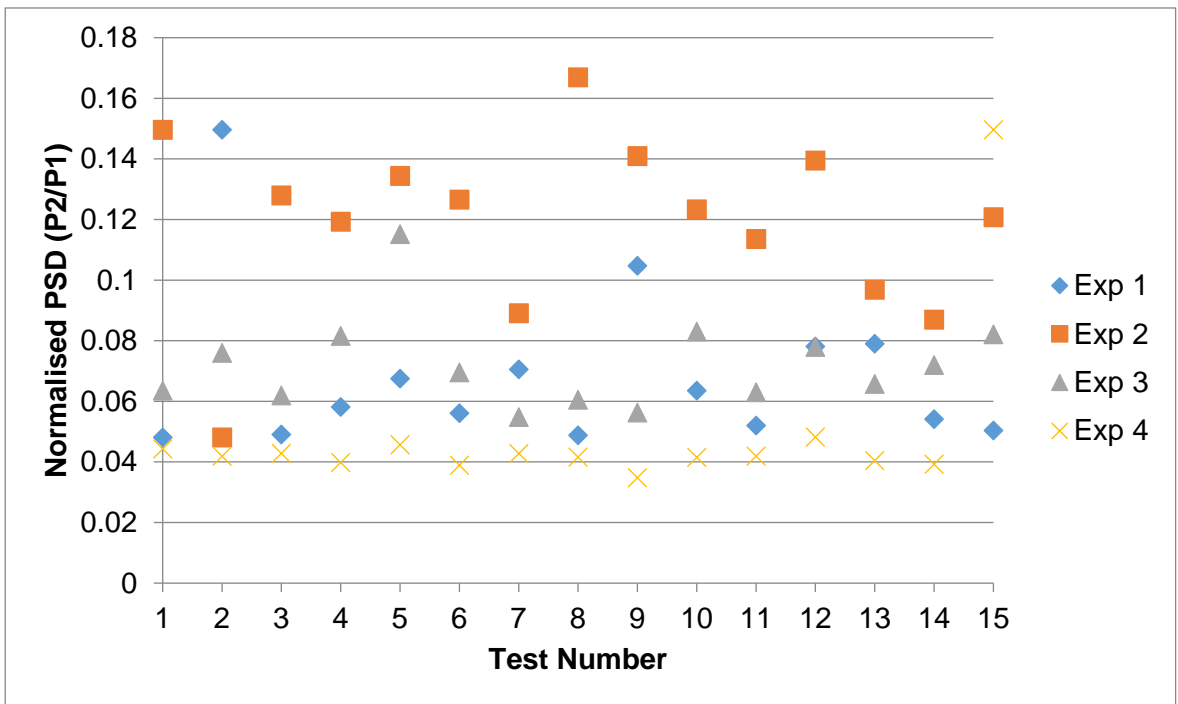
(c)

Figure B - 11: At (a) S1 and (b) S2, variation in PSD of the recorded AE signals for all the experiments. (c) Normalsied PSD (P2/P1). P1 and P2 refers to PSD for S1 and S2 respectively.
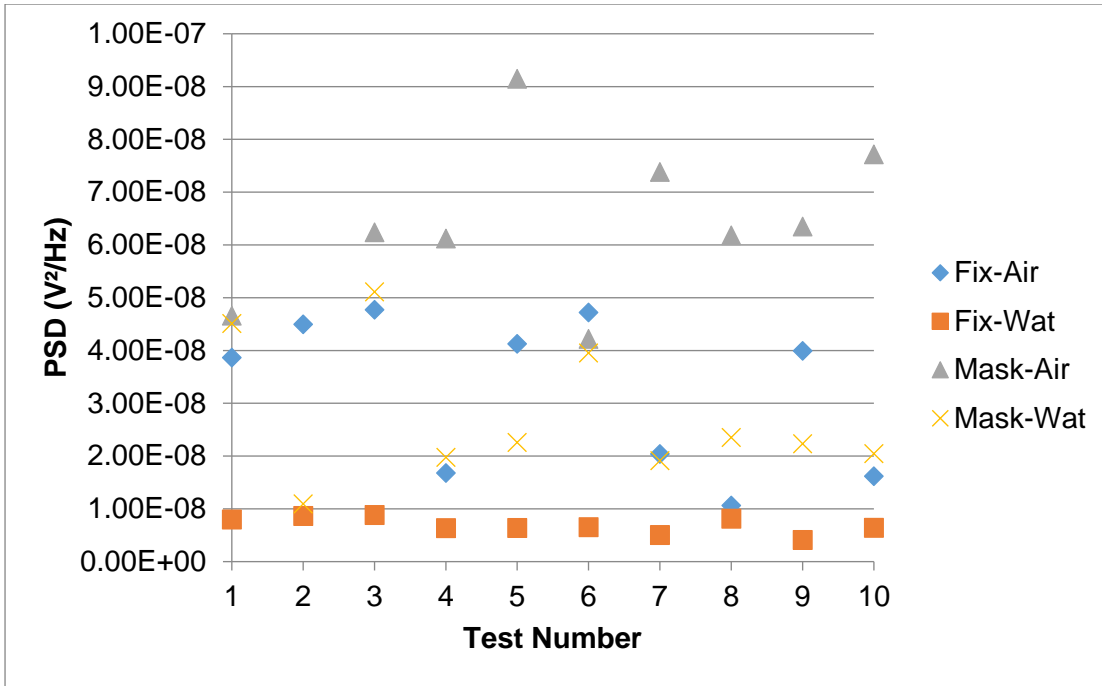
(a)
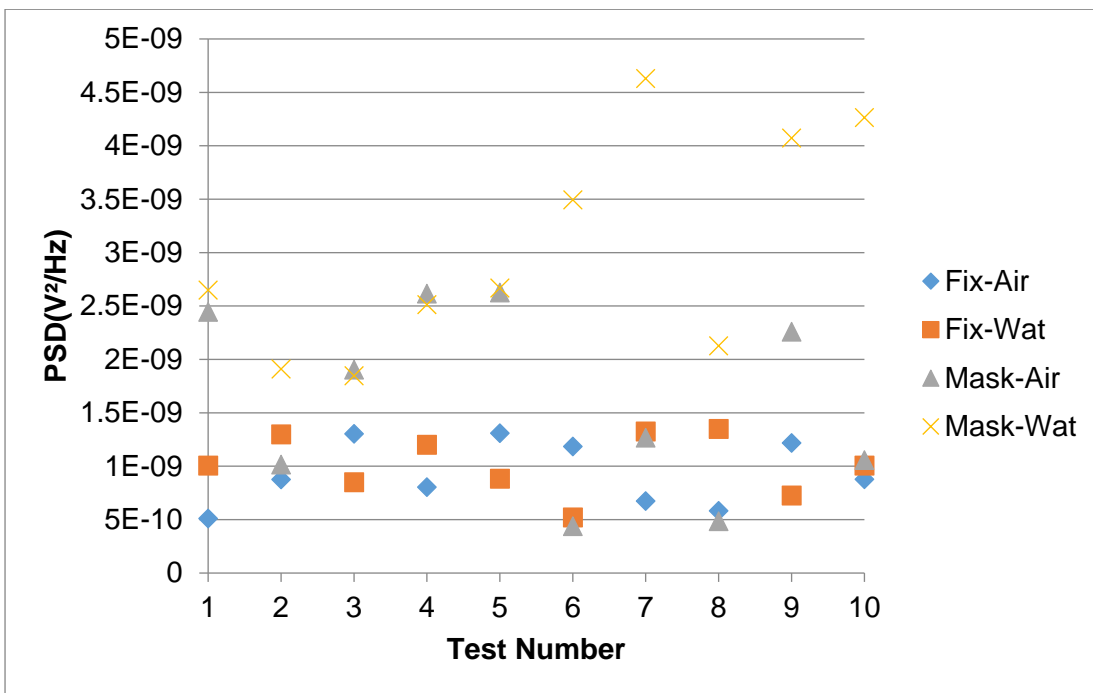
(b)

Figure B - 12: At sensor positions, (a) S1 and (b) S2, variation of PSD for all the recorded AE signals in the experiments performed in four environments: Fixed, Fixed – Water, Masked and Maksed - Water.

B7. Maximum PSD Frequency
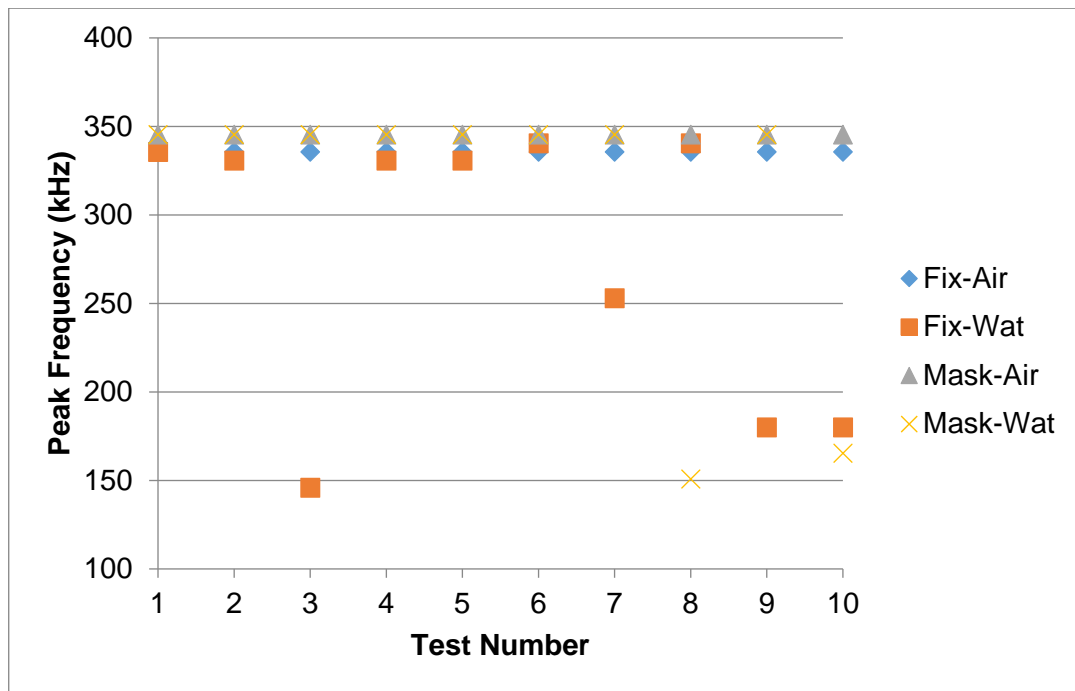
(a)
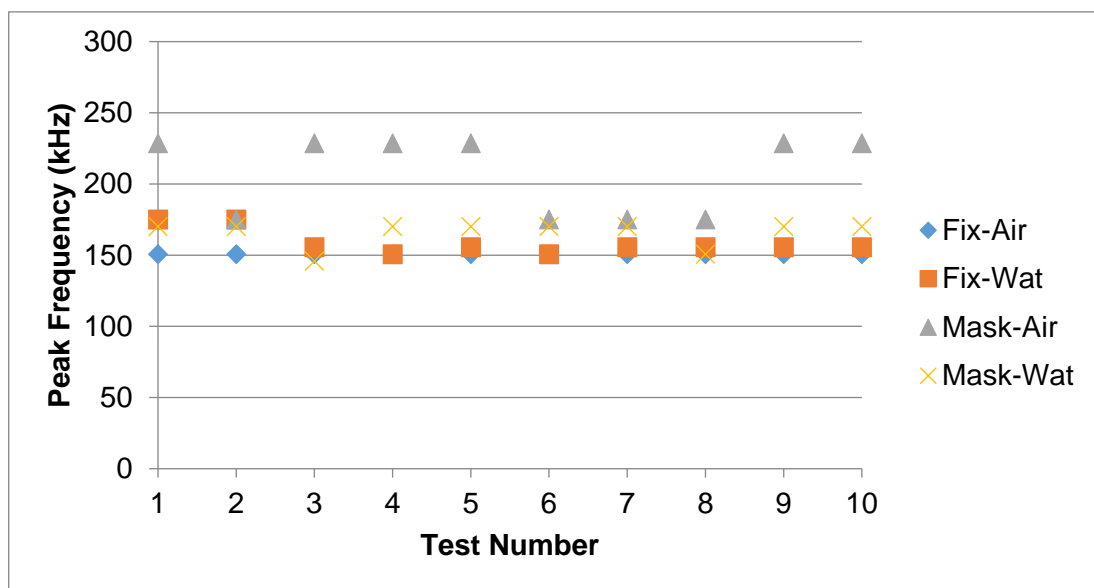
(b)

Figure B - 13: At sensor positions, (a) S1 and (b) S2, variation in peak PSD frequency for all the recorded AE signals performed in four experimental environments: Fixed, Fixed – Water, Masked and Maksed - Water.

Appendix C : Standard AE parameters analysis for populations of similar sized particle impacts with PLB on mild steel target plate

C1. Maximum Amplitude
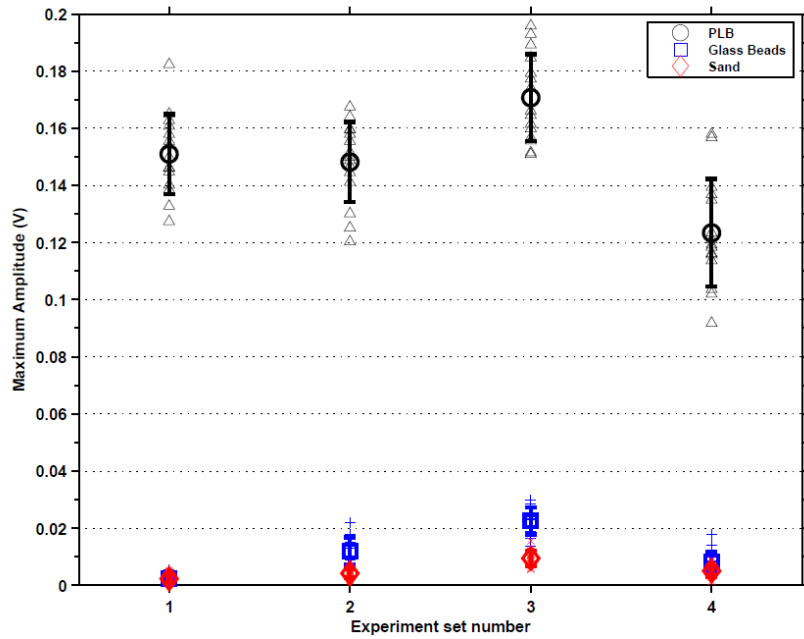

(a)
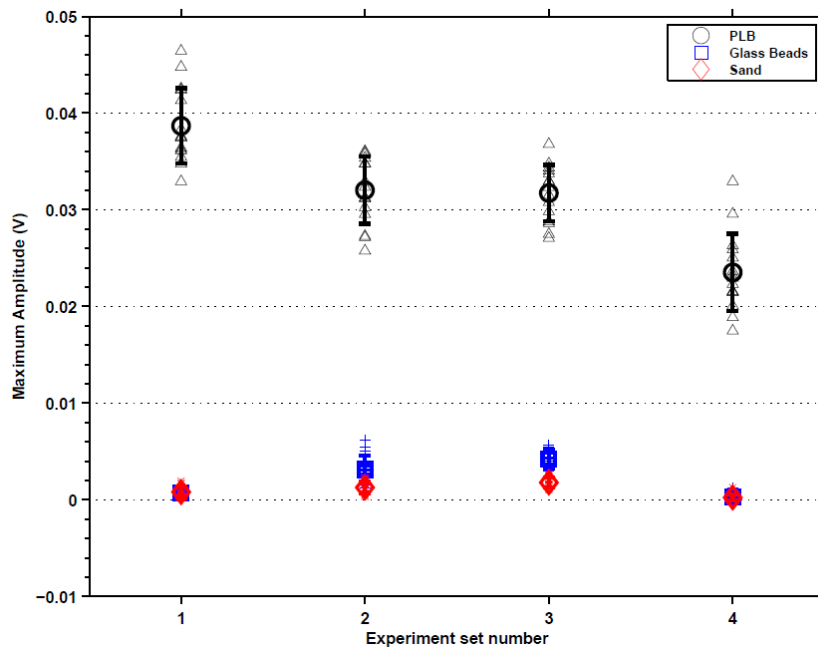
(b)

Figure C - 1: Variations in maximum amplitude of similar sized particle impacts populations with PLB in four experiments on mild steel target plate for (a) S1 & (b) S2.

## C2. Event Duration
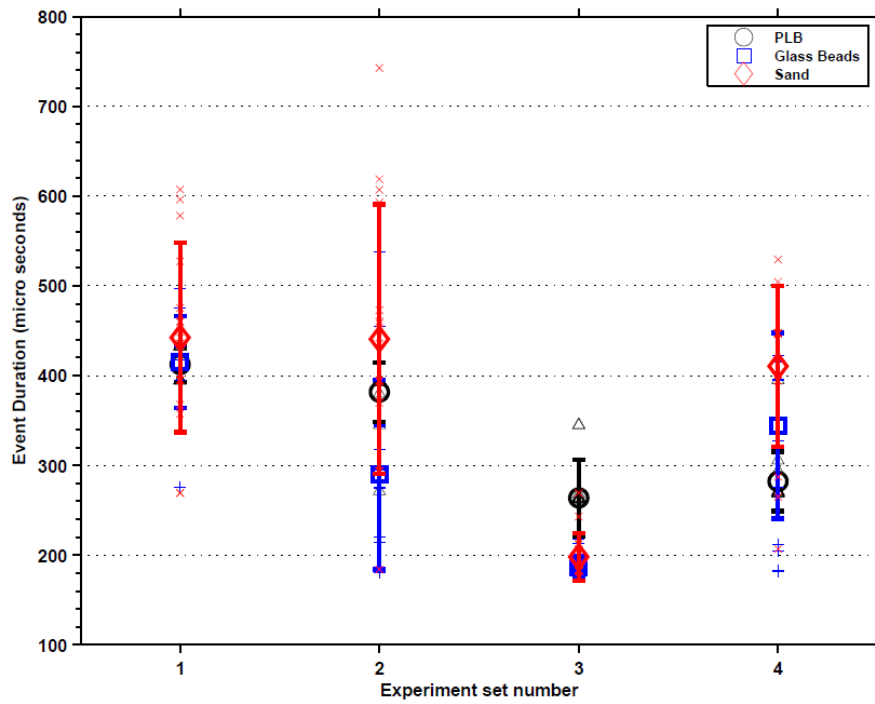
(a)
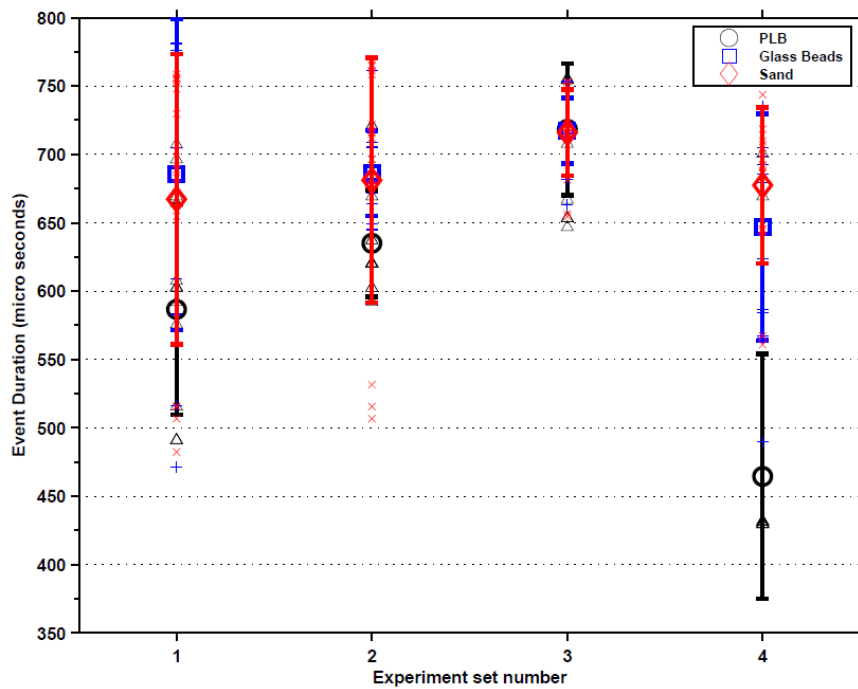
(b)

Figure C - 2: Variations in event durations of similar sized particle impacts populations with PLB in four experiments on mild steel target plate for (a) S1 & (b) S2.

C3. Event Energy
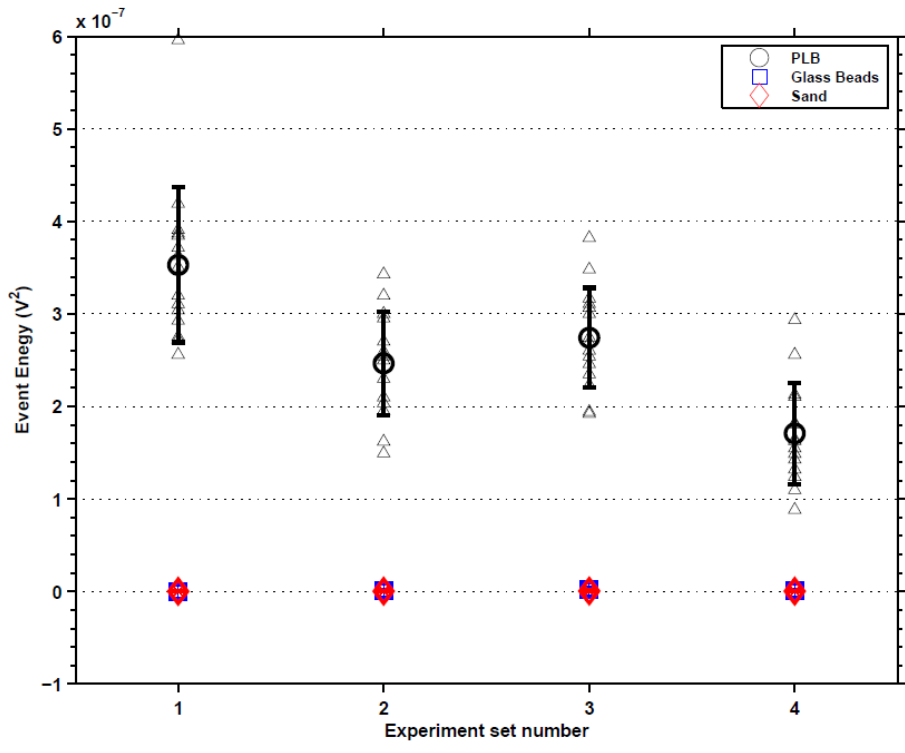

(a)
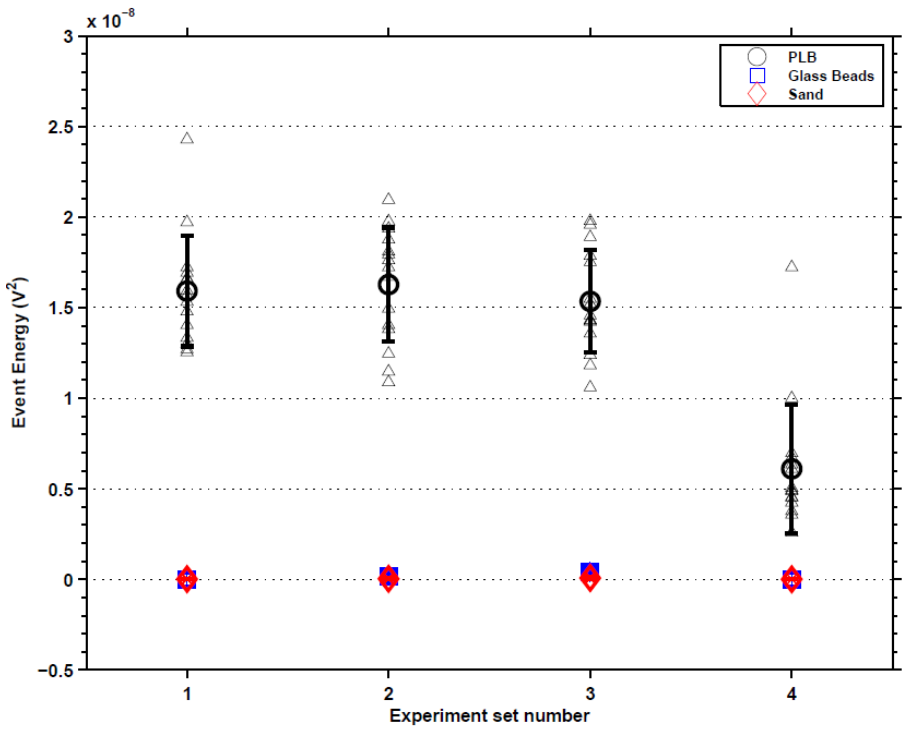
(b)

Figure C - 3: Variations in event energy of similar sized particle impacts populations with PLB in four experiments on mild steel target plate for (a) S1 & (b) S2.

C4. Maximum Power Spectral Density
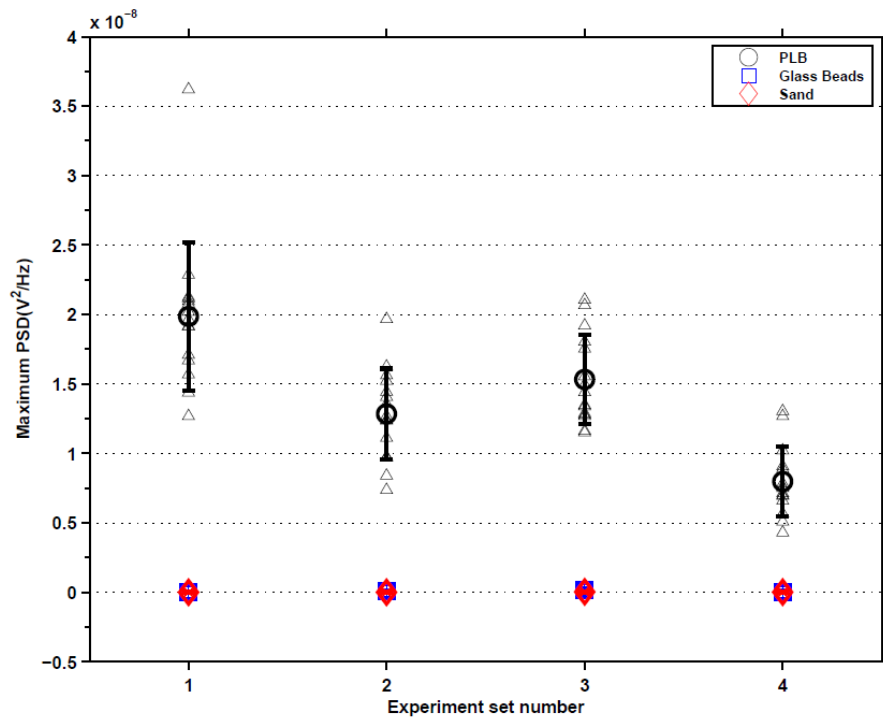
(a)
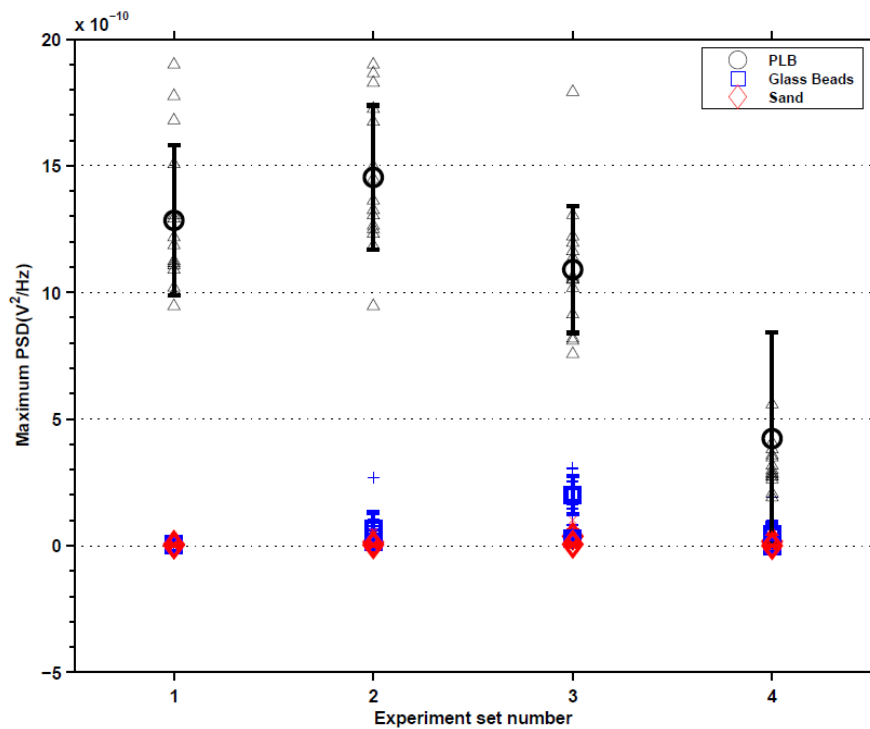
(b)

Figure C - 4: Variations in maximum PSD of similar sized particle impacts populations with PLB in four experiments on mild steel target plate for (a) S1 & (b) S2.

C5. Maximum Frequency
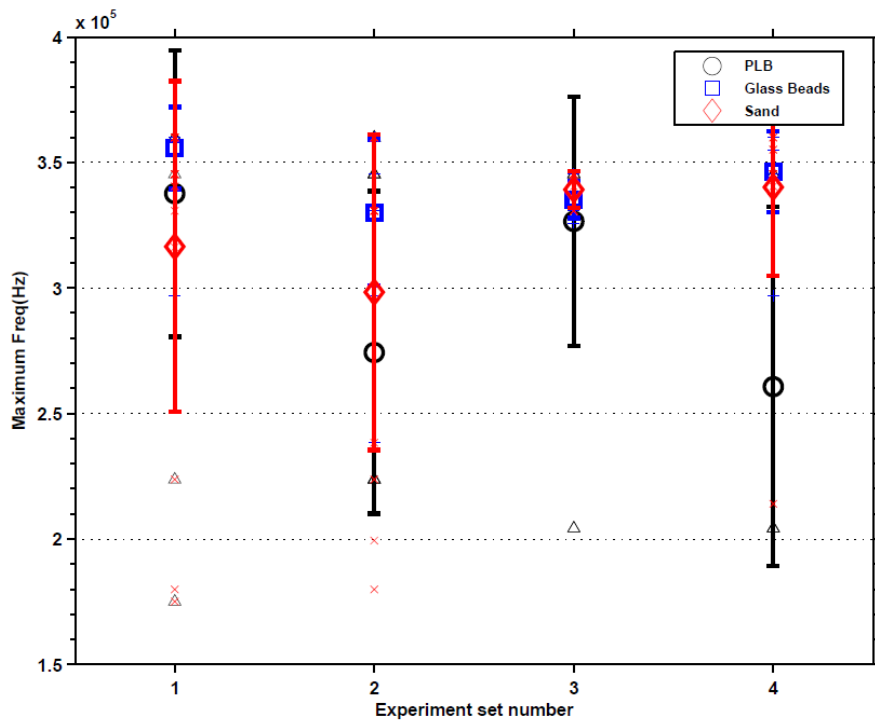

(a)
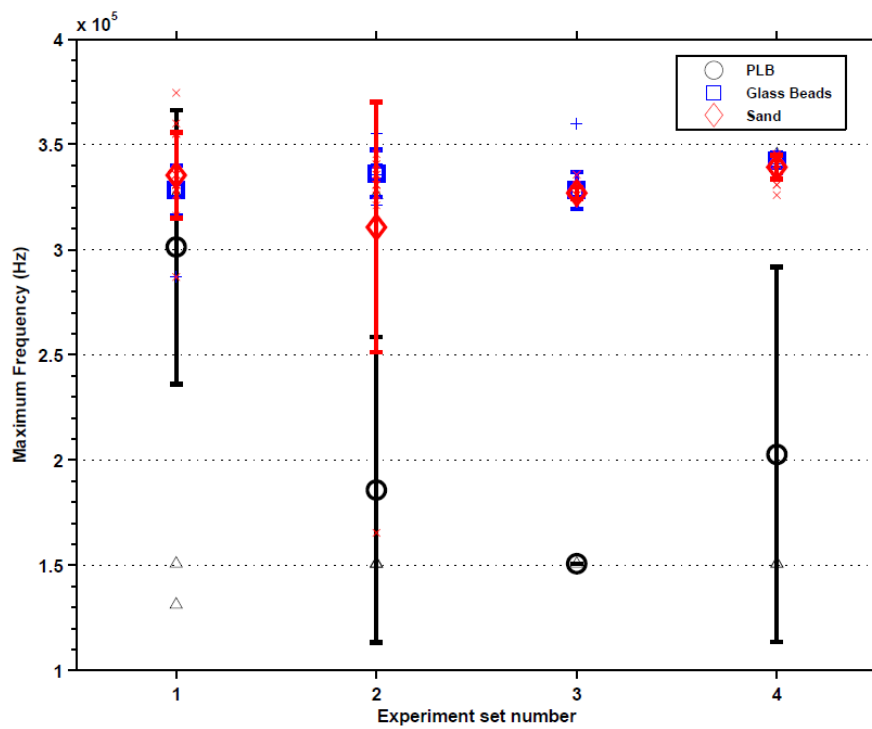
(b)

Figure C - 5: Variations in maximum Frequency of similar sized particle impacts populations with PLB in four experiments on mild steel target plate for (a) S1 & (b) S2.

C6. Frequency Centroid
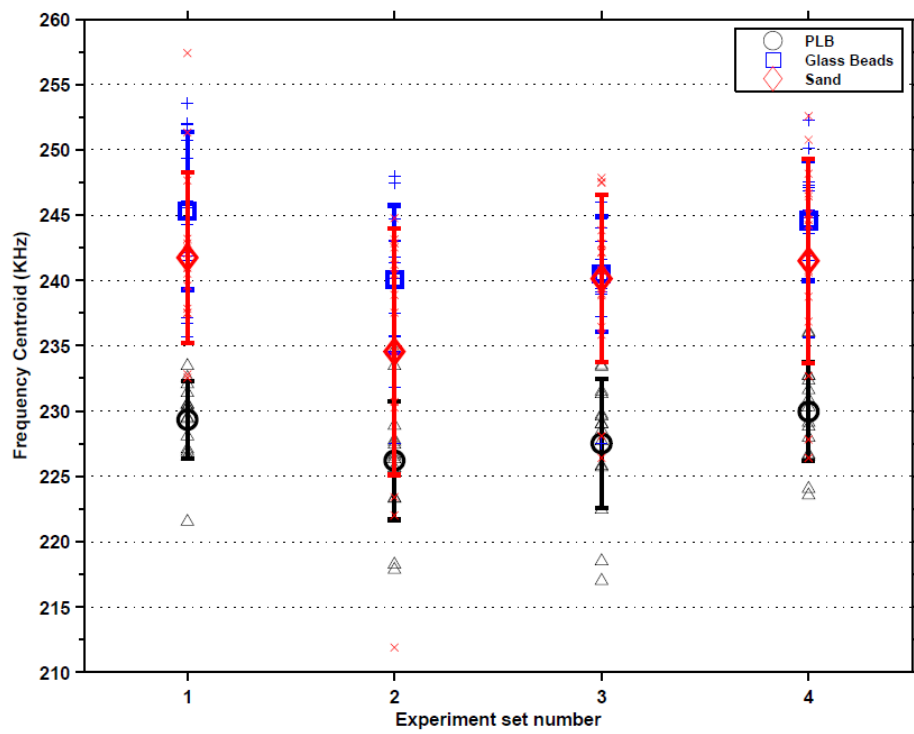
(a)
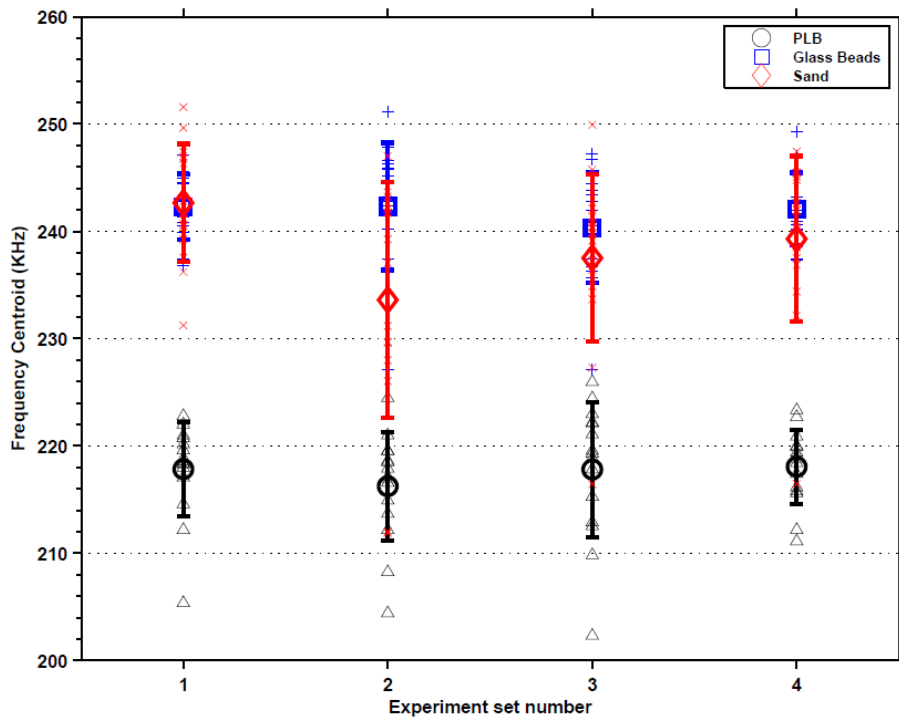
(b)

Figure C - 6: Variations in Frequency centroid of similar sized particle impacts populations with PLB in four experiments on mild steel target plate for (a) S1 & (b) S2.

Appendix D Standard AE parameter analysis of single bubble signals

D1. Maximum Amplitude
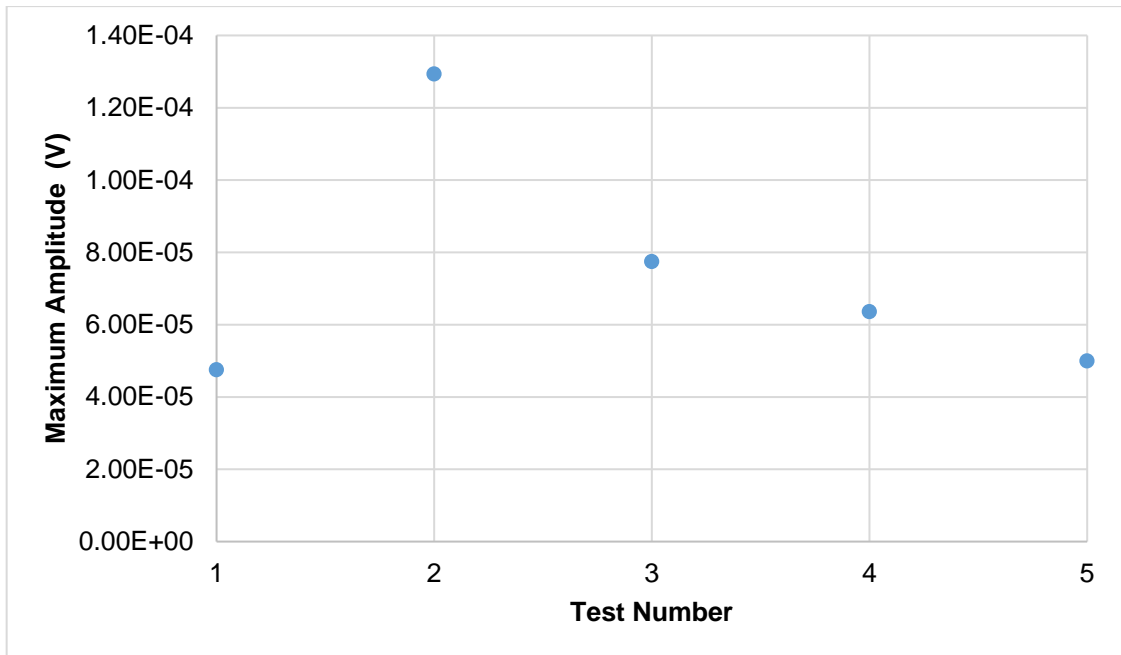
(a)
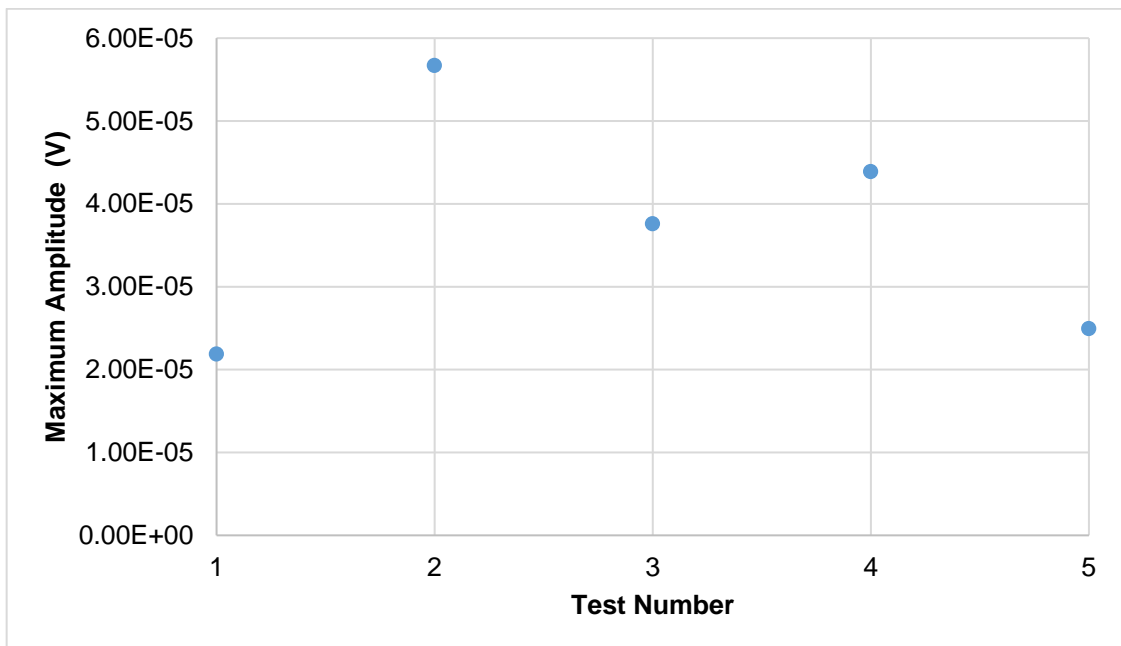
(b)

Figure D - 1: Maximum amplitude of single bubble signals at (a) S1 & (b) S2.

D2. Event Duration
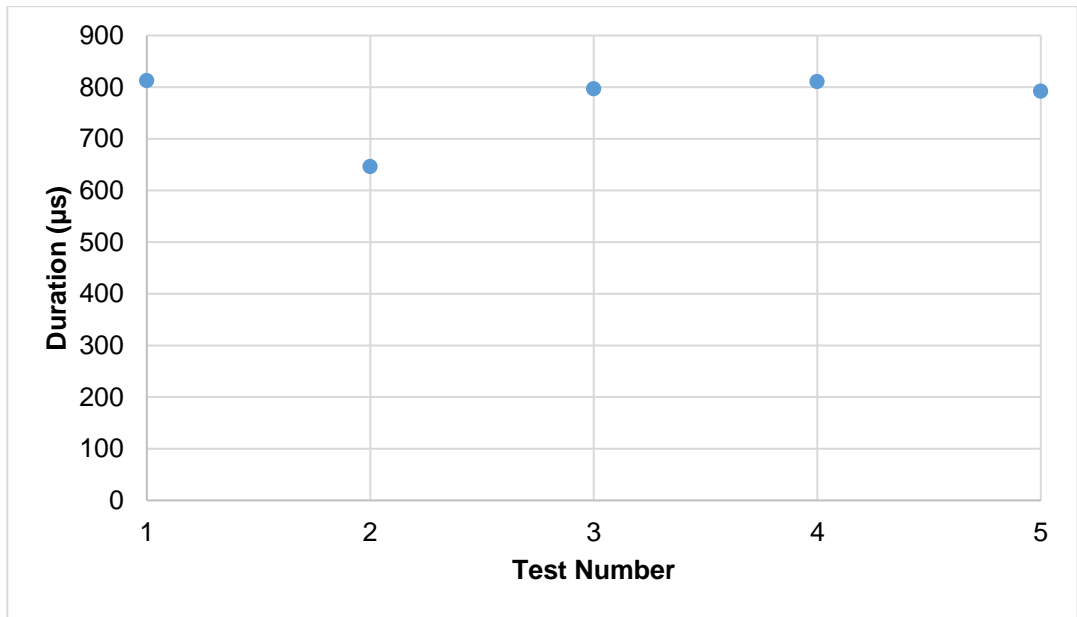
(a)
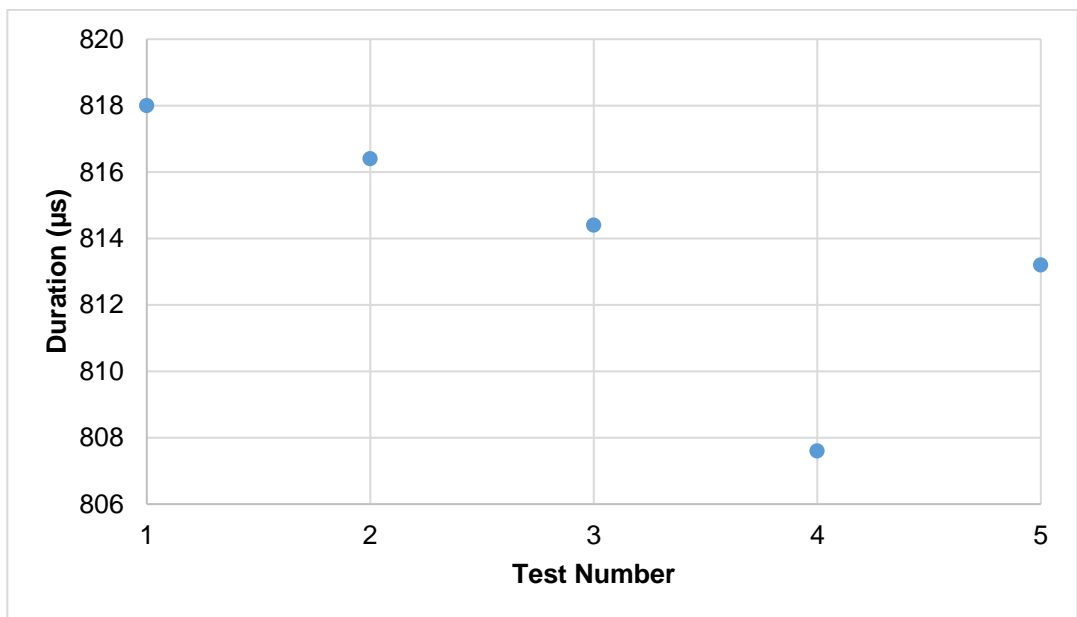
(b)

Figure D - 2: Event duration for single bubble signals at (a) S1 & (b) S2.

D3. Rise Time
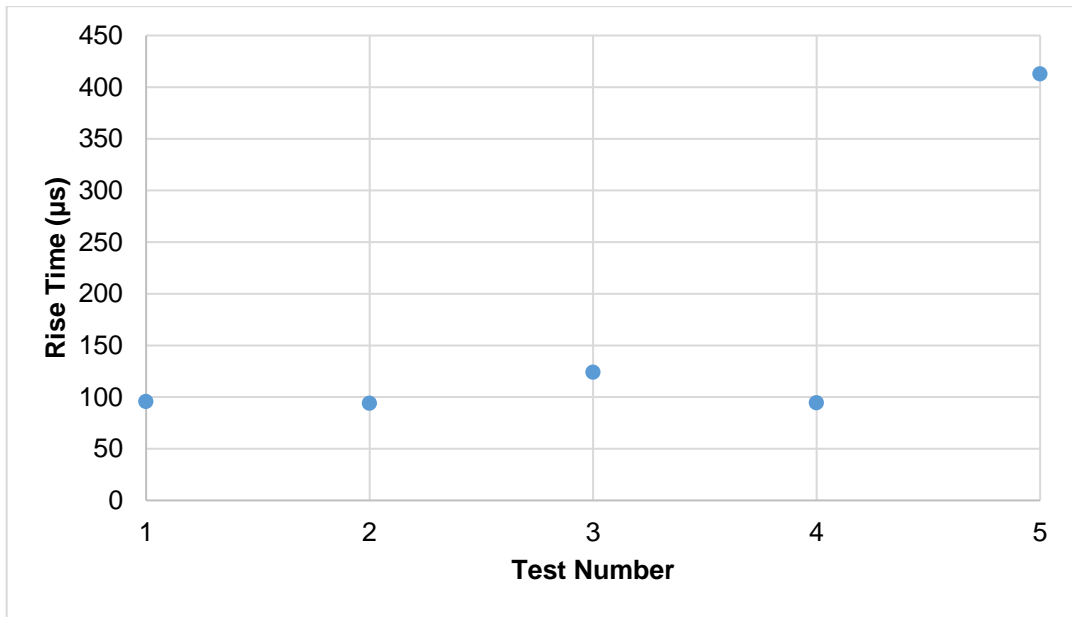
(a)
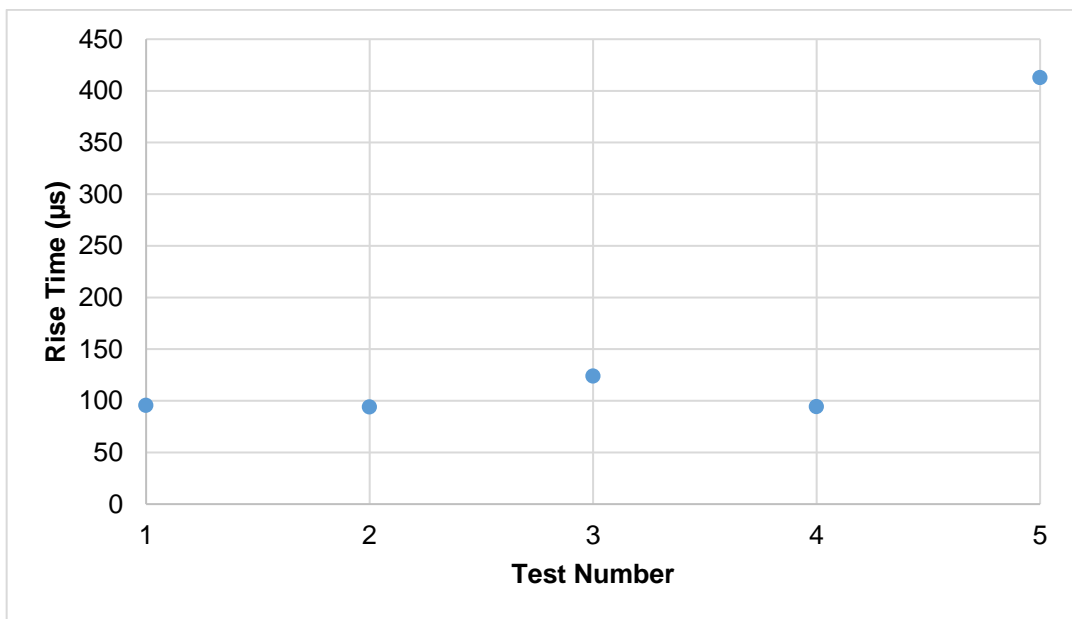
(b)

Figure D - 3: Rise time of single bubble signals at (a) S1 & (b) S2.

D4. Event Energy
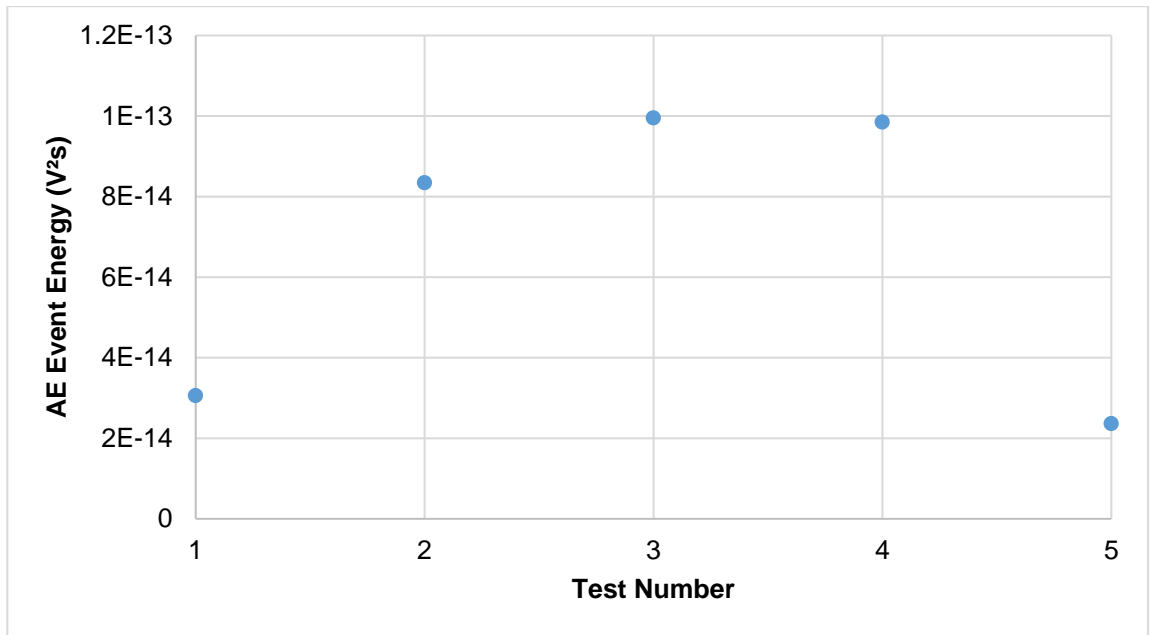
(a)
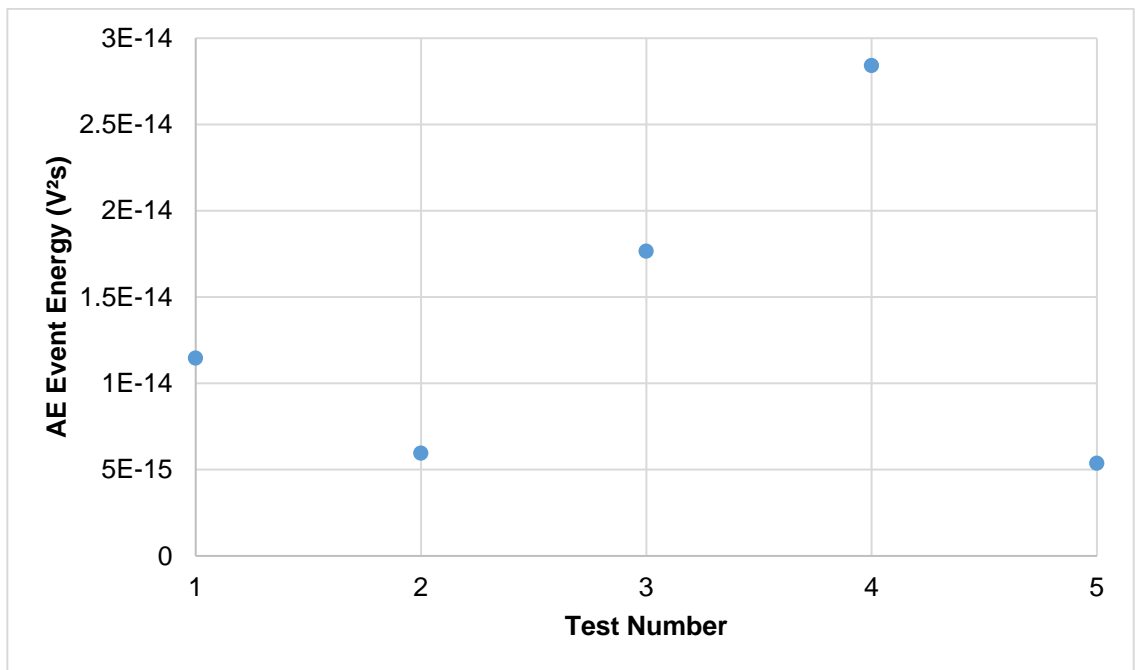
(b)

Figure D - 4: AE event energy for single bubble signals at (a) S1 & (b) S2.

D5. Spectral centroid
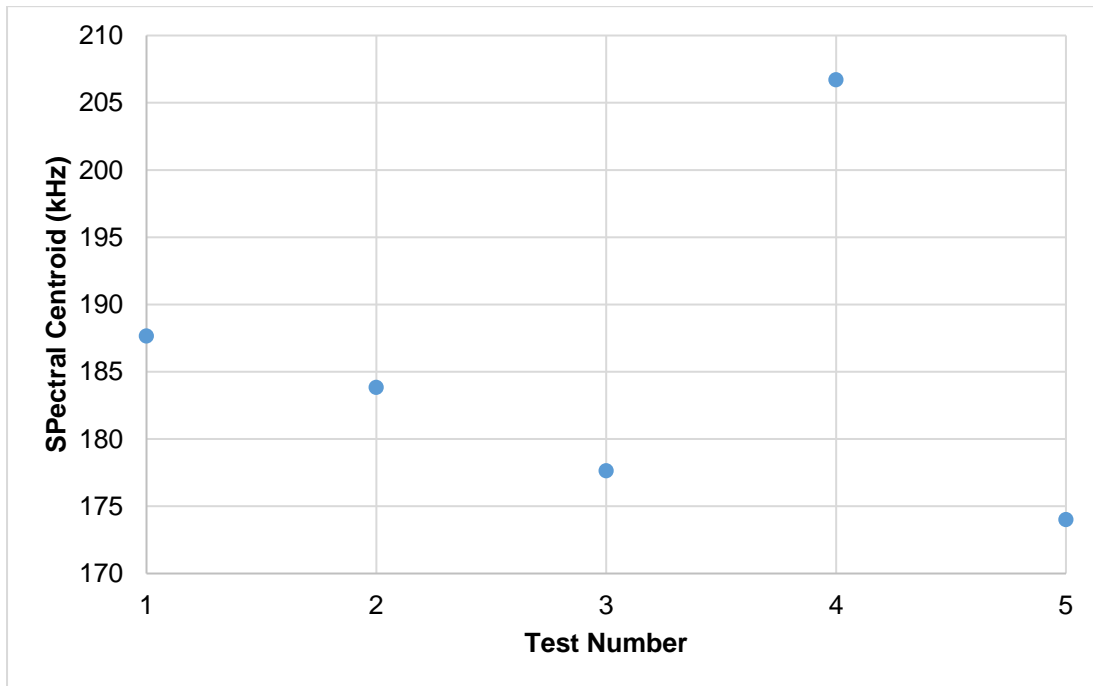
(a)
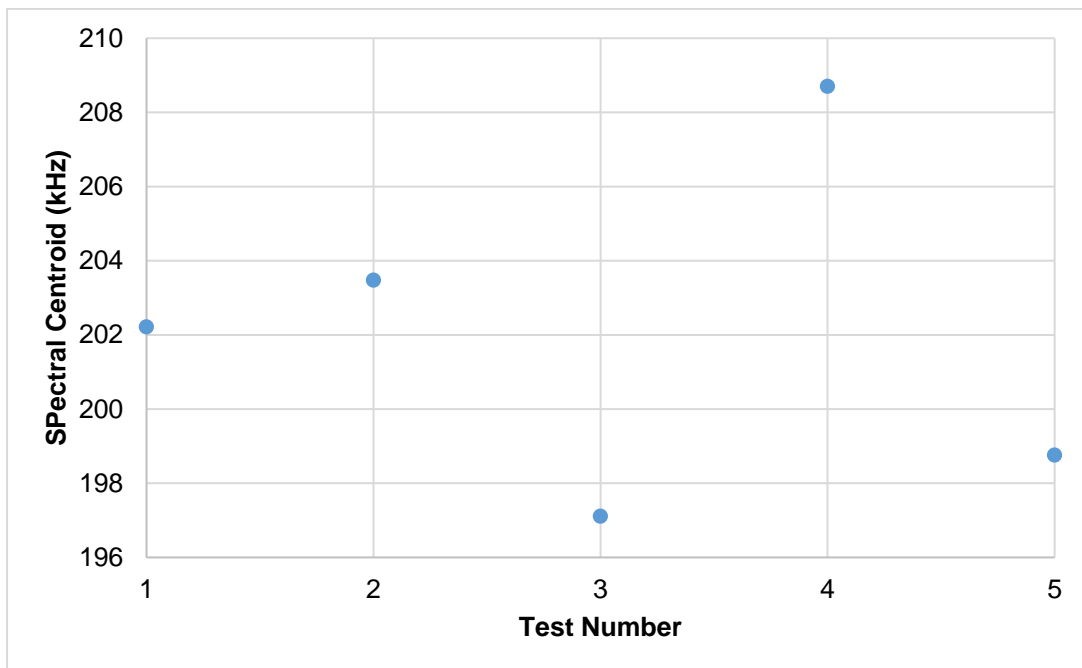
(b)

Figure D - 5: Spectral centroid of single bubble signals at (a) S1 & (b) S2.

D6. Maximum PSD
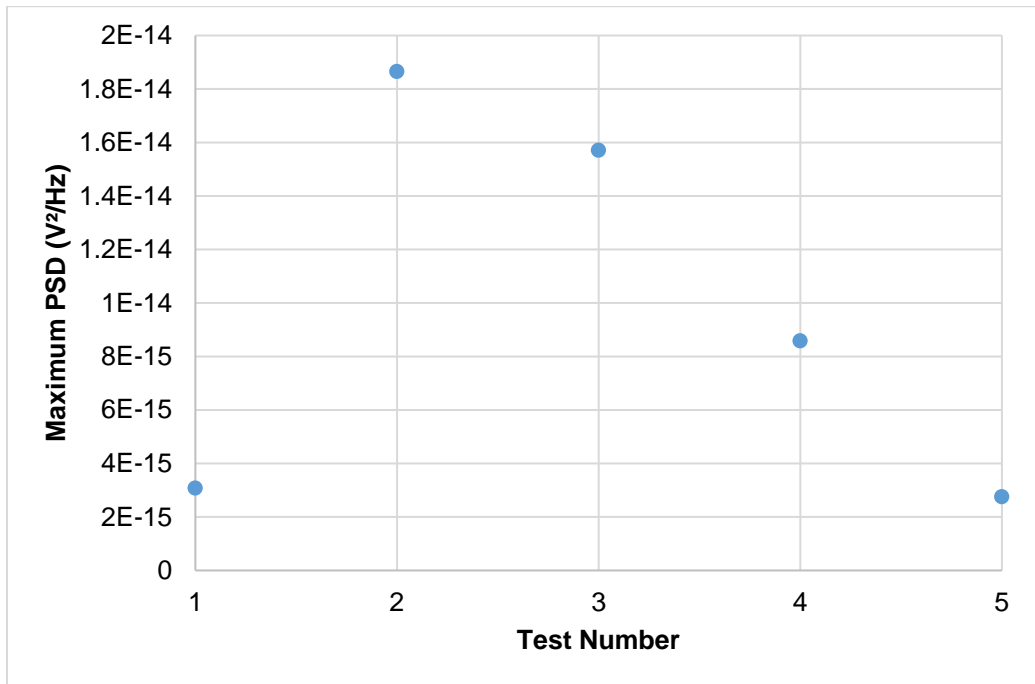
(a)
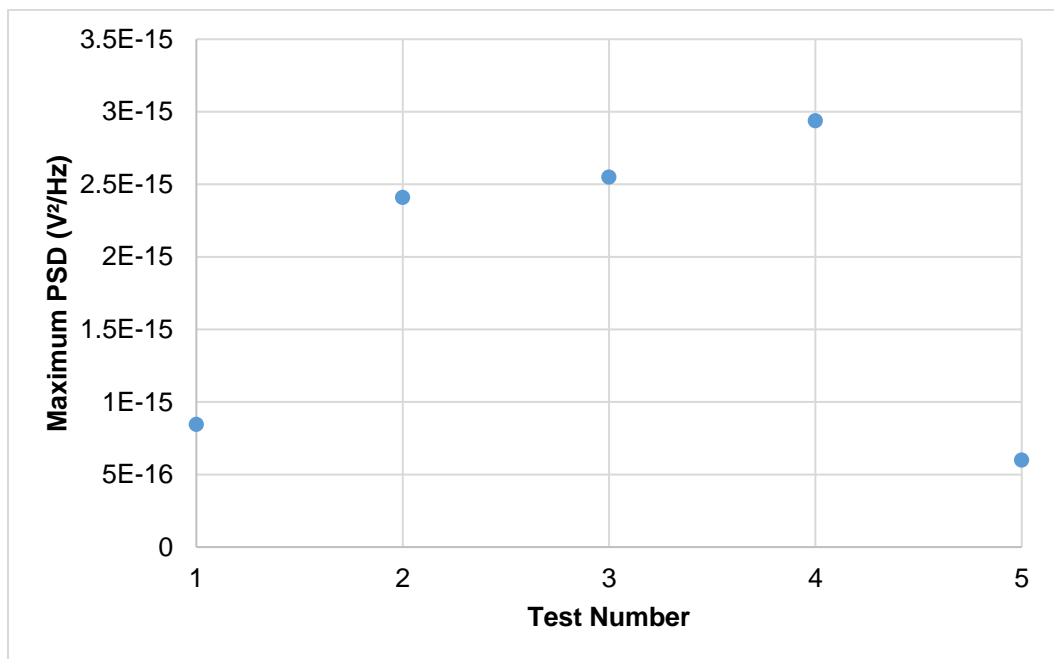
(b)

Figure D - 6: Maximum PSD of single bubble signals at (a) S1 & (b) S2.

D7. Maximum PSD Frequeny
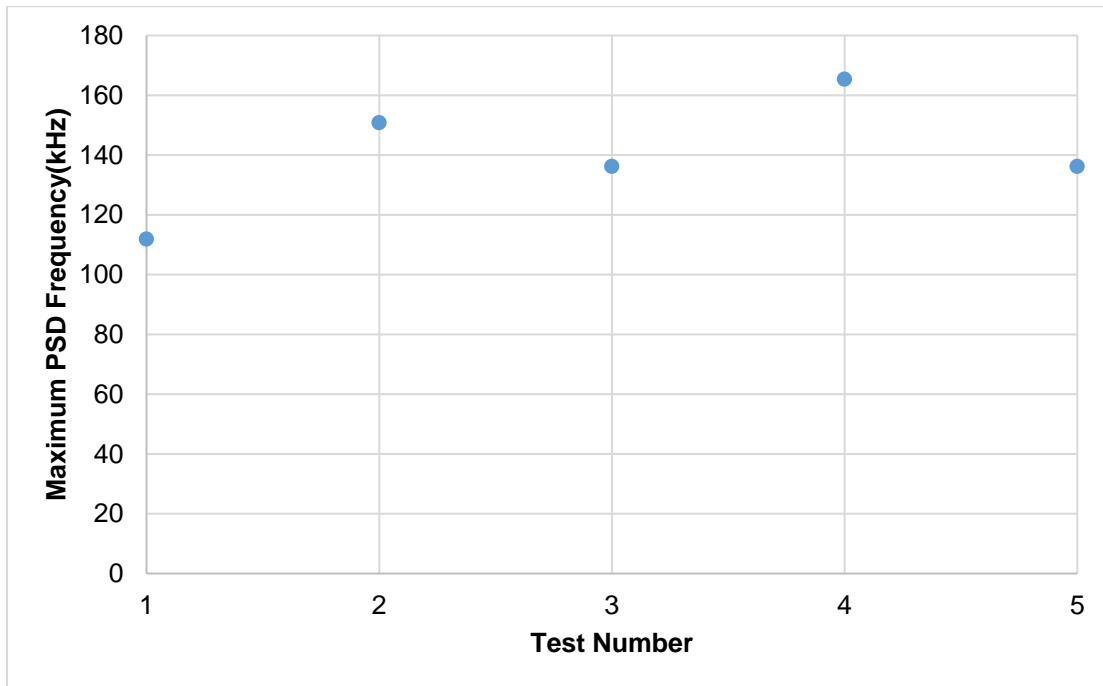
(a)
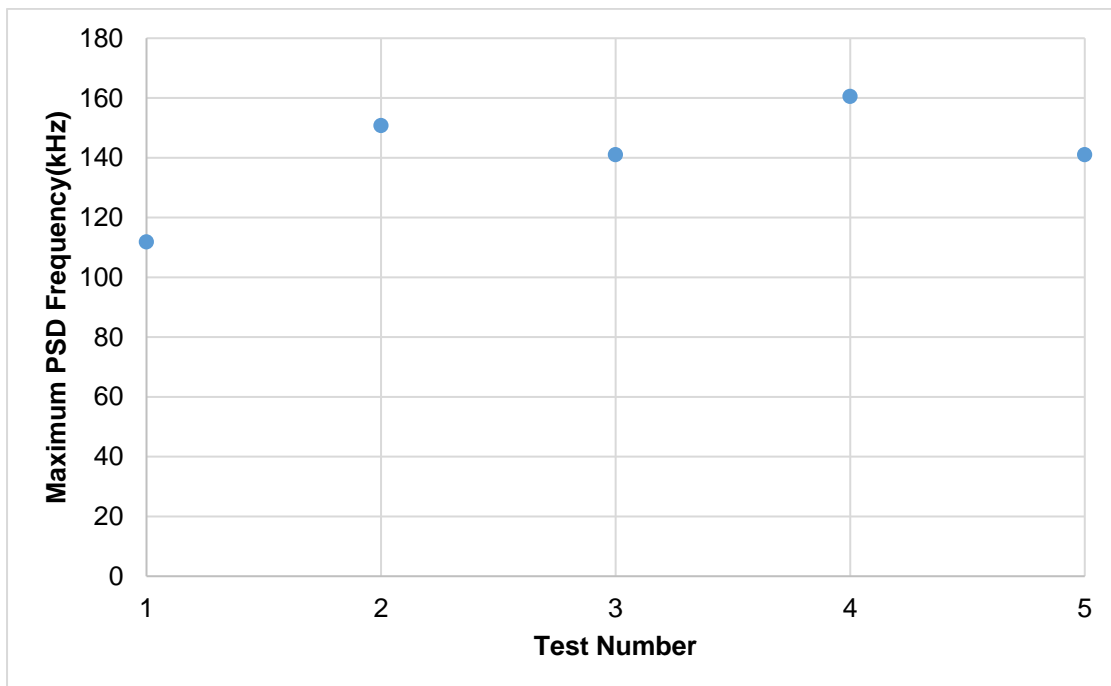
(b)

Figure D - 7: Maximum PSD frequency of single bubble signals at (a) S1 & (b) S2

Appendix E Standard AE parameter analysis of single particle impacts on fixed target plate in air

E1. Maximum Amplitude
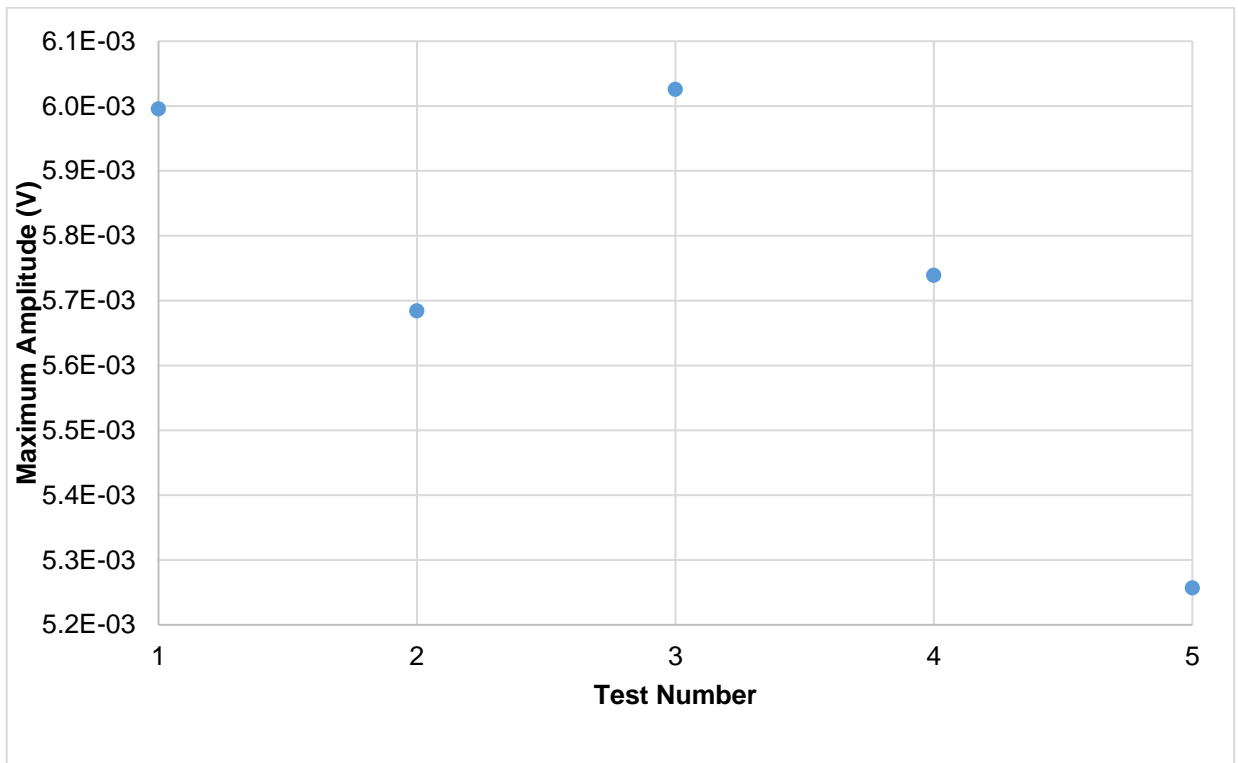
(a)
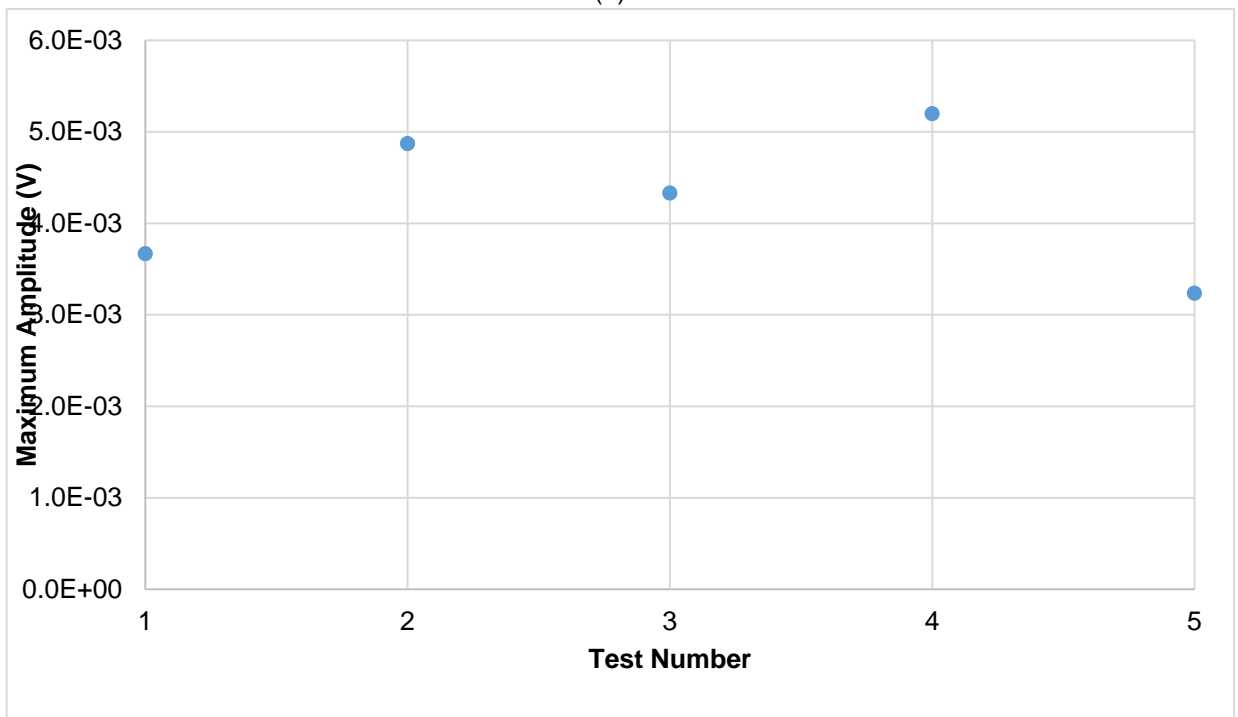
(b)

Figure E - 1: Maximum amplitude of single sand particle impact on target plate signals at (a) S1 & (b) S2

E2. Event Duration
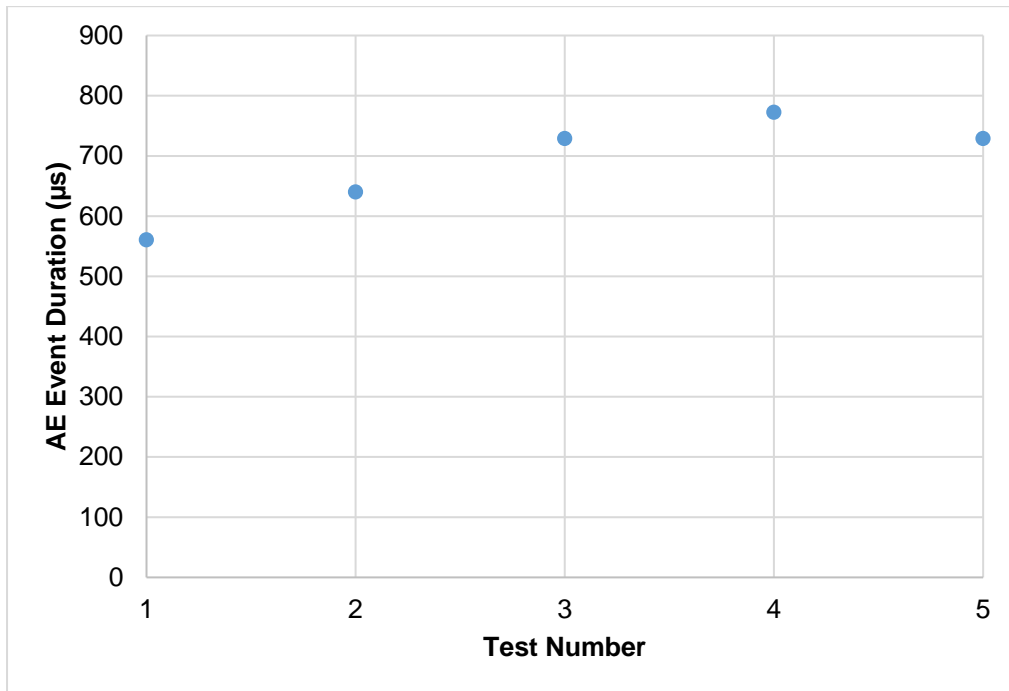
(a)
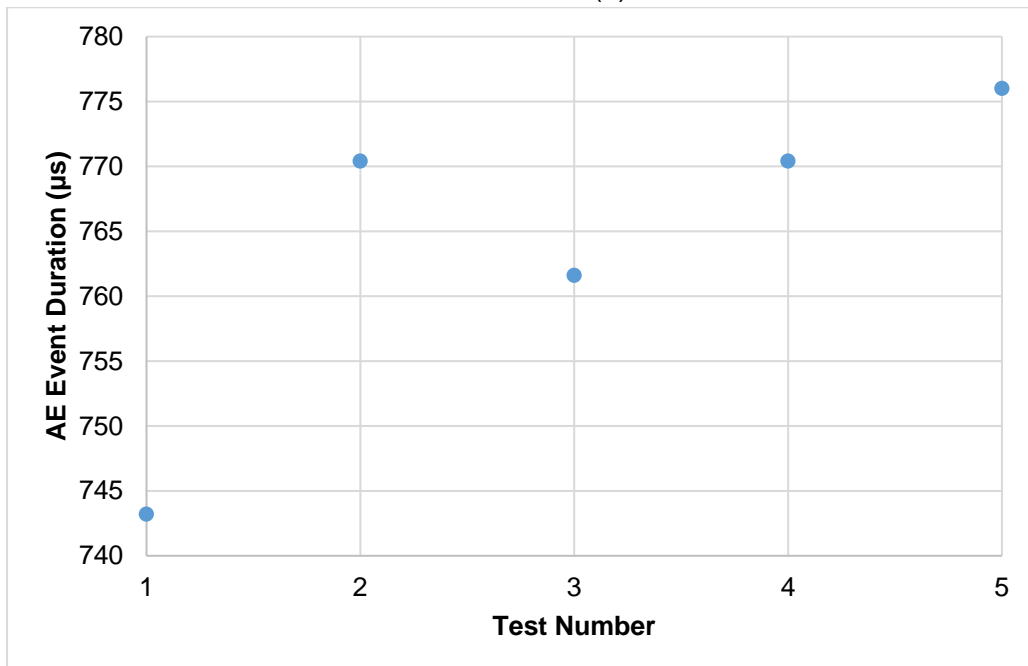
(b)

Figure E - 2: Event durations of AE records for single sand particle impacts on fixed target plate in air at (a) S1 & (b) S2.

E3. Rise Time
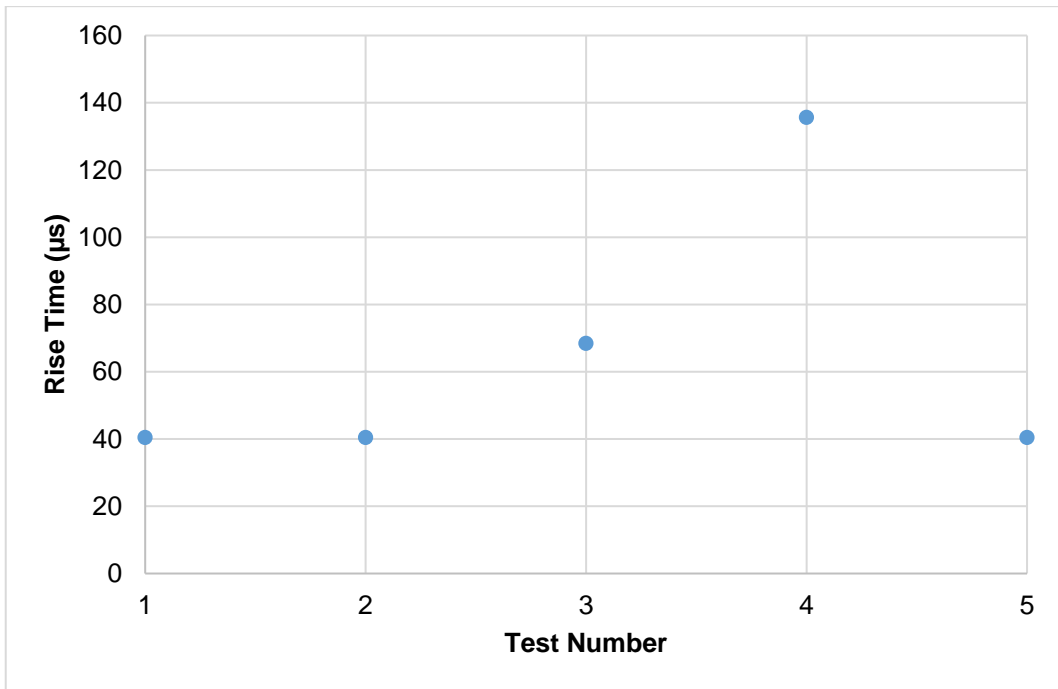
(a)
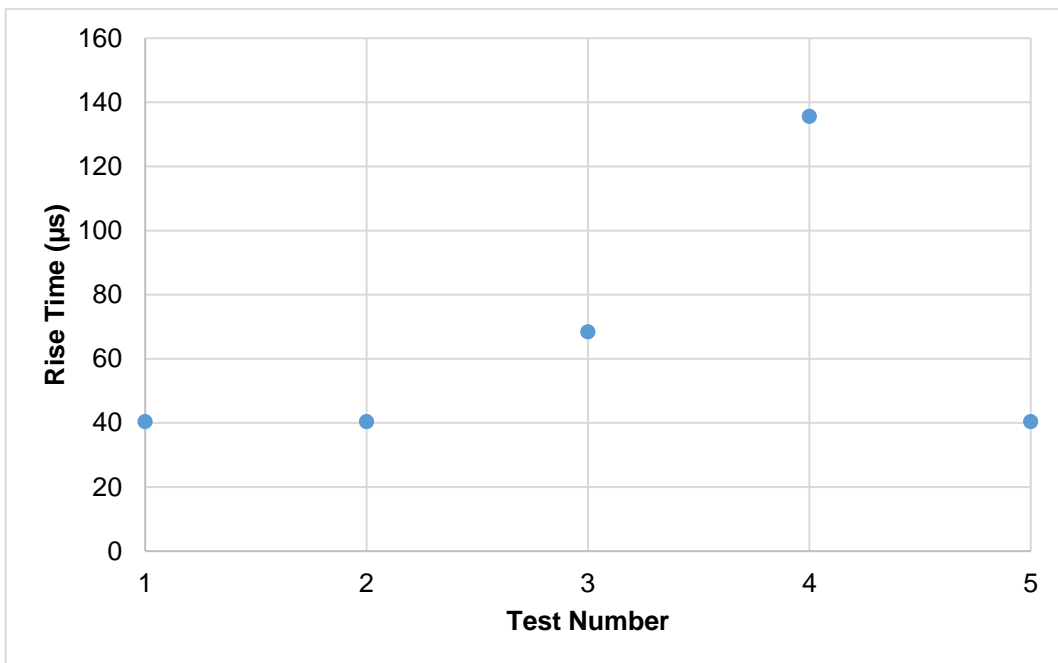
(b)

Figure E - 3: Rise times of AE records for single sand particle impacts on fixed target plate in air at (a) S1 & (b) S2.

E4. Event Energy
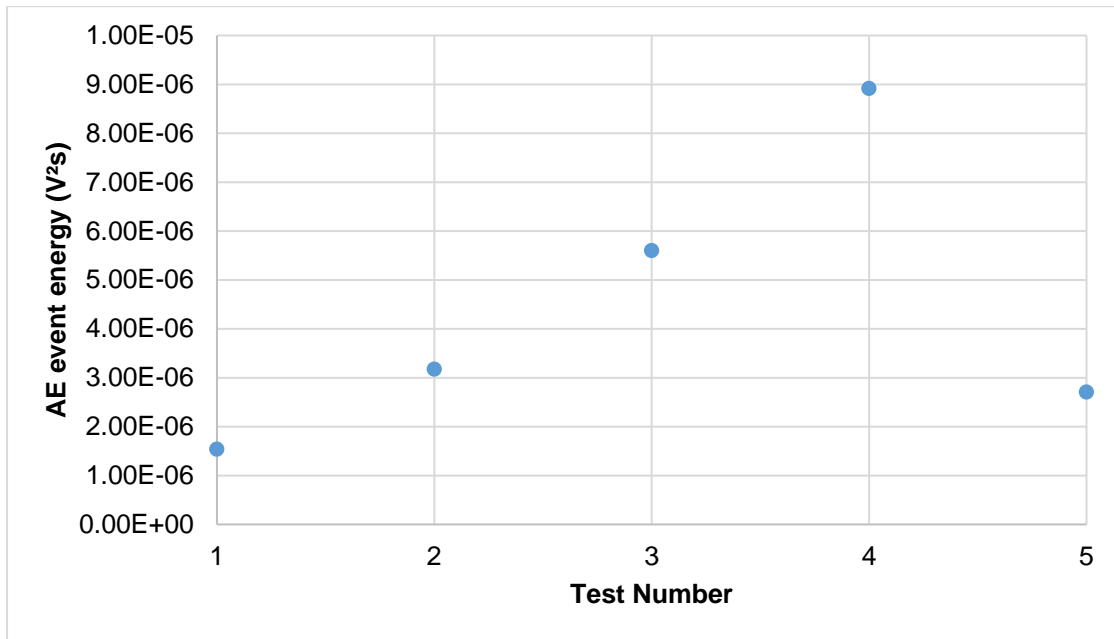
(a)
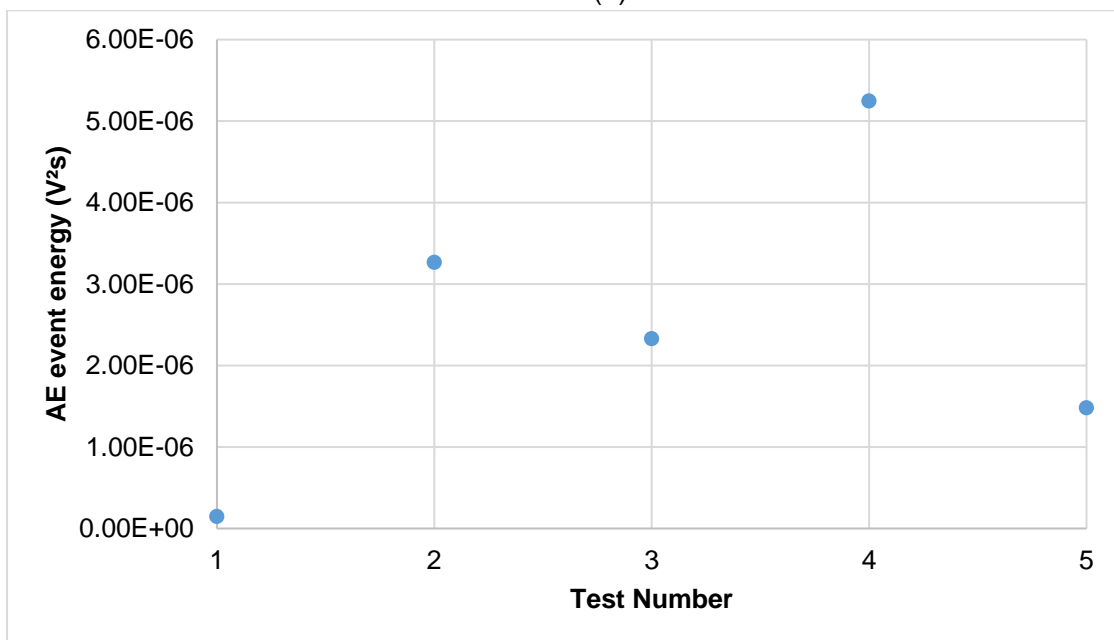
(b)

Figure E - 4: Event energy of AE records for single sand particle impacts on fixed target plate in air at (a) S1 & (b) S2.

E5. Spectral centroid
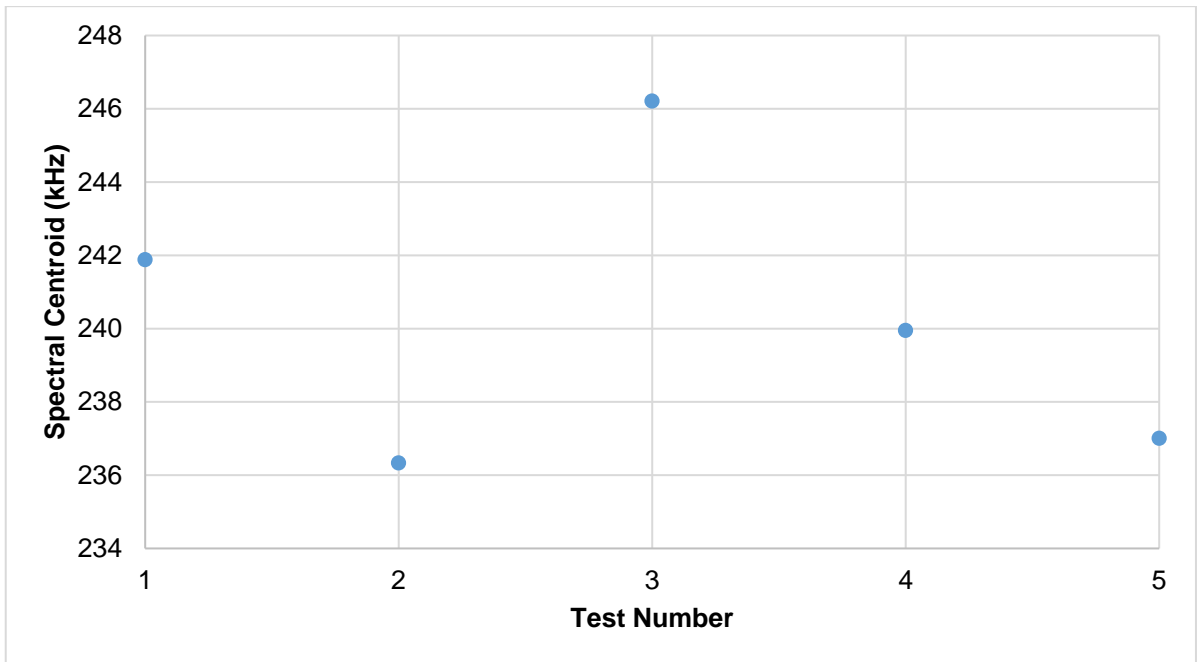
(a)
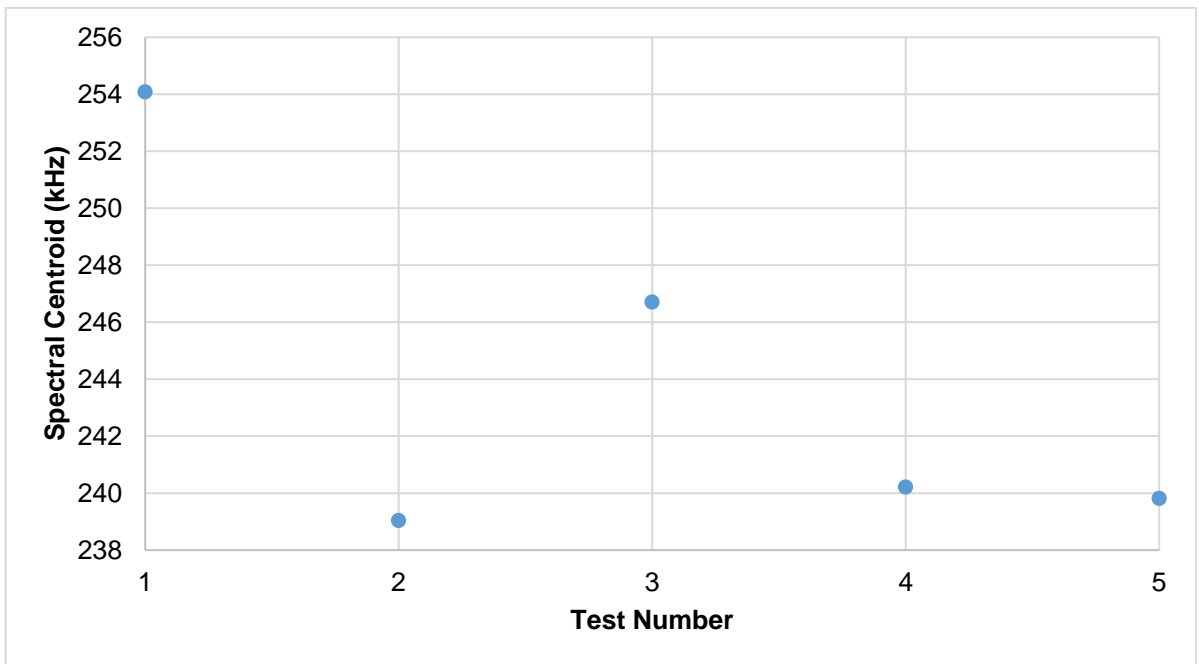
(b)

Figure E - 5: Spectral centroid of single sand particle impact on target plate signals at (a) S1 & (b) S2.

E6. Maximum PSD
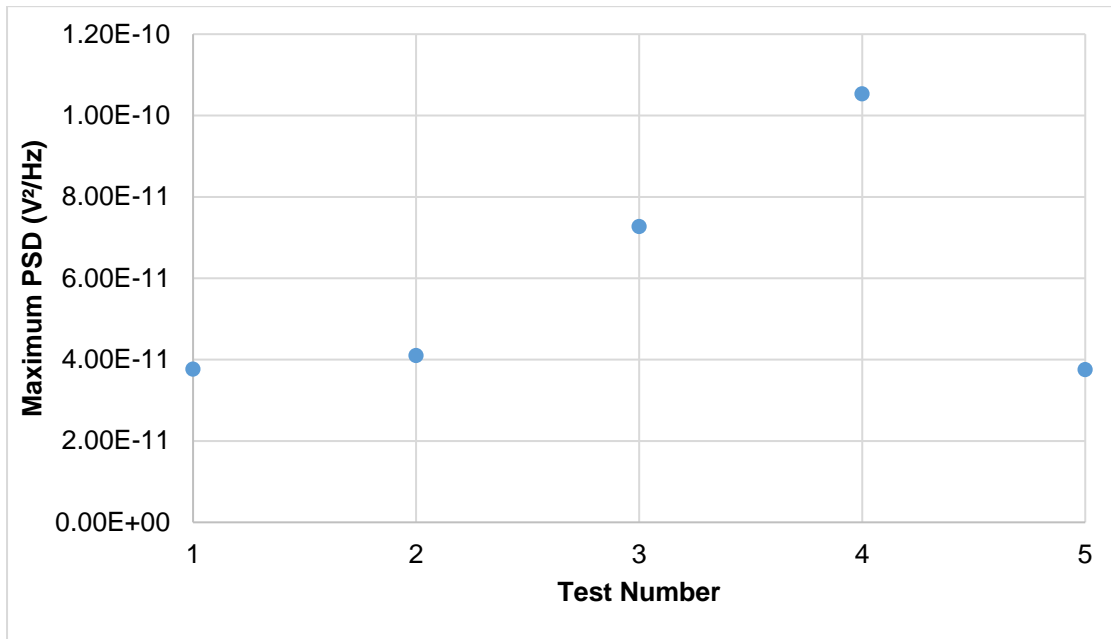
(a)
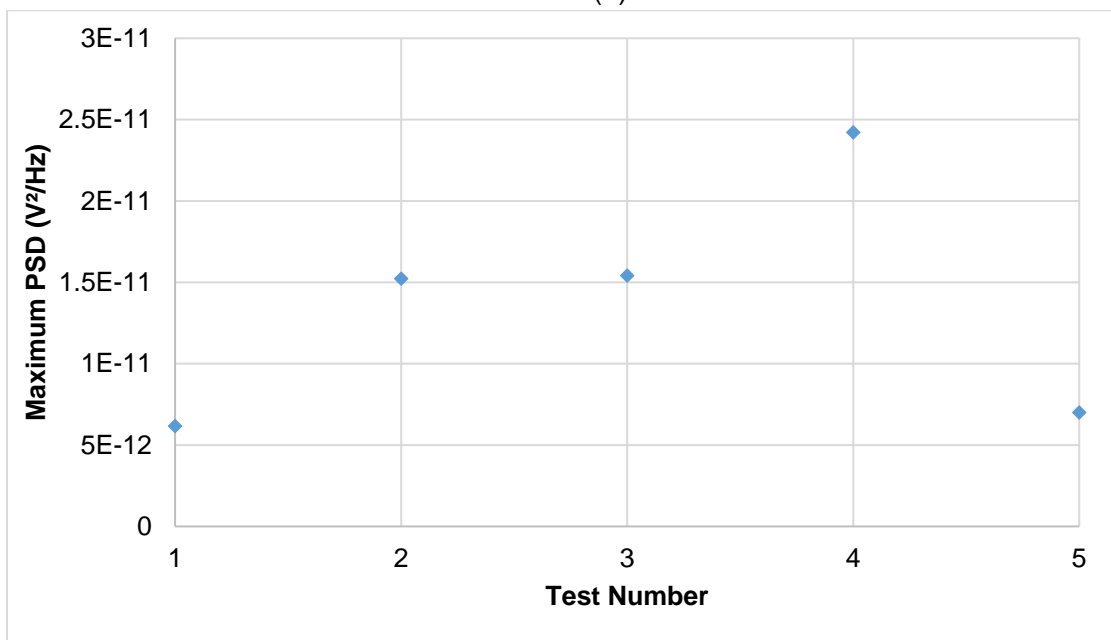
(b)

Figure E - 6: Maximum PSD of single sand particle impacts on target plate signals at (a) S1 & (b) S2.

E7. Maximum PSD Frequency
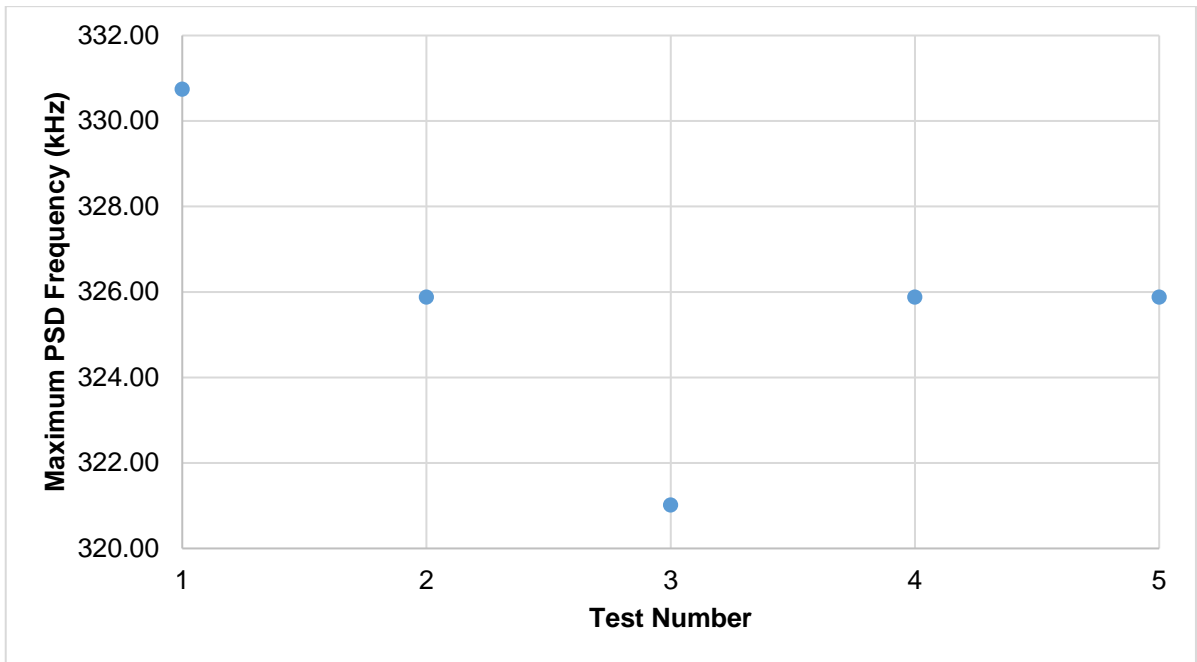
(a)
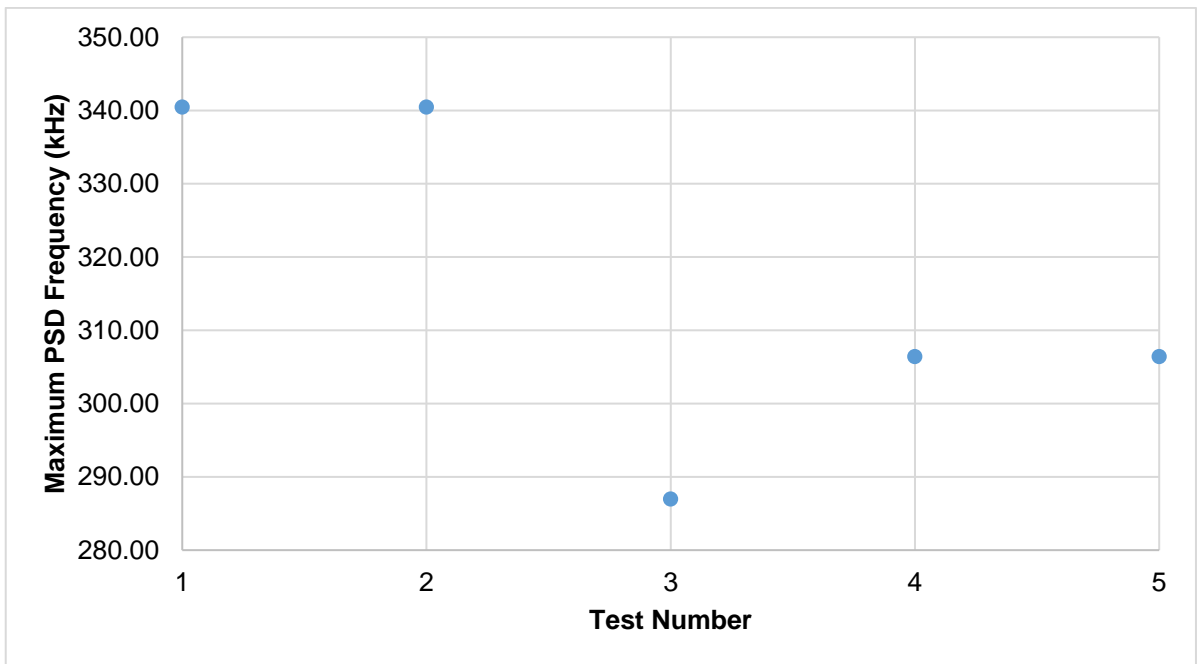
(b)

Figure E - 7: Maximum PSD Frequency of AE records for single sand particle impacts on fixed target plate at (a) S1 & (b) S2.

References

1. Hii NC, Tan CK, Wilcox SJ, Chong ZS. An investigation of the generation of Acoustic Emission from the flow of particulate solids in pipelines. Powder Technol. 2013;243:120–9.

2. MYLVAGANAM S. Some Applications of Acoustic Emission in Particle Science and Technology. Part Sci Technol. 2003 Jul 6;21(3):293–301.

3. Villa Briongos J, Aragón JM, Palancar MC, Briongos JV, Aragón JM, Palancar MC. Fluidised bed dynamics diagnosis from measurements of low-frequency out-bed passive acoustic emissions. Powder Technol. 2006;162(2):145–56.

4. Tsujimoto H, Yokoyama T, Huang CC, Sekiguchi I. Monitoring particle fluidization in a fluidized bed granulator with an acoustic emission sensor. Powder Technol. 2000;113(1–2):88–96.

5. Ren C, Wang J, Song D, Jiang B, Liao Z, Yang Y. Determination of particle size distribution by multi-scale analysis of acoustic emission signals in gas-solid fluidized bed. J Zhejiang Univ Sci A. 2011 Apr 20;12(4):260–7.

6. Carson G, Mulholland a. J, Nordon a., Tramontana M, Gachagan a., Hayward G. Particle sizing using passive ultrasonic measurement of particle-wall impact vibrations. J Sound Vib. 2008;317(1–2):142–57.

7. Hou R, Hunt a., Williams R a. Acoustic monitoring of pipeline flows: Particulate slurries. Powder Technol. 1999;106(1–2):30–6.

8. WR Boyd J, Varley J. The uses of passive measurement of acoustic emissions from chemical engineering processes. Chem Eng Sci. 2001;56(5):1749–67.

9. Odigie M, Shirazi SA, McLaury BS, Cremaschi S. Acoustic Monitor Threshold Limits for Sand Detection in Multiphase Flow Production System. SPE Int Conf Exhib Oilf Corros. 2012;154378:1–13.

10. Albion K, Briens L, Briens C, Berruti F. Flow regime determination in horizontal pneumatic transport of fine powders using non-intrusive acoustic probes. Powder Technol. 2007;172(3):157–66.

11. Folkestad T, Mylvaganam KS (Michelsen IB (NO)). Acoustic measurements detect sand in North Sea flow lines. Oil Gas Journal; 1990 Aug 27.

12. Andersen M. System and method for passive acoustic monitoring of fluids and solids in pipe flow. US Pat App 13/202,158. 2010;

13. Buttle DJ, Scruby CB. Characterization of particle impact by quantitative acoustic emission. Wear. 1990;137(1):63–90.

14. Petersen TB. Acoustic Emission From Impacts of Rigid Bodies. J Acoust Emiss.

2009;27:98–113.

15. Droubi MG, Reuben RL, White G. Acoustic emission monitoring of abrasive particle impacts on carbon steel. Proc Inst Mech Eng Part E J Process Mech Eng. 2012;226(3):187–204.

16. Droubi MG. Monitoring particle impact energy using acoustic emission technique. PhD[Dissertation].Edinburgh:Heriot-Watt University;2013.

17. Duclos J, Reuben R, Steel J. A study of particle impacts in fluid flow using acoustic emission. Proc COMADEM, Cambridge. 2004.

18. Ukpai JI, Barker R, Hu X, Neville A. Determination of particle impacts and impact energy in the erosion of X65 carbon steel using acoustic emission technique. Tribol Int. 2013;65:161–70.

19. Ferrer F, Idrissi H, Mazille H. On the potential of acoustic emission for the characterization and understanding of mechanical damaging during abrasion–corrosion processes. Wear. 1999.

20. Petersen TB. Acoustic emission from impact of rigid bodies. JAE. 2009;27:98.

21. Droubi MG, Reuben RL, White G. Statistical distribution models for monitoring acoustic emission (AE) energy of abrasive particle impacts on carbon steel. Mech Syst Signal Process. 2012;30:356–72.

22. Ukpai JI. Erosion-corrosion characterisation for pipeline materials using combined acoustic emission and electrochemical monitoring.PhD[Dissertation].Leeds: Institute of Engineering Thermofluids, Surfaces & Interfaces (iETSI) (University of Leeds); 2014.

23. Miinshiou H,Liang J,Peter KL,Charlie RB, Rodger S, Dwaine LK. Using Acoustic Emission in Fatigue and Fracture Materials Research. JOM-e [Internet]. 2012 [cited 2016 Jun 5]. Available from:
http://www.tms.org/pubs/journals/jom/9811/huang/huang-
9811.html?r=1&l=ri&fst=0

24. Miller RK, Hill EK, Moore PO. Nondestructive Testing Handbook: Acoustic emission testing. Third Edit. Vol 6. American Society for Nondestructive Testing; 2005.

25. Guidelines on use of acoustic emission technique (AET) on railway bridges. Research Designs and Standards Organisation [document on the internet]. 2009[cited 2016 Jun 5]. Available from:
http://www.rdso.indianrailways.gov.in/uploads/files/1296882731408-bs_104.pdf

26. Addali A. Monitoring gas void fraction in two-phase flow with acoustic emission. PhD[Dissertation].Cranfield: Cranfield University; 2010.

27. Husin S. An experimental investigation into the correlation between Acoustic

Emission (AE) and bubble dynamics. PhD[Dissertation].Cranfield: Cranfield University; 2011.

28. Grosse CU. Acoustic emission testing: basics for research - applications in civil engineering. New York: Springer; 2008.

29. Ding Y. Damage monitoring of carbon fibre reinforced composites using acoustic emission. PhD[Dissertation].Edinburgh:Heriot-Watt University; 2010.

30. El-Alej ME. Monitoring sand particle concentration in multiphase flow using acoustic emission technology. PhD[Dissertation].Cranfield: Cranfield University; 2014.

31. Alssayh MAA. Slug Velocity Measurement and Flow Regime Recognition Using Acoustic Emission Technology.PhD[Dissertation].Cranfield:Cranfield University; 2013.

32. Chowdhury NM. Theoretical analysis of acoustic emission signal propagation in fluid-filled pipes. Masters [Thesis].Toronto:Ryerson University; 2010.

33. Prosser WH, Gorman MR, Humes DH. Acoustic emission signals in thin plates produced by impact damage. J Acoust Emiss. 1999;17:29–36.

34. Beattie AG. Acoustic Emission Non -Destructive Testing of Structures using Source Location Techniques [Internet]. 2013. Available from: http://energy.sandia.gov/wp-content/gallery/uploads/SAND2013-7779BeattieAE-NDTmonograph1.pdf

35. Muravin B. Acoustic Emission Method.Acoustic Emission Portal at Muravin.com [document on the Internet]. 2013 [cited 2016 Jun 5]. Available from: http://www.muravin.com/ae/

36. What is Signal Conditioning?.Developer Zone. National Instruments [document on the Internet]; 2016 [cited 2016 Jun 5]. Available from: http://www.ni.com/white-paper/10630/en

37. Staras S. Acoustic Waves [document on the Internet]. Vilnius, Lithuania: Vilnius Gediminas Technical University; 2009 [cited 2016 Jun 5]. Available from: http://www2.el.vgtu.lt/en/index.htm

38. Braile LW. Seismic Waves and the Slinky: A Guide for Teachers [document on the Internet]. Purdue University; 2010 [cited 2016 Jun 5]. Available from: http://web.ics.purdue.edu/~braile/edumod/slinky/slinky.htm

39. Hambric SA. Structural Acoustics Tutorial Part-1: Vibrations in structures. Acoust Today. 2006;(October):21–33.

40. Viktorov IA. Lamb Waves [document on the Internet]. University of Cincinnati; 2014 [cited 2016 Jun 5]. Available from: http://www.ase.uc.edu/~pnagy/ClassNotes/AEEM7028 Introduction to

Ultrasonics/part5.pdf

41. Jimenez N. Wave simulations [Internet]. Universitat Polytecnica de Valencia; 2015 [cited 2016 Jun 5]. Available from: http://www.nojigon.webs.upv.es/simulations.php

42. Waves Used in NDE. Waves Propagation Fundamentals [document in the Internet]. Iowa State University of Science and Technology; 2010 [cited 2016 Jun 5]. Available from: http://www.public.iastate.edu/~e_m.350/Waves in NDE 14.pdf

43. Aggelis DG, Matikas TE. Effect of plate wave dispersion on the acoustic emission parameters in metals. Comput Struct. 2012;98:17–22.

44. Rindorf HJ. Acoustic Emission Source Location In Theory and In Practice. Bruel & Kajer Technical Review. Bruel & Kajer; 1981.

45. Kazys R, Sanderson R. Condition monitoring of large oil and chemical storage tanks using guided waves. In: Proceedings of BINDT Annual Conference; 2004 Sep 14-16; Torquay. Cambridge: TWI Ltd.; 2004. Available from: http://www.twi.co.uk/technical-knowledge/published-papers/condition-monitoring-of-large-oil-and-chemical-storage-tanks-using-guided-waves-september-2004/

46. Sansalone M, Carino N. Transient impact response of thick circular plates. J Res Natl. 1987;92(6):355 - 367.

47. AE Sources. NDT Resource Center [document on the Internet]. Iowa State University of Science and Technology; 2001 [cited 2016 Jun 5]. Available from: http://www.ndt-ed.org/EducationResources/CommunityCollege/Other Methods/AE/AE_Theory-Sources.htm

48. Swindlehurst W. Acoustic emission-1 Introduction. Non-Destructive Test. 1973;6(3):152–8.

49. Scruby CB. An introduction to acoustic emission. J Phys E. 1987;20:946.

50. Hutchings I. Energy absorbed by elastic waves during plastic impact. J Phys D Appl Phys. 1979;12(11):1819-1824.

51. Hutchings I. A model for the erosion of metals by spherical particles at normal incidence. Wear. 1981;70(3):269-281.

52. Hunter S. Energy absorbed by elastic waves during impact. J Mech Phys Solids. 1957;5(3):162-171.

53. Reed J. Energy losses due to elastic wave propagation during an elastic impact. J Phys D Appl Phys. 1985;18(12):2329-2337.

54. Wu C-Y, Li L-Y, Thornton C. Energy dissipation during normal impact of elastic and elastic–plastic spheres. Int J Impact Eng. 2005 Dec;32(1–4):593–604.

55. Pecorari C. Characterizing Particle Flow by Acoustic Emission. J Nondestruct

Eval. 2013;32(1):104–11.

56.   Bragg W. The world of sound. BoD-Books on Demand. 2013.

57.   Minnaert M. XVI. On musical air-bubbles and the sounds of running water. London, Edinburgh, Dublin Philos Mag J Sci. 1933;16(104):235–48.

58.   Husin S, Mba D. Acoustic emission of a single bubble activities. In: Proceedings of the World Congress on Engineering 2010 Vol II. 2010.

59.   Cartwright J. Bubbles never forget. Vol. 2013. Bristol BS1 6HG, UK: IOP Publishing; 2006.

60.   Strasberg M. Gas bubbles as sources of sound in liquids. J Acoust Soc Am. 1956; 28(1):20-26.

61.   Manasseh R, Riboux G, Risso F. Sound generation on bubble coalescence following detachment. Int J Multiph Flow. 2008;34(10):938–49.

62.   Deane G, Czerski H. A mechanism stimulating sound production from air bubbles released from a nozzle. J Acoust Soc. 2008; 123(6): EL126 - EL132.

63.   Lamb H. Hydrodynamics. Cambridge: The University Press; 1914.

64.   Pandit A, Varley J, Thorpe R, Davidson J. Measurement of bubble size distribution: an acoustic technique. Chem Eng. 1992; 47(5):1079-1089.

65.   Leighton T. The acoustic bubble. London: Academic Press. 2012.

66.   Kracht W. Using sound to study bubble coalescence. science J of colloid and interface.2009;332(1):237-245.

67.   Ross DR. Mechanics of underwater noise. Oxford:Pergamon. 2013.

68.   Farhat M, Obreschkow D, Kobel P, Dorsaz N, De Bosset A. Interaction of cavitation bubble with a spherical free surface. In: Sixth International Symposium on Cavitation (CAV2006); 2006 Sep 11-15; Wageningen, The Netherlands. The Netehrlands:CAV2006; 2006. Available from : https://infoscience.epfl.ch/record/90713

69.   de Bosset A, Obreschkow D, Kobel P, Dorsaz N, Farhat M. Direct effects of gravity on cavitation bubble collapse. In: 58th International Astronautical Congress(IAC-2007); 2007 Sep 24-28; Hyderabad, India. NY:USA: Curran Associates Inc;2008. Available from : https://infoscience.epfl.ch/record/162238/files/IAC2007_Paper_v11.pdf

70.   Benjamin T, Ellis A. The collapse of cavitation bubbles and the pressures thereby produced against solid boundaries.Trans R.1966; 260(110):221-240.

71.   Kloeppel JE. Scientists measure energy dissipation in a single cavitating bubble. Phys Sci. 2002;22(3).

72.   Shangguan H, Casperson L, Prahl S. Pressure impulses during microsecond laser ablation. Appl Opt. 1997; 36(34): 9034-9041.

73. Divoux T, Vidal V, Melo F, Géminard J-C. Acoustic emission associated with the bursting of a gas bubble at the free surface of a non-Newtonian fluid. Phys Rev E. 2008;77(5):56310.

74. AE Signal Features. NDT Resource Center [document on the Internet]. Iowa State University of Science and Technology; 2001 [cited 2016 Jun 5]. Available from: http://www.ndt-ed.org/EducationResources/CommunityCollege/Other Methods/AE/AE_Signal Features.htm

75. Jeffers JRT, Browne M, Taylor M. Damage accumulation, fatigue and creep behaviour of vacuum mixed bone cement. Biomaterials. 2005;26(27):5532–41.

76. From Fourier Analysis to Wavelet Analysis [document on the Internet]. [cited 2016 Jul 20]. Available from: http://uk.mathworks.com/help/wavelet/gs/from-fourier-analysis-to-wavelet-analysis.html

77. Jiao J, He C, Wu B, Fei R, Wang X. Application of wavelet transform on modal acoustic emission source location in thin plates with one sensor. Int J Press Vessel Pip. 2004;81(5):427–31.

78. Dunegan HL. Modal analysis of acoustic emission signals. J Acoust Emiss. 1997;15:53–61.

79. Holford KM, Davies AW, Pullin R, Carter DC. Damage location in steel bridges by acoustic emission. J Intell Mater Syst Struct. 2001;12(8):567–76.

80. Ding Y, Reuben RL, Steel JA. A new method for waveform analysis for estimating AE wave arrival times using wavelet decomposition. NDT E Int. 2004;37(4):279–90.

81. Jeong H, Jang Y-S. Wavelet analysis of plate wave propagation in composite laminates. Compos Struct. 2000;49(4):443–50.

82. Hamstad MA, O'GALLAGHER A, Gary J. A wavelet transform applied to acoustic emission. J Acoust Emiss. 2002;20:39–61.

83. Surgeon M, Wevers M. One sensor linear location of acoustic emission events using plate wave theories. Mater Sci Eng A. 1999;265(1):254–61.

84. Hamstad MA. Acoustic emission signals generated by monopole (pencil lead break) versus dipole sources: finite element modeling and experiments. J Acoust Emiss. 2007;25:92–106.

85. Hamstad MA. Some Observations on Rayleigh Waves and Acoustic Emission in Thick Steel Plates. J Acoustic Emiss. 2009;27:114–36.

86. Hutton P. Detecting acoustic emission in the presence of hydraulic noise. Non-Destructive Test. 1969; 2(2):111-115.

87. Darling, J. & Johnston DN. The Use of Acoustic Emission for Condition Monitoring in High-pressure Hydraulic Pumps. In: EUROTECH Direct 91. 1991. p. 137–43.

88. Leighton TG, Fagan KJ, Field JE. Acoustic and photographic studies of injected bubbles. Eur J Phys. 1991 Mar 1;12(2):77–85.

89. Boyd JWR, Varley J. Acoustic emission measurement of low velocity plunging jets to monitor bubble size. Chem Eng J. 2004;97(1):11–25.

90. Sause M, Horn S. Simulation of acoustic emission in planar carbon fiber reinforced plastic specimens. J Nondestruct Eval. 2010; 29(2):123-142.

91. Sause M, Gribov A, Unwin A, Horn S. Pattern recognition approach to identify natural clusters of acoustic emission signals. Pattern Recognit Lett. 2012;33(1):17-23.

92. Anastassopoulos A, Philippidis T. Clustering methodology for the evaluation of acoustic emission from composites. J Acoust Emiss. 1995;30(2)-108.

93. Philippidis T, Nikolaidis V, Anastassopoulos A. Damage characterization of carbon/carbon laminates using neural network techniques on AE signals. NDT E Int. 1998;31(5):329-340.

94. Marec A, Thomas J, Guerjouma R El. Damage characterization of polymer-based composite materials: Multivariable analysis and wavelet transform for clustering acoustic emission data. Mech Syst signal. 2008; 22(6):1441-1464.

95. Li X, Ramirez C, Hines E, Leeson M. Pattern recognition of fiber-reinforced plastic failure mechanism using computational intelligence techniques. In: IEEE International Joint Conference on Neural Networks; 2008 Jun 1-8; Honkong,China. Institute of Electrical and Electronics Engineers (IEEE); 2008. Available from: http://ieeexplore.ieee.org/abstract/document/4634122/

96. Godin N, Huguet S, Gaertner R. Integration of the Kohonen's self-organising map and k-means algorithm for the segmentation of the AE data collected during tensile tests on cross-ply composites. NDT E Int. 2005;38(4):299-309.

97. Oliveira R De, Marques A. Health monitoring of FRP using acoustic emission and artificial neural networks. Comput Struct. 2008;86(3-5):367-373.

98. Vesanto J, Himberg J, Alhoniemi E. Self-organizing map in Matlab: the SOM Toolbox. In: Proceedings of the Matlab DSP Conference; 1999 Nov 16-17; Espoo, Finland.Availablefrom: http://citeseerx.ist.psu.edu/viewdoc/download?doi=10.1.1.97.179&rep=rep1&type=pdf

99. McCormick A, Nandi A. Classification of the rotating machine condition using artificial neural networks. Proceedings of the IMechE, Part C: Journal of Mechanical Engineering Science.1997;211(6).

100. Samanta B, Al-Balushi K. Use of time domain features for the neural network based fault diagnosis of a machine tool coolant system. , Part I. J Syst .

2001;215(3):199-207.

101. Samanta B, Al-Balushi K. Artificial neural network based fault diagnostics of rolling element bearings using time-domain features. Mech Syst Signal Process. 2003;17(2):317-328.

102. Dellomo M. Helicopter gearbox fault detection: a neural network based approach. J Vib Acoust. 1999; 121(3):265-272.

103. El-Ghamry M, Reuben R, Steel J. The development of automated pattern recognition and statistical feature isolation techniques for the diagnosis of reciprocating machinery faults using acoustic. Mech Syst Signal. 2003;17(4):805-823.

104. Scaglione L. Neural network application to particle impact noise detection. In : IEEE International Conference on Neural Networks; 1994 Jun 28 - Jul 2; Orlando, FL, USA. IEEE. Available from:
http://ieeexplore.ieee.org/abstract/document/374785/

105. Guangcheng M, Guoxing Y, Qiyong W. Particle impact noise detection in sealed relays based on neural network. Proceedings of the Forty-Ninth IEEE Holm Conference on Electrical Contacts; 2003 Sep 10; Wahington,DC,USA. IEEE. 2003. Available from:
http://ieeexplore.ieee.org/abstract/document/1246500/

106. Zhai G, Chen J, Wang S, Li K, Zhang L. Material identification of loose particles in sealed electronic devices using PCA and SVM. Neurocomputing. 2015;148:222–8.

107. XU B, WANG S, ZHAI G. The Research of Remainder Particle Auto-detection System for Aerospace Electronic Installation. Electromechanical Components. 2008;2.

108. WANG S, GAO H, ZHAI G. The Research of Auto-Detection Algorithms For Remainder Particles of Aerospace Relay. J Astronaut. 2008; 1.

109. Yella S, Gupta N, Dougherty M. Comparison of pattern recognition techniques for the classification of impact acoustic emissions. Transp Res Part C. 2007; 15(6):345-360.

110. Anastasopoulos A. Pattern recognition techniques for acoustic emission based condition assessment of unfired pressure vessels. J Acoust Emiss. 2005;23:318-330.

111. Fernández-Delgado M, Cernadas E, Barro S. Do we need hundreds of classifiers to solve real world classification problems. J Mach Learn Res. 2014;15:3133-3181.

112. Wu X, Kumar V, Quinlan J, Ghosh J, Yang Q. Top 10 algorithms in data mining.

Inf Syst. 2008;14(1):1-37.

113. Hearst M, Dumais S, Osuna E, Platt J. Support vector machines. Syst their. 1998 ;13(4):18 - 28.

114. Marafino BJ, Davies JM, Bardach NS, Dean ML, Dudley RA, Boscardin J. N-gram support vector machines for scalable procedure and diagnosis classification, with applications to clinical free text data from the intensive care unit. J Am Med Informatics Assoc. 2014 Sep 1;21(5):871–5.

115. Hsu C, Chang C, Lin C. A practical guide to support vector classification [document on the internet]. 2003 [cited 2016 Jun 5]. Available from: http://citeseerx.ist.psu.edu/viewdoc/summary?doi=10.1.1.224.4115

116. Bhavsar H, Ganatra A. A comparative study of training algorithms for supervised machine learning. Int J Soft Comput. 2012;2(4):74-81.

117. Han J, Pei J, Kamber M. Data mining: concepts and techniques. Waltham(MA): Elsevier; 2011.

118. Wang G. A survey on training algorithms for support vector machine classifiers. In: Proceedings of Fourth International Conference on Network Computing and Advanced Information Management; 2008 Sep 2-4; Gyeongju, South Korea. IEEE. 2008. Available from: http://ieeexplore.ieee.org/abstract/document/4623990/

119. Kotsiantis S. Supervised machine learning: A review of classification techniques. In: Maglogiannis, I, Karpouzis K, Wallace M, editors. Emerging Artificial Intelligence Applications in Computer Engineering: Real World AI Systems with Applications in Ehealth, HCI, Information retrieval and Pervasive Technologies. Amsterdam: IOS Press;2007. p. 3-24.

120. Soman KP, Diwakar S, Ajay V. Insight into data mining : theory and practice. Prentice-Hall of India; 2006. 403 p.

121. Cichosz P. Data Mining Algorithms: Explained Using R. Hoboken (NJ): J. Wiley & Sons; 2014.

122. Zumel N, Mount J, Porzak J. Practical data science with R. New York:Manning Publications; 2014.

123. Kuhn M, Johnson K. Applied predictive modeling. Berlin:Springer;2013.

124. Standard Guide for Determining the Reproducibility of Acoustic Emission Sensor Response. ASTM-E976. West Conshohocken, PA: American Society for Testing and Materials; 2010.

125. Nivesrangsan P. Multi-source, multi-sensor approaches to diesel engine monitoring using acoustic emission. PhD[Dissertation].Edinburgh:Heriot-Watt University;2004.

126. Rossing T, Russell D. Laboratory observation of elastic waves in solids. Am J Phys. 1990;58(12):1153.

127. Sause M. Investigation of pencil-lead breaks as acoustic emission sources. J Acoust Emiss. 2011;29:184-196.

128. Vallen, J.; Vallen H. Latest improvements on Freeware AGU-Vallen-Wavelet. In: 29th European Conference on Acoustic Emission Testing; 2010 Sep 8 - 10; Vienna. European Working Group of Acoustic Emission; 2010. Available from: http://www.ndt.net/article/ewgae2010/papers/78_Vallen.pdf

129. Kuhn M. A Short Introduction to the caret Package. The Comprehensive R Archive Network [document on the internet]. 2016 [cited 2017 Feb 18]. Available from: http://camoruco.ing.uc.edu.ve/cran/web/packages/caret/vignettes/caret.pdf

130. Kuhn M. Caret package. J Stat Softw. 2008;8(5): 1- 26.

131. Husin S, Addali A, Mba D. Feasibility study on the use of the Acoustic Emission technology for monitoring flow patterns in two phase flow. Flow Meas Instrum. 2013;33:251–6.

132. Burstein GT, Sasaki K. Effect of impact angle on the slurry erosion–corrosion of 304L stainless steel. Wear. 2000;240(1):80–94.

133. Fuyan L, Hesheng S. The effect of impingement angle on slurry erosion. Wear. 1991;141(2):279–89.

134. McLaskey GC, Glaser SD. Acoustic Emission Sensor Calibration for Absolute Source Measurements. J Nondestruct Eval. 2012;31(2):157-168.

135. Hamstad M, O'Gallagher A, Gary J. Effects of lateral plate dimensions on acoustic emission signals from dipole sources. JAE.2001;19(1-4):258-274.

136. Prosser W, Hamstad M, Gary J. Finite element and plate theory modeling of acoustic emission waveforms. J. Nondestr. Eval. 1999:18(3):83-90.

137. Eaton M, Holford K, Featherston C, Pullin R. Damage in carbon fibre composites: the discrimination of acoustic emission signals using frequency. JAE. 2007;25:140–8.

138. Aljets D, Chong A, Wilcox S, Holford K. Acoustic emission source location in plate-like structures using a closely arranged triangular sensor array. JAE. 2010;28:85-98.